A GEM BASED TIME PROJECTION CHAMBER WITH PIXEL READOUT

Dissertation

zur Erlangung des Doktorgrades (Dr. rer. nat.) der
Mathematisch-Naturwissenschaftlichen Fakultät
der Rheinischen Friedrich-Wilhelms-Universität Bonn
vorgelegt von

CHRISTOPH BREZINA
aus Gießen

Bonn 2013

Christoph Brezina: *A GEM based Time Projection Chamber with Pixel Readout*, Commissioning of and measurements with a TPC with highly granular readout, © 2013

Die Deutsche Nationalbibliothek verzeichnet diese Publikation in der Deutschen Nationalbibliografie; detaillierte bibliografische Daten sind im Internet über http://dnb.ddb.de abrufbar.

Dieses Werk ist urheberrechtlich geschützt. Alle Rechte, auch die der Übersetzung, des Nachdruckes und der Vervielfältigung des Buches, oder Teilen daraus, vorbehalten.
This document is protected by copyright law. No part of this document may be reproduced in any form by any means without prior written authorization of the author/publisher.

This thesis has been published under ISBN: 9 783 863 873 301 by *Mensch und Buch Verlag, Berlin, Germany*.
Copies can be purchased at any bookstore.

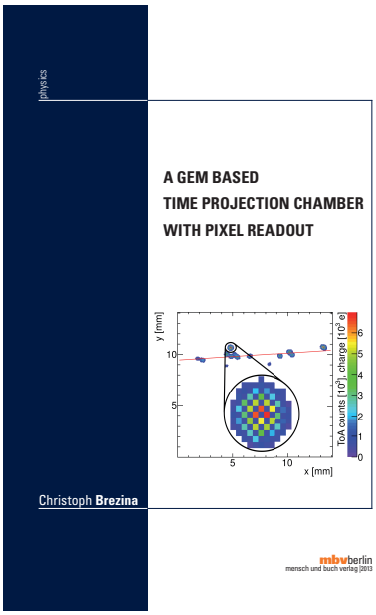

Angefertigt mit Genehmigung der Mathematisch-Naturwissenschaftlichen Fakultät der Rheinischen Friedrich-Wilhelms-Universität Bonn

1. Gutachter: Prof. Dr. Klaus Desch
2. Gutachter: Prof. Dr. Norbert Wermes

Tag der Promotion: 02.05.2013
Erscheinungsjahr: 2013

ABSTRACT

The large number of measured track points and the low material budget make a Time Projection Chamber (TPC) the ideal tracking device for particle flow optimized experiments. A highly segmented readout scheme, based on GEMs (Gas Electron Multipliers) or Micromegas, offers best performance.

The potential of charge collection on the bare pixels of a CMOS chip placed directly underneath a short-spaced triple GEM stack is evaluated in a TPC prototype with 26 cm drift distance. The employed Timepix ASIC features 256×256 pixels with 55 µm edge length. These allow for characterization of electron avalanches started by individual primary electrons. Down to small drift distances, where the pitch of the GEM holes (140 µm) becomes dominant, the spatial resolution of this pixel TPC is limited only by single electron diffusion.

For the readout of next generation gaseous detectors, development of an improved ASIC with 65 k pixels, offering simultaneous charge and arrival time measurements with nanosecond accuracy, is pursued.

ZUSAMMENFASSUNG

Aufgrund der großen Zahl der detektierten Spurpunkte sowie wegen der außerordentlich geringen Materialbelegung ist eine Zeitprojektionskammer (Time Projection Chamber / TPC) der ideale Spurdetektor für Experimente, die das Teilchenflusskonzept verfolgen. Die beste Detektorleistung wird mit einer sehr fein segmentierten Auslesestruktur in Verbindung mit GEMs (engl. Gas Electron Multipliers) oder Micromegas erreicht.

Die direkte Ladungssammlung auf den Pixeln eines CMOS Chips wird mit einem 26 cm langen TPC-Prototypen untersucht. In diesem ist ein Timepix ASIC mit 256×256 Pixeln mit je 55 µm Kantenlänge ohne Halbleitersensor direkt unter einem Stapel aus drei GEMs platziert. Die geringe Pixelgröße ermöglicht es, die Strukturen von, durch einzelne Primärelektronen verursachten, Elektronenlawinen aufzulösen. Bis hin zu sehr kleinen Driftdistanzen, bei denen der Abstand der GEM-Löcher (140 µm) limitierend wird, ist die räumliche Auflösung dieser Pixel-TPC nur durch die Diffusion der einzelnen Primärelektronen beschränkt.

Für die Auslese zukünftiger gasbasierter Teilchendetektoren wird die Entwicklung eines verbesserten Mikrochips mit 65 000 Pixeln zur gleichzeitigen Ladungs- und Ankunftszeitmessung voran getrieben.

LIST OF PUBLICATIONS

Some of the ideas and concepts elaborated in this thesis have already been presented in the reports and articles listed below:

A. Status of the Bonn R&D Activities for a Pixel Based TPC, In: *EUDET Memo 34 (2007)*.
A. Bamberger, C. Brezina, K. Desch, M. Henseler, M. Killenberg, T. Krautscheid, W. Ockenfels, U. Renz, M. Titov, M. Ummenhofer, N. Vlasov, P. Wienemann, S. Zimmermann and A. Zwerger

B. Update to the Status of the Bonn R&D Activities for a Pixel Based TPC, In: *EUDET Memo 30 (2008)*.
H. Blank, C. Brezina, K. Desch, J. Kaminski, M. Killenberg, T. Krautscheid, W. Ockenfels, and S. Zimmermann

C. Time projection chamber with triple GEM and pixel readout, In: *IEEE MIC/NSS CR (2008)*.
J. Kaminski, M. Killenberg, A. Bamberger, H. Blank, C. Brezina, K. Desch, T. Krautscheid, W. Ockenfels, U. Renz, M. Ummenhofer, P. Wienemann, S. Zimmermann and A. Zwerger

D. A Time Projection Chamber with triple GEM and pixel readout, In: *JInst 4.11 (2009)*.
C. Brezina, K. Desch, J. Kaminski, M. Killenberg, F. Klöckner, T. Krautscheid, U. Renz and M. Schumacher

E. Time projection chamber with triple GEM and highly granulated pixel readout, In: *DESY Conf. Proc. C0908171 (2009)*.
J. Kaminski, C. Brezina, K. Desch, M. Killenberg, F. Klöckner, T. Krautscheid and M. Schultens

F. GOSSIPO 3 - A front-end pixel chip prototype for readout of MPGDs, In: *EUDET Memo 02 (2009)*.
C. Brezina, K. Desch, H. van der Graaf, V. Gromov, R. Kluit, A. Kruth and F. Zappon

G. Gossipo-3: A prototype of a Front-End Pixel Chip for Read-Out of Micro-Pattern Gas Detectors, In: *TWEPP proceedings (2009)*.
C. Brezina, K. Desch, H. van der Graaf, V. Gromov, R. Kluit, A. Kruth and F. Zappon

H. GOSSIPO-3: measurements on the prototype of a read-out pixel chip for Micro-Pattern Gaseous Detectors, In: *JInst 5.12 (2010)*.
A. Kruth, C. Brezina, S. Celik, V. Gromov, R. Kluit, F. Zappon, K. Desch and H. van der Graaf

i. Development and Applications of the Timepix3 Readout Chip, In: *Proceedings of Science: Vertex 2011*.
V. Gromov, M. van Beuzekom, R. Kluit, F. Zappon, V. Zivkovic, M. Campbell, T. Poikela, X. Llopart, C. Brezina, K. Desch, X. Fang and A. Kruth

j. Architectural modeling of pixel readout chips Velopix and Timepix3, In: *JInst 7.1 2012*.
T. Poikela, J. Plòsila, T. Westerlund, J. Buytaert, M. Campbell, X. Llopart, R. Plackett, K. Wyllie, M. van Beuzekom, V. Gromov, R. Kluit, F. Zappon, V. Zivkovic, C. Brezina, K. Desch, X. Fang and A. Kruth

k. Operation of a GEM-TPC with pixel readout, In: *IEEE MIC/ NSS CR (2011)*.
C. Brezina, K. Desch, J. Kaminski, M. Killenberg and T. Krautscheid
Updated version published in: *IEEE TNS 59.6 (2012)*.

CONTENTS

LIST OF FIGURES

LIST OF TABLES

ACRONYMS

ASIC	Application Specific Integrated Circuit
CLIC	Compact LInear Collider
CMOS	Complementary Metal-Oxide-Semiconductor
CSA	Charge Sensitive Amplifier
DME	DiMethyl Ether
ENC	Equivalent Noise Charge
ESR	Equivalent Series Resistance
FEM	Finite Element Method
GEM	Gas Electron Multiplier
GOSSIP(O)	Gas On Slimmed Silicon Pixels (read Out)
IC	Integrated Circuit
ILC	International Linear Collider
ILD	International Linear Detector
InGrid	Integrated Grid
LHC	Large Hadron Collider
MPGD	Micro Pattern Gaseous Detector
Micromegas	MICRO MEsh GASeous
PCB	Printed Circuit Board
PLL	Phase Locked Loop
PSSR	Power Supply Rejection Ratio
SiD	SIlicon Detector
SPI	Serial Peripheral Interface
TDC	Time to Digital Converter
ToA	Time of Arrival
ToT	Time over Threshold
TPC	Time Projection Chamber
TtT	Time to Threshold

INTRODUCTION AND OUTLINE

During the last decades of the 20th century, the standard model of particle physics was established as gauge theory for the electro-weak and strong interactions. It precisely predicted phenomena and particles, partly long before they have been confirmed experimentally. It is common believe that the last missing corner stone of the standard model, the Higgs boson, just has been discovered at the Large Hadron Collider (LHC) in proton-proton collisions at center of mass energies of 7 TeV and 8 TeV [1, 2].

Though successful in general, the standard model has several shortcomings calling for extensions. The most prominent ones are:

- Only three of four known fundamental forces are described.
- The standard model does not account for the neutrino masses observed in neutrino oscillation experiments.
- The baryon asymmetry observed in the universe can not be explained by the standard model.
- Furthermore, it does not provide an explanation for dark matter nor dark energy, postulated by observational cosmology.

Hence, the discovery of the Higgs boson is not the final answer to particle physics but the first step in searches for physics beyond the standard model.

Without question, the LHC at CERN is the machine with the best discovery potential for new phenomena to date. However, due to the unknown initial state, the LHC experiments can not provide self-contained precision measurements determining all properties of new particles. Especially the total decay width of the observed Higgs like particle or its absolute couplings are not accessible model independently [3].

A lepton collider with a well controlled initial state, for example the International Linear Collider (ILC) [4] or the Compact LInear Collider (CLIC) [5] could overcome the limitations of the LHC and precisely determine the properties of newly developed or already known particles. The main goal is to measure the coupling strength between the Higgs boson and quarks, leptons and vector bosons at the few percent level, revealing whether the observed Higgs-like particle is the standard model object or something more complex [6].

Since ILC and CLIC pursue the same physics goals and differ primarily in the beam line technology, the detector concepts are similar, albeit different in machine-related aspects. Two different concepts are

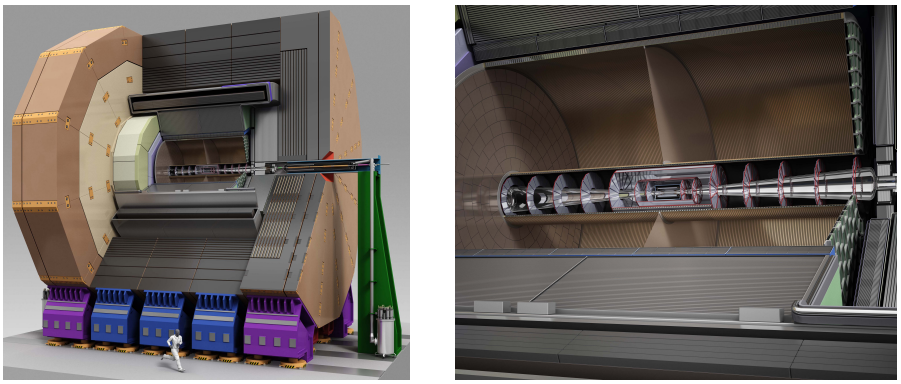

(a) (b)

Figure 0.1: Artistic view of of the ILD [9]. The entire detector arrangement (a) and a scale-up of the TPC and the inner silicon detectors are shown (b). Copyright Rey.Hori/KEK

pursued, the Silicon Detector (SiD) [7] and the International Large Detector (ILD) [8]. The conceptual difference between these two is the choice of the tracking detector. SiD will come with an all-silicon tracker, ILD with a gaseous device, namely a Time Projection Chamber (TPC). Due to these choices, the concepts differ in overall size and hence in the magnetic field necessary for momentum measurements.

One of the performance goals is to distinguish Z and W bosons in their hadronic decays. This imposes a jet energy resolution σ_E/E of 3 % to 4 % at $\mathcal{O}(100\,\text{GeV})$. The ILD concept is based on the belief that this ambitious goal is best reached by means of particle flow calorimetry [10].

An artistic view of the ILD is shown in figure 0.1. From the central to the outer regions, the main detector subsystems are:

- Three silicon pixel double layers compose the vertex detector.
- Silicon strip detectors close the gap between the central vertex detector and the surrounding TPC. Tracking at low angles is provided by silicon pixel and strip detectors in forward direction.
- A large TPC with $2\times2.3\,\text{m}$ length, 0.3 m inner and 1.8 m outer diameter provides $\mathcal{O}(100)$ 3-dimensional track points. This allows track, momentum and dE/dx measurements at the same time.
- The TPC is enclosed by a system of silicon strip detectors, which provide high precision entry points to the calorimeters.
- The calorimeter system is divided into an electro-magnetic and a hadronic calorimeter in the barrel region. High-precision radiation-hard calorimetric detectors are employed in the forward

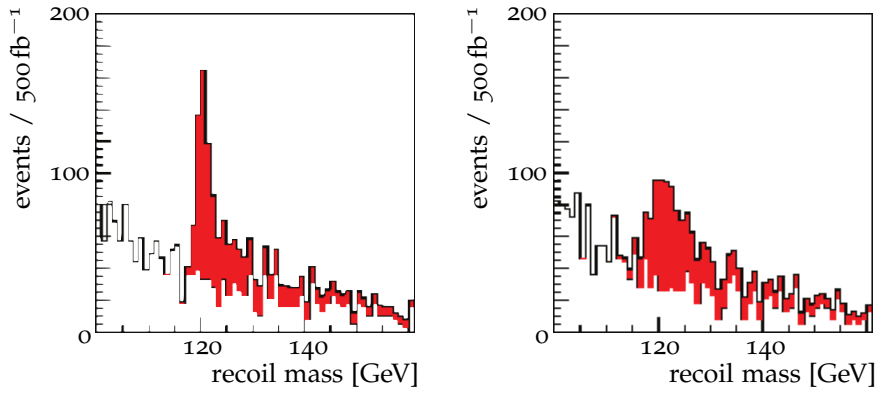

(a) $\delta(1/p_T) = 2 \times 10^{-5}$ /GeV/c (b) $\delta(1/p_T) = 8 \times 10^{-5}$ /GeV/c

Figure 0.2: Recoil mass spectrum expected for 120 GeV Higgs mass. The significance of the signal is crucially dependent on the achieved momentum resolution $\delta(1/p_T)$ [4].

direction. Following the particle flow paradigm, the calorimeters are highly segmented.

- The calorimeter system is surrounded by a superconducting solenoid, creating an axial magnetic field of up to 3.5 T.
- The magnetic field is confined by an iron return yoke which is instrumented with scintillators for muon detection.

In comparison with silicon detectors, both single-point and double-hit resolution of a TPC are moderate, a deficit which is compensated for by the enormous number of 3-dimensional track points. Besides, a TPC introduces only a modest amount of material in front of the calorimeters. This allows not only for best particle flow performance but helps also to reduce the background caused by beamstrahlung [11].

A total momentum resolution $\delta(1/p_T)$ better than 7×10^{-5} /GeV/c allows for precise determination of the Higgs mass from the recoil of the Z boson in Higgs-strahlung processes, see figure 0.2. Therefore, the momentum resolution of the TPC has to be at least 10^{-4} /GeV/c. This translates to a single-point resolution better than 100 µm perpendicular to the magnetic field and less than 1.4 mm in field direction. The double hit resolution of the TPC has to be in the order of a few millimeters. An energy resolution dE/dx better than 5 % would allow for distinct particle identification [8].

As a matter of fact, these demands exceed the performance of existing TPCs by up to an order of magnitude. Thus, the development of improved readout techniques, based on Micromegas [12] or Gas Electron Multipliers (GEMs) [13], is pursued. The classical approach, employing pads of a few square millimeters size for charge collec-

tion, is followed up in [14–17]. In the present thesis, an alternative approach is studied.

The theoretical and technical basis for setup and operation of a TPC is outlined in the first chapters:

- Starting with creation of the primary signal in the drift gas, the Fundamentals of Time Projection Chambers are elaborated in chapter 1. Discussion of the movement of free charge carriers and signal amplification in the gas phase allows to eventually outline how TPC drift gases are composed.
- Setup, operation, and performance of a versatile Gas Mixing System are described in chapter 2.

In the central chapters, a pixel TPC, which collects charges not on large pads but on pixels measuring $55 \times 55\,\mu m^2$, is comprehensively discussed:

- With special focus on operation and calibration of the integrated circuit, the setup of a TPC with a triple GEM stack for gas amplification and a bare Timepix [18] microchip for direct charge collection is presented in chapter 3.
- In chapter 4, Reconstruction and Basic Analysis of a data set recorded with cosmic rays are performed.
- After a detailed discussion of the detected charge depositions in chapter 5, the Detector Performance, namely the ionization density and the single-point resolution, is extracted from above data set.
- From time to time, Delayed Primary Electrons are observed. This new phenomenon is discussed in chapter 6.
- A heuristic Detector Simulation, based on microscopic simulations of single GEMs is presented in chapter 7.

In the last chapter, new readout electronics are described:

- Chapter 8 is dedicated to the development of Next Generation Readout Electronics, not only for readout of TPCs but also for a new type of gaseous detectors named GOSSIP.

1

FUNDAMENTALS OF TIME PROJECTION CHAMBERS

Improving classical drift chambers, D. Nygren proposed a new 4π detector for charged particles, the Time Projection Chamber (TPC) in 1974 [19]. With the TPC, a new concept for 3-dimensional track detection and momentum measurement was introduced.

The sensitive medium in a TPC is a gas, sometimes a liquid. Typically, it is contained in a cylindrical volume of up to a few cubic meters. Cathode and anode are placed at the cylinder end-caps, thus forming a capacitor. Field forming electrodes (field strips) along the cylinder homogenize the electric field, see figure 1.1.

Incident charged particles cause ionization along their trajectory in the medium. The created electrons and ions drift along the electric field towards the anode and the cathode, respectively. After being multiplied in a gas amplification stage, the primary electrons are detected on the segmented readout plane, while the ions are neutralized on the cathode.

Eventually, a projection of the track is recorded. The knowledge of the electron drift velocity v_{Drift} allows for reconstruction of the third

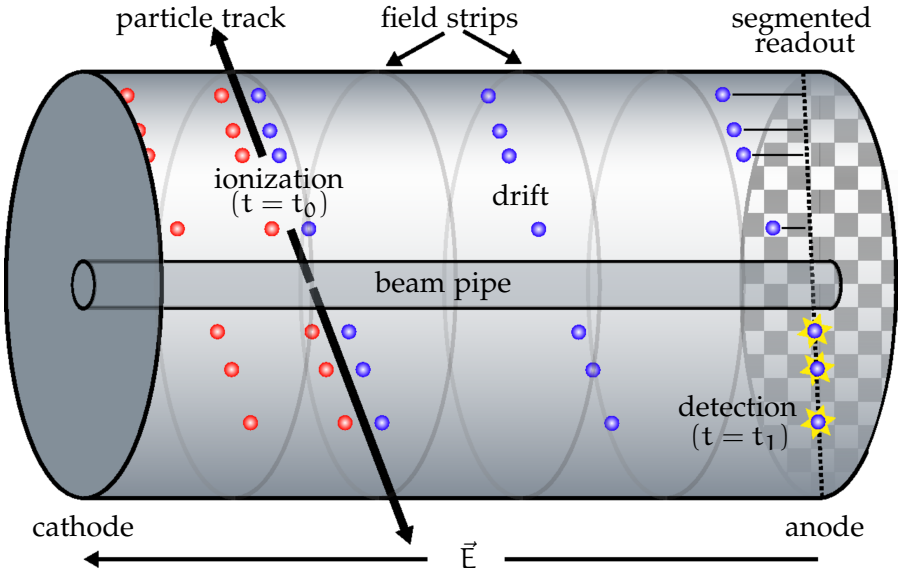

Figure 1.1: Operation principle of a TPC. An additional magnetic field in parallel with the electric field enhances the spatial resolution and enables measurements of particle momenta.

coordinate of the primary electrons from the drift time $t_{Drift} = t_1 - t_0$:

$$z = v_{Drift} \cdot t_{Drift}. \tag{1.1}$$

Commonly, TPCs are built with a central cathode and anodes at both ends of the field cage. This halves the read out times by dividing the detector into two subdetectors. If a TPC is applied as tracking detector at a particle accelerator, it is usually built around the beam pipe, which then forms an inner cylinder.

Although the single-point resolution of a TPC is excelled by modern silicon detectors, their track reconstruction is unmatched due to the enormous number of track points. Application of a magnetic field in parallel to the drift field bends the tracks of incident charged particles in the TPC, while the drift direction of the created free charge carriers remains unaffected. This allows for measurement of the particle momenta and enhances the single-point resolution as explained later.

In this chapter, the processes relevant for signal detection in a TPC are discussed. Section 1.1 covers the creation of the primary signal, section 1.2 the movement of free charge carriers in a gas. The signal amplification in the gas phase is discussed in section 1.3. The composition of the drift gas is strongly constrained by all of these processes which is why the last section (1.4) deals with the choice of TPC drift gases.

1.1 INTERACTION OF CHARGED PARTICLES WITH MATTER

Charged particles passing through matter cause ionization and excitation in the medium by scattering off atomic electrons. They may also lose energy by bremsstrahlung, pair production and photonuclear interactions. As stated in [20], the total energy loss dE per track segment $dx = \rho ds$ (ρ: absorber density, ds: covered distance) is given by:

$$-\left.\frac{dE}{dx}\right|_{total} = -\left.\frac{dE}{dx}\right|_{ion./exc.} - \left.\frac{dE}{dx}\right|_{brems.} - \left.\frac{dE}{dx}\right|_{pair\ prod.} - \left.\frac{dE}{dx}\right|_{photonucl.}. \tag{1.2}$$

It is sketched in figure 1.2 for muons in copper.

1.1.1 *Processes Causing Energy Loss*

The influence of the radiative processes represented by the latter three terms of equation 1.2 is proportional to the energy of the incident particle. Therefore, for muons, these processes are negligible up to particle energies of several hundred GeV [22].

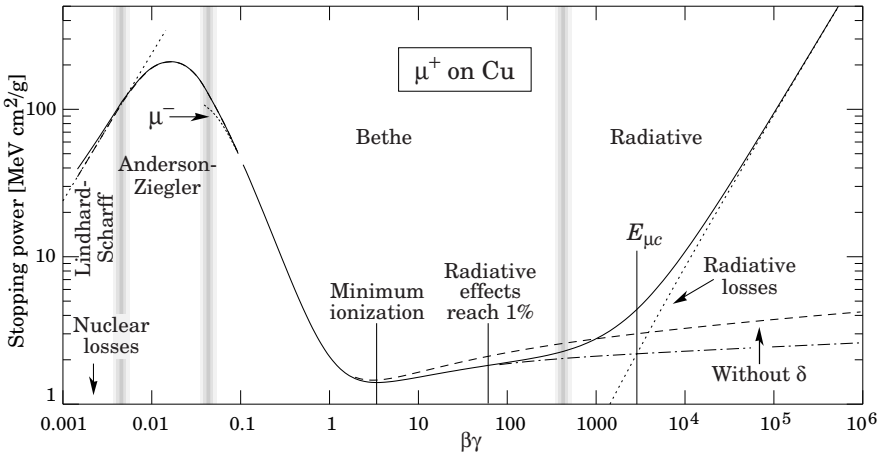

Figure 1.2: Stopping power (energy loss) for myons in copper as a function of the momentum $\beta\gamma$ [21].

1.1.1.1 *Ionization and Excitation*

The maximal amount of energy transferred per scattering process from an incident particle with mass m to an atomic electron with mass m_e is given by:

$$E_{kin}^{max}(\beta\gamma) = \frac{2m_e c^2 \beta^2 \gamma^2}{1 + 2\gamma m_e/m + (m_e/m)^2}. \tag{1.3}$$

In Eq. 1.3, γ denotes the Lorentz factor, c the speed of light in vacuum and $\beta c = v$ the velocity of the particle [22]. If the incident particle has a moderate energy ($2\gamma m_e/m \ll 1$) and is heavier than an electron ($m \gg m_e$), this simplifies to:

$$E_{kin}^{max}(\beta\gamma) = 2m_e c^2 \beta^2 \gamma^2. \tag{1.4}$$

The Bethe equation [23, 24] approximates the average energy loss by ionization and excitation $\frac{dE}{dx}|_{ion./exc.}$ for heavy particles with energies up to several 100 GeV:

$$-\frac{dE}{dx}\bigg|_{ion./exc.} = \kappa \frac{1}{\beta^2}\left[\frac{1}{2}\ln\left(\frac{2m_e c^2 \beta^2 \gamma^2 E_{kin}^{max}(\beta\gamma)}{I^2}\right) - \beta^2 - \frac{\delta(\beta\gamma)}{2}\right]. \tag{1.5}$$

For convenience $\kappa = 4\pi N_A r_e^2 m_e c^2 z^2 \frac{Z}{A}$ has been introduced, with:

- $N_A = 6.022 \cdot 10^{23}/\text{mol}$ the Avogadro number,
- $r_e = e^2/4\pi\epsilon_0 \cdot m_e c^2$ the classical electron radius; ϵ_0 the vacuum permittivity,
- z the charge of the incident particle in units of the elementary charge e,

- Z and A atomic number and weight of the absorber material.

If the dependency on the molecular state is neglected, the mean excitation energy I of an absorber atom can be approximated for $Z > 1$ by $I \approx 16 \cdot Z^{0.9}\text{eV}$. A function $I(Z)$ was found first by F. Bloch. Therefore, equation 1.5 is usually referenced as Bethe-Bloch formula.

Originally, the parameter $\delta(\beta\gamma)$ was not part of the Bethe formula. It was introduced by E. Fermi [25] and describes to what extent polarizable absorber atoms shield the electric field of an incident relativistic particle and reduce, therefore, the energy loss. The screening increases with the absorber density, hence, the correction is called density effect. For absorbers with low densities like gases at moderate pressures the density effect may be neglected, while it has to be taken into account for dense absorbers like lead or iron.

The Bethe formula is only valid for particles with $\beta \gg \alpha z$ (fine structure constant $\alpha = e^2/4\pi\epsilon_0\hbar c$). Within the region of validity, the energy loss drops with rising $\beta\gamma$ of the incident particle like $1/\beta^2$, reaches a broad minimum at $\beta\gamma \approx 4$ and increases again due to the logarithmic term which is suppressed by the density correction, see figure 1.2. In light absorber materials the minimal energy loss is given by $\frac{dE}{dx}|^{\text{min}}_{\text{ion./exc.}} \approx 2\,\frac{\text{MeV}}{\text{g/cm}^2}$. Particles with this energy loss are called Minimally Ionizing Particles (MIPs). Above $\beta\gamma \approx 100$, the energy loss is dominated by bremsstrahlung. Thus, the Bethe approximation is not valid in this regime.

The Bethe equation describes the mean energy loss of charged particles by scattering processes. For single collisions, a broad spread around the mean value with a long tail to high energies is found. This tail is caused by single collisions with a large energy transfer to atomic electrons. These highly energetic δ- or knock-on electrons depose their kinetic energy by further ionization along their track in the gas. Because of the kinematics, such secondary tracks tend to have a large angle ($\approx 90°$) with respect to the track of the primary particle.

Due to the tail, the most probable value is significantly lower than the mean, calculated from the Bethe approximation. For absorbers of moderate thickness, the energy loss distribution is described by a Landau distribution [26]. Thin absorbers as the gas in a TPC or thinned silicon sensors cause distributions significantly wider than the Landau distribution [27]. In thick absorbers, when the mean energy transfer of several interactions is measured, the distribution gets less skewed.

1.1.1.2 *Bremsstrahlung*

Charged particles emit photons when a force acts on them. This process is called bremsstrahlung. The energy loss by bremsstrahlung in the Coulomb field of absorber nuclei rises linearly with the energy E

of incident charged particles, c.f. Fig. 1.2. For high energies, it can be parametrized by:

$$-\left.\frac{dE}{dx}\right|_{\text{Brems.}} = 4\alpha N_A \frac{z^2 Z^2}{A} \ln\left(\frac{183}{\sqrt[3]{Z}}\right)\left(\frac{1}{4\pi\epsilon_0}\cdot\frac{e^2}{mc^2}\right)\cdot E. \tag{1.6}$$

All symbols have the same meaning as in section 1.1.1.1 [28].

Bremsstrahlung is the dominant contribution to the total energy loss of light particles as electrons. The bremsstrahlung of electrons is used to define the radiation length X_0. The latter is the mean distance in which electrons loose all but $1/e$ of their starting energy E_0:

$$-\left.\frac{dE}{dx}\right|_{\text{Brems.}} = \frac{E_0}{X_0}. \tag{1.7}$$

The radiation length is a good measure for the transparency of matter. In order to minimize track distortions by scattering processes, the radiation length should be large in tracking detectors.

1.1.1.3 *Direct Pair Production*

Above an energy threshold of two electron masses m_e, a photon γ may cause the production of an electron-positron pair in the vicinity of a nucleus X. The latter absorbs any excess momentum in the process:

$$\gamma + X \longrightarrow e^- + e^+ + X. \tag{1.8}$$

If the photon energy is larger than $2m_e$, the additional energy is converted to kinetic energy of the created electron-positron pair.

If an incident massive particle A has enough energy, this process may be triggered by a virtual photon emitted in the Coulomb field of an absorber nucleus X:

$$A + X \longrightarrow A + e^- + e^+ + X. \tag{1.9}$$

The energy loss of massive particles due to direct pair production can be parameterized by:

$$-\left.\frac{dE}{dx}\right|_{\text{pair prod.}} = b_{\text{pair prod.}}(A, Z, E)\cdot E. \tag{1.10}$$

The variation of the parameter $b_{\text{pair prod.}}(A, Z, E)$ with the energy E is small for energies above 100 GeV [22]. Therefore, the effect of direct pair production can be considered to be proportional to the energy of the incident particle in this regime.

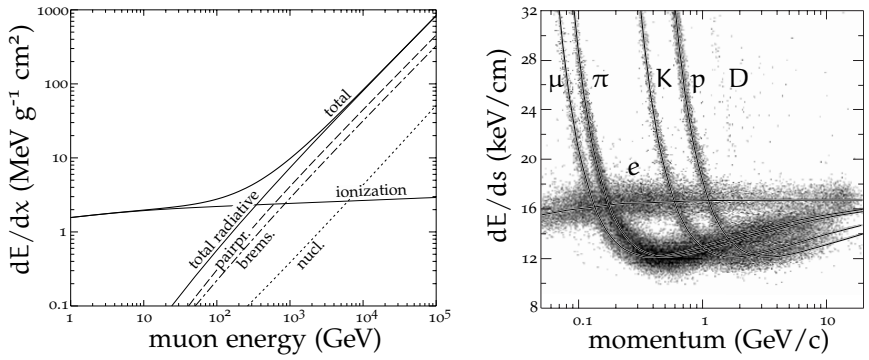

(a) (b)

Figure 1.3: a) Contributions to the energy loss of muons in iron [21].
b) Specific dE/ds for high energetic particles detected with the PEP4/9-TPC [21].

1.1.1.4 *Photonuclear Interactions*

Virtual photons may be exchanged also directly with an absorber nucleus. The energy loss by photonuclear interactions can be parameterized like the energy loss for direct pair production:

$$-\left.\frac{dE}{dx}\right|_{\text{photonucl.}} = b_{\text{photonucl.}}(A, Z, E) \cdot E. \tag{1.11}$$

Since the factor $b_{\text{photonucl.}}$ does hardly depend on the energy, the process is considered to be proportional to the energy of the incident particle [22]. However, compared to bremsstrahlung and direct pair production the effect is small.

1.1.2 *Total Energy Loss*

As stated in the beginning of this section, the total energy loss per track segment is given by the sum of the processes described in section 1.1.1. The separate contributions are depicted in figure 1.3a for high energetic muons in iron. The energy at which radiative and ionization losses are equal for incident particles is labeled critical energy E_C [24]. The critical energy of muons in iron $E_{\mu C}$ is roughly 200 GeV.

As long as the energy of the incident particles is well below the critical energy, radiative losses may be neglected and the energy loss is well described by the Bethe formula (Eq. 1.5). Thus, the energy loss depends not only on the momentum of the incident particle, but also on the particle type. Therefore, dE/dx measurements can be used for particle identification if the particle momentum is known. This is the case in TPCs or other detectors with a sufficient granularity. The specific energy loss of high energetic particles detected with the PEP4/9-TPC is shown in figure 1.3b. It is clearly visible that the specific energy loss of electrons differs qualitatively from the energy loss of heavy particles.

Gas	I_0 [eV]	W [eV]	$\frac{dE}{dx}$ [$\frac{keV}{cm}$]	n_P [$\frac{1}{cm}$]	n_T [$\frac{1}{cm}$]
He	24.5	41	0.32	4.2	8
Ne	21.56	36.3	1.56	12	43
Ar	15.7	26	2.44	23	94
Xe	12.1	22	6.76	44	307
CF_4	15.9	54	7	51	100
DME	10.0	23.9	3.9	55	160
CO_2	13.7	33	3.01	35.5	91
CH_4	15.2	28	1.48	25	53
C_2H_6	11.7	27	1.15	41	111
iC_4H_{10}	10.6	23	5.93	84	195

Table 1.1: Effective ionization potential I_0, average energy needed to create an electron-ion pair W, energy loss $\frac{dE}{dx}$, number of primary produced electrons n_P and total number of created electron-ion pairs n_T for selected gases at standard conditions for minimally ionizing particles [29].

1.1.3 *Ionization Yield*

The excitation energy of an atom or molecule A may exceed the ionization energy of an atom B in inhomogeneous absorber materials as gas mixtures. In this case, excitation of A may cause ionization of B:

$$A^* + B \longrightarrow A + B^+ + e^-. \tag{1.12}$$

This is called Penning effect. In consequence, the number of created electron-ion pairs increases.

The total number of electron-ion pairs created by an energy deposition ΔE is labeled n_T. This includes not only n_P, the number of primary created electron-ion pairs, but also secondary ionization by δ-electrons, the Penning effect or other processes. The value of n_T is given by:

$$n_T = \frac{\Delta E}{W}, \tag{1.13}$$

where W denotes the average energy needed to create an electron-ion pair. For gas mixtures, a weighted average for n_P and n_T may be computed [29].

The ionization potential I_0 of a gas is exceeded by W since a fraction of the absorbed energy is dissipated by excitation processes. For most gases, W is around 30 eV. There is only a small dependency on the type of the ionizing particle. Exemplary values for I_0, W, n_P and n_T are summarized in table 1.1.

1.2 CHARGE TRANSPORT IN GASES

If free charge carriers in gases do not recombine, they move through the gas volume. This movement originates from two different processes happening simultaneously. One is drift caused by an external field, the other is diffusion due to collisions with the gas molecules.

1.2.1 *Drift*

When exposed to electric ($\vec{E}$) and magnetic ($\vec{B}$) fields, free charge carriers with charge q are subject to the Lorentz force. The resulting energy gain causes a directed movement that adds to the thermal undirected movement.

Since charge carriers are not only deflected but also decelerated in collisions with gas molecules, their drift velocity does not rise ad infinitum. Averaged over several collisions, a limited drift velocity $\vec{v}_{\text{Drift}} = \dot{\vec{x}}$ is reached instead. This has to be considered in the equation of motion for drifting particles.

Following P. Langevin [30, 31] the effect of repeated collisions can be expressed by a friction force: $m\vec{A} = -m\dot{\vec{x}}/\tau$, where τ is the average time between two collisions and m the mass of the drifting particle. Thus, for a drifting particle with charge q, the equation of motion reads:

$$\vec{F} = m\ddot{\vec{x}} = q \cdot \left(\vec{E} + \dot{\vec{x}} \times \vec{B}\right) + m\vec{A}. \tag{1.14}$$

Assuming that the acceleration by the Lorentz force is compensated by the friction force at some point, a steady state ($\vec{F} = 0$) is reached for long times $t \gg \tau$. In this case, the drift velocity $\vec{v}_{\text{Drift}}$ is given by:

$$\vec{v}_{\text{Drift}} = \dot{\vec{x}} = \frac{\mu}{1 + \omega^2\tau^2} \cdot \left(\vec{E} + \frac{\vec{E} \times \vec{B}}{B}\omega\tau + \frac{\left(\vec{E} \cdot \vec{B}\right)\vec{B}}{B^2}\omega^2\tau^2\right). \tag{1.15}$$

For convenience, the cyclotron frequency $\omega = qB/m$ and the mobility $\mu = q\tau/m$ have been introduced.

If $\vec{E}$ and $\vec{B}$ are (anti-)parallel equation 1.15 simplifies to:

$$\vec{v}_{\text{Drift}} = \mu\vec{E}. \tag{1.16}$$

This is usually the case in Time Projection Chambers.

If there is a significant angle between the electric and the magnetic field, so-called $\vec{E} \times \vec{B}$ effects become important. In this case the (Lorentz-) angle between $\vec{E}$ and $\vec{v}_{\text{Drift}}$ is given by $\tan\alpha_L = \omega\tau$. In the extreme case with $\vec{E}$ and $\vec{B}$ being orthogonal to each other, the absolute value of $\vec{v}_{\text{Drift}}$ is given by:

$$|\vec{v}_{\text{Drift}}| = \frac{\mu|\vec{E}|}{\sqrt{1 + \omega^2\tau^2}}. \tag{1.17}$$

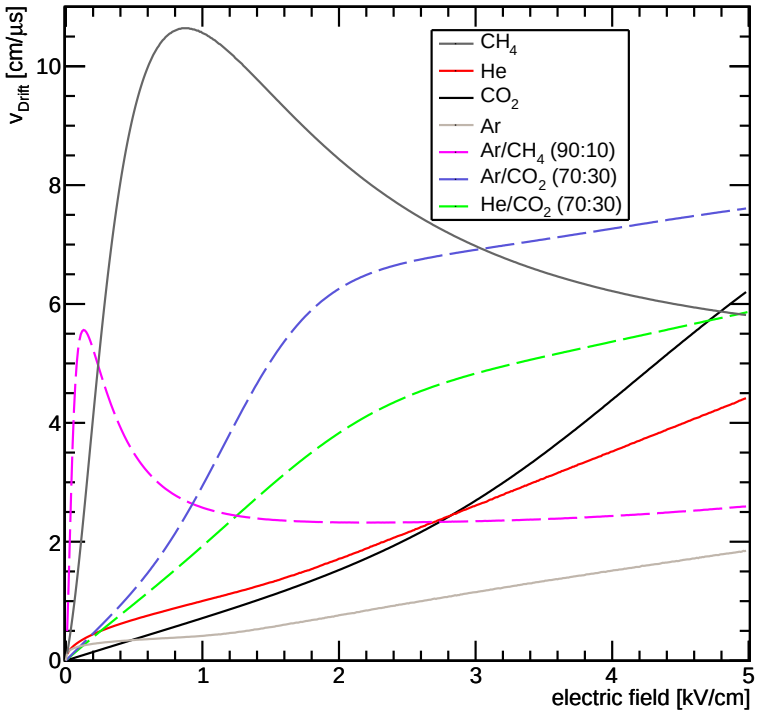

Figure 1.4: Electron drift velocity as a function of the electric field in several gases at normal conditions. Dashed lines depict data for gas mixtures. Data computed with Magboltz [33].

The charge carrier mobility μ is proportional to the mean time between two encounters with gas molecules. The latter depends on the cross section for scattering processes σ:

$$\tau = 1/\left(N\sigma v_{mfp}\right), \tag{1.18}$$

where N is the number density of the gas and v_{mfp} the velocity of the drifting particle on the mean free path between two encounters [32].

For electrons, the cross section is strongly dependent on the energy and accordingly on the electric field. This dependence originates from the Ramsauer effect which results in a drop of the cross section when the electron wavelength approaches the de Broglie wavelength of atomic electrons. In consequence, no simple correlation between v_{Drift} and $\vec{E}$ can be derived. Nevertheless, Monte Carlo calculations allow for prediction of the drift velocities, see section 3.4.2. Simulated electron drift velocities in dependence on the electric field are shown in figure 1.4 for several gases. The characteristics of the electron scattering cross section eventually result in a distinct maximum for some gases.

The scattering cross section for ions, in contrast, is independent of the energy in a wide range. Therefore, the ion drift velocity is proportional to the electric field, if $\vec{B} = 0$ or $\vec{E} \parallel \vec{B}$. The drift velocity of ions is up to three orders of magnitude smaller than the drift velocity of electrons due to the mass dependency.

1.2.2 *Diffusion*

Electrons and ions exchange energy with gas molecules in collisions. Thus, when no external field is applied, their energy approaches the thermal Maxwell-Boltzmann distribution of the gas. After thermalization, their thermal energy is given by $\epsilon = 3/2 k_B T$, with the Boltzmann constant k_B and the gas temperature T. The resulting instantaneous velocity is randomly oriented. The magnitude is given by $v_{\text{Therm.}} = \sqrt{2\epsilon/m}$, where m is either the electron or the ion mass.

If an external field is applied, the total energy ϵ_{total} of a drifting charge carrier is given by the sum of the thermal energy and the kinetic energy ϵ_E from drift:

$$\epsilon_{\text{total}} = \epsilon_E + 3/2 k_B T = \frac{1}{2} m v_{\text{total}}^2 = \frac{1}{2} m (\vec{v}_{\text{Therm.}} + \vec{v}_{\text{Drift}})^2. \quad (1.19)$$

For many gases (e.g. Ar, CH_4), $\epsilon_{\text{total}} = \epsilon_E$ is a good approximation for drifting electrons. In contrast to these *hot* gases, there are *cold* gases like CO_2 where ϵ_{total} is close to $3/2 k_B T$. In the latter case, vibrational and rotational degrees of freedom are available even at very low collision energies. Therefore, the cross section is large and the time between two collisions is small. This prevents electrons from achieving high velocities between two collisions.

A point-like electron cloud diffuses due to thermal movement and ongoing collisions with gas molecules, even if no external field is applied. If an electric field is applied along the z-axis, the electron cloud simultaneously diffuses apart and drifts along the field. Assuming an isotropic behavior, a point-like cloud which has drifted the distance $z_{\text{Drift}} = t v_{\text{Drift}}$ after a time t shows a Gaussian density distribution:

$$N(t) = (4\pi \tilde{D} t)^{-3/2} \cdot \exp\left(-\frac{r^2(t)}{4\tilde{D}t}\right), \quad (1.20)$$

with $r^2(t) = x^2 + y^2 + (z - z_{\text{Drift}}(t))^2$ and the diffusion coefficient $\tilde{D}$ [34]. The width of the distribution σ in any direction is given by:

$$\sigma = \sqrt{2\tilde{D}t}. \quad (1.21)$$

Introducing the diffusion constant $D = \sqrt{2\tilde{D}/v_{\text{Drift}}}$ allows to describe the width of the distribution in dependence on the drift distance:

$$\sigma = \sqrt{2\tilde{D}\frac{z_{\text{Drift}}}{v_{\text{Drift}}}} = D\sqrt{z_{\text{Drift}}}. \quad (1.22)$$

Since the diffusion is caused by collisions with the gas, the diffusion coefficient is dependent on the mean free path $\lambda = \tau v_{\text{total}}$. Following [34] this dependence is given by:

$$\tilde{D} = \frac{\lambda^2}{3\tau} = \frac{1}{3}\tau v_{\text{total}}^2 = \frac{2}{3}\frac{\epsilon_{\text{total}}\tau}{m}. \quad (1.23)$$

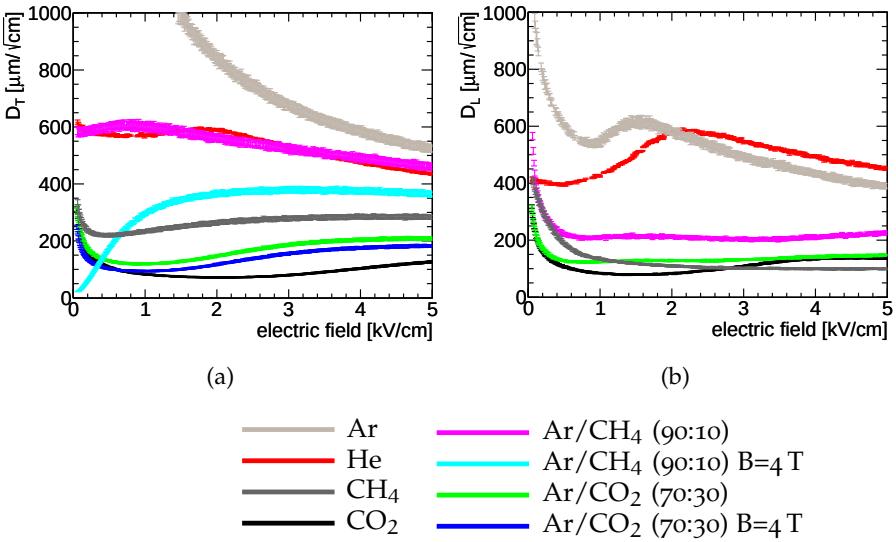

Figure 1.5: Transversal (a) and longitudinal (b) diffusion constants for several gases. Data computed with Magboltz [33].

Close inspection of equation 1.23 reveals that an anisotropy is introduced by an external electric field because the mean time τ between two encounters varies from the leading to the trailing edge of the drifting charge cloud since the cross section is energy dependent. This results in different diffusion constants in longitudinal (D_L along $\vec{E}$) and transversal (D_T perpendicular to $\vec{E}$) direction. The width of a charge cloud after a drift distance z is given by:

$$\sigma_{xy} = D_T\sqrt{z} \qquad \text{and} \qquad \sigma_z = D_L\sqrt{z} \tag{1.24}$$

in transversal and longitudinal direction respectively. An exact calculation of the ratio between the diffusion constants can be found in [32].

If a magnetic field $\vec{B}$ is applied in parallel to the electric field, the electron trajectory between two encounters is a helix around $\vec{B}$. This curling of any motion in the x-y plane reduces the transversal diffusion by a factor of $1/(1+\omega^2\tau^2)$:

$$D_T(B) = \frac{1}{(1+\omega^2\tau^2)} D_T(B=0). \tag{1.25}$$

The longitudinal diffusion is not affected by the magnetic field.

Transversal and longitudinal diffusion constants in dependence on the applied drift field are shown in figure 1.5 for several gases. The suppression of the transversal diffusion by an external magnetic field can be seen on the example of argon with CO_2 or CH_4 admixtures.

1.3 GAS AMPLIFICATION

Although there have been reasonable achievements in the development of readout electronics in the last years, it is not possible to directly detect single electrons with a charge sensitive amplifier. To overcome this limitation, it is necessary to amplify the signal within the gas phase.

This is done in high electric fields in which drifting electrons may gain enough energy to cause ionization. The newly created free electron is accelerated together with the first electron. As long as the electric field strength is sufficient, both of them may cause ionization again. Eventually, an electron avalanche develops. During the movement of N_0 electrons along a path dr, dN new electron-ion pairs are created:

$$dN(r) = \alpha(r) N_0 \, dr. \tag{1.26}$$

In this equation, $\alpha = 1/\lambda$ is the first Townsend coefficient, i.e. the inverse of the mean free path for ionization λ. Since the ionization cross section depends on the electric field, which in turn may depend on the position, the Townsend coefficient may depend on the position as well.

If one assumes that the ionization threshold is exceeded between positions r_1 and r_2 the total number of electron-ion pairs created by N_0 primary electrons is given by:

$$N = N_0 \exp\left(\int_{r_1}^{r_2} \alpha(r)\, dr\right) = N_0 \cdot \bar{G}, \tag{1.27}$$

where $\bar{G}$ is the mean gas gain.

In inhomogeneous electric fields, the gain resembles a Pólya distribution:

$$P(G) = \frac{1}{\bar{G}} \frac{(\Theta+1)^{\Theta+1}}{\Gamma(\Theta+1)} \left(\frac{G}{\bar{G}}\right)^{\theta} \cdot \exp\left(-(\Theta+1)\frac{G}{\bar{G}}\right). \tag{1.28}$$

The parameter Θ is calculated from the width of the distribution σ, by $\Theta = (\bar{G} - \sigma^2)/\sigma^2$ [32].

The simulated total gas gain in a GEM (Sec. 1.3.4) is depicted in figure 1.6. The histogram entries for vanishing gas gains evoke from attachment to electronegative gases (Sec. 1.4). They are not covered by the Pólya distribution.

Up to now, virtually all large TPCs have been operated with wires as gas amplification stage. An exception is the TPC at the T2K experiment [35]. Therefore, the gas amplification in Multi Wire Proportional Chambers (MWPCs) is explained first in this section.

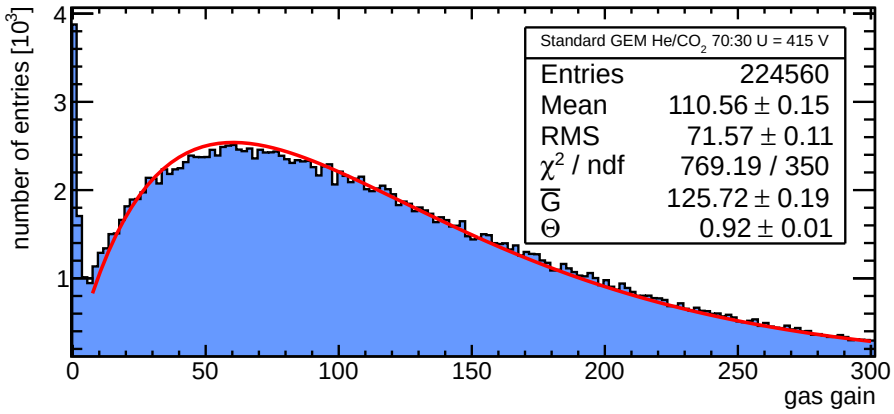

Figure 1.6: Simulated total gas gain in a standard CERN GEM in helium with 30 % CO_2 admixture at $\Delta U_{GEM} = 415\,V$. The Data are resembled by a Pólya distribution.

However, common belief is that the performance of wire chambers is excelled by Micro Pattern Gaseous Detectors (MPGDs). Hence, this section focuses on micro patterned amplification stages like MICRO MEsh GAseous Structures (Micromegas) or Gas Electron Multipliers (GEMs) which are introduced later on.

1.3.1 *Wires*

The electric field of a wire has a $1/r$ dependence, where r is the distance to the wire center. Therefore, the limits for the integral in equation 1.27 are given by the critical radius at which the field is large enough for amplification and the diameter of the wire. Obviously small wire diameters are favorable in order to achieve large electric fields respectively large gain factors.

The dependence of the gain on the wire potential is discussed in full detail in [32, 36, 37]. Here, the characteristics are only roughly sketched. The gain factor rises with the wire potential until a region of saturated gain, the Geiger-plateau, is reached. Here, the electron energies allow to excite electrons from the inner shells of the gas atoms. The subsequently emitted UV-photons have a relatively long mean free path and enough energy to start secondary avalanches. Thus, the signal is no longer localized but propagated over the whole wire. In consequence, the proportionality between the signal and the incoming charge is lost.

While the electrons created in an avalanche are drained quickly by the wire, the ions form a quasi stationary flux tube around the wire. The space charge of the ions causes a reduction of the effective electric field which in turn terminates the signal. On a longer time scale, the ions drift slowly to the cathode. With a certain probability, they liberate new electrons on their impact which, in the end, cause

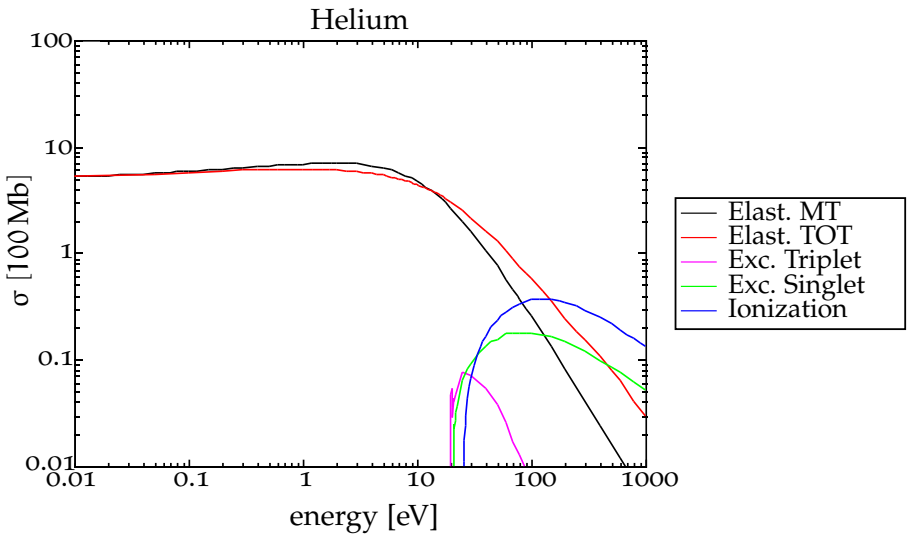

Figure 1.7: Scattering cross sections for electrons drifting in He. The energy needed for ionization is in the same range as the other possible inelastic interactions [38].

secondary avalanches. A further increase in the wire potential results in a continuous glow discharge with a plasma path between anode and cathode.

A stable wire chamber operation can only be achieved, if glow discharges and secondary avalanches are suppressed. This can be done by turning down the wire potential after a signal has been detected; either actively or with a charging resistor in series with the wire. More commonly, a self-quenching is achieved by adding gases with rotational or vibrational degrees of freedom to the counting gas which is usually a noble gas.

Quenching

A characteristic of noble gases is that there exists no internal degree of freedom at low energies. From the exemplary graph for helium, depicted in figure 1.7, it can be seen that the first excited states are in the same energy range as ionization. This has a strong impact on the usage of noble gases in gaseous detectors.

On the one hand, free electrons reach a high energy between two encounters. This results in a large multiplication factor during amplification. On the other hand, the gas is transparent for UV-photons emitted in the amplification process. This causes a delocalization of the signal. Both effects result eventually in discharges. These can be prevented by the admixture of a quenching gas.

Commonly, organic gases as hydrocarbons or alcohols are used as quenching gas, sometimes CO_2 or halides. All these have in common that they introduce several vibrational and rotational degrees of freedom to the mixture. Furthermore, the total cross section is about one

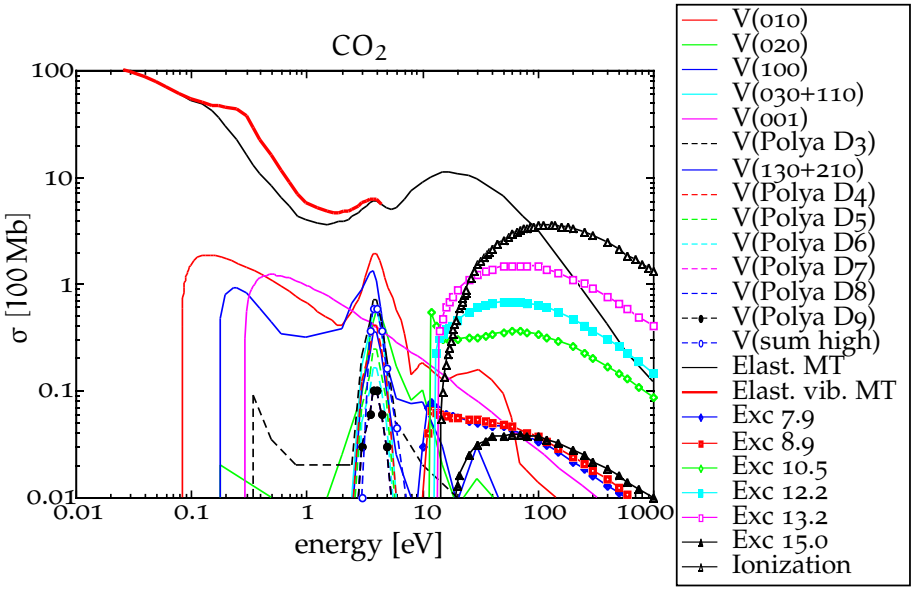

Figure 1.8: Scattering cross sections for electrons drifting in CO_2. Several excited and vibrational states are available at low energies [38].

order of magnitude larger than in noble gases. In figure 1.8 the cross sections for CO_2 are shown exemplarily.

The absorption length for UV photons is drastically reduced in gases with quenching admixtures. Thus, electron avalanches remain localized [39]. In localized ionization clouds, the space charge created by the slowly drifting ions reduces the electric field down to a noncritical value where no further ionization happens. Thus, the amplification process is self-terminated.

Additionally, the ions of the counting gas become neutralized in collisions with the quencher:

$$Ar^+ + CH_4 \longrightarrow Ar + CH_4^+. \tag{1.29}$$

The energy of the molecule ions is not sufficient to liberate electrons from the cathode. Therefore, no secondary avalanches are started upon the ion impact on the cathode [22].

1.3.2 *Multiwire Proportional Chambers*

The MWPC was invented in 1968 by G. Charpak [40]. This achievement was honored 1992 with the Nobel Prize in physics. Nowadays, the most famous gaseous detector with wire readout may be the ALICE TPC [41] at the LHC (CERN). The drift chamber is read out with several wires strained perpendicular to the drift field. Due to their operation mode such detectors are called Multi Wire Proportional Chambers (MWPCs).

Simple readout of only the anode wires does not give a two dimensional information. A two dimensional readout can be realized if a

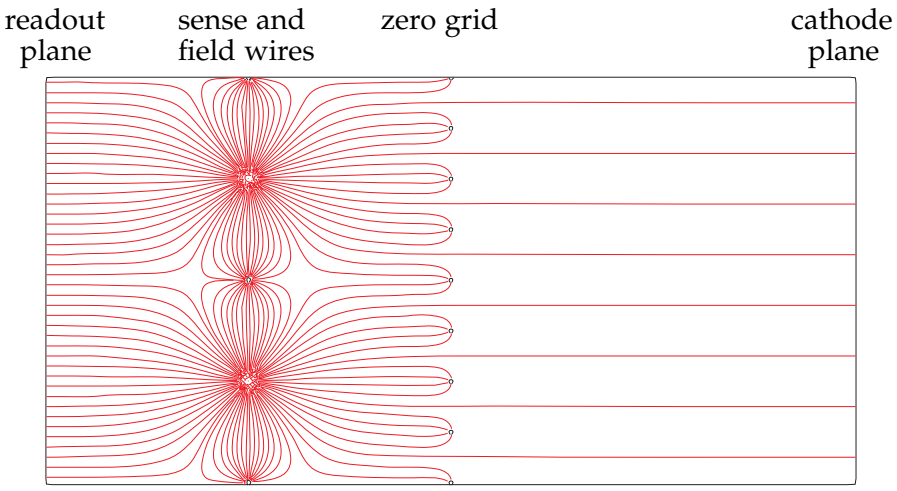

Figure 1.9: Electrical field lines and electrode positions in a drift chamber with MWPC readout [42].

segmented cathode is placed underneath the anode wires. Originally, strips perpendicular to the wires were foreseen. Nowadays, pads of a few square millimeters size are used.

The field configuration in a drift chamber with MWPC like gas amplification stage is depicted in figure 1.9. The drift area is terminated by the cathode plane and the zero grid. The latter is usually fixed at ground potential. The anode wires are centered between the zero grid and the readout plane, which is on the same potential as the zero grid. Crosstalk between the anode wires can be reduced by straining field wires alternating with the anode wires. Leaving out the field wires allows not only to reduce the anode wire spacing, but also increases the amount of charge collected on the readout plane.

In principle, the signal seen on the readout pads originates from both, the ion and the electron movement. However, the readout electronics usually cut away the signal after a few µs. Thus, the signal contribution of the slowly drifting ions is limited.

If a signal is induced on neighboring pads it is possible to calculate the original position of the electron avalanche based on a center of gravity algorithm. This allows to obtain spatial resolutions significantly smaller than the pad size. However, the spatial resolution is not only limited by the detector geometry, but also by $\vec{E} \times \vec{B}$ effects. In the vicinity of the wires, the electric field is curved and not pointing exactly parallel to a magnetic field applied along the main TPC axis. Thus, the $\vec{E} \times \vec{B}$ term in the Langevin formula (eq. 1.14) does not vanish and the drifting electrons become displaced. Furthermore, the spatial resolution is degraded if the wires get displaced in case their tension is insufficient to compensate for gravitational and electrostatic forces.

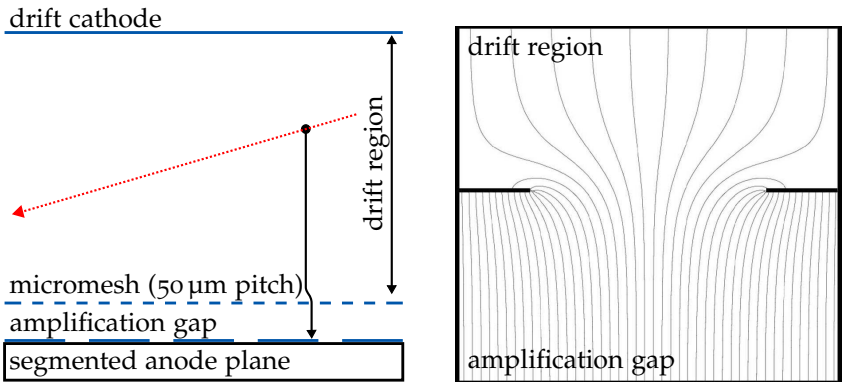

Figure 1.10: a) Schematic of a Micromegas detector
b) Configuration of the electrical field in the amplification region of a Micromegas detector [43].

1.3.3 *Micromegas*

Micromegas were invented in 1996 [12] by Y. Giomataris. Their small structure size minimizes $\vec{E} \times \vec{B}$ effects and allows for improvement of the spatial resolution in comparison with wire chambers.

As shown in figure 1.10a, a Micromegas detector is made of a few micrometers thick mesh placed 50–100 µm above the readout plane. This micro-mesh divides the detector volume into two parts, the drift- or conversion zone where the primary ionization is created and the amplification zone where gas amplification takes place.

As in wire chambers, the field in the drift region usually does not exceed a few hundred V/cm. The field in the amplification zone is at least one order of magnitude larger. The electrical field lines in vicinity of the amplification mesh are shown in figure 1.10b.

After their passage through the drift region, primary electrons are focused into the holes in the mesh and enter the amplification gap. Electron avalanches develop in the high electric field here.

As in modern MWPCs, the signal is collected on pads. The signal that is induced by the ions is very short ($\approx$ 100 ns) since the amplification gap is very narrow. Due to the higher electron mobility, the signal induced by electrons during their drift towards the readout pads is even shorter. This allows to record both, the ion and the electron signal. Thus, it is possible to operate the detector with moderate gains.

The short time needed by the ions to leave the amplification region allows to operate Micromegas detectors in experiments with very high rates of up to 1 GHz/mm² [44].

As in wire chambers, special care has to be taken in order to obtain a stable operation. The gas mixture and the electric field have to be selected properly in order to avoid discharges. Stable operation can

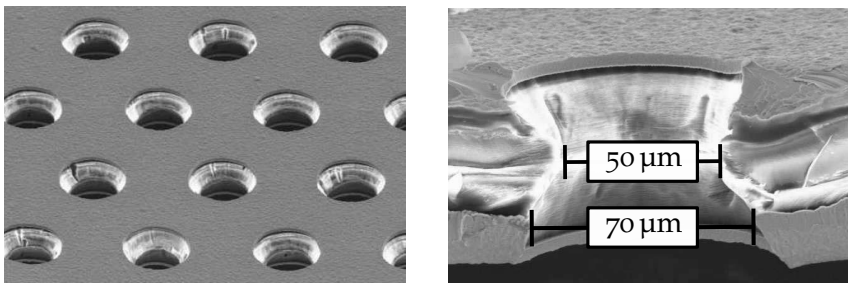

(a) (b)

Figure 1.11: Scannig electron microscope pictures of a GEM [46]. The hole pitch is 140 µm, the copper and Kapton thicknesses are 3 µm and 50 µm respectively. The holes are double conically shaped.

be achieved with gas gains of up to 300.000 [45]. Nevertheless a gas gain of a few thousand is more common.

The transversal diffusion in the narrow amplification gap is small. Thus, the charge cloud is strongly localized and the charge is detected only by a single readout pad. This makes it impossible to improve the spatial resolution by a center of gravity reconstruction method. It has turned out that this is the limiting factor to the spatial resolution in several applications. This limit is overcome if a thin resistive film is applied on top of the readout pads. This film spreads out the collected charge over a larger area. Thus, the signal is detected by several readout pads allowing to apply center of gravity algorithms.

1.3.4 *GEMs*

GEMs were introduced by F. Sauli in 1997 as preamplification stage for gaseous detectors [13]. A standard CERN GEM consists of a 50 µm thin, highly insulating polyimide foil, labeled Kapton, which is coated with 3 µm of copper on the top and bottom sides. This sandwich is perforated by means of acid etching with double conical holes in a hexagonal pattern with 140 µm pitch. Scanning electron microscope pictures of the structure are shown in figure 1.11.

Gas amplification is achieved by applying a potential difference of a few hundred volts between the GEM cathode (top) and GEM anode (bottom). The electric field in a GEM is depicted in figure 1.12a. Depending on the external fields, the electric field in the holes can easily exceed 80 kV/cm.

As shown in figure 1.12b, the mean gas gain in a GEM rises exponentially with the applied voltage. The gain distribution is described by a Pólya function (c.f. Sec. 1.3).

Especially during the first minutes of operation, a fraction of the free electrons in a GEM hole becomes attached to the surface of the insulator. The resulting space charge causes a rise in the field strength

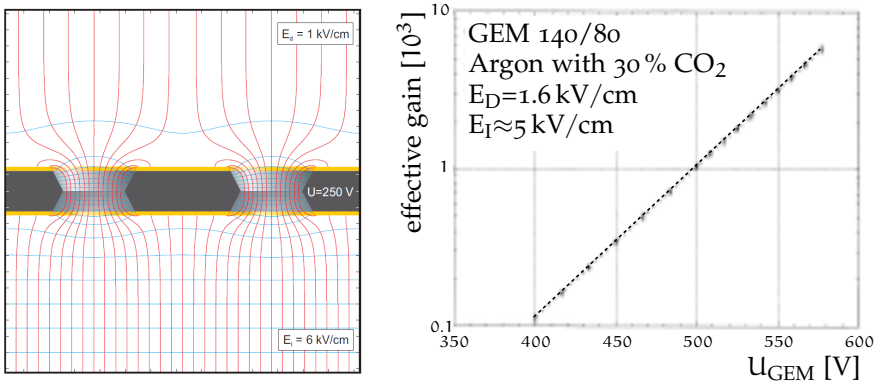

(a) (b)

Figure 1.12: a) Electric field in a standard CERN GEM with $\Delta U_{GEM} = 250\,V$. The field strength above and below the GEM is 1 kV/cm and 6 kV/cm respectively [47, 48].
b) Mean effective gain of a GEM in Ar with 30 % CO_2 admixture as function of the applied potential difference ΔU_{GEM}.
Reprinted from [49], with permission from Elsevier.

until an equilibrium between newly attached and drained electrons is achieved. This charge-up effect has been studied in some detail in [50, 51].

Most of the ions created in the amplification process are captured by the GEM cathode. As discussed briefly in section 1.3.5, some are released into the volume above the GEM.

1.3.4.1 *GEM Transparency*

In case of a hexagonal hole pattern, the optical transparency of a GEM with hole pitch p and hole diameter d is given by:

$$\tau_{opt.} = \frac{\pi d^2}{2\sqrt{3}p^2}. \tag{1.30}$$

For a standard CERN GEM, it is about 0.12. In case of a quadratic hole pattern, the optical transparency is given by:

$$\tau_{opt.} = \frac{\pi d^2}{4p^2}. \tag{1.31}$$

Not necessarily all electrons are amplified but some may be absorbed on the GEM cathode or get attached to the insulator before causing ionization. The ratio between the number of electrons collected in a GEM hole ($N_{col.}$) and the number of electrons drifting towards the GEM (N_{start}) is labeled collection efficiency or electrical transparency:

$$C = \frac{N_{col.}}{N_{start}}. \tag{1.32}$$

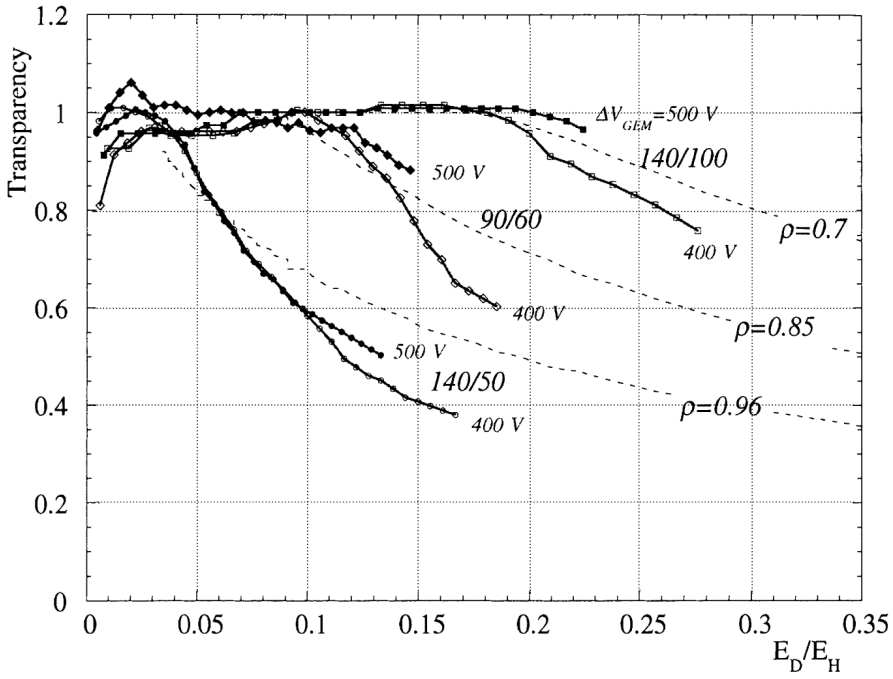

Figure 1.13: Electrical transparency in dependence on the ratio of the field above the GEM and the field in the hole center E_D/E_H. Measurements for GEMs with different geometries are shown. X/Y denotes a GEM with X µm hole pitch and Y µm hole diameter. The dashed lines are computed from a model, ρ is proportional to the optical opacity.
Reprinted from [49], with permission from Elsevier.

As shown in figure 1.13, the collection efficiency does not only depend on the optical transparency, but also on the field configuration. By adapting the electric field above the GEM to the field in the GEM holes the collection efficiency can be maximized ($C = 1$).

According to [47], the field in the GEM holes can be parameterized by:

$$E_{hole} = a \cdot \Delta U_{GEM} + b \cdot (E_{drift} + E_{ext.}), \tag{1.33}$$

where E_{drift} and $E_{ext.}$ are the fields above and beneath the GEM, respectively. The parameters a and b are determined by the GEM geometry.

1.3.4.2 *Effective Gain*

The total GEM gain is given by the ratio of the total number of electrons in the GEM after the gas amplification ($N_{prod.}$) and the number of electrons entering the amplification area:

$$G = \frac{N_{prod.}}{N_{col.}}. \tag{1.34}$$

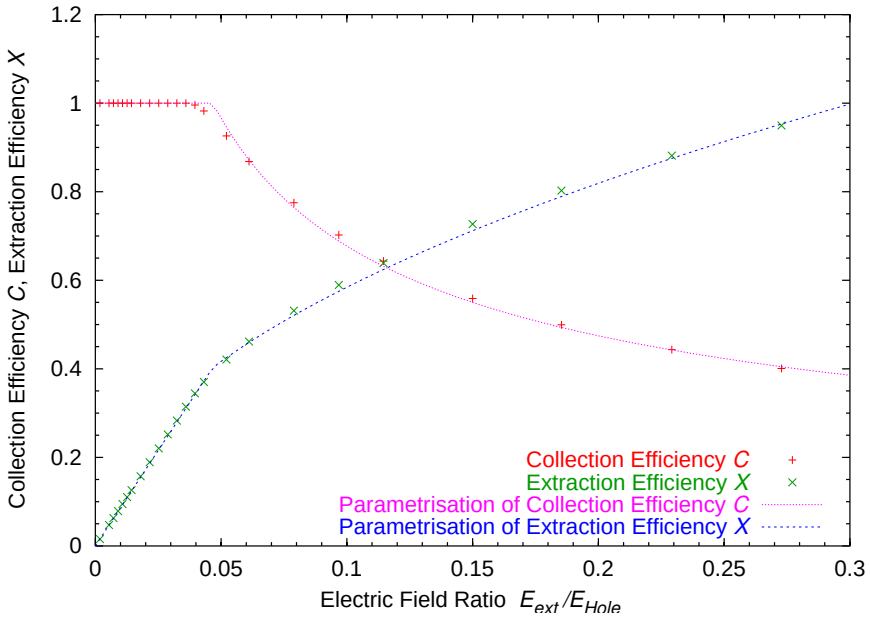

Figure 1.14: Collection and extraction efficiencies in dependence on the ratio between the external field and the electric field in the GEM holes. In the first case, the external field is given by the field above the GEM, in the second case by the field below the GEM [47].

The extraction efficiency is calculated from the ratio of the number of electrons leaving the GEM perimeter and the number of electrons in an avalanche:

$$X = \frac{N_{extr.}}{N_{prod.}}. \tag{1.35}$$

The effective gain of a GEM is defined by the ratio of the number of electrons approaching the GEM (N_{start}) and the number of electrons leaving the GEM perimeter ($N_{extr.}$). It can be calculated from the product of the collection efficiency (C), the total gain (G) in the amplification region and the extraction efficiency (X):

$$G_{eff.} = \frac{N_{start}}{N_{extr.}} = C \cdot G \cdot X. \tag{1.36}$$

In figure 1.14, the extraction efficiency is shown in dependence on the ratio between the electric field below the GEM and the field in the GEM hole. In the same figure, the collection efficiency as a function of the ratio between the field above the GEM and the field in the GEM hole is shown.

The extraction efficiency is smaller than unity if electrons emerging the amplification area are absorbed by the bottom electrode of the GEM. It can also be lowered if recombination or attachment (c.f. Sec.1.4) occur in the GEM.

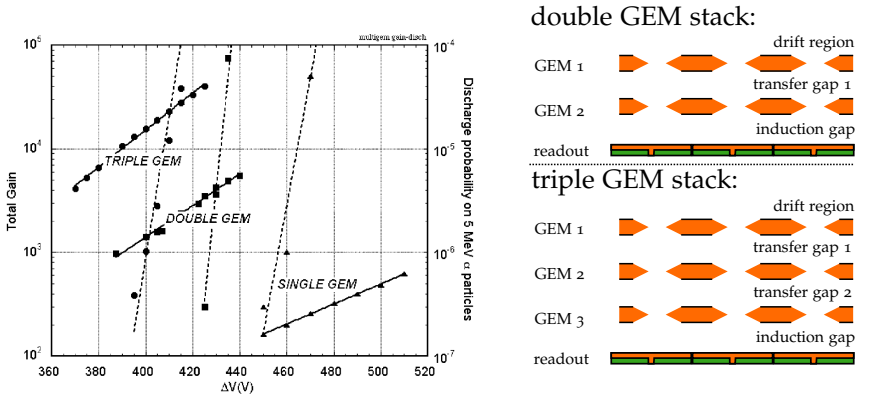

(a) (b)

Figure 1.15: a) Gain (solid lines) and discharge probability for 5 MeV α particles (dashed lines) in dependence on the voltage over the GEMs for single, double and triple GEM structures.
Reprinted from [55], with permission from Elsevier.
b) Scheme of a double and a triple GEM stack. The GEM holes are not necessarily aligned. Since the charge cloud spreads out in the gaps, this has no effect on the resolution.

Detailed discussions and measurements of the collection and extraction efficiencies together with the total gain of GEMs can be found in [47, 52–54].

1.3.4.3 *GEM Stacks*

The effective gain achieved in a single GEM is in the order of 10^2 to 10^4. Cascading two or three GEMs in a GEM stack results in even higher gains. This allows to use GEMs not only as preamplification stages, but to rely on GEMs alone for gas amplification.

The effective gain in a GEM stack is given by the product of the individual effective gains of the single GEMs. In a triple GEM setup, an effective gain of $\mathcal{O}(10^5)$ can be easily achieved. An example plot showing the effective gain of a single, double and triple GEM structure is depicted in figure 1.15a. In this figure, also the discharge probability for multi GEM structures is given. It can be seen that the stability can be kept constant while the gain is increased by several orders of magnitude if a GEM stack instead of a single GEM is used.

The construction scheme for a stack of two and three GEMs is sketched in figure 1.15b. Usually, the gaps measure 1 to 2 mm. The GEM holes are not necessarily aligned. The gap underneath a GEM usually has a sizeable height. Thus, the transversal diffusion is not negligible and the resulting charge clouds are wider than in the case of Micromegas.

The signal induced on the readout structure is mainly created by the fast moving electrons since no ions are created in the induction

gap. There is only a tiny contribution from the ions created in the holes of the last GEM [34].

The ion drift times in GEMs are even shorter than those in Micromegas. Therefore, GEM based detectors can be operated in principle at comparable rates. As in the case of Micromegas the small structure size of GEMs reduces $\vec{E} \times \vec{B}$ effects to a minimum, thus the spatial resolution obtained with GEMs is outstanding. However, for single electrons, it is limited by the hole pitch.

The separation of the gas amplification and the readout structure allows to implement complex GEM shapes as shown in [56, 57] as well as manifold readout architectures. The influence of shape and size of the readout pads for instance has been investigated in [58, 59]. Minimizing the size of the readout pads is one of the topics discussed in this thesis (chapters 3 to 7).

1.3.5 *Ion Backdrift*

It is easy to understand that ions which emerge from the gas amplification stage into the drift volume distort the homogeneity of the drift field. Good spatial resolutions can only be obtained if such distortions are minimized.

In large detectors with wire readout, the ion backdrift is suppressed by usage of gating wires between the amplification and the drift area [22]. In case of Micromegas, the ion backdrift is intrinsically suppressed by the field configuration. Only a few ppm of the created ions are released into the drift volume, the majority becomes neutralized at the grid [60].

If a GEM is used for amplification, it is possible to minimize the ion backdrift by tuning the fields. It has to be noted that gain and the collection efficiency might suffer from this optimization. In a GEM stack, the large number of fields allows to achieve a good collection efficiency, gain and ion backdrift suppression at the same time. Some rules to achieve this have been established in [52] and are summarized in [42]:

- Transfer field 1 and the induction field should be maximized.
- The second transfer field should be minimized.
- The gain in the bottom GEM should be maximized. Ions which are produced here will be very likely neutralized at the GEMs above.
- The gains of the other GEMs have only a small influence on the ion backdrift.

Following these instructions, an ion backdrift of 0.2 % to 0.5 % can be achieved, depending on the magnetic field [61].

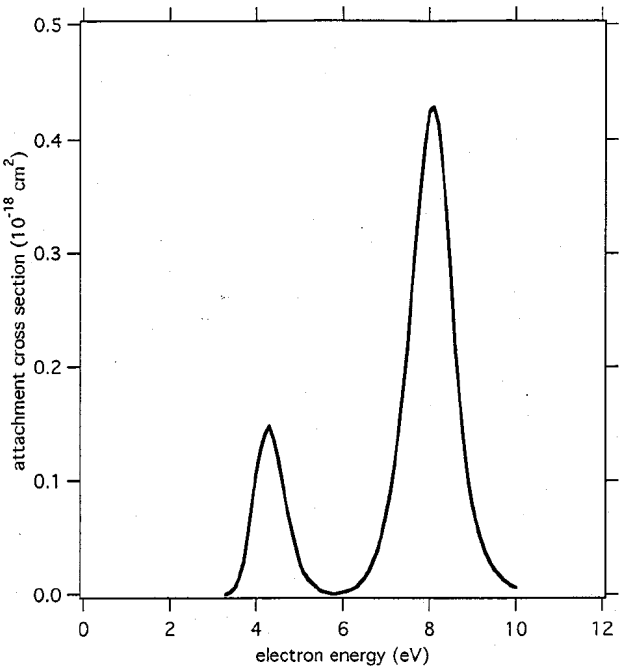

Figure 1.16: Cross section for dissociative attachment in CO_2 [62]. Reprinted with permission. Copyright 2002 American Institute of Physics.

1.4 CHOICE OF DRIFT GASES

Although gaseous detectors have been subject of interest for several decades, there exists no general or even simple recipe to compose the gas mixture for a specific application. However, this section addresses the most relevant topics.

1.4.1 *Attachment and Detachment*

When a free electron encounters a molecule with electron affinity it may become attached to the molecule, forming an anion. Due to the high mass, anions drift significantly slower than a free electron. Furthermore, they do not undergo gas amplification. Therefore, attached electrons evade detection. Thus, attachment is a severe problem in TPCs since the track reconstruction as well as dE/dx measurements for particle identification are degraded.

1.4.1.1 *Dissociative Attachment*

A very effective attachment mechanism sets in when the energy of the drifting electrons is in the region of the resonance energy for

dissociation processes, see figure 1.16. In these processes, ion-anion pairs are created. For instance:

$$CO_2 + 4.4\,eV \rightarrow CO^+ + O^- \tag{1.37}$$

or

$$H_2O + 6.4\,eV \rightarrow H^+ + OH^-. \tag{1.38}$$

The free electron is then easily absorbed by the positive ion [63].

Usually, the energy threshold for dissociative attachment is not reached by electrons during drift. However, it can be exceeded when the drifting electrons enter the amplification structure.

1.4.1.2 *Three Body Attachment*

In three body processes, electrons can become attached to electronegative molecules even if the electron energy is well below the dissociation threshold [64]. A mechanism explaining such processes was first proposed by F. Bloch and E. Bradbury [65]. Later, the proposed mechanism was modified by A. Herzenberg [66]. In [67], the model is described using the example of the most prominent electro-negative contamination in gaseous detectors, namely oxygen:

If an electron encounters oxygen, an anion in one of the lower vibrational states may form:

$$O_2 + e^- \rightarrow O_2^{-*}. \tag{1.39}$$

The excited anion has a lifetime in the order of 0.1 ns [32]. Either the electron is released in a spontaneous decay:

$$O_2^{-*} \rightarrow O_2 + e^-, \tag{1.40}$$

or the anion deexcites and thus gets stabilized. Deexcitation can happen by the emission of a photon:

$$O_2^{-*} \rightarrow O_2^- + \gamma, \tag{1.41}$$

or in a collision with a buffer molecule M:

$$O_2^{-*} + M \rightarrow O_2^- + M^*. \tag{1.42}$$

In the latter process, the excitation energy is transferred to the buffer molecule encountered. Naturally, the attached electron may also be released in the encounter with another molecule:

$$O_2^{-*} + M \rightarrow O_2 + M + e^-. \tag{1.43}$$

Obviously, stable attachment occurs only if one of the deexcitation processes happens during the lifetime of the excitation. Deexcitation

by photon emission is only relevant at very low pressures, since collisions with buffer molecules become more and more probable with rising pressure.

Whether the electron is released or the anion becomes stabilized in an encounter is strongly dependent on the nature of the buffer gas. Complex molecules like iC_4H_{10} have several and dense vibrational degrees of freedom to which the excitation energy is easily transferred. Therefore, it is more likely that the anion is stabilized in the presence of complex molecules than in presence of more simple ones.

Noble gases are not efficient as buffer molecules since they feature no vibrational degrees of freedom. Nevertheless, attachment to oxygen in pure noble gases has been reported [68]. This can be explained by another three body process which is based on the formation of unstable van der Waals molecules as:

$$O_2 + M \rightarrow (O_2M), \tag{1.44}$$

where M is a noble gas. These molecules are disintegrated when hit by an electron, which then remains attached to the oxygen molecule.

The extent to which these processes contribute to the electron attachment is strongly dependent on the specific gas mixture. In some mixtures van der Waals attachment prevails, in some others Bloch-Bradbury attachment. A rule of thumb is that an oxygen contamination of a few 10 ppm_V is acceptable in TPCs [69].

1.4.1.3 *Detachment Mechanisms*

The electron affinity is 1.46 eV for atomic and 0.45 eV for molecular oxygen [70, 71]. Since these binding energies are rather low, negative ions formed by electron attachment may spontaneously eject the attached electron by autoionization. The anion lifetimes range from a few femtoseconds to several hundred microseconds and are crucially dependent on the molecular state and the internal energy of the anion [63].

Except by autoionization, negative ions may loose the attached electron due to external effects:

- If the energy of an incident photon exceeds the ionization threshold of an anion, photodetachment may take place. Determination of the threshold allows to precisely measure the electron affinity of atoms. For diatomic molecules, the photodetachment threshold may differ from the electron affinity since molecules are subject to the Franck-Condon principle [72, 73].

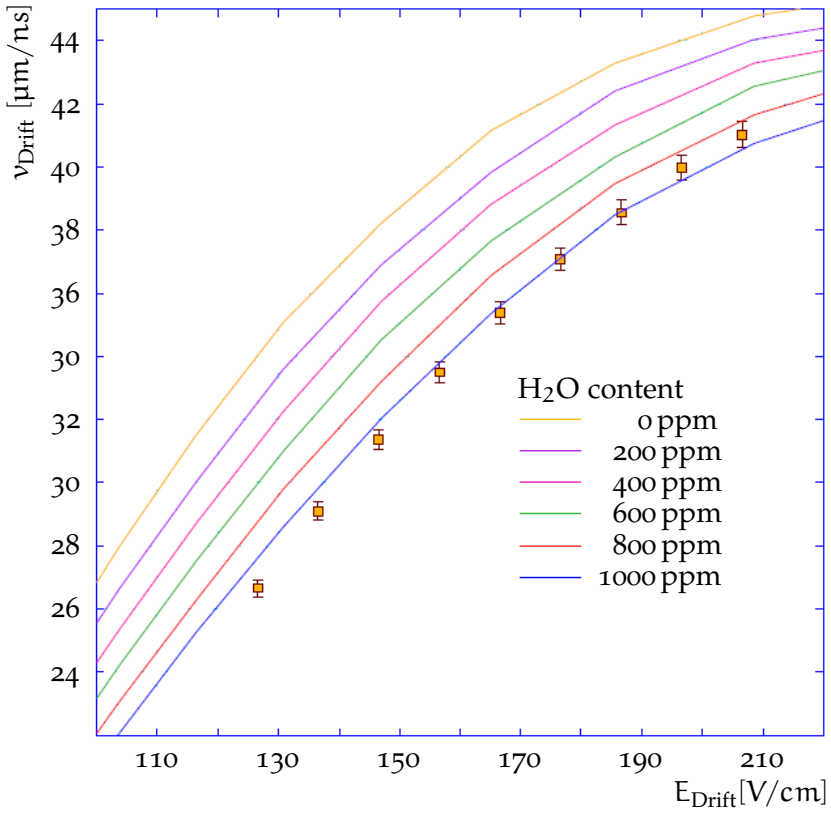

Figure 1.17: Magboltz simulations of the drift velocity in dependence on the electric drift field for a mixture of 93 % Ar, 5 % CH_4 and 2 % CO_2 at standard conditions for different H_2O contaminations. Additionally, data points from measurements with 1000 ppm_V H_2O contamination are shown [75].

- If the relative kinetic energy is large enough, an anion A^- may loose the attached electron upon electron impact:

$$A^- + e \rightarrow A + 2e, \tag{1.45}$$

or in a collision with another molecule B:

$$A^- + B \rightarrow AB + e \quad \text{or} \quad A^- + B \rightarrow A + B + e. \tag{1.46}$$

Clearly, the detachment mechanisms are governed by temperature, pressure and composition of the gas, as well as by externally applied fields [74].

1.4.2 *Influence of H_2O Contaminations*

Although H_2O molecules do not attract electrons themselves, their presence fosters the attachment to oxygen via the Bloch-Bradbury mechanism [67]. Furthermore, even tiny H_2O fractions in hot gases reduce the drift velocity, as shown in figure 1.17. This effect is caused by the static electric dipole moment of the molecule, which results in an extremely large scattering cross section for low energy electrons [32].

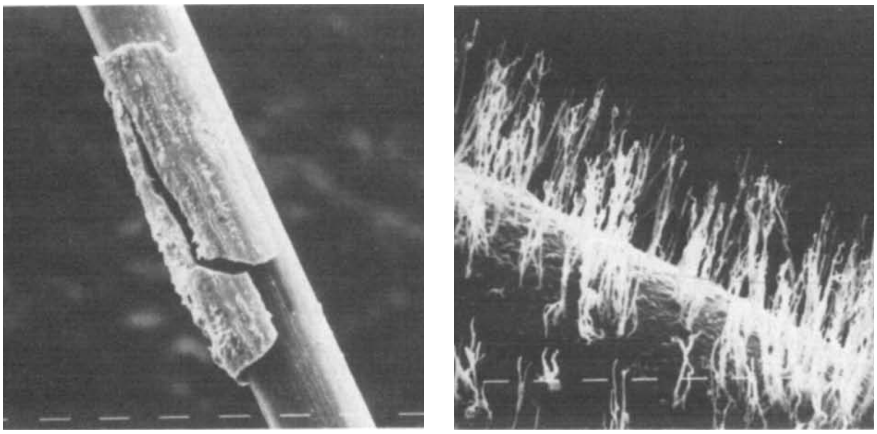

(a) (b)

Figure 1.18: Anode wires after aging in a test-chamber.
Reprinted from [77], with permission from Elsevier.
a) Anode wire after collecting a charge of 50 mC/cm in a mixture of Ar, C_2H_6 and methylal. Most of the deposited silicon coating broke away during disassembly.
b) When the same gas was cleaned with a cold trap during operation, the deposits formed whiskers on the anode wire.

1.4.3 *Aging in Gaseous Detectors*

Several experiments have reported that the performance of gaseous detectors degrades with rising amount of charge collected on the anode. This effect is called aging. It originates from reactions of the gas with the detector hardware. Gas constituents from outgassing or leakage as well as volitional admixtures can contribute.

1.4.3.1 *Aging Effects*

Many molecules are broken up in the avalanche plasma during the amplification process. Therefore, a large number of free radicals is created. The remarkable reactivity of these radicals can result either in recombination or in polymerization. Once a polymer chain reaches a critical size, it can condense on one of the chamber electrodes.

The connection between the polymer and the electrode can be relatively weak in the beginning and may be stabilized only after another chemical reaction. Once a mono-layer is formed on an electrode the further deposition of polymers may increase drastically. This is especially the case if the electrode is gold plated and, therefore, highly nonreactive in the first place. Moreover, many free radicals have a dipole moment which can play a role in the deposition process [76].

The coating of anode wires may take very different forms, depending on the conditions during polymerization, see figure 1.18. The coatings cause a drop in the achieved gain and, therefore, a reduced detector sensitivity. Silicon whisker growth during aging tests for the

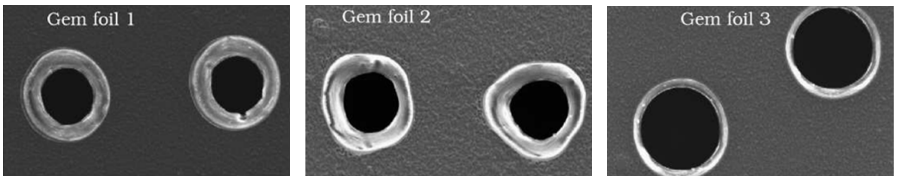

Figure 1.19: Irradiation tests for the LHCb experiment resulted a dilation of the GEM holes. The gas mixture was 45 % Ar, 15 % CO_2 and 40 % CF_4. The effect scales with the charge density as seen from the increasing hole diameter from GEM 1 to GEM 3. It can be prevented by an increased gas flow.
©2005 IEEE. Reprinted, with permission, from [80].

ATLAS TRT with 70 % Xe, 20 % CF_4 and 10 % CO_2 resulted in a gain reduction of 30 % [78].

As the anode wires, also the cathode may be affected by deposits. When an insulating layer is formed on the cathode surface, collected ions can not be neutralized. Thus, a space charge builds up and electrons are extracted from the cathode via field emission. Such thin-film emission was first described by L. Malter in [79], it is called Malter-effect, therefore.

A fraction of the electrons extracted by thin-film emission starts to drift through the detector. Once they reach the amplification region, they cause a fake signal. Additionally, the Malter-effect may become sustained since the ions created during amplification cause a further increase in the space charge on the cathode. A continuous dark current is the consequence.

Usually, free radicals are formed only during the amplification process. Thus, the aging rate scales not with time but with the amount of charge collected on the anode. In high rate experiments at the LHC or future accelerators, charges of up to 1 C/cm per year will be collected on the anode wires [76]. Therefore, it is inevitable to rely on gas mixtures which at least do not foster aging processes.

GEM and Micromegas structures largely withstand aging processes in many gas mixtures [81–83]. This makes them favorable for usage in high rate experiments. Admittedly, it has been observed that GEMs can be affected in mixtures with CF_4 under certain conditions. During an irradiation test for the LHCb experiment for instance, a small gas flow caused a high fluorine concentration near the GEMs. Eventually, this resulted in plasma etching in the GEM holes, see figure 1.19. The effect could be prevented when the gas flow was increased, thereby reducing the fluorine concentration.

1.4.3.2 *Anti-Aging Gases*

Slightly simplifying, it can be said that halides, hydrocarbons and silicon foster the aging process [84]. Hence, their usage should be avoided as far as possible. In general, the latter two are introduced by outgassing from the materials used in the detector or the gas supply. It has been reported for instance that the usage of even a short PVC tube can initiate an aging process [85]. Also Viton sealings are known to foster aging. Therefore, it is necessary to pay special attention to the materials used in a gaseous detector. A list of materials and their influence on aging processes can be found in [86].

Especially the polymerization of hydrocarbons can be suppressed by a considerable admixture of oxygen [87]. The admixture causes oxidation before long polymer chains are formed. The oxide remains in the gas phase and can be removed by a continuous flow of clean gas. However, one has to keep in mind that the electro-negativity of oxygen might be highly undesirable in gaseous detectors, as described in section 1.4.1.

From plasma chemistry, it is known that CF_4 can be disintegrated to CF_3 and a highly aggressive free fluorine atom. In combination with oxygenated species, an admixture of CF_4 therefore causes etching. This can counter or even revert aging effects.

Whenever fluorine based gas components are used, toxicity and electronegativity of free fluorine have to be considered. Furthermore, CF_4 together with water can form hydrofluoric acid. This might be too aggressive for the detector as seen in [87]. Additionally, it has been shown in [88] that CF_4 combined with hydrocarbons even fosters polymerization.

A dark current can be suppressed by small amounts of alcohols or water [89, 90]. However, Malter-discharges reappear when the admixture is removed, the effect itself is not cured. The suppression of the dark current can be explained by the dipole moment of the molecules. The dipole moment causes a significant concentration near the electrodes. Thus, the conductivity through the insulating film is increased and the space charge reduced.

1.4.4 *General Considerations*

The following compilation summarizes favorable properties of TPC drift gases:

- A large ionization density respectively many track points allow a precise track reconstruction. On the other hand, the ionization

density must not be too high but allow an operation in high rate applications.

- The detector gas should have a low density and a high radiation length to avoid track distortions by multiple scattering.
- A small electron diffusion and a stable drift velocity are necessary for a good spatial resolution.
- Discharges in the amplification structure have to be prevented. Furthermore, the gas gain has to be high enough to ensure that all primary electrons are detected.
- High ion and electron drift velocities help to keep the detector occupancy low. Drift field distortions are minimized if the ions are removed quickly from the active volume.
- Electron attachment has to be negligible.
- The drift gas may not disintegrate during operation, reactivity has to be well controlled. Aging has to be avoided.

Especially the last point makes the choice of a noble gas as main ingredient of the drift gas self-evident. However, a quenching admixture is needed to ensure stability in the amplification stage as discussed in section 1.3.1.

Actually, not only the stability of the detector is increased when a quencher is admixed, but also the drift velocity. This effect is shown in figure 1.20 on basis of an Ar-CO_2 mixture. It can be explained by the characteristics of the electron cross sections and their effect on the transversal diffusion coefficient:

For electron energies up to a few electronvolts, the total cross sections of the quencher gas is typically an order of magnitude larger than the total cross section of noble gases. Therefore, the cross section of the mixture rises with increasing quencher fraction. The mean energy ϵ of drifting electrons decreases in consequence, see figure 1.20. Simultaneously with the mean electron energy, the transversal diffusion σ_T decreases when the amount of admixture is increased. Therefore, the electron movement becomes more directed [91].

Hence, the naively expected drop in the drift velocity is not observed in figure 1.20, but the drift velocity actually rises. This effect is exhausted at some point, then the drift velocity decreases down to the value of the pure admixture. Usually, the amount of quenching gas needed to achieve a stable amplification is larger than the amount of admixture at which the drift velocity peaks. Therefore, most TPCs are not operated with the gas mixture that offers the maximal drift velocity. In consequence, the drift velocity has a significant dependence on the accuracy of the gas mixture.

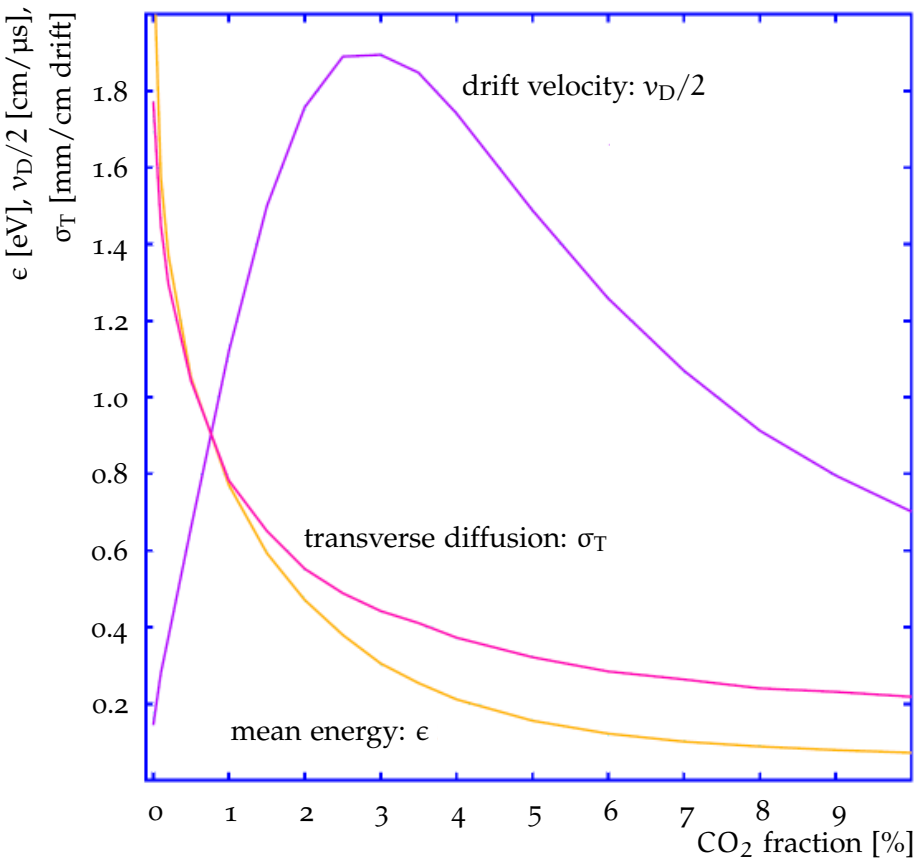

Figure 1.20: The mean electron energy ϵ, the transversal diffusion σ_T and the electron drift velocity v_D (scaled by a factor of 0.5) in Ar are plotted for a electric field of 200 V/cm in dependence on the amount of CO_2 admixture (Magboltz simulations) [91].

Gases with a pronounced Ramsauer dip show a maximum of the drift velocity if the drift field is varied, c.f. Fig. 1.4. Commonly, the drift field in a TPC is chosen such that the primary electrons reach this saturated drift velocity. Thus, the influence of drift field inhomogeneities caused by the space charge of back drifting ions or technical limitations is minimized.

The diffusion in a TPC can be reduced by a magnetic field, as described in section 1.2.2. If no magnetic field is available, a small diffusion coefficient is obtained when the properties of the gas mixture are dominated by a cold gas as CO_2 or DME. In such gases, the mean energy of the drifting electrons is comparable to the thermal energy and the diffusion is inherently small. One drawback of cold gases is that the operating point has to be chosen in a region where the drift velocity is not saturated and may suffer from field inhomogeneities.

Experiment	Drift length [cm]	Drift gas
PEP4	2×100	80 % Ar, 20 % CH_4
Topaz	2×122	90 % Ar, 10 % CH_4
Aleph	2×220	91 % Ar, 9 % CH_4
Delphi	2×134	80 % Ar, 20 % CH_4
CDF	2×15	50 % Ar, 50 % C_2H_6
STAR	2×210	90 % Ar, 10 % CH_4
ALICE	2×255	85.7 % Ne, 9.5 % CO_2, 4.8 % N_2
T2K	2×90	95 % Ar, 3 % CF_4, 2 % iC_4H_{10}

Table 1.2: Drift gases of some TPCs [32, 92–95].

1.4.5 *Common Gas Choices for TPCs*

In table 1.2, gas mixtures of some experiments are summarized. As explained before, the base component of the drift gas is usually a noble gas. The lightest noble gas, helium, has a high leakage rate and is hard to contain in a closed loop. The heavy gases Kr and Xe are literally rare and, therefore, expensive. Besides, frequent Kr isotopes are radioactive. Even of more importance is the strong effect of multiple scattering causing track distortions in these gases. The high ionization rate may cause discharges in the readout.

The remaining two noble gases Ar and Ne are used frequently in TPCs (PEP4, Topaz, Aleph, Delphi, CDF, STAR, ALICE). However, both have in common that they are less resistant against discharges in the amplification stage than helium. The mobility of argon ions is four times lower than the mobility of neon ions. At the same time the ionization density is higher. Thus, large space charges are expected in experiments with high event rates. For these reasons, Ne was chosen as main gas component in the ALICE-TPC [91].

Amount and type of the quencher gas is chosen such that a stable operation is possible. UV photons emitted from the noble gas have to be absorbed within small perimeters. Although hydrocarbon quenchers offer a higher drift velocity than CO_2 admixtures, they come with the drawback that the detector may age under their influence. The admixture of CF_4 is attractive to counter aging effects but also may destroy a detector by over-etching. Furthermore, fluorine created in the amplification plasma is toxic and electronegative.

Nitrogen admixtures are avoided in most experiments since ^{14}N can transform to ^{15}N by neutron capture. The latter emits a 10.8 MeV photon which results in a background signal. Nevertheless, nitrogen was considered recently as quencher in the ALICE TPC since it comes with a high cross section for the absorption of UV photons emitted by neon and increases the detector stability [96].

2 GAS MIXING SYSTEM

The performance of any particle detector is in principle defined by the properties of the detection media. This holds especially for gaseous detectors which are strongly dependent on the chosen drift gas.

This dependence begins with the ionization density described by the Bethe-Bloch-Formular (Sec. 1.1), covers the characteristics during the drift of the primary electrons (Sec. 1.2) and ends with the achievable gas amplification in the detector end cap (Sec. 1.3). Due to these manifold dependencies trade-offs are to be expected and it can be taken for sure that different measurements will require different drift gas compositions.

A dynamic and versatile gas mixing system that meets these requirements has already been drafted in [97] and [98]. In this chapter, it is described in detail. The system allows to vary the mixture of up to three gases and the total gas flow in a wide range. At the same time, the absolute pressure in the detector is kept constant. It offers the possibility to change or fine-tune the gas composition easily and introduces a monitoring of the most relevant gas mixture properties.

In the first section of this chapter, the piping schematic and the hardware are explained. The second section describes the monitoring of the gas properties, while the third section gives some insights to the electronics that are used to control the gas mixing system. The operating system which was developed for the controlling embedded PC is briefly sketched in the fourth section. In the last section, the achieved functionality is summarized.

2.1 LAYOUT OF THE GAS MIXING SYSTEM

As shown in the piping schematic (Fig. 2.1), the gas flow into the detector is controlled by two mass flow controllers (Sec. 2.1.1) with slightly overlapping gas-flow ranges for each gas type. This doubling of the mass flow controllers allows to achieve a large range of possible gas flows while it avoids to operate the controllers in the lower end of the calibration range, where the precision of the devices degrades.

The ranges of the mass flow controllers are optimized for a mixture of 93 % Argon, 5 % Methane and 2 % carbon dioxide, the gas composition foreseen in the technical design report for the TESLA-detector [99]. Since the products of the specific heat capacity and the density are equal for both gases, the mass flow controllers for argon may be used for helium as well (c.f. Sec. 2.1.1).

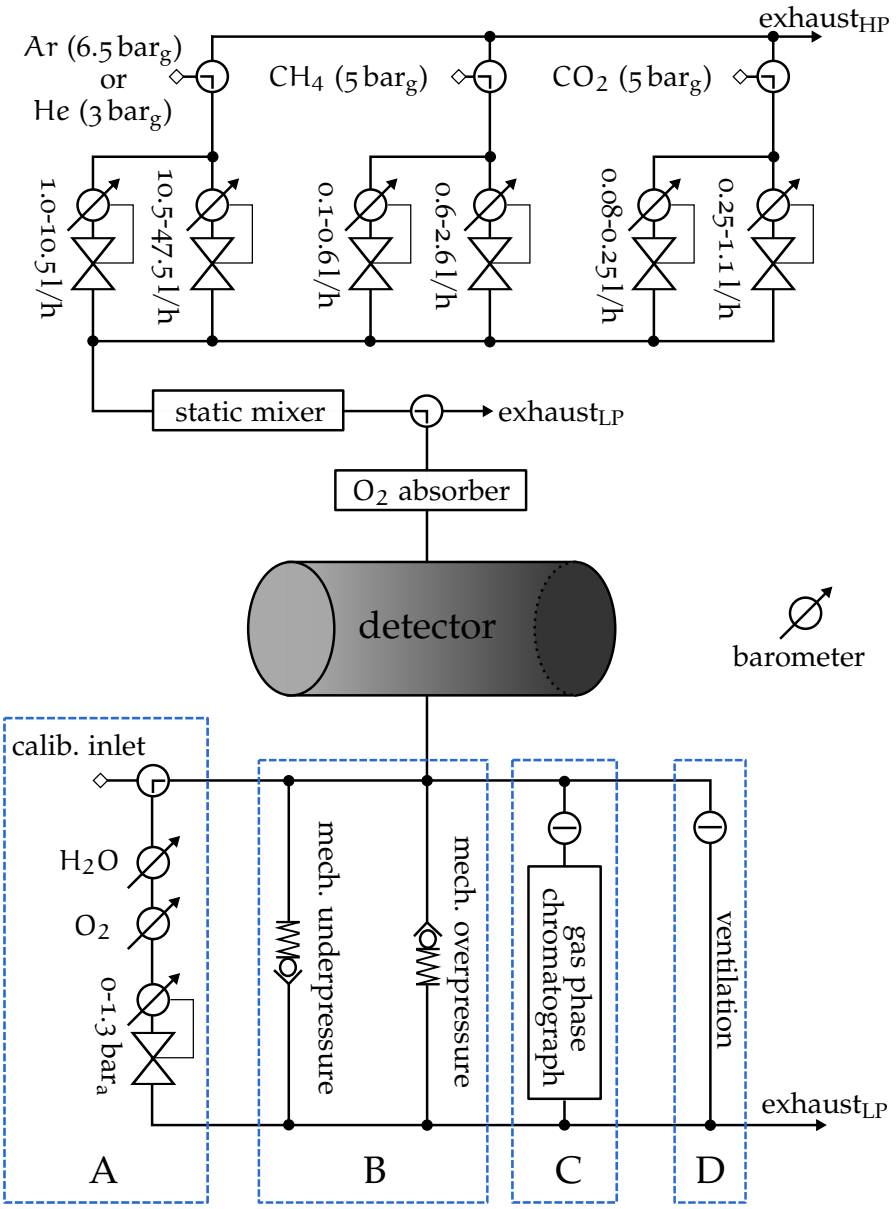

Figure 2.1: Schematic showing all devices and connections in the Gas Mixing System. All valves are set like in the standard operation mode. Recently, the flow controller for small CO_2 flows has been replaced by a device enabling CO_2 flows up to 12 l/h.

It is possible to flush the pipes from the gas bottles to the mass flow controllers by turning the 3-way valves to the exhaust position. This should be done to remove contaminations in the pipes after changing the supply bottles.

The separate gas flows are combined and mixed within a static mixer device (Sec. 2.1.2). This mixer device is placed upstream of a 3-way valve which allows to flush either the detector or to channel the mixed gas directly to the low pressure exhaust. Two different exhaust lines are foreseen in order to avoid a valve setting that generates a path from the mid-pressure part (3-6.5 $\mathrm{bar}_{\mathrm{gauge}}$) to the low-pressure part (0-30 $\mathrm{mbar}_{\mathrm{gauge}}$) of the gas mixing system. Such a path could lead to a large destructive overpressure in the detector.

When the gas is directed into the detector, it passes an oxygen absorber before entering the detector volume. Downstream of the detector there are several paths to the low pressure exhaust:

A. The main exhaust line leads through a hygrometer (Sec. 2.2.1) and an oximeter (Sec. 2.2.2) to the pressure controller (Sec. 2.1.1). This line may not only be flushed by the gas mixing system, but also from a calibration inlet, selectable by a 3-way valve. This allows the calibration of the oximeter as well as flushing the oximeter with nitrogen in case the gas mixing system is not used.

B. To avoid relative pressures larger than 30 $\mathrm{mbar}_{\mathrm{gauge}}$, mechanical over- and underpressure valves are installed. In normal operation, these valves stay closed since the electronics of the gas mixing system detect and avoid these undesired pressure conditions. However, they may occur in case of a power failure or misusage of the system.

C. To monitor the quality and composition of the gas mixture, a gas-phase chromatograph (C2V-200 micro GC) is installed in parallel with the main exhaust line. Details on commissioning and operation of this device may be found in [100].

D. The ventilation valve can be opened if the relative pressure should be minimized. In particular, if the detector is not flushed with any gas.

A constant gas flow into the detector is guaranteed by the mass flow controllers at the input. The absolute pressure in the system is held constant by adjusting the flow in the main exhaust line with the pressure controller. The barometric pressure is monitored by a BSDXBaro device from Sensortechnics (absolute accuracy: ± 3 mbar). If the gauge pressure, derived from the barometric pressure and the reading of the pressure controller, exceeds a 5-30 $\mathrm{mbar}_{\mathrm{gauge}}$ range, the total pressure in the detector is no longer held constant but adapted.

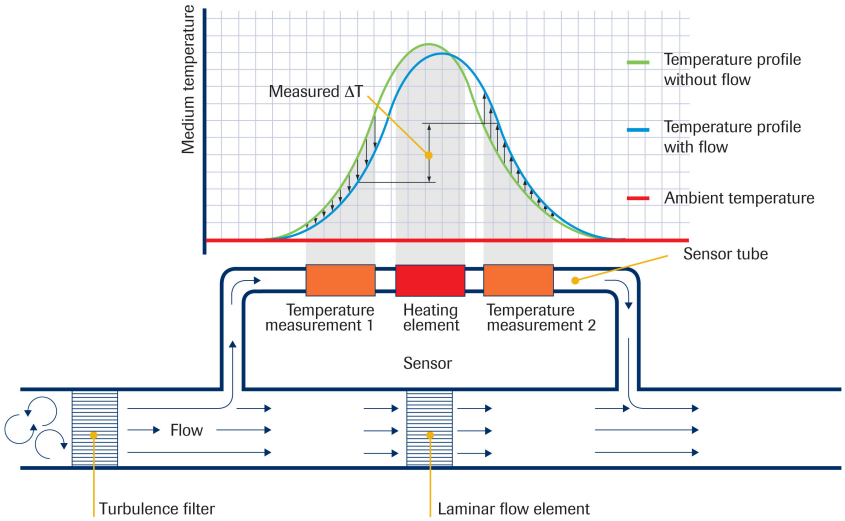

Figure 2.2: Mass flow measuring principle. The measured temperature gradient ΔT is proportional to the total flow in the device. Illustration by permission of Bronkhorst High-Tech [101].

2.1.1 *Flow Controllers*

The calorimetric El-Flow mass flow controllers from Bronkhorst High-Tech are controlled and read out by analog signals. They feature a mass flow sensor which is internally coupled to a solenoid valve controlling the gas flow.

As depicted in figure 2.2, the flow is made laminar in the device and a small fraction of the main flow is led into a the sensor tube. Only the bypassed fluid is monitored. Since the flow in the mass flow controller is laminar, this is a constant fraction of the total flow through the device.

The gas flow passes a temperature sensor, a heating element and a second temperature sensor in the bypass. While the temperature profile is symmetric around the heating element as long as there is no flow, it becomes asymmetric with rising flow.

The heat transfer between the capillary sensor tube and the gas is described in [102]. As pointed out in [103], for small gas flows the measured temperature difference $\Delta T = T_2 - T_1$ is proportional to the mass flow Φ_m respectively the volume flow Φ_V in the sensor tube. Taking into account the influence of the specific heat capacity of the gas at constant pressure c_p and the density ρ one receives:

$$\Delta T = k \cdot c_p \Phi_m = k \cdot c_p \rho \Phi_V, \tag{2.1}$$

where the proportionality constant k represents the thermal and geometric properties of the sensor tube as well as the heating power of the heating elements [104]. This constant has to be derived from a calibration for each device.

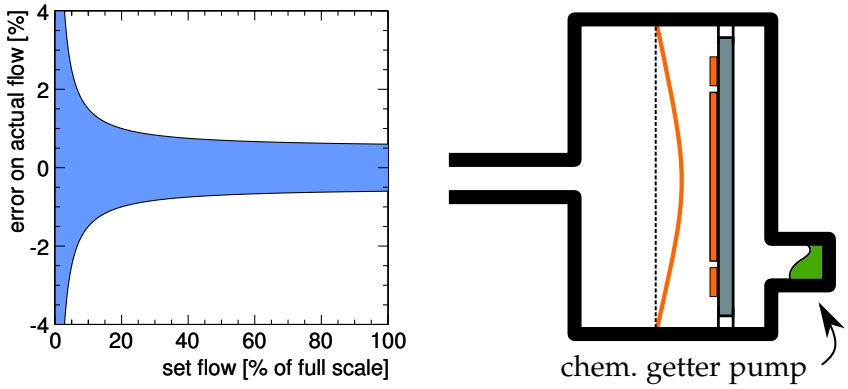

(a) (b)

Figure 2.3: a) Precision of the received flow in dependence on the requested flow in a mass flow controller.
b) Drawing of the capacitance manometer. The left handed side is connected to the monitored volume. Pressure variations influence the bow of the membrane electrode and, therefore, the distance to the reference electrode in the evacuated right handed side.

The precision is limited by an absolute error of $\pm 0.1\,\%$ of the maximal flow, which adds to an error of $\pm 0.5\,\%$ of the actual reading. This results in a degrading absolute performance for gas flows which are much smaller than the full scale flow, see figure. 2.3a. For this reason, a lower bound to the selectable flow is defined in the steering software (c.f.Fig. 2.1).

As the mass flow controllers, the pressure controller (MKS 640A) is controlled and read out by analog signals. The gas flow is again controlled by an integrated solenoid valve. The absolute accuracy is $\pm 0.5\,\%$ of the reading, while the repeatability is better than $\pm 0.1\,\%$ of the full scale.

The pressure monitoring is done with an integrated Baratron™ capacitance manometer (Fig. 2.3b). Main elements of the manometer are two electrodes forming a capacitor. One of the electrodes is placed on a flexible membrane, which divides the sensor volume into two halves. One half is connected to the monitored gas volume, the other half is evacuated. Within this half, the reference electrode is placed. The vacuum is maintained by a chemical getter pump inside the device.

When the pressure on the measurement side changes, the deformation of the membrane varies and the distance between the electrodes is modified. Thus, a change in capacitance can be measured to monitor the pressure.

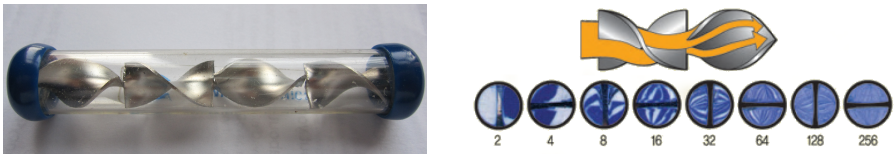

(a) (b)

Figure 2.4: a) Promotional sample of a Kenics helical mixer [105].
b) Simulation of the situation after several mixer elements.
Illustration by permission of Samhwamix Co. [106].

2.1.2 *Static Mixer*

The gas mixture is homogenized by a static helical mixer. The mixer consists of a set of eight bent elements enclosed within a pipe segment (Fig. 2.4).

In a laminar flow application, the main mixing mechanism is the flow division at each element: The leading edge of any element divides the fluid and rotates the separated streams. The subsequent element splits the flows again, followed by a further rotation in the opposite direction. With any subsequent element the fluid is divided once again. The number of mixings after n elements is therefore 2^n.

The laminar mixing is further supported by turbulences introduced in the flow by changing the direction of rotation after each element.

2.2 IMPURITY MONITORING

The most prominent contaminants in gaseous detectors are traces of water (H_2O) and oxygen (O_2). In [100], it was shown that the accuracy of a simple gas chromatograph is not sufficient to determine these impurities in the ppm region. To overcome this limitation, dedicated detectors for H_2O and O_2 are integrated into the gas mixing system.

2.2.1 *Hygrometer - GE HygroPro*

Most hygrometers use an optical method (chilled mirror hygrometer) to determine the dew point of water in a gas sample. A more reliable measuring technique is used in the aluminum oxide hygrometer of the GE Sensing HygroPro (Fig. 2.5a).

This device measures directly the water vapor pressure in the fluid. The measuring principle relies on the impedance change between capacitor electrodes which are directly exposed to the fluid. To avoid water deposition on the sensor, the detector has to be operated at least 10 K above the dew point.

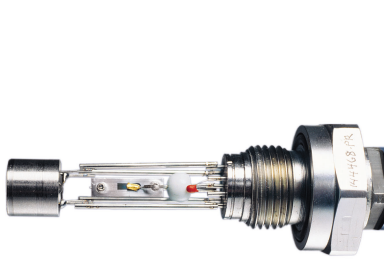

(a)

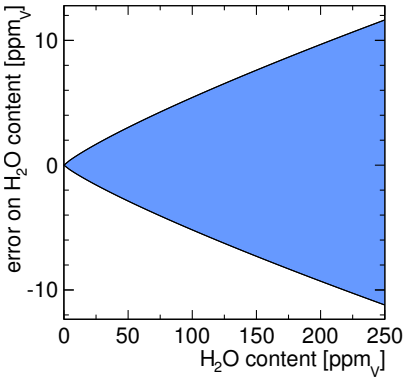

(b)

Figure 2.5: a) Probe of the hygrometer, showing the temperature sensor (right), the pressure sensor (left) and the aluminum oxide sensor (center) [107].
Photograph by permission of GE Measurement & Control.
b) Error on the measured water content. The ±-asymmetry of the error is negligible.

dew/frost point range	α [mbar]	β	λ [°C]	max. error
0 ... 200 °C	6.0964	16.8862	230.50	0.38 %
−20 ... 50 °C	6.1162	17.4748	240.71	0.09 %
−70 ... 0 °C	6.1134	22.5448	273.47	0.05 %

Table 2.1: Coefficients for the Magnus formula [110].

To calculate parameters as ppm_V or percent relative humidity from the measurement, the device features internal pressure (piezoresistive) and temperature (NTC) senors.

Commonly, the water content in gases is stated as temperature of the frost or dew point. This is the temperature at which the gas is saturated with water vapor and the water vapor condensates as fluid or ice. The saturation vapor pressure over water (e_W) or ice (e_I) can be calculated from the dew or frost point temperature (T) using the Magnus formula [108]:

$$e_{W/I}(T) = \alpha \cdot \exp\left(\frac{\beta T}{\lambda - T}\right). \tag{2.2}$$

Coefficients for different temperature ranges of this empirical formula can be found in [109] or [110] for example. For convenience, coefficients for the most relevant ranges are stated in table 2.1.

From the partial pressure, the relative water content in ppm_V can be easily calculated. This was used to show the absolute measurement accuracy ($\Delta T_{D/F} < \pm 2\,°C$ for $-65\,°C < T_{D/F} < 10\,°C$) of the HygroPro sensor as error on the measured relative water content in ppm in figure 2.5b.

Since the measurement is a partial pressure, it is not dependent on the flow-rate of the monitored gas. If the measurement changes with the gas flow it can be assumed that off-gassing or a leak in the gas system is causing this dependence. Especially the copper pipes used in the gas mixing system are known to be hygroscopic. Once they have been exposed to H_2O enriched gas it might take days until the H_2O contamination drops to an acceptable value ($\mathcal{O}(10\,\mathrm{ppm_V})$).

2.2.2 *Oxymeter - TAI 3190*

The Teledyne Analytical Instruments 3190 is a micro-fuel cell based O_2-sensor. Free electrons are generated in a chemical reaction, the resulting current is proportional to the total amount of oxygen in the gas sample.

The design of the micro-fuel cell used is comparable to the composition of a zinc-carbon battery. The single yet important difference between these is that all reactants are stored within a battery, while in case of the micro-fuel cell one component, namely the oxygen, comes from the outside as a constituent of the gas sample.

The cell consists of a cathode, a lead anode and a 15 % aqueous KOH electrolyte (caustic potash). The sample gas diffuses through a membrane on the top of the cell into the electrolyte. Any oxygen solved in the electrolyte is then reduced at the cathode:

$$O_2 + 2H_2O + 4e^- \rightarrow 4OH^-, \tag{2.3}$$

while simultaneously the lead is oxidized at the anode:

$$2Pb + 4OH^- \rightarrow 2PbO + 2H_2O + 4e^-. \tag{2.4}$$

Altogether, four electrons are released at the anode for each reacting oxygen molecule [111].

Since the current is proportional to the total (and not the relative) amount of available oxygen it is necessary to have the sensor calibrated at a total pressure and flow equal to the operational conditions. This is why the sensor is placed in the pressure regulated part of the gas mixing system. Under the correct operating conditions, the measurement is correct within ± 5 % of the calibrated full scale.

The micro-fuel cell is burnt after being exposed to a certain total amount of oxygen. In order to avoid excessive wastage, the cell always has to be flushed with gas with a low oxygen content.

2.3 ELECTRONICS

The electronics of the gas mixing system are built of the central embedded PC (TERN Ethernet-LCD, Fig. 2.6) and a customized expansion PCB (Printed Circuit Board). The embedded PC has two main

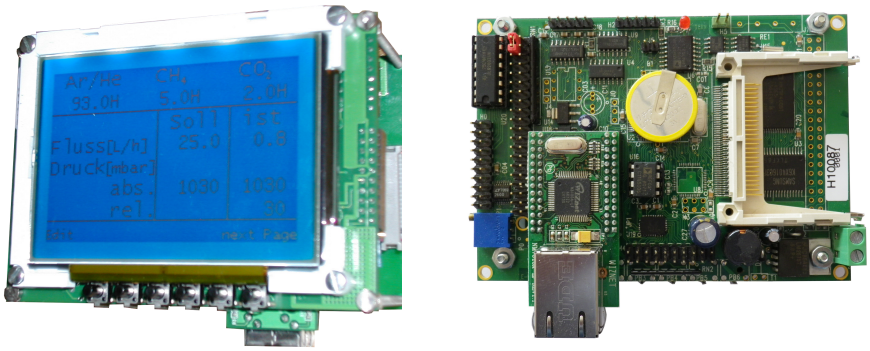

(a) (b)

Figure 2.6: Embedded PC front (a) and back view (b)

tasks: One is to set the desired target values of the connected mass flow controllers. The other is to monitor the parameters of the gas mixing system. All values are provided for the read-out with another PC (Sec. 2.4.2).

Central building block of the embedded PC is the AM186™ES CPU. The programming is briefly sketched in section 2.4. The CPU is connected to several other devices allowing interaction with other hardware and the user:

- 192 × 128 pixel graphic display
- 6 buttons
- hardware TCP/IP stack for 100 base-T Ethernet
- 16 channel 24-bit ΔΣ-ADC (LTC2448)
- 8 channel 16-bit DAC (LTC2600)
- compact flash card drive
- RS232 port
- RS485 port

Some of the programmable I/O pins of the CPU are used to implement a SPI (Serial Peripheral Interface), which is used to interface the ADC (Analog to Digital Converter) and the DAC (Digital to Analog Converter). Fan-out and reorganization of DAC, ADC and power lines are realized on the expansion PCB. The schematics are depicted in figure 2.7.

The system is powered by ± 15 V according to the requirements of the flow controllers. Supply voltages of the embedded PC, the temperature sensors and the barometer are derived with voltage regulators.

The control voltage of the flow controllers ranges from 0 to 5 V (in and out). This matches the DAC output, while the ADC has an

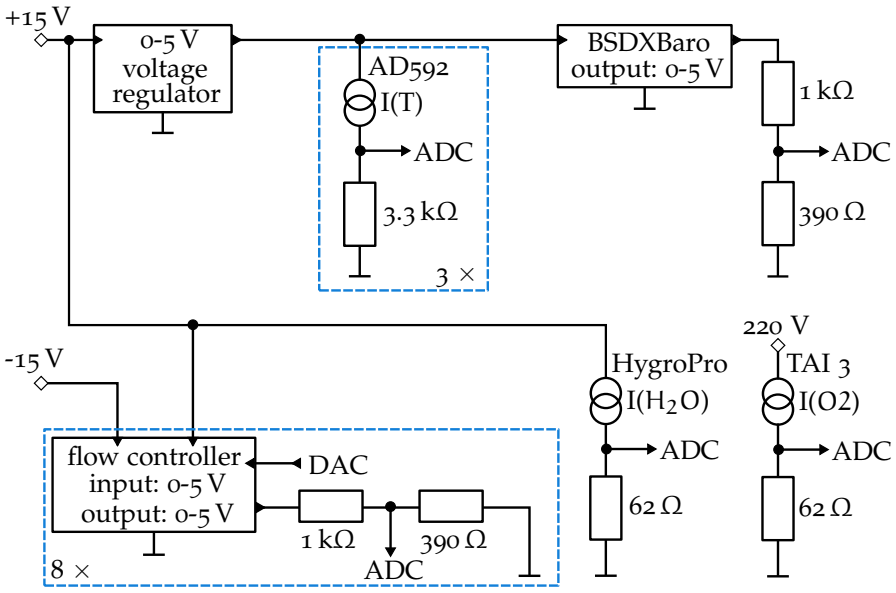

Figure 2.7: Draft of the schematic of the expansion PCB for the embedded PC. The ADC and DAC signals are routed to the corresponding ports on the PCB of the embedded PC.

input range of only $-1.25\,\mathrm{V}$ to $1.25\,\mathrm{V}$. Therefore, a voltage divider is needed between the flow controller output and the ADC. Due to the architecture of the ADC, this voltage divider has to be rather low ohmic. In a more sophisticated approach, the flow controller output would not be directly connected to the voltage divider, but with a unity gain amplifier in between. This would reduce demands to the voltage output of the flow controllers and improve the accuracy of the analog to digital conversion. However, both the DAC and the ADC are high precision devices and the expected error from the conversion is much smaller than the accuracy of a mass flow controller.

The AD592 temperature sensors are temperature controlled current sources. They are directly connected to the $5\,\mathrm{V}$ supply rail. The measured voltage builds over $3.3\,\mathrm{k\Omega}$ resistors.

The barometer data is transmitted via a 0 to $5\,\mathrm{V}$ output. Therefore, a voltage divider, identical to the ones of the flow controllers, is used for the readout.

The oximeter transmits the data via two analogue signals. One signal encodes the measurement range, the other encodes the measured value as percent of the actual range as current signal (4 to $20\,\mathrm{mA}$). The range signal is not evaluated due to a lack of ADC channels. The range may be reconstructed from the retrieved data. Like the oximeter, the hygrometer transmits the data as 4 to $20\,\mathrm{mA}$ current signal. Both current signals are evaluated by measuring the resulting voltage over $62\,\Omega$ resistors.

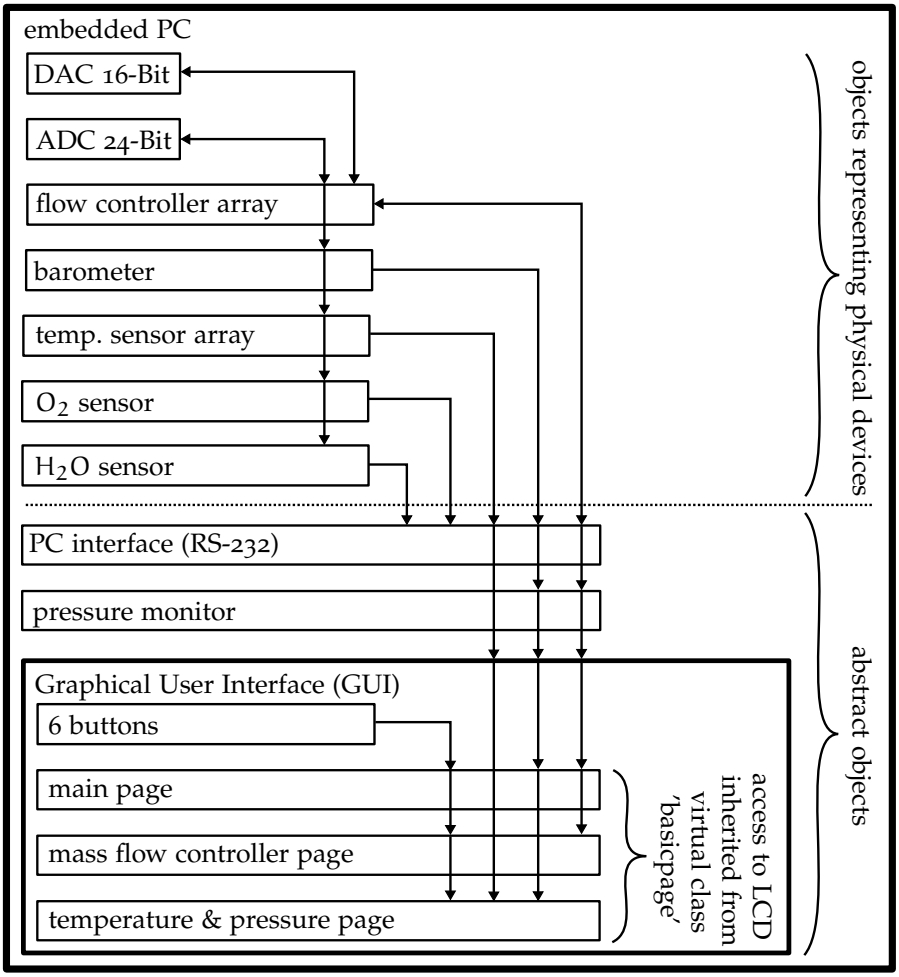

Figure 2.8: Hierarchy of the objects implemented in the operating system of the embedded PC. The arrows indicate the direction of the data flow.

2.4 SOFTWARE OF THE EMBEDDED PC

The operating system running on the embedded PC is written in object-oriented C++. During start-up of the system, several static objects representing physical devices of the gas mixing system are instantiated together with some abstract objects. The hierarchy of these objects is shown in figure 2.8. The arrows indicate the direction of the data flow. This implementation of the hardware objects allows the abstract objects to access the parameters of the gas mixing system.

2.4.1 *Program Flow*

Since the CPU of the embedded PC does not allow real multitasking, the abstract software objects are activated one after the other in an infinite loop:

- First, the current settings and readings are transmitted via the RS232 interface by the PC interface object. If the connected PC has sent new target settings, these are applied.
- Afterwards, the pressure monitor routine checks whether the pressure limits are exceeded. If so, the settings are adjusted. The system returns to the previously selected settings as soon as possible.
- Finally, the GUI checks for user input and applies the new settings if they are valid. If not, valid settings close to the chosen ones are suggested.

2.4.2 *PC Interface*

All data concerning the gas mixing system are collected in the embedded PC. For further processing, it is necessary to transfer them from the embedded PC to a desktop PC. This is done via the serial port (RS232). The protocol parameters are:

Parameter	Value
bps	19200
data bits	8
parity	none
stop bits	1
flow control	none

According to the implemented ASCII communication protocol, a read or set command has to be sent from the desktop PC that is then processed and answered by the embedded PC.

2.5 OPERATION OF THE GAS MIXING SYSTEM

2.5.1 *Leakage Tests*

A good gas quality within the TPC can only be ensured if the gas system and the TPC are tight. Obviously, the term tight needs to be defined, since virtually no system will be absolutely tight.

A quantitative measure for the tightness of a system is the leakage rate Q_L. The leakage rate is defined in [112] as the quantity of gas that leaks into or out of a system during a timespan Δt. Since the quantity of a gas is given by the product of the pressure p and the volume V, the leakage rate reads:

$$Q_L = \frac{\Delta(pV)}{\Delta t}. \tag{2.5}$$

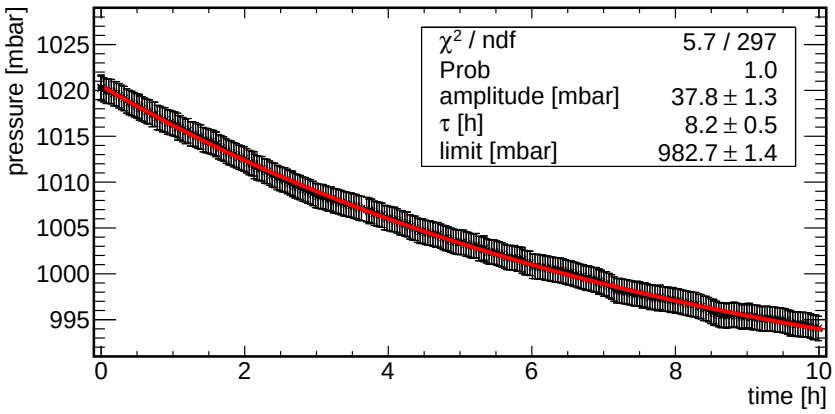

Figure 2.9: The system, including a safety-bubbler, is brought to an overpressure for a leakage test. After turning off the helium gas flow, the pressure drops exponentially. The leakage rate is less than $2.5 \times 10^{-4}\ \frac{\text{mbar}\cdot\text{l}}{\text{s}}$. The error bars shown include repeatability, hysteresis and linearity.

Following this definition, several leakage tests have been performed for the gas mixing system. The TPC has been disconnected for all tests in order to investigate only the tightness of the instrumentation. The investigated gas volume is therefore given by the piping of approximately 15 m length with 4 mm inner diameter. The volume is estimated to be smaller than 0.2 l.

For each test, the gas system is flushed with helium in order to build up an overpressure. Once the overpressure is established, the flow is turned off. The pressure controller then closes the exhaust valve to maintain the pressure within the system. In this state, the overpressure drops only due to leakage and diffusion. Monitoring the system pressure p in dependence on the time t gives therefore a handle to calculate the leakage rate. The decay time τ can be extracted from the observed pressure decay, which follows:

$$p_{\text{meas}}(t) = A \cdot \exp\left(\frac{t}{\tau}\right) + p_{\text{offset}}. \tag{2.6}$$

The overpressure at $t = 0$ is given by A, the environmental pressure by p_{offset}.

1. The first leakage test has been performed with a safety-bubbler for over- and underpressure protection. A disadvantage of this safety-bubbler is that it introduces some dead volume and is a source for water vapor in the system. Consequently, it has been replaced by mechanical valves later.

   The observed pressure decay is shown in figure 2.9. The decay time is 8.2 h. The leakage rate can be calculated from the decay in the first hours $\frac{\Delta p}{\Delta t} \leqslant \frac{9\,\text{mbar}}{2\,\text{h}}$. It is determined to be $Q_L < 2.5 \times 10^{-4}\ \frac{\text{mbar}\cdot\text{l}}{\text{s}}$.

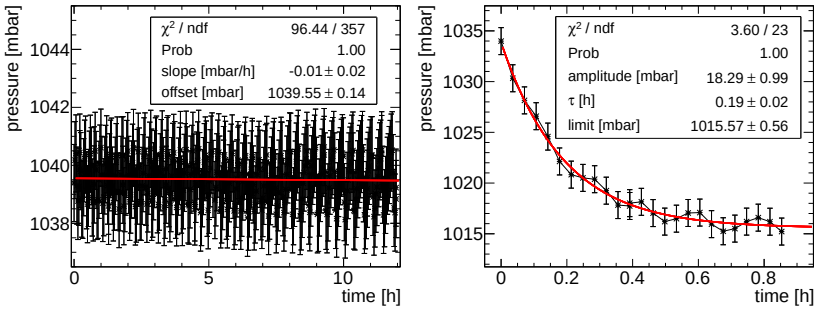

(a) (b)

Figure 2.10: Leakage tests:
a) Without hardware over- or underpressure protection, the leakage rate Q_L is less than $4 \times 10^{-7} \frac{\text{mbar}\cdot\text{l}}{\text{s}}$.
b) With mechanical over- and underpressure valves, the leakage rate is in the order of $10^{-2} \frac{\text{mbar}\cdot\text{l}}{\text{s}}$.

2. The second test has been carried out without dedicated hardware for over- and underpressure protection. As shown in figure 2.10a, the tightness is significantly improved in this case. The pressure decrease is too small to identify an exponential decay. Therefore, a linear function was fitted to the data in order to extract the leakage rate. The latter is found to be less than $4 \times 10^{-7} \frac{\text{mbar}\cdot\text{l}}{\text{s}}$. The periodic pressure fluctuation observed in the data is introduced by the working cycle of the air conditioning system.

3. The last leakage test has been conducted with two mechanical valves, one for the over- and one for the underpressure protection. As shown in figure 2.10b, these devices are less tight than the safety-bubbler. The decay time is only 0.19 h, the leakage rate in the order of $10^{-2} \frac{\text{mbar}\cdot\text{l}}{\text{s}}$. This can be explained by the construction of the valves which are closed by a spring causing a continuous opening of the valves when the opening pressure is approached.

   The leakage caused by these valves is accepted, because they allow to get rid of the dead volume and the water vapor source introduced by the safety-bubbler.

From all pressure curves, it can be seen that the accuracy of the pressure measurement is better than stated by the manufacturer (c.f. Sec. 2.1.1). This results in a vanishing χ^2 for the fitted exponential curves.

Comparable measurements have been carried out for the MediTPC at Desy, for example. The first version of the MediTPC gas system lost the pressure exponentially with a decay time of 30 minutes [48] corresponding to a loss of more than 30 mbar/h. According to [113],

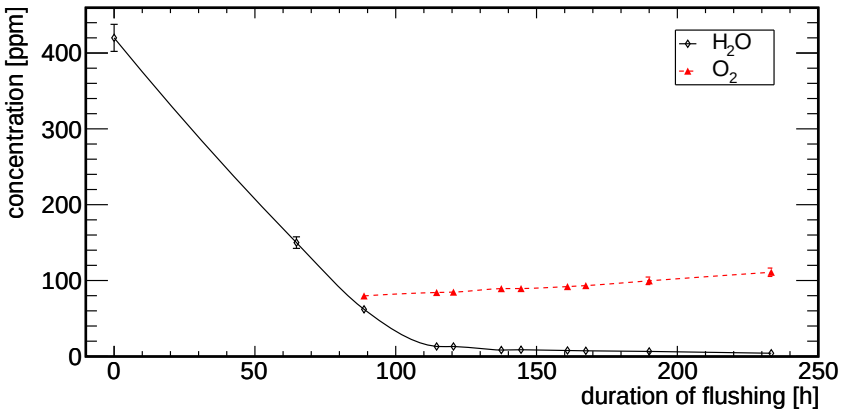

Figure 2.11: Hygrometer and Oximeter are flushed with a calibration gas ($Ar{:}CO_2$ 70:30 with 80 ppm O_2) at 5 l/h. After 90 h of flushing the oximeter is calibrated to 80 ppm.

this was improved later down to a loss of less than 5 mbar/h. However, a comparison is difficult since the decay time was not updated and the investigated gas volume is not stated in any of the reports.

2.5.2 *Calibration of the Trace-Analyzers*

While the hygrometer is calibrated by the manufacturer, the oxygen sensor has to be calibrated by the user every time the micro-fuel cell is exchanged. In principle, the calibration could be done with air (21 % O_2). The maximal accuracy, however, can only be achieved with a calibration at conditions which are comparable to the actual operating point.

Therefore, the calibration inlet was used to flush the main exhaust line, including the trace contamination sensors and the pressure controller, at 5 l/h and 1020 mbar with calibration gas ($Ar{:}CO_2$ 70:30 with 80 ppm O_2). According to the manufacturer, a few hours are needed to reach an equilibrium state. After 90 h of flushing, it has been expected that the instrumentation is free from remnant contaminations and the oximeter was calibrated, see figure 2.11. While the water contamination drops as expected during flushing, the measured oxygen content does not settle as expected but suffers from a time drift.

This malfunction is repeatable and can be neither explained by leakage nor by outgassing effects since any of these should lead to an equilibrium state after some hours of flushing. In order to exclude the micro fuel cell as malfunction source, this cell was exchanged, but no change was observed. The remaining most prominent error source is a malfunction in the analyzer electronics itself. This could not be replaced up to now, so no final solution can be given.

However, the use of the Teledyne 3190 has been proven in several other experiments, for example in the FOPI GEM-TPC, Medi-TPC

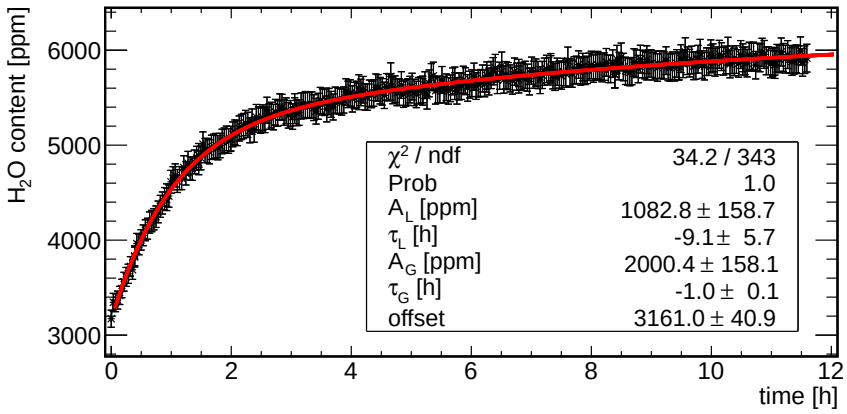

Figure 2.12: The water contamination increases with time if the system is not flushed with dry gas. This increase is explained by outgassing and leakage.

and Large-TPC at DESY [48] or the NEXT project [114]. Therefore, it should be possible to achieve the same performance once the defect is located and fixed.

Meanwhile, an estimated O_2 contamination can be extracted from the data obtained with the TPC as shown in section 5.2.

2.5.3 H_2O *Contamination*

Two different mechanisms lead to a H_2O contamination of the gas in the mixing system. The first is leakage, the second is outgassing from the instrumentation, including the pipes. The first effect can be minimized by a tight system, the second by dry-flushing.

While the system is flushed with dry gas, a certain amount of water molecules is dissolved from the pipes per unit time. This amount depends on the difference in humidity in the gas and on the piping. After some days of flushing, no water remains attached to the pipes. In this case, very low H_2O contaminations of 10 to 20 ppm_V have been observed.

If one fills the system with dry gas and turns off the flow, the effect of outgassing and leakage can be seen (Fig. 2.12). Since both effects are described by exponential functions the water contamination W(t) is described by:

$$W(t) = A_G(1 - \exp(t/\tau_G)) + A_L(1 - \exp(t/\tau_L)) + A_{Offset}. \quad (2.7)$$

The quick rise (τ_G) in the beginning is caused by outgassing. After some hours, an equilibrium between dissolving and newly attached water molecules is reached. The mere shallow rise (τ_L) which becomes dominant after long times is caused by leakage.

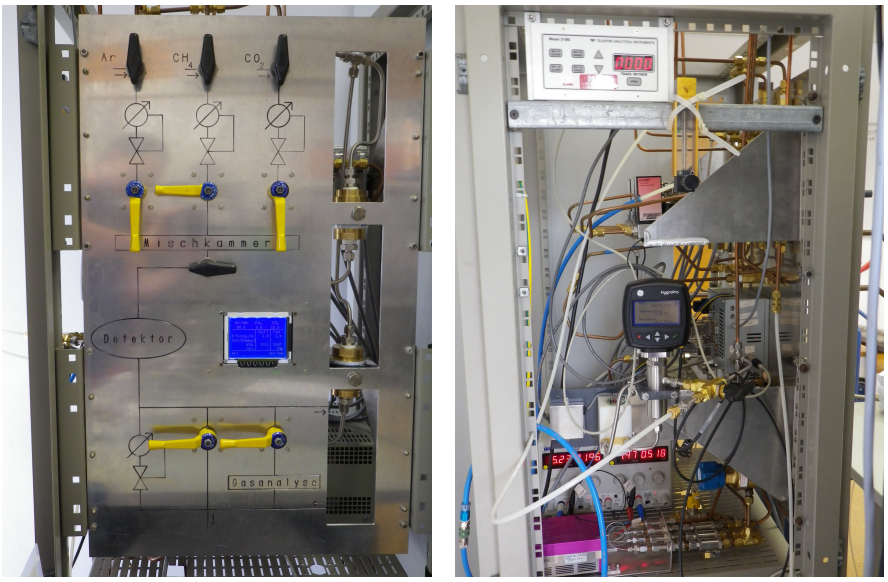

(a) (b)

Figure 2.13: Front (a) and side (b) view of the gas mixing system. In the side view, the oximeter (top), the hygrometer (center) and the gas chromatograph (bottom left) are visible.

2.6 SUMMARY

The gas mixing system as shown in figure 2.13 and discussed in this chapter was used during several data taking periods with the TPC prototype described in chapter 3. Since then, it is in operation during the commissioning of other gaseous detectors and during tests of new detector and read out architectures.

Commercially available gas mixing solutions like the Environics Series 4000 or the Gas Mixing System GMS 150 from Photon System Instruments do not offer the same functionality, especially no pressure controlling or temperature surveillance. Also an unmatched gas flow range is achieved by duplicating each gas channel.

The gas mixing system can be considered to be sufficiently tight. The leakage rate achieved with mechanical pressure protection valves corresponds to a hole with a diameter of roughly 10 µm. However, if the valves would be removed and one relies on the electronic pressure surveillance, this could be improved largely (leak diameter $<$ 100 nm).

Due to the benefits of the gas mixing system, it was decided to build a second unit for another laboratory with only small changes. The most important modification was to ensure that all sealings are compatible with isobutane which will be used in an upcoming X-ray detector for the CAST-Experiment [115].

3

THE PIXEL TPC

A TPC operated at a TeV linear collider must feature at least a spatial resolution of 100 µm in the xy-plane and 400 µm to 1400 µm in drift direction (from zero to full drift length of 2.3 m). This allows for a momentum resolution $\delta(1/p_T)$ better than 1×10^{-4} /GeV with the TPC only. Furthermore, the double hit resolution aimed at is about 2 mm in the xy-plane and 6 mm in drift direction respectively [8]. These demands exceed the performance of existing TPCs by up to one order of magnitude. Therefore, existing readout techniques have to be vastly improved.

The required specifications come within reach, when MPGDs (c.f. Sec. 1.3) are combined with a readout plane which fully exploits the potential of the gas amplification stage. Obviously, the dimensions of typical readout pads (few mm²) are not matched to the pitch of MPGDs (50-140 µm).

The effective granularity of a readout pad plane is enhanced, if the charge is spread out over several pads, for example by application of a resistive foil. This allows to resolve the characteristics of a charge deposition and to reconstruct the original position of a primary ionization from the center of gravity of the detected charge distribution. This well approved method works with both GEMs and Micromegas. Spatial resolutions of $\sigma_{xy} = 80$ µm and less can be achieved [116].

Alternatively, the characteristics of a charge deposition can be resolved, if the size of the readout pads is reduced down to the dimension of a charge cloud emerging from the gas amplification stage. Calculations presented in [117] predict that this largely improves the spatial resolution.

Shrinking the readout pads obviously increases the total number of pads. Since all of them have to be connected to external readout electronics, the routing effort is increased as well. Typically, the signals are routed on a printed circuit board through the readout plane to the readout electronics on the backside. Yet rather large pads of a few 100 µm² result in a channel density which makes it virtually impossible to rely on this approach. Even if advanced production techniques would allow to route the wires in the necessary density, the signal quality would suffer from channel to channel crosstalk and noise caused by the large capacitances connected to the electronics.

Although shrinking classical readout pads down to a few 10 µm² is not possible, such pad dimensions can be achieved by combining

the readout electronics directly with the charge collecting anode pad on an Integrated Circuit (IC).

In [118, 119], this approach has been followed up. Here, micro patterned gas amplification stages have been combined with pixel chips featuring 2101 respectively 65 536 pixels, each equipped with a charge collecting anode pad on the chip surface as well as the necessary readout electronics. This brought gaseous detectors for the first time to a level of integration and granularity usually reserved to semiconductor pixel detectors.

Several studies using Medipix2 [120], Timepix [18] or FEI3 [121] chips for the readout of drift chambers with a few centimeters drift distance have been performed [122–125]. The high granularity allows for precise information on the charge cloud caused by single primary electrons. In particular, it is possible to separate individual charge depositions originating from different primary electrons. This allows precise dE/dx measurements by mere counting of charge depositions. Furthermore, it is expected that the probability to separate two adjacent tracks is increased. Besides, the advanced readout integration potentially simplifies the mechanical setup and allows for a minimal material budget.

In Bonn, for the first time a TPC with Timepix pixel readout and a rather long drift distance is operated. First insights into this project are given in [126–133].

The experimental setup is described in some detail in the first section of this chapter. The most relevant properties of the readout ASIC (Application Specific Integrated Circuit) are summarized in section 3.2. The value of the gathered data is increased with the calibration explained in section 3.3. Simulations of the drift gas properties are presented in section 3.4.2. Finally, a short summary is given in section 3.5.

3.1 EXPERIMENTAL SETUP AND OPERATING CONDITIONS

The cylindric field cage of the pixel TPC was designed and manufactured at the RWTH Aachen [134]. It is formed by a sandwich of glass-fiber reinforced plastic and Kapton, supported by an Aramid honeycomb structure, see figure 3.1a. The material budget is only 1 % of a radiation length.

The drift field is homogenized down to $\Delta E/E < 10^{-3}$ by 187 field strips with 2.8 mm pitch. The field strip potentials are defined by a resistor chain. Drift fields of up to 1 kV/cm are possible.

The drift volume has a length of 26.32 cm and a diameter of 23 cm. Anode and cathode are formed by copper planes resting on nylon pillars in the field cage. A triple GEM stack with 1 mm transfer gaps is inserted into the anode plane as shown in figure 3.1b. The GEMs,

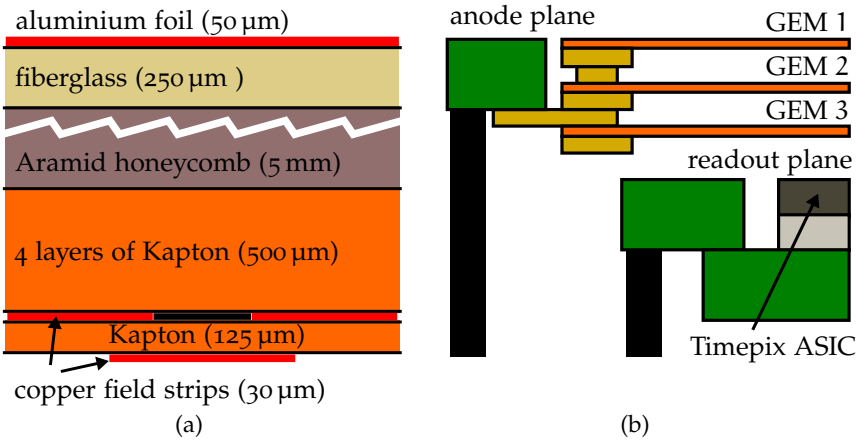

Figure 3.1: a) Cross section of the field cage cover. The field strips face towards the drift volume.
b) Tripple GEM stack and readout plane equipped with the Timepix ASIC.

produced at CERN, have a thickness of 56 µm and cover an area of 10 cm × 10 cm. The holes have a diameter of 60–70 µm. They are arranged in a hexagonal pattern with 140 µm pitch.

The readout plane, located 1 mm below the GEM stack, is equipped with a bare Timepix ASIC operated with a 55.4 MHz clock. The bump-bond pads of the pixels, originally foreseen for interconnection with a silicon sensor, act as charge collecting anodes.

Since it offers a good stability for the operation of the GEM stack, a mixture of 70 % helium and 30 % CO_2 was chosen as drift gas. A continuous gas flow of 5 l/h ensured drift gas purity. The operating pressure was kept a few millibar above the environmental pressure.

The drift field was set to 495 V/cm. The voltage across each GEM was 415 V. The transfer fields were set to 2200 V/cm, the induction field to 3000 V/cm.

The particle tracks, recorded in a cosmic ray test-stand, originate mainly from minimal ionizing muons passing the chamber. The readout is triggered by coincident signals from scintillators placed above and below the TPC. A photograph of the test-stand and a representative event are shown in figure 3.2. The individual charge depositions are clearly visible.

3.2 THE TIMEPIX ASIC

The Timepix ASIC was developed in 2007, based on the Medipix2 chip which was originally designed to be used in connection with a semiconductor sensor for medical imaging. It features 256×256 pixels on a 2.27 cm² die. The peripheral electronics and bump-bond pads

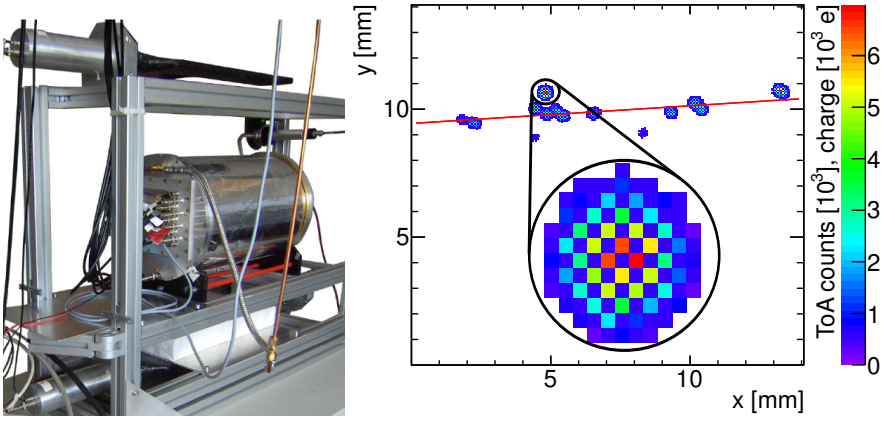

(a) (b)

Figure 3.2: a) Test-stand photograph showing the TPC and two scintillators which are used for triggering [127].
©IOP Publishing Ltd. and Sissa Medialab srl. Reproduced by permission of IOP Publishing. All rights reserved.
b) Display of a typical event recorded with the pixel TPC. Depending on the pixel mode, the arrival time of a hit (blue) or the detected charge (colorful) is displayed for each pixel (c.f. Sec. 3.2.1.3).

are located on one side of the die, utilizing only 13 % of the chip area. This allows to neighbor several chips with virtually no dead space in between. The total power consumption during operation is less than 2 W. A photograph of the Timepix chip, placed in the center of the readout plane, is shown in figure 3.3a. The conventional pads (1 mm × 4 mm) surrounding the Timepix ASIC are not read out, but simply connected to ground potential.

3.2.1 *Pixel Electronics*

Each Timepix pixel measures 55 µm×55 µm and features a Charge Sensitive Amplifier (CSA) and a single threshold discriminator in the analog section as well as a 14 bit counting logic in the digital domain. The pixel layout is depicted in figure 3.3b.

3.2.1.1 *CSA*

The Timepix front-end circuitry, sketched in figure 3.4, is discussed in full detail in [135]. It is based on a scheme proposed in [136].

The feedback circuitry allows integration of either positive or negative charge carriers. At the same time, the output signal is shaped. Thus, no dedicated shaping amplifier is needed. Key feature of the so-called Krummenacher feedback is a split of the feedback current into two branches:

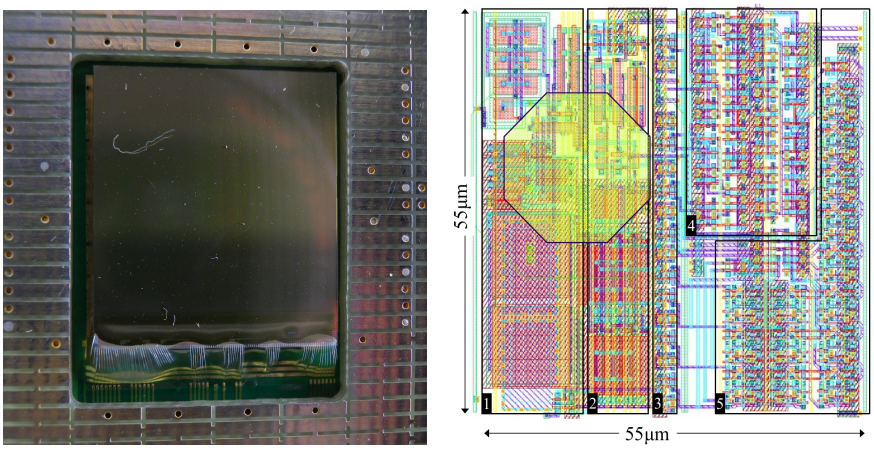

(a) (b)

Figure 3.3: a) Photograph of the Timepix chip centered in the readout plane. Bond wires are only located at the bottom of the chip.
b) Timepix pixel layout. The analog block consists of a CSA (1) which is DC-coupled to a discriminator (2). In the digital section, 8 Configuration bits (3), the control logic (4) and 14 flip-flops (5) are located. The octagonal bump bond pad is located in the upper left. Reprinted from [18], with permission from Elsevier.

The p-MOSFET T1a with transconductance g_m^{T1a} acts as resistive feedback $R_f = 1/g_m^{T1a}$ in parallel with the feedback capacitance C_f. The second feedback path through the n-MOSFET T2 is controlled by the current through T1b. The latter is integrated on capacitor C. This path operates equivalently to an inductor connected in parallel with C_f. It drains DC leakage currents at the CSA input node. Short charge signals on the other hand are drained by T1a, since T2 withstands quick potential changes. When

$$\frac{C}{g_m^{T2}} > 2\frac{C_f}{g_m^{T1a}} \tag{3.1}$$

holds for all leakage currents ($g_m \propto I_D$), the feedback loop is damped correctly. However, this leakage current compensation is relevant only for semiconductor sensors. In gaseous detectors, this feature is of no use.

The operating point of the CSA is defined by three Digital to Analog Converters (DACs):

- $DAC_{I,Krum}$ defines the feedback current and therefore the time needed for a return to the baseline.
- DAC_{FBK} shifts the output potential. This is necessary since the discriminator is DC-coupled to the CSA.
- DAC_{GND} controls the potential of the CSA input node.

The internal error-amplifier can be tuned by two additional DACs:

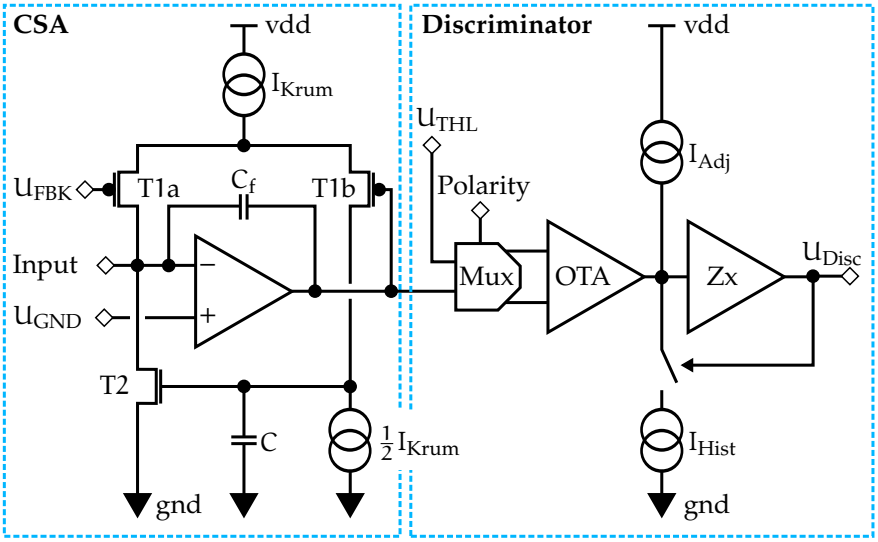

Figure 3.4: Front-end of the Timepix ASIC. The CSA with Krummenacher feedback is DC-coupled to the discriminator circuitry.

- DAC_{Preamp} regulates the bandwidth of the error-amplifier.
- DAC_{VCas} allows to trade signal to noise ratio for dynamic range.

With typical DAC settings, the CSA has a gain of roughly 14.5 µV/e and a peaking time of 100 ns. The output noise is equivalent to an input charge of 70 e [135].

3.2.1.2 *Discriminator*

The discriminator, drafted in figure 3.4, is built of a multiplexer (Mux), an operational transconductance amplifier (OTA) and a zero crossing detection circuit (Zx). The multiplexer allows to operate the subsequent circuitry independently of the polarity of the input charge.

The output current of the OTA is positive if the CSA output potential is below the threshold potential U_{THL} and negative if the threshold is exceeded. The zero crossing circuit, based on a scheme proposed in [137], sets the discriminator output high (true) if a negative current is detected.

An adjustable current source I_{Adj} is implemented in each pixel. This allows for modulation of the OTA output current and is used to compensate for threshold and gain dispersion between individual pixels.

If a negative current is detected by the zero crossing detection circuit, the additional current sink I_{Hist} is activated. Thus, the current is further reduced and a hysteresis effect is achieved. High frequency output pulses, potentially disturbing subsequent logic, are avoided therefore.

Following DACs control the discriminator:

- DAC_{THL} and $DAC_{THL,Coarse}$ define the threshold level.

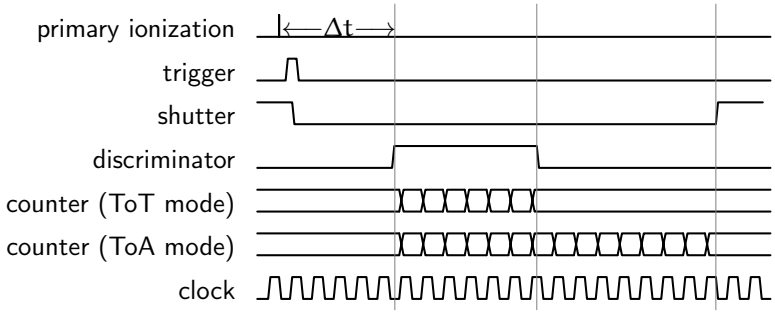

Figure 3.5: Timing diagram showing the counter operation in ToT and ToA mode. The time elapsing until a charge deposition is sensed in a pixel is labeled Δt.

- $DAC_{I,Adj}$ is instantiated in each pixel. It is used to compensate for pixel to pixel mismatch.
- DAC_{THS} defines the step size of $DAC_{I,Adj}$.
- $DAC_{I,Hist}$ allows to enable and control the hysteresis.
- $DAC_{I,Disc}$ controls the current consumed by the transconductance amplifier and the zero crossing detection circuit. This directly influences the reaction speed.

3.2.1.3 *Counting Logic*

Besides the analog circuitry, a 14 bit counting logic is located in each pixel. The counters are enabled by a global shutter signal (active low) and sensitive to the rising edge of a clock signal. In order to avoid glitches, the shutter signal is synchronized to the clock in each pixel.

The clock is provided by external readout hardware and distributed from pixel column to pixel column by minimum sized inverters. The clock network is specified for frequencies up to 100 MHz.

For deactivation of individual pixels, the connection between the analog and the digital domain can be interrupted by a so-called mask switch.

The counting logic in each pixel is configured individually to one of four modes:

- In the single hit mode, only the boolean information whether a hit was detected is stored.
- The Medipix mode is inherited from the Medipix ASIC. In this mode, the number of discriminator transitions is counted. It can be used for X-ray imaging.
- In the Time over Threshold (ToT) mode, all clock cycles occurring while the discriminator output is high are counted. This is a measure for the input charge.

- The Time of Arrival (ToA) mode allows to determine the time at which a hit is detected. Counting of the clock cycles is started on the first discriminator transition and stopped when the shutter returns to the high state. The ToA with respect to the pixel activation is calculated by:

$$\mathrm{ToA} = t_{\mathrm{shutter}} - \frac{n}{f_{\mathrm{clock}}}, \tag{3.2}$$

  where t_{shutter} is the length of the shutter signal, n the number of counted clock cycles and f_{clock} the clock frequency.

For operation of a TPC, especially the ToA and ToT modes, allowing measurement of the drift time and the charge deposition, are relevant. They are visualized in the timing diagram shown in figure 3.5.

Due to the diffusion in the GEM stack, the charge cloud caused by a primary electron activates several neighboring pixels, see figure 3.2b. Configuring the pixels in a checker board pattern to ToA or ToT mode allows therefore to measure the charge and the arrival time of a charge cloud emerging from the GEM stack, although a single pixel can measure either one or the other.

3.2.2 *Timepix Readout*

The Timepix chip is operated in a shutter controlled mode with sequential read out. When the global shutter signal is low, the pixel logic is in data taking mode. When the shutter is inactive (high), the pixel counters are operated as linear shift register. In this case all counters are daisy-chained, forming one large memory block. Either 32 parallel CMOS or one Low Voltage Differential Signal (LVDS) line can be used for data transfer. The serial LVDS readout takes 917 768 clock cycles, the parallel readout 28 688 clock cycles.

It is possible to directly interconnect several Timepix chips in a daisy chain. In this case the pixel matrices of the combined chips appear as one large matrix to the readout electronics.

In the presented setup, the Timepix chip was read out with the Medipix reUsable ReadOut System 2.1 (MUROS 2.1) developed at NIKHEF (Amsterdam) [138]. Nowadays, also other readout systems are available [139–144]. All come with slightly different specifications. The logic modules available on the MUROS FPGA allow to read out up to 8 daisy-chained Timepix chips at a time.

The MUROS is interfaced by a National Instruments DIO PCI-card and controlled by the Pixelman software developed at the IEAP of the CTU Prague [145, 146]. The latter provides routines for data taking, chip configuration and some basic diagnostics as well as an algorithm determining the optimal setting of the threshold adjustment DACs in the individual pixels.

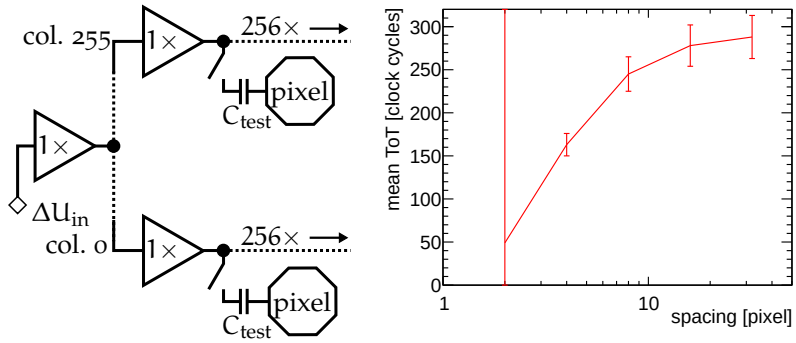

(a) (b)

Figure 3.6: a) Schematic visualizing the test-pulse network.
b) Mean measured ToT in dependency of the pixel spacing during application of an arbitrary test-pulse. The error bars show the width of the observed ToT distributions.

3.3 TIMEPIX CALIBRATION

A calibration curve relating counted ToT clock cycles to the input charge can be obtained by manual charge injection into the pixels. Furthermore, the manual charge injection allows to compensate for the time walk effect caused by the finite CSA peaking time.

It has to be noted that a calibration is only valid for one set of DAC settings and one clock frequency.

3.3.1 *Manual Charge Injection*

A 8 fF capacitor C_{test}, connected in series with a switch to the CSA input, is located in each pixel. Application of a voltage step ΔU_{in} to this capacitor injects a well defined amount of charge Q_{in} into the front-end electronics:

$$Q_{in} = C_{test} \cdot \Delta U_{in}. \tag{3.3}$$

A positive voltage step gradient causes injection of positive charge carriers, a negative gradient results in the injection of negative charge carriers.

For maximum accuracy, rise and fall times of the voltage steps should be as short as possible, in particular smaller than the peaking time of the CSA which is roughly 150 ns. Unity gain buffers located at the bottom of each pixel column as well as at the test-pulse input pad help to keep rise and fall times small. Furthermore, these buffers increase test-pulse homogeneity within the pixel matrix. The test-pulse network is drafted in figure 3.6a.

The linear range of the test-pulse buffers extends from 335 mV to 2.18 mV. This limits the maximally injectable charge to roughly 90 000 electrons [147]. Although the buffers are designed to drive the

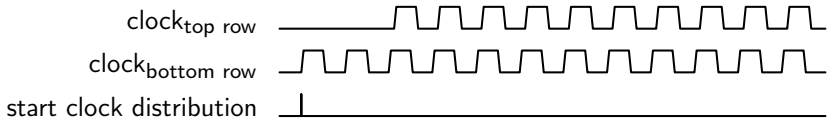

Figure 3.7: Distributing the clock signal with minimum sized buffers from pixel to pixel results in a phase shift between the pixel rows. The accumulated delay between pixels located at top and bottom of the pixel matrix is expected to be roughly 50 ns.

capacitive load of the test-pulse network, they are not capable to drive the summed test-pulse capacitances of all pixels in a column. If too many pixels are connected at the same time, amplitude and homogeneity of the charge injection are degraded.

The mean ToT measured by test-pulse application in dependency on the spacing between the active pixels is shown in figure 3.6b. A spacing of n means that in a square of $n \times n$ pixels only one pixel is active. If different pixels are chosen in n^2 subsequent acquisitions, test-pulses are applied to all pixels – however not at the same time. It is found that the measured ToT becomes insensitive to the number of simultaneously connected pixels, if 16 or less pixels are connected to the test-pulse network per column and row. Clearly, eq. 3.3 is only valid in this case.

3.3.2 *Clock Delay*

As mentioned previously, the clock is distributed across the pixel matrix by clock buffers in every pixel. Clock rise time and buffer response cause a propagation delay of roughly 200 ps between two subsequent pixel rows. On the one hand, this phase shift results in a homogeneous power consumption by the clock network. On the other hand, the clock signal is not instantaneous available in all pixels, see figure 3.7.

A hit arriving in a pixel to which the clock has not been distributed at this time will result in too low ToA and ToT measurements. Once the clock signal is available in all pixels, the clock distribution delay has no effect on the measurements. Thus, activating the pixels at least 50 ns after the clock distribution has started ensures that the measurement is not affected by the clock distribution.

The Pixelman software takes care that the clock is available in all pixels before the shutter is lowered. This is shown with a test-measurement in which all pixels but those on the pixel matrix diagonal are deactivated by the mask bit. The threshold is set below the noise level and the pixels are configured to the ToA mode. Thus, the selected pixels start counting as soon as the shutter is lowered.

The measured ToAs are shown in 3.8a. Only two different ToA values are measured, a gradient from the top to the bottom pixels is not observed. Also in complementary measurements, in which the pixels

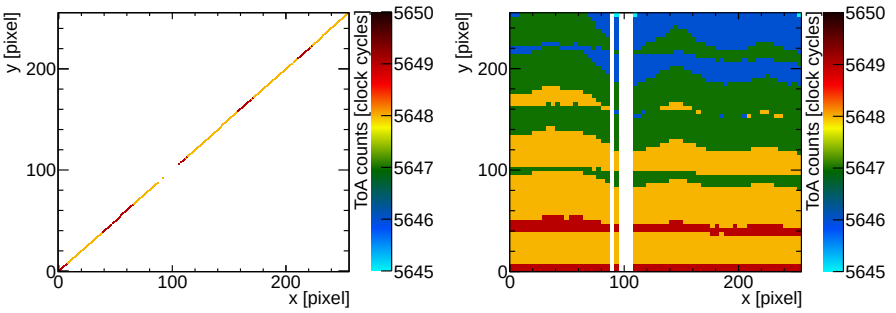

(a) (b)

Figure 3.8: a) The clock distribution scheme does not affect the measured ToA, if the column occupancy is low.
b) With a large column occupancy (shown is a spacing of 4), a gradient in the measured ToAs is observed. Increasing the occupancy further pronounces the effect. The chip used for these tests has several defective pixels which are visible as white columns in the plots.

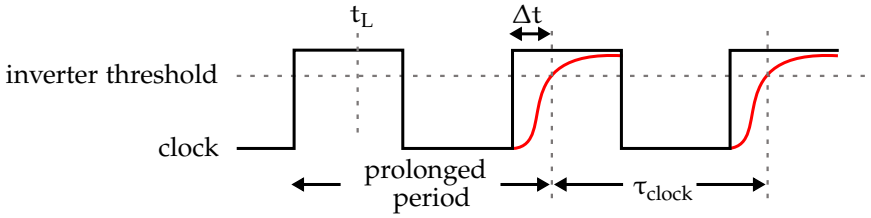

Figure 3.9: When the nominal supply voltage is available, the clock edges are steep (black). A voltage drop caused by a large load, activated at $t = t_L$, reduces the clock slope (red). This results in a load dependent phase shift Δt, prolonging one clock period. The overall frequency remains unchanged.

have been activated by test-pulses at different times with respect to the shutter, no gradient from the lower to the upper pixels was observed. Hence, it is reasoned, that the clock distribution delay does not affect the measurement.

Contrary to the above situation, the clock distribution scheme affects the measurement if many pixels in one column are activated at the same time. In a test-measurement shown in figure 3.8b, a spacing of 4 is applied to the pixel matrix. Again, the pixels are triggered by noise. Equivalent results are obtained if the counters are activated by test-pulses.

The observed ToA gradient is caused by the simultaneous operation of the counting logic in many pixels, eventually resulting in a voltage drop on the digital supply rail. This in turn reduces the driving strength of the clock buffers and causes an additional phase shift, see figure 3.9. Over all pixel rows, this small phase shift adds up to a few full clock cycles.

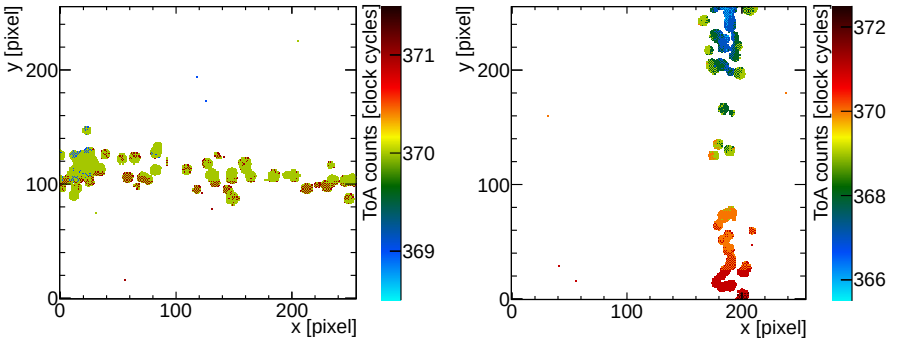

(a) (b)

Figure 3.10: ToA, measured when pixels representing a track are activated at the same time by test-pulses. If the hits are distributed along the x-axis, virtually no clock delay is observed (a). If the particle tracks are oriented along the y-axis, the clock delay causes a systematic mismeasurement (b).

In the data set discussed in the following chapters, the tracks run basically in parallel to the rows. Test-measurements, in which only pixels distributed as in a representative event are activated, show that the occupancy per column is low enough to cause virtually no clock delay, see figure 3.10a. Thus, a compensation for the clock delay is not necessary.

If higher column occupancies occur, for instance when a track runs in parallel with the pixel columns, the clock delay causes systematic mismeasurements. This situation is reproduced for the measurement shown in figure 3.10b. Only pixels that are distributed like in an event with a vertical particle track are activated by test-pulsing. In this case, a clock delay of several clock cycles is observed. Since it varies with the occupancy from event to event, it is virtually impossible to entirely compensate for the clock delay. However, based on a mean occupancy, correction values could be assumed and used for compensation during reconstruction.

3.3.3 *Charge Calibration*

The charge calibration of a bare Timepix chip operated in the prototype TPC is done similarly to the energy calibration of a Timpix chip bump bonded to a semiconductor sensor which is described in [148, 149]. Negative charges are injected into the pixel electronics by applying voltage steps with a slow rise (1.5 µs) and a steep drop (5 ns) to the test-pulse input. A spacing of 32 pixels results in a homogeneous response over the pixel matrix. Thus, assuming uniform gain, threshold and feedback current in all pixels, it is not necessary to calibrate pixel by pixel. Instead all pixels can be combined in one calibration.

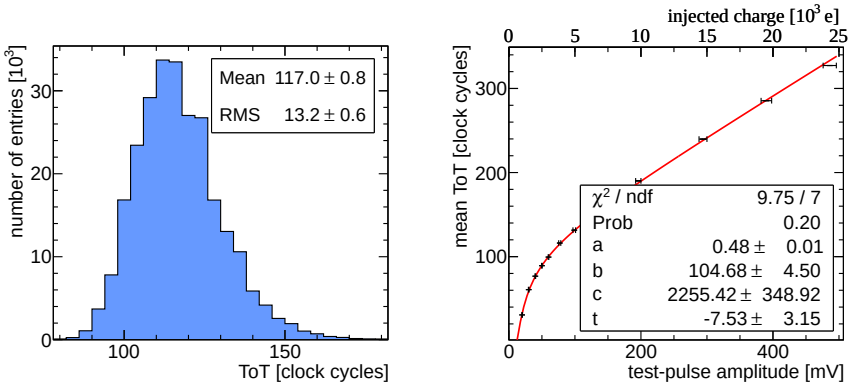

(a) (b)

Figure 3.11: a) ToT spectrum obtained for test-pulses with 80 mV amplitude. b) Dependency of the measured ToT on the test-pulse amplitude. The data is approximated by the surrogate function 3.4.

The influence of noise in single random pixels is reduced by not only averaging over all pixels, but also over several charge injections. ToT distributions as shown in figure 3.11a are obtained for each test-pulse amplitude. The asymmetry in the ToT spectra originates from the nonlinear relation between input charge and ToT.

Plotting the mean measured ToT in dependence on the injected test-pulse amplitudes ΔU_{in} results in the graph depicted in figure 3.11b. The dependency is highly nonlinear for small input charges. If the free parameters a, b, c and t are chosen correctly, the data can be described by a surrogate function:

$$\mathrm{ToT}(\Delta U_{in}) = a\Delta U_{in} + b - \frac{c}{\Delta U_{in} - t}. \tag{3.4}$$

Replacing ΔU_{in} by Q_{in}/C_{test} (eq. 3.3) and solving for the charge yields:

$$Q_{in\,1,2}(\mathrm{ToT}) = C_{test} \cdot \frac{(\mathrm{ToT} + ta - b) \pm \sqrt{(ta + b - \mathrm{ToT})^2 + 4ac}}{2a}. \tag{3.5}$$

Solution 2 ($-\sqrt{(\dots)}$) is not physical and, therefore, discarded. The other solution is used for data reconstruction.

The parameters are determined with a rather large uncertainty. Therefore, the surrogate function can not be used to convert between charge and ToT values with high precision but only to obtain the correct order of magnitude. Especially for the threshold, only a rough value of 700 e can be given. As discussed in [150], the latter can be more precisely determined by so-called S-curve measurements.

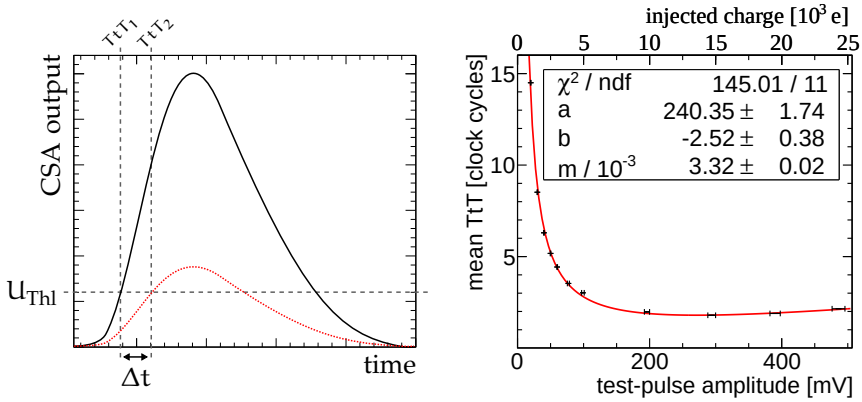

(a) (b)

Figure 3.12: a) CSA Output for large (black, solid) and small (red, dotted) input charges. The time to threshold (TtT) is dependent on the input charge, this effect is called time walk.
b) Measured TtT for different test-pulse amplitudes. The data is approximated by the surrogate function 3.8.

3.3.4 *Time Walk Compensation*

While the amplitude of the CSA output is proportional to the input charge, the peaking time is constant. Hence, the slope of the CSA output increases with the input charge, see figure 3.12a. Accordingly, the delay between charge injection and the moment the hit is sensed by the discriminator drops with rising input charge. This delay is labeled Time to Threshold (TtT). The variation of the TtT is called time walk effect and can be compensated for if the TtT is known for a hit.

The TtT for different input charges is measured by injecting negative charges into the pixels. While the test-pulse setup is in general identical to the setup during charge calibration, the pixels are configured to measure the ToA instead of the ToT. The clock delay is avoided by a spacing of 32 pixels. Thus, the ToA spectrum obtained from all pixels and several charge injections is narrow ($\sigma < 1$ clock count). The mean measured ToA in dependence on the test-pulse amplitude is approximated by a surrogate function:

$$\mathrm{ToA}(\Delta U_{in}) = \frac{a}{\Delta U_{in} + b} + m\Delta U_{in} + t_{injection}, \tag{3.6}$$

where a,b,m and $t_{injection}$ are free parameters. The latter is determined by the moment in which the charge has been injected. Thus, the TtT is given by:

$$\mathrm{TtT}(\Delta U_{in}) = \mathrm{ToA}(\Delta U_{in}) - t_{injection}. \tag{3.7}$$

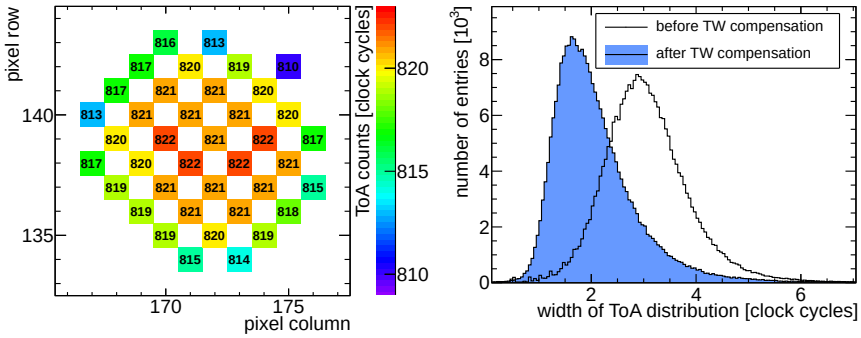

(a) (b)

Figure 3.13: a) ToA values measured in a charge deposition, counter values of pixels not configured to the ToA mode are not shown. Without the time walk effect, all pixels should show the same ToA value.
b) Widths of the ToA distributions for all charge depositions in a data taking run before (black line) and after the time walk compensation is applied (solid).

Eventually, the data shown in figure 3.12b is obtained. In the reconstruction software

$$\mathrm{TtT}(\Delta U_{in}) = \frac{a}{\Delta U_{in} + b} + m\Delta U_{in} \tag{3.8}$$

is used as surrogate function to approximate the TtT for time walk compensation. The free parameters are identical to the ones of eq. 3.6.

For recorded data, the input charge of a pixel configured to the ToA mode is interpolated from neighboring pixels configured to the ToT mode. The obtained charge is converted to an equivalent input test-pulse by means of equation 3.3.

Naively, a monotonic decreasing TtT is expected with rising input charge. This is not observed: After a minimum is reached for roughly 15 000 electrons input charge, the TtT starts to rise again. This effect is introduced by a shift of the operating point of the pixel electronics caused by the injected charge. It is accounted for by the linear term in the surrogate functions.

The measured ToA values of the pixels activated by a charge cloud emerging from the GEM stack are shown in figure 3.13a. Without the time walk effect, all pixels would show the same ToA value. In reality, the pixels in the center start counting before the pixels in the outer region.

The success of the time walk compensation can be seen on the histogram shown in figure 3.13b, where the width of the ToA distributions of all charge depositions in an arbitrary set of events is entered. The mean width of the ToA spectra is about 3.1 clock counts. After ap-

plication of the time walk compensation, this value is reduced down to 2.1 clock counts.

The quality of the time walk compensation is limited by inaccuracies caused by interpolating the input charge from neighboring pixels as well as by the accuracy with which the surrogate function 3.8 describes the time walk effect. Thus, the time walk compensation works in some cases better than in others. Eventually, this results in the skewness of the distribution after application of the time walk compensation.

3.4 SIMULATION OF THE DRIFT GAS PROPERTIES

In this section, simulations on the primary ionization along the track of a charged particle and the charge transport in gaseous media are discussed. Simulation results for the helium based gas mixture used as drift gas in the Pixel TPC are presented.

3.4.1 *Primary Ionization*

The ionization rate of a fast charged particle in a medium depends on the cross section for ionization of the medium by real photons as well as on the dielectric permeability [151]. The PhotoAbsorption Ionization (PAI) model gives the energy transfer cross section from a particle to the traversed medium. Usually, it is assumed that the total deposited energy is proportional to the amount of ionization. The small range of created δ-electrons is taken as argument that the total transfererd energy is converted into ionization at the point of interaction. However, this argument is not valid in case of gaseous detectors with a very fine spatial resolution.

In order to meet the requirements of modern gaseous detectors, an enhanced model is implemented in HEED [151] (High Energy Electro-Dynamics) – the PhotoAbsorption Ionization and Relaxation (PAIR) model. This algorithm evaluates the atomic cross sections to compute the energy transfer in every interaction of an incident particle with the medium. It allows for prediction of the spatial distribution of primary ionizations by assuming that the energy transferred from the incident particle is absorbed by a single atomic electron which is then traced. The created vacancy in the atomic shell is filled from the shell with the next principal quantum number under emission of an Auger electron. The newly created vacancies are filled from the next shell and so on. The cascade stops, when the atom is left with the outer most shell being ionized.

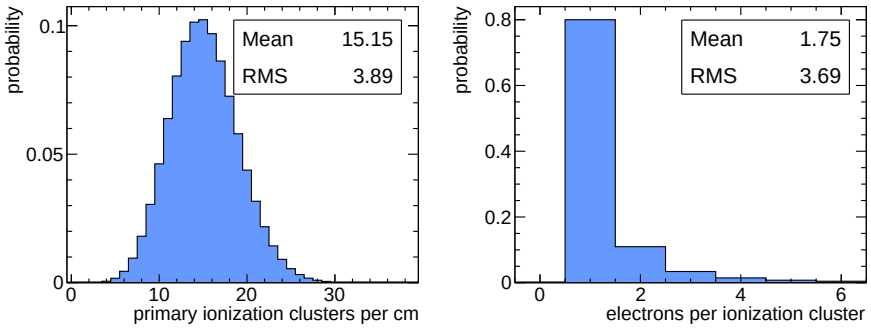

(a) Number of interaction points per cm track length.

(b) Number of primary electrons created in an interaction.

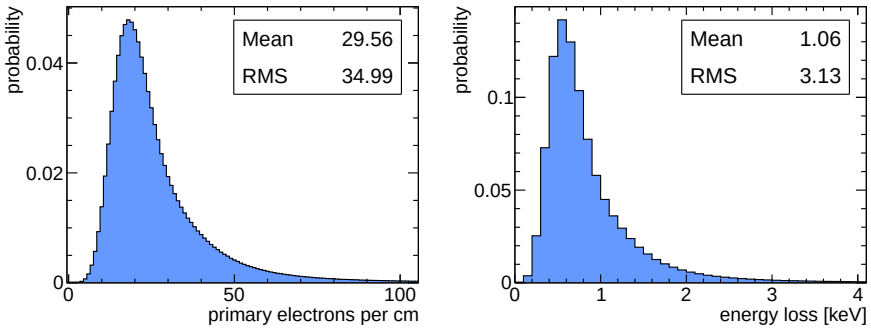

(c) Number of primary electrons per cm track length.

(d) Energy loss per cm track length.

Figure 3.14: Heed simulation results for muons with 4 Gev traversing Helium with 30 % CO_2 admixture.

Expected Primary Ionization in Helium with 30 % CO_2 Admixture

The ionization density in the gas mixture used in the pixel TPC has been computed with the most recent HEED version (28.02.2010). Since the mean energy of cosmic muons at sea level is roughly 4 GeV [152], it was assumed that the incident particles are cosmic muons with 4 GeV energy. In fact, the exact energy is of inferior importance, since cosmic muons are basically minimally ionizing particles.

The number of interactions between the incident muons and the gas is distributed as shown in figure 3.14a. Roughly 80 % of these primary ionization clusters consist of a single primary electron. Depending on the energy transfer, more electron-ion pairs may be created in a single interaction. The probability to have double, triple or even larger ionization clusters is shown in figure 3.14b.

Most probably, the incident muons create about 18 electrons per centimeter track length, see figure 3.14c.

However, the mean number of primary electrons per centimeter is significantly larger due to the probability of extreme energy transfers in single interactions. The total energy loss per centimeter track length is distributed as shown in figure 3.14d.

3.4.2 *Charge Transport*

Based on the experimentally and theoretically obtained cross sections given in [38], the basic parameters describing the movement of electrons in virtually any gas mixture can be predicted by Magboltz [33]. In this software, the Monte Carlo integration technique is used to solve the electron transport equations. Basically, the algorithm cuts the electron path into finite elements and updates the velocity vector after each step. Depending on the angular distributions of a collision, the new direction of the movement is determined. The length of each finite element is determined from the distribution of the free path lengths between two collisions with the gas [153].

In recent revisions, Magboltz does not only allow elastic, but also inelastic scattering. Furthermore, Penning effects are included in the simulation. Thus, it is possible to predict, the drift velocity, Townsend and diffusion coefficients as well as the attachment rate in a gas mixture with a high accuracy.

3.4.2.1 *Drift and Diffusion in Helium with 30 % CO_2 Admixture*

Magboltz version 8.9.5 was used to compute the drift velocity and the diffusion coefficients in a mixture of 70 % Helium(2010) and 30 % of CO_2(2007) – in brackets, the cross section database revision is given. The influence of the applied drift field as well as the effect of mixture inaccuracies, pressure and temperature variations and small H_2O(2004) and O_2(2004) contaminations has been studied at a temperature of 20 °C and a pressure of 1013.25 mbar.

As shown in figure 3.15, the drift velocity v_{Drift} is nearly linearly dependent on the electric field, the mixture accuracy, pressure and temperature as well as the H_2O contamination. It is basically independent on small O_2 contaminations.

Graphs showing the relation between the diffusion constants and the boundary conditions are shown in figures 3.16 and 3.17. As expected from section 1.2.2, both the transversal and the longitudinal diffusion constants drop with increasing drift field, drift velocity respectively. The dependence on the mixture accuracy, pressure and impurities in the ppm level is negligible if existing. Due to the increase in thermal energy, the diffusion constants increase slightly with the the temperature, c.f. Eq. 1.23.

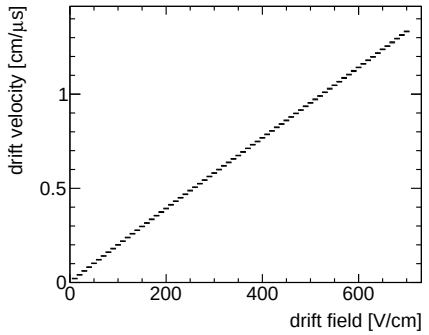

(a) Drift velocity in dependence on the drift field.

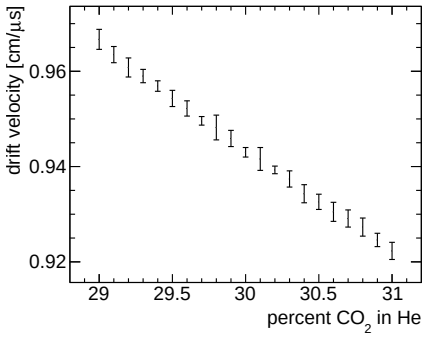

(b) Drift velocity in dependence on the ratio between Helium and CO_2.

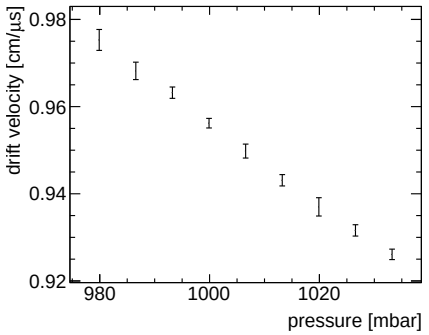

(c) Drift velocity in dependence on the pressure.

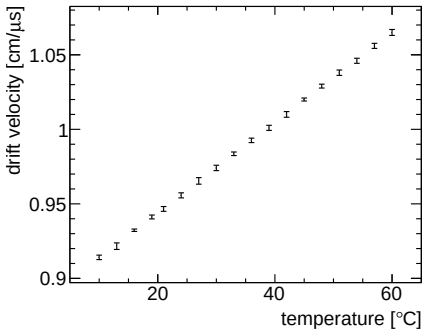

(d) Drift velocity in dependence on the temperature.

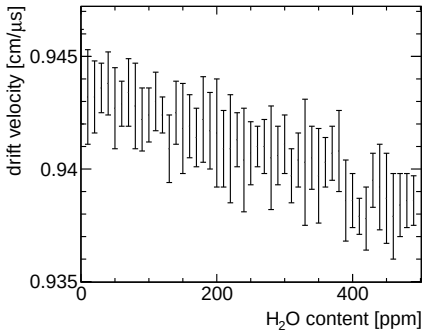

(e) Drift velocity in dependence on the H_2O content.

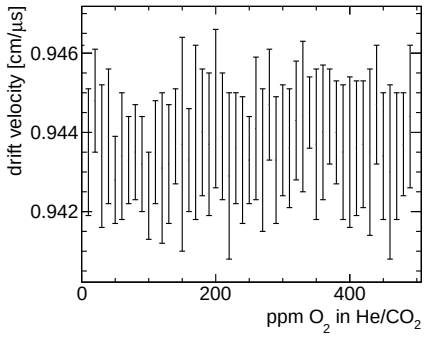

(f) Drift velocity in dependence on the O_2 content.

Figure 3.15: Simulated drift velocity in Helium with 30 % CO_2 admixture. If not varied, the parameters are: temperature 20 °C, pressure 1013.25 mbar, drift field 495 V/cm, no impurities.

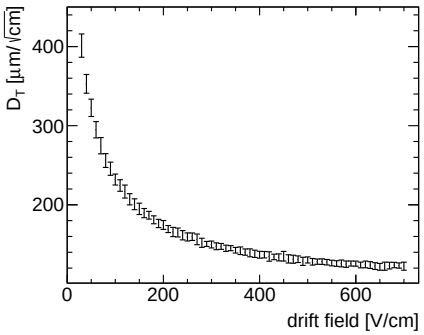

(a) Transversal diffusion constant D_T in dependence on the drift field.

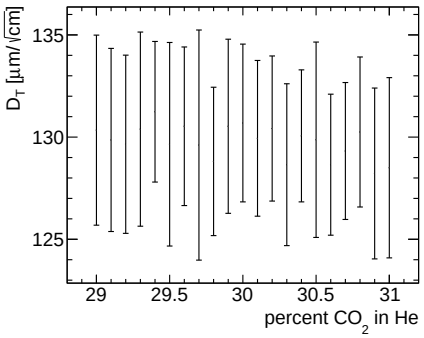

(b) Transversal diffusion constant D_T in dependence on the ratio between Helium and CO_2.

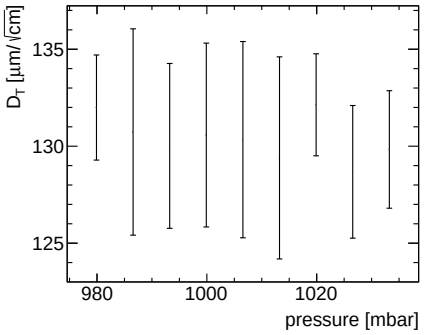

(c) Transversal diffusion constant D_T in dependence on the pressure.

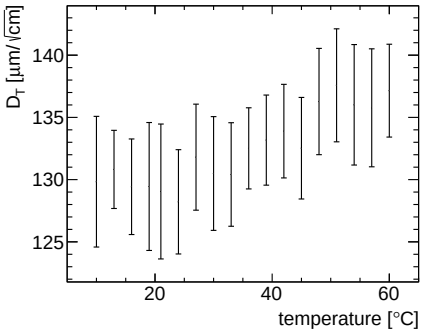

(d) Transversal diffusion constant D_T in dependence on the temperature.

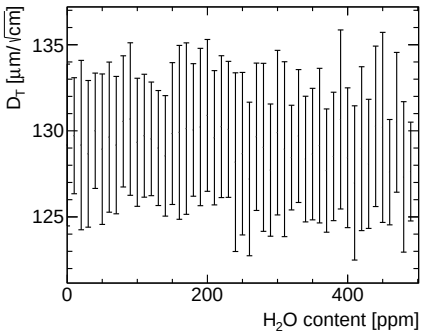

(e) Transversal diffusion constant D_T in dependence on the H_2O content.

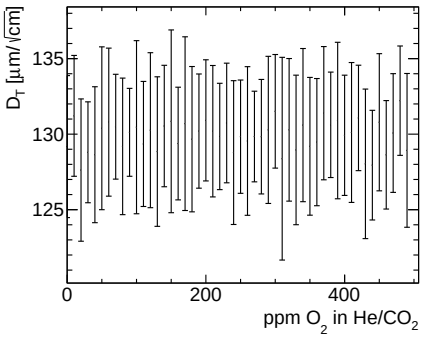

(f) Transversal diffusion constant D_T in dependence on the O_2 content.

Figure 3.16: Simulated transversal diffusion D_T in Helium with 30 % CO_2 admixture. If not varied, the parameters are: temperature 20 °C, pressure 1013.25 mbar, drift field 495 V/cm, no impurities.

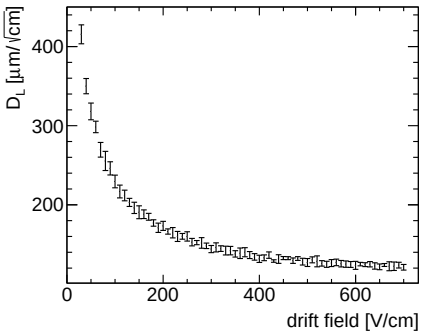

(a) Longitudinal diffusion constant D_L in dependence on the drift field.

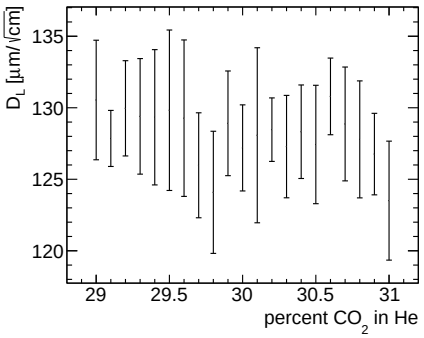

(b) Longitudinal diffusion constant D_L in dependence on the ratio between Helium and CO_2.

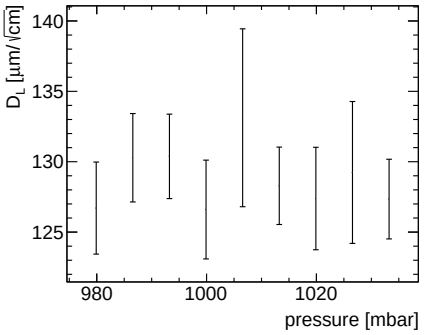

(c) Longitudinal diffusion constant D_L in dependence on the pressure.

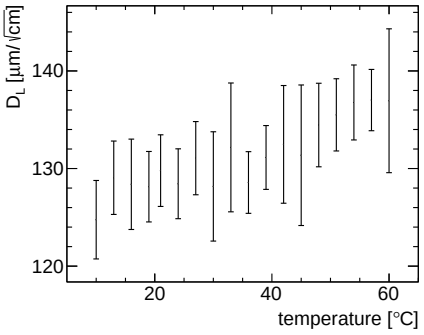

(d) Longitudinal diffusion constant D_L in dependence on the temperature.

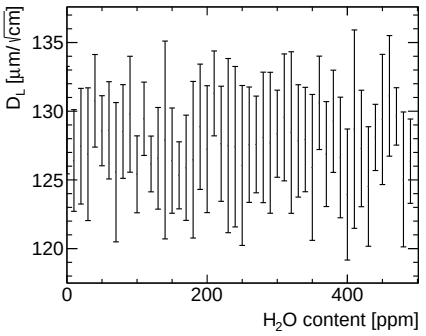

(e) Longitudinal diffusion constant D_L in dependence on the H_2O content.

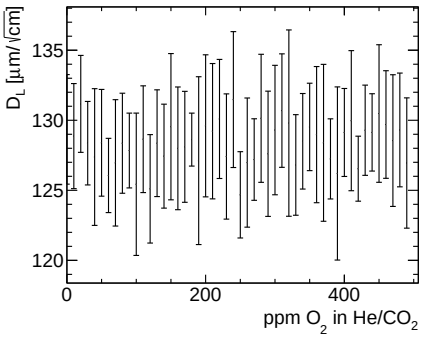

(f) Longitudinal diffusion constant D_L in dependence on the O_2 content.

Figure 3.17: Simulated longitudinal diffusion D_L in Helium with 30 % CO_2 admixture. If not varied, the parameters are: temperature 20 °C, pressure 1013.25 mbar, drift field 495 V/cm, no impurities.

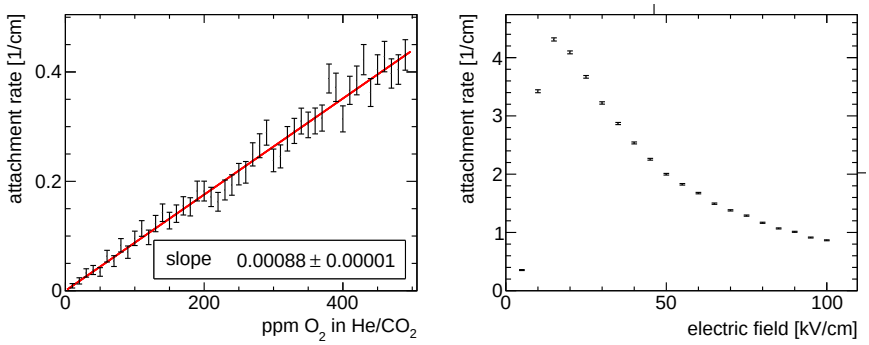

Figure 3.18: Attachment rate in Helium with 30 % CO_2 admixture. Temperature and pressure are 20 °C and 1013.25 mbar, respectively.
a) Attachment rate to molecular O_2 at a drift field of 495 V/cm in dependence on the O_2 concentration.
b) Rate for dissociative attachment at high electric fields.

3.4.2.2 *Attachment Rate in Helium with 30 % CO_2 Admixture*

The probability that a drifting electron becomes attached to molecular oxygen rises exponentially with the drift distance z:

$$p_{\text{Att.}} = 1 - \exp(-zB). \tag{3.9}$$

For small impurities, Magboltz simulations predict the attachment rate B to rise linearly with the oxygen content in the Helium-CO_2 mixture used, see figure 3.18a.

In the relatively low drift field, dissociative attachment to CO_2 as described in section 1.4.1 does not occur. The electric field in the amplification region in contrast reaches up to 100 kV/cm. As shown in figure 3.18b, dissociative attachment becomes, therefore, important.

3.5 SUMMARY

The setup of a GEM-TPC with 26.32 cm drift distance and a bare Timepix pixel chip for charge collection and detector readout has been described in this chapter. The operating conditions during 3 weeks of data taking are summarized in table 3.1 and 3.2.

Besides a brief review of the ASIC design, the properties of the electronics, especially the behavior of the test-pulse injection and the clock distribution networks have been elaborated. This eventually allowed to introduce procedures for charge calibration and compensation for the time walk effect. Data corruption due to the clock distribution delay as claimed in [131, 133] has been disproved. Instead, the effects described in these works are explained by the load induced clock delay.

Finally, simulations on the drift gas properties have been presented. These results are used in the following chapters to cross-check the data analysis.

DRIFT GAS	He with 30 % CO_2 admixture
DRIFT FIELD	495 V/cm
MAGNETIC FIELD	not applied
DRIFT GAS PRESSURE	$\approx$ 1013 mbar (estimated)*
DRIFT GAS TEMPERATURE	$\approx$ 30 °C (estimated)*
DRIFT VELOCITY	0.974 cm/µs
TRANSVERSAL DIFFUSION	$131 \pm 6\,\mu m/\sqrt{cm}$
LONGITUDINAL DIFFUSION	$128 \pm 6\,\mu m/\sqrt{cm}$
GAS AMPLIFICATION	Triple GEM stack
GEM VOLTAGES	415 V per GEM
TRANSFER AND INDUCTION GAP	1 mm
TRANSFER FIELDS	2200 V/cm
INDUCTION FIELD	3000 V/cm
READOUT	bare Timepix ASIC H09-W0019
CLOCK FREQUENCY	55.4 MHz
SHUTTER LENGTH	32.4 µs
THRESHOLD	$\approx$ 700 electrons

* The gas mixing system described in section 2 was not operational when the data were taken.

Table 3.1: Operating conditions of the pixel TPC during 3 weeks of data taking with He/CO_2 as drift gas.

I_{Krum}	Disc	Preamp	I_{Hist}	THL
5	127	255	0	342
THL_{Coarse}	V_{Cas}	FBK	GND	THS
7	130	128	80	76

Table 3.2: Settings of the Timepix DACs during the data taking phase.

4 DATA RECONSTRUCTION AND BASIC ANALYSIS

Roughly 100 000 events with particle tracks have been recorded in several runs during 3 weeks of data taking with the pixel TPC. Reconstruction and analysis of the data is based on the MarlinTPC package [154]. This Modular Analysis and Reconstruction framework for the LINear collider TPC features virtually all routines needed for reconstruction and analysis of TPC data. However, since MarlinTPC primarily aims for TPCs with pad readout, some algorithms dedicated to pixel TPCs had to be especially developed.

The reconstruction chain established for the pixel TPC data is described in the first section of this chapter. In sections 4.2 to 4.5, the data quality is examined. Besides, the criteria fulfilled by properly recorded, self-contained particle tracks are discussed.

4.1 RECONSTRUCTION PROCEDURE

Although some patches and improvements have been applied, the reconstruction algorithms are basically identical to the ones described in [132]. In general parlance, tracks of particles passing the sensitive TPC volume are reconstructed from the recorded pixel data as follows:

1. The counter values of pixels known to be defective or noisy are interpolated from the surrounding pixels operated in the same pixel mode.

2. Charge calibration and time walk compensation as explained in section 3.3 are applied to the data.

3. Neighboring pixels which have detected a charge deposition are combined to an object called raw cluster. These represent the charge deposition caused by one or more primary electrons. It is expected that a charge deposition covers at least 5 pixels. Smaller raw clusters are rejected.

4. Based on the charge distribution characteristics, the raw clusters are separated into objects presumably originating from one primary electron each. These objects are labeled cluster. The projection separation algorithm used is outlined in the following:

   First, the cluster axis is determined by a linear regression over all pixels forming a raw cluster, see figure 4.1a. Then, the charge detected in each pixel of the raw cluster is projected onto the cluster axis. Significant minima in the resulting charge profile

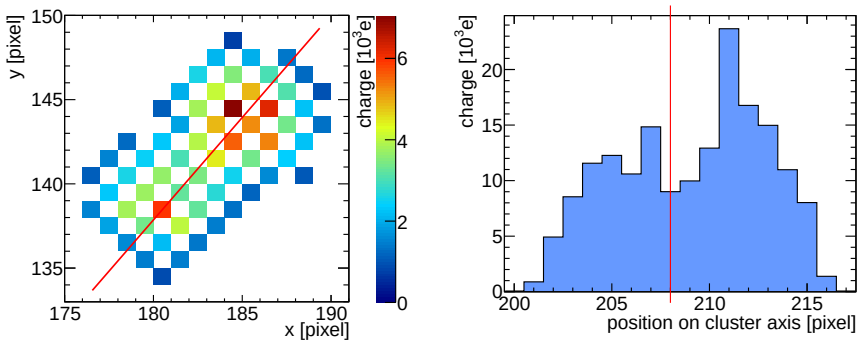

(a) (b)

Figure 4.1: a) A raw cluster may be formed by overlapping charge depositions caused by different primary electrons. The red line depicts the axis of the raw cluster.
b) A raw cluster is split if a significant minimum (red line) is found in the charge profile.

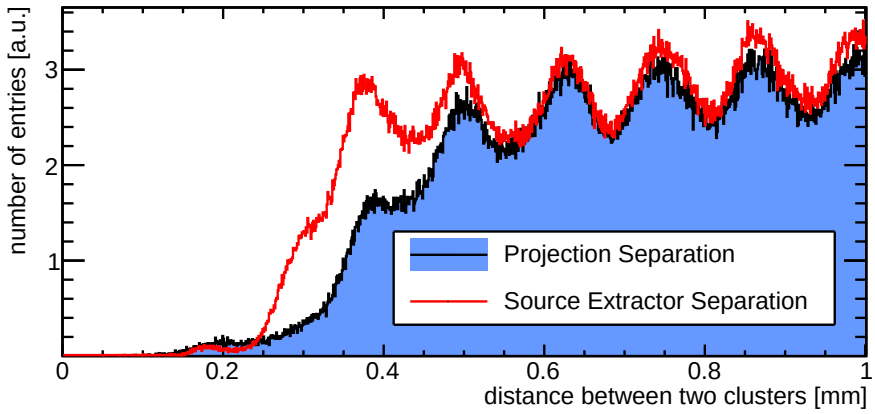

Figure 4.2: The distribution of the distances between the centers of two clusters is a benchmark for the separation algorithm. The periodic structure is caused by the GEM pitch of 140 µm. The histograms are normalized to each other.

are located, c.f. Fig. 4.1b. If a minimum is found and the resulting clusters are formed by at least 5 pixels each, the raw cluster is split along the vertical line crossing the cluster axis at this minimum.

This algorithm compresses all available information on the raw cluster into a 1-dimensional charge profile. Hence, the separation power of the algorithm is limited. Even though it is applied twice, charge depositions less than 350 µm apart are virtually never identified as separate clusters, see figure 4.2. A better raw cluster separation could be achieved, if the full 2-dimensional information would be taken into account. Based on a software named Source Extractor, this approach is followed in [155]. There, it is shown that the minimally required dis-

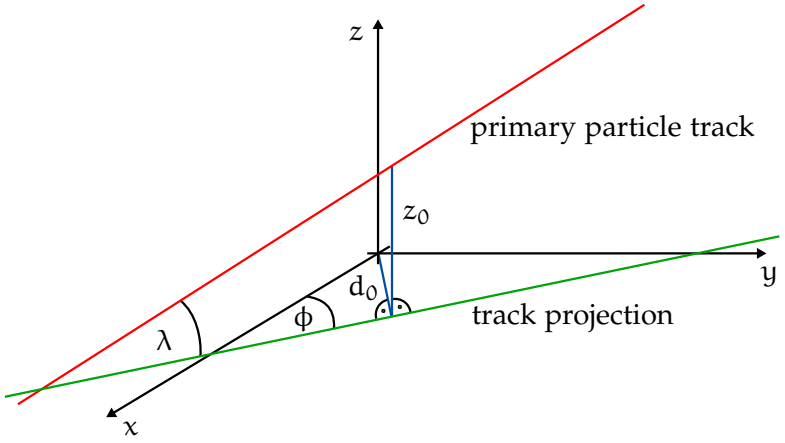

Figure 4.3: Definition of the coordinate system and the track parameters. The track projection is recorded by the Timepix ASIC which is located in the xy-plane. The z-axis points along the drift field. The reconstructed particle track is defined by the distances d_0 and z_0 as well as the angles λ and ϕ.

tance for separation of nearby charge depositions can be reduced down to roughly 280 µm. However, up to now, Source Extractor is not embedded in the MarlinTPC analysis flow. Therefore, it was not applied to the data discussed in the following.

5. The center of gravity of the charge distribution in a cluster is identified with the x- and y-coordinates of the parent primary ionization.

   Equations 1.1 and 3.2 are used to derive the z-coordinate of the parent primary ionization from the mean ToA value in the clusters. Single outliers, which originate from pixels wrongly assigned to a cluster or caused by noise activating the ToA counter before the pixel is hit by a charge deposition, can distort the mean determined ToA value. Therefore, ToA values further than 30 clock cycles apart from the center of the ToA distribution are not taken into account for calculation of the mean ToA.

6. Finally, a 2-dimensional Hough transformation of the readout plane is used to identify primary ionizations originating from the same particle track. The tracks are described by the parameters λ, ϕ, d_0 and z_0 as shown in figure 4.3. They are obtained by a linear regression over all reconstructed track points.

4.2 TIMEPIX OCCUPANCY

Primary ionizations are randomly distributed in the drift volume. Assuming homogeneous electric fields, a smooth pixel occupancy is expected, therefore, when a large number of recorded events is superimposed. The actually observed occupancy of the Timepix ASIC is

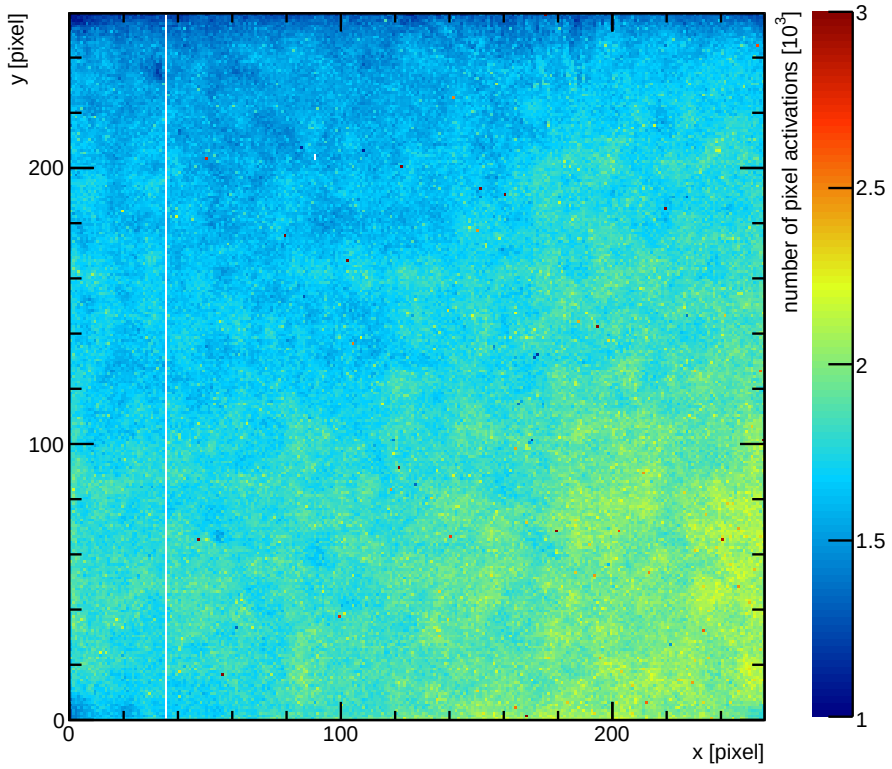

Figure 4.4: Occupancy of the readout chip. Clearly, column 30 of the ASIC is defective. The occupancy of a few pixels (dark red) is significantly higher-than-average.

shown in figure 4.4. It can be seen that the pixels in column 35 are defective. Furthermore, some pixels with a higher noise level or a lower threshold than the others tend to be activated more often than the others. This causes peaks looming out of the occupancy pedestal. The counter values of both, defective and noisy pixels are discarded and replaced by values interpolated from neighboring pixels operated in the same mode.

It is noted that the pedestal is not absolutely flat as expected, but rises slightly towards the lower right edge of the chip. This tendency is most likely caused by the fitting of the pixel chip which is not necessarily exactly in parallel with the GEM stack. In consequence, the induction field varies over the chip surface. Another cause for the observed tendency is given by the geometry of the triggering scintillators which are not exactly aligned with the readout chip.

The gap between readout ASIC and the surrounding readout plane skirting (c.f. Fig. 3.3a) causes an additional inhomogeneity of the induction field. This explains the occupancy characteristics at the chip edges.

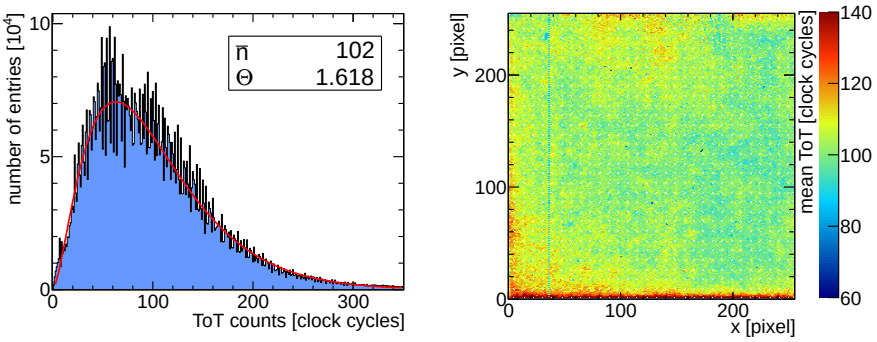

(a) (b)

Figure 4.5: a) ToT spectrum for a run during the data taking phase. The data are approximated by a Polyá function.
b) Mean ToT per pixel measured during the data taking phase.

4.3 TOT DISTRIBUTION

The number of electrons emerging from the GEM stack is Polyá distributed (c.f. Sec. 1.3). Consequently, the ToT spectra obtained in the data runs can be approximated by a Polyá function, see figure 4.5a. While a smooth ToT distribution is expected, it occurs that some ToT values are preferred to others. This electronic effect is not entirely understood by now.

Calculating the mean measured ToT per pixel activation results in the 2-dimensional plot shown in figure 4.5b. As expected from section 4.2, an inhomogeneity is observed. Near the chip periphery and the chip edges in general, significantly more charge is detected per pixel activation. In the center of the pixel matrix, the mean detected charge is rather homogeneous.

4.4 TOA SPECTRUM

Recalling the functionality of the ToA measurement (eq. 3.2), it is noted that the Timepix counters technically can not count more than n_{max} clock cycles during a shutter opening:

$$n_{max} = t_{shutter} \cdot f_{clock}, \tag{4.1}$$

where f_{clock} is the Timepix reference clock frequency and $t_{shutter}$ the length of the shutter signal.

The time needed by a primary electron to cover the maximal drift distance l is fixed by the electron drift velocity v_{Drift}. Thus, also the minimally possible ToA value n_{min} can be calculated:

$$n_{min} = \left(t_{shutter} - \frac{l}{v_{Drift}} \right) \cdot f_{clock}. \tag{4.2}$$

Summing up, two characteristic edges at n_{min} and n_{max} are expected in the ToA spectrum. These edges can be identified with the

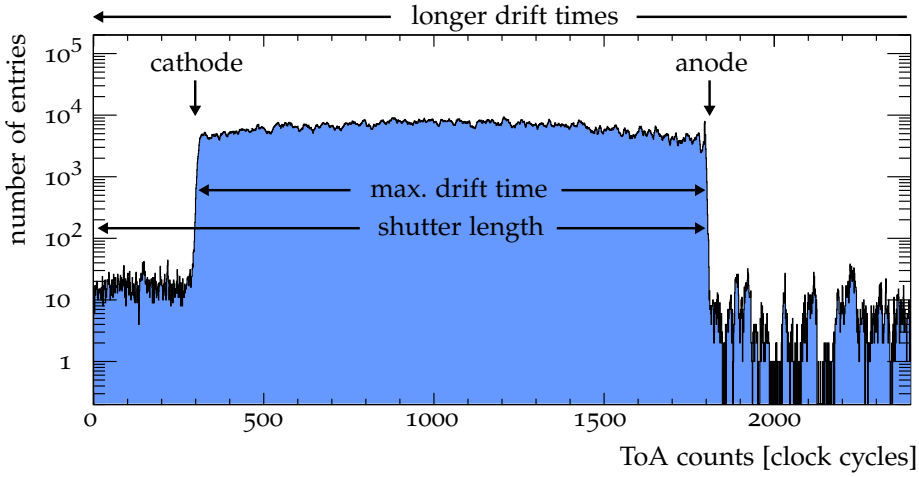

Figure 4.6: ToA spectrum for a run during the data taking phase.Time walk compensated ToA values are shown.

positions of cathode and anode in the ToA space. The edge at n_{max} can be described by:

$$D_{max}(x) \propto \int_{x}^{\infty} \exp\left(-\frac{(n-n_{max})^2}{2\sigma_{phase}^2}\right) dn. \tag{4.3}$$

The width σ_{phase} of the underlying Gaussian distributions is predetermined by the variation of the phase shift between the shutter signal and the clock.

The steepness σ_{min} of the edge at n_{min} is additionally limited by the longitudinal diffusion and the time walk remaining after compensation. The step is approximated by:

$$D_{min}(x) \propto \int_{-\infty}^{x} \exp\left(-\frac{(n-n_{min})^2}{2\sigma_{min}^2}\right) dn. \tag{4.4}$$

The widths σ_{phase} and σ_{min} are found to be about 2 clock cycles ($\hat{=}350\,\mu m$) and 5.5 clock cycles ($\hat{=}960\,\mu m$), respectively. Due to the remaining uncertainties caused by the secondary effects mentioned above, a deviation from the expected value:

$$\sigma_{diff,\, z=26\,cm} = D_L\sqrt{z} \approx 670\,\mu m \tag{4.5}$$

is observed if it is tried to extract the longitudinal diffusion from these widths via:

$$\sqrt{\sigma_{min}^2 - \sigma_{phase}^2} = 894\,\mu m. \tag{4.6}$$

Other than expected, ToA values smaller than n_{min} and larger than n_{max} are observed in the representative ToA spectrum depicted in figure 4.6. These are discussed in sections 4.4.1 and 4.4.2.

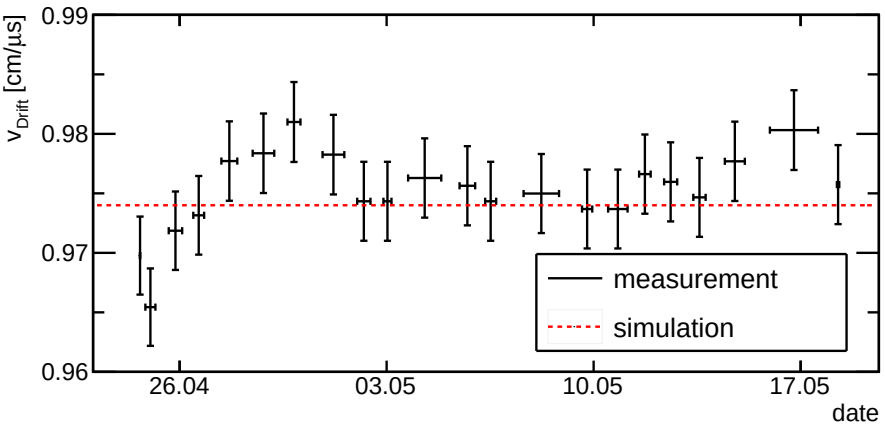

Figure 4.7: Drift velocities reconstructed from ToA spectra of all investigated runs. The values vary only by ±0.8 % during the whole data taking phase. They are in agreement with the prediction from Magboltz simulations for the used Helium CO_2 mixture at $E_{Drift} = 495\,V/cm$, 1013 mbar and 30 °C.

If the clock frequency is known, the length of the shutter signal $t_{shutter}$ can be calculated from n_{max} by means of eq. 4.1. Using also the mechanically fixed maximal drift length l allows to extract the drift velocity v_{Drift} from the difference between n_{max} and n_{min}.

The reconstructed drift velocities for subsequent periods during the data taking phase are plotted in figure 4.7. The determined drift velocities are in good agreement with the drift velocity predicted by a Magboltz Monte Carlo simulation for the used Helium CO_2 mixture at $E_{Drift} = 495\,V/cm$, 1013 mbar and 30 °C.

Although the drift velocity varies only by ±0.8 %, one might argue that the operating conditions have not been stable during the first few days of data taking, since here a positive trend can be seen in the reconstructed drift velocities. Consequently, runs earlier than April 27th are discarded in later analyses.

4.4.1 *High ToA Counts*

Infrequently, counter values exceeding the limit given by eq. 4.1 are observed in the ToA spectrum shown in figure 4.6.

The inspection of these events reveals that only those are affected which show charge depositions of two superimposed primary particle tracks. An illustrative example is displayed in figure 4.8. The z-coordinates of the first track correspond to ToA values of roughly 1540 clock cycles, the z-coordinates of the other track to 920 clock cycles. Pixels hit by charge depositions of both tracks count 2460 clock cycles, i.e. the sum of the former two.

The high counter values are explained by a malfunction of the trigger logic, which should take care that the chip is read out and re-

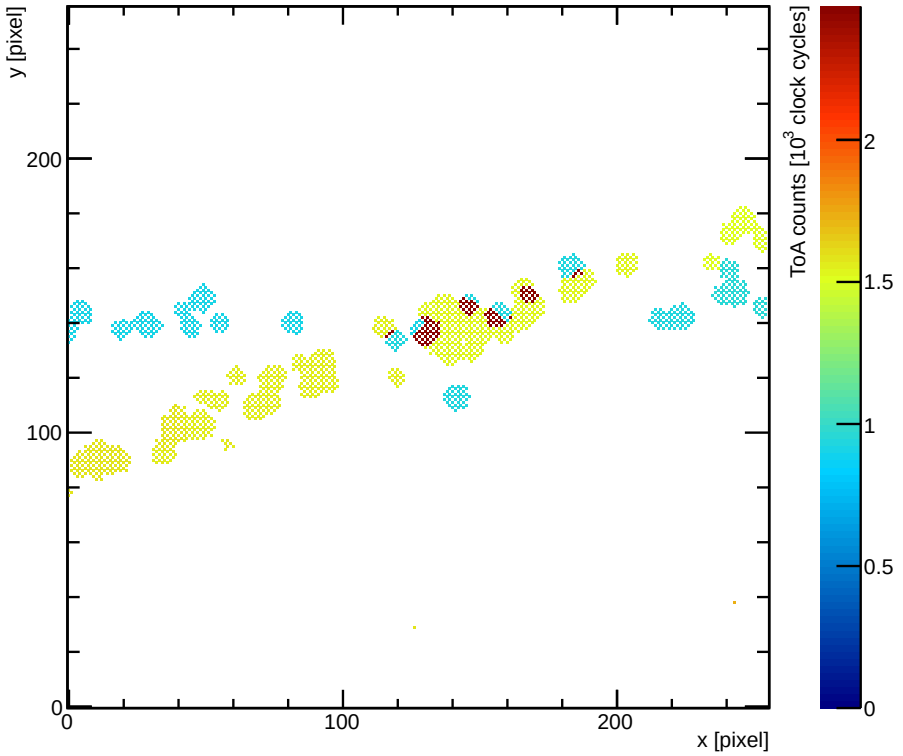

Figure 4.8: Example for an event with high ToA counts, caused by subsequent shutter openings without pixel reset in between.

set once the shutter becomes inactive. It occurs that in some rare cases neither readout nor reset are performed between two subsequent shutter signals. In consequence, one recorded event may consist of two physical events. Pixels activated in both show the summed counter values.

Although this effect was discovered due to ToA values being larger than n_{max}, it is clear that it may occur also in events which are not obviously corrupted. Though, it is estimated that less than 200 ppm of the recorded tracks are affected.

4.4.2 *Low ToA Counts*

ToA counts lower than the expected minimal value n_{min} appear in the ToA spectrum shown in figure 4.6. These are caused by two different effects explained in the following.

By chance, primary electrons can be created in the TPC while the shutter is active. For these electrons, the shutter signal appears shorter than the actual shutter signal. If, for instance, primary electrons are created directly above the readout plane right before the shutter is deactivated, the hit pixels will count only a few clock cycles while, actually, the maximal amount of ToA counts would have been mea-

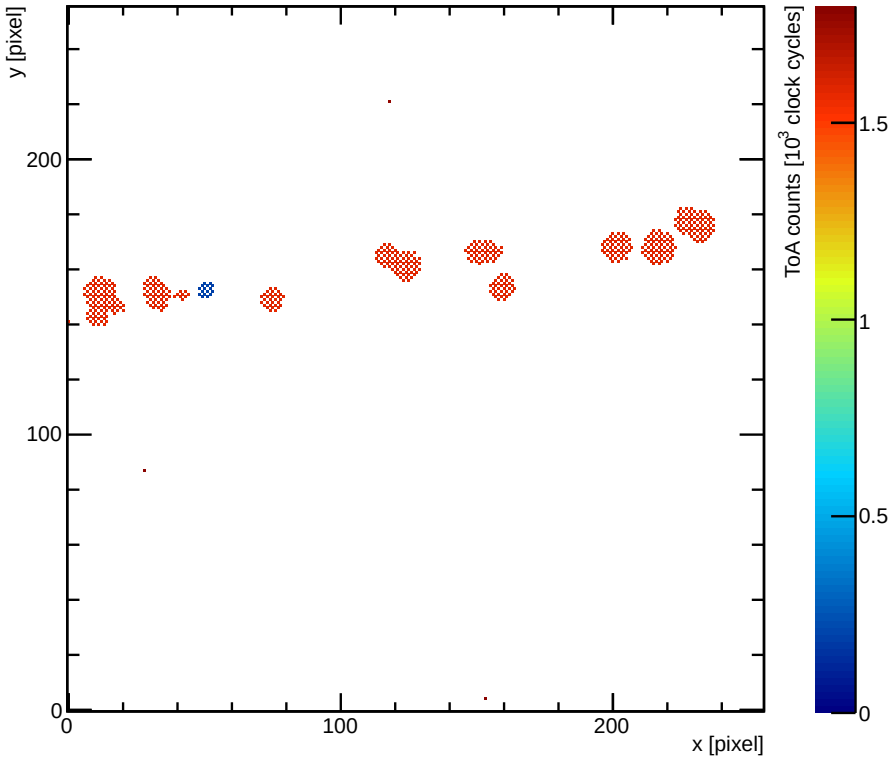

Figure 4.9: Exemplary event display showing a cluster which appears delayed with respect to the rest of the clusters created by the same particle passing the drift volume.

sured, if the shutter signal would have been triggered by the particle passage. Thus, in some extreme cases, the obtained ToA values are smaller than n_{min}.

Eventually, primary ionizations which are created in the drift volume during the active phase of the shutter, result in falsely reconstructed z-coordinates. Particle tracks reconstructed from such events are hardly identified. However, with respect to the reconstructed z-coordinates, the diffusion is obtrusively small.

From time to time, it is observed that a single charge deposition on a track shows significantly lower ToA counts than the others. Primary electrons causing such clusters seem to be delayed with respect to the others created by the same particle passing the TPC. A representative event with a single delayed cluster is shown in figure 4.9. Mechanisms giving rise to these delayed primary electrons are discussed in chapter 6.

If a delayed electron is associated with a track, the track will not be reconstructed with the correct parameters. Such tracks should be excluded from the data analysis, since especially the longitudinal resolution determined from this track is not correct. For identification

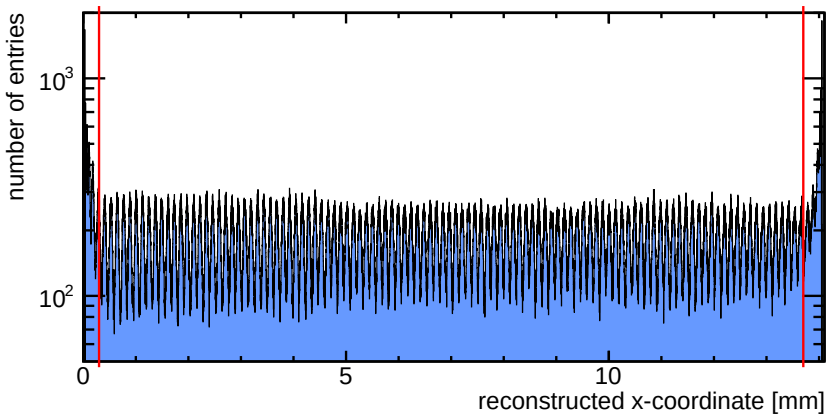

Figure 4.10: X-coordinates of the reconstructed primary ionizations. The vertical lines mark the minimally and maximally accepted x-coordinate.

of tracks with an associated delayed electron, all electrons forming a track are examined as follows:

> An electron under investigation is removed from the complete set of electrons forming the track. Based on the new set of primary electrons, the track is re-reconstructed. Now, the longitudinal distance r_L between the new track and the electron under investigation is determined. For a delayed electron, r_L is significantly larger than for an electron which is not delayed. When r_L is larger than 6σ of the individually expected diffusion, it is considered to be delayed. As long as the track and all associated electrons have been reconstructed correctly in the first place, this rather loose criterion ensures that only a few electrons are misidentified as delayed ones.

4.5 DATA SELECTION

In this section, the geometric parameters of the reconstructed data are reviewed. Based on the findings, some data are excluded from the analyses in the next chapter.

4.5.1 *Reconstructed Coordinates of the Primary Ionizations*

It might happen that a charge deposition is not entirely detected on the chip but extends beyond the chip boundaries. In this case, the center of a detected cluster is not identical with the xy-coordinates of the primary ionization. Therefore, it has to be ensured that only self-contained clusters are taken into account for data analysis.

Charge depositions with the center of gravity being closer to the chip edge than the most probable cluster radius are disregarded in the further analysis. This ensures that only correctly reconstructed

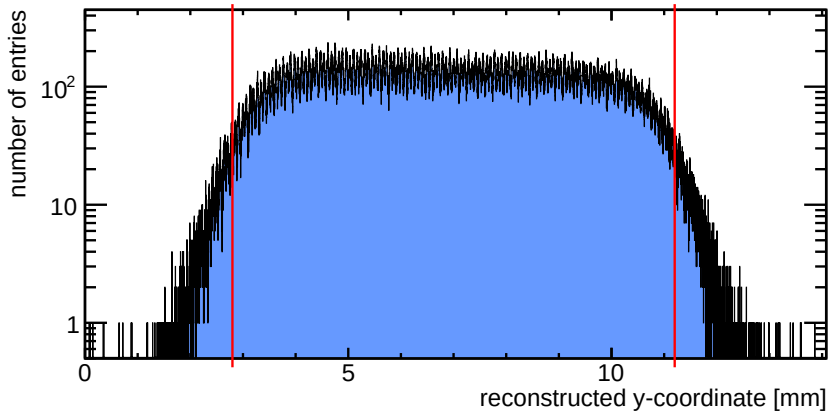

Figure 4.11: Y-coordinates of the reconstructed and accepted primary ionizations. If a reconstructed track crosses the border to the chip perimeter (vertical lines), it is discarded in further analyses. Before this criterion is applied to the data, the distribution looks similar to the distribution of x-coordinates (Fig. 4.10.)

primary electrons are taken into account for reconstruction of the primary particle tracks. A histogram of the reconstructed x-coordinates of all detected charge depositions is shown in figure 4.10. The periodical structure is caused by the pattern of the top GEM.

If the xy-projection of a particle track is close to one of the chip edges, it is possible that some primary electrons associated with that track are not detected on the chip due to transversal diffusion. In consequence, not only the wrong number of charge depositions is associated with this track, but the whole track is reconstructed with wrong parameters.

The recorded tracks run essentially in parallel with the x-axis of the readout chip. Discarding tracks closer than 4σ of the maximally expected transversal diffusion to the top or bottom edge of the readout chip ensures therefore that virtually all primary electrons of a track are detected and the track is properly reconstructed. The y-coordinates of the reconstructed and accepted primary ionizations are shown in the histogram depicted in figure 4.11. Again, the periodical structure originating from the pattern of the top GEM is observed.

The minimally expected z-coordinate of a primary electron is 0 mm, the maximally expected 263.2 mm (plus the expected diffusion). Occurring mismeasurements are discussed in sections 4.4.1 and 4.4.2. If a primary electron outside this interval is found on a reconstructed track, this track is disregarded in further analyses. See figure 4.12 for a histogram of the reconstructed z-coordinates of all reconstructed primary electrons. Due to the trigger geometry, less primary electrons are observed near anode or cathode than in the center of the TPC.

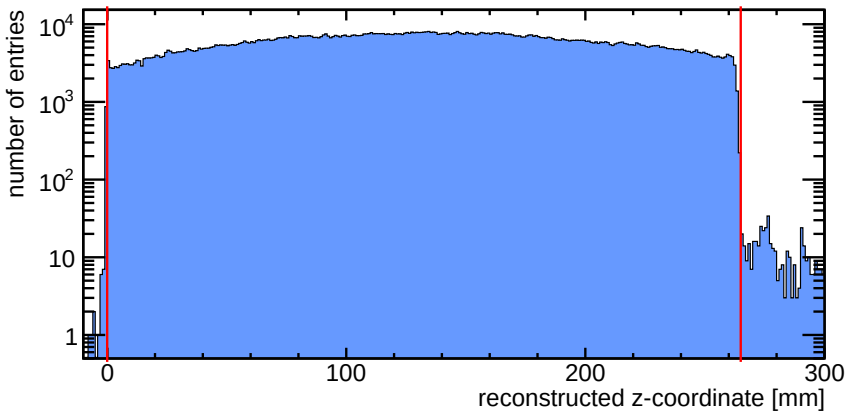

Figure 4.12: Z-coordinates of the reconstructed primary ionizations. The vertical lines mark the minimally and maximally accepted z-coordinate.

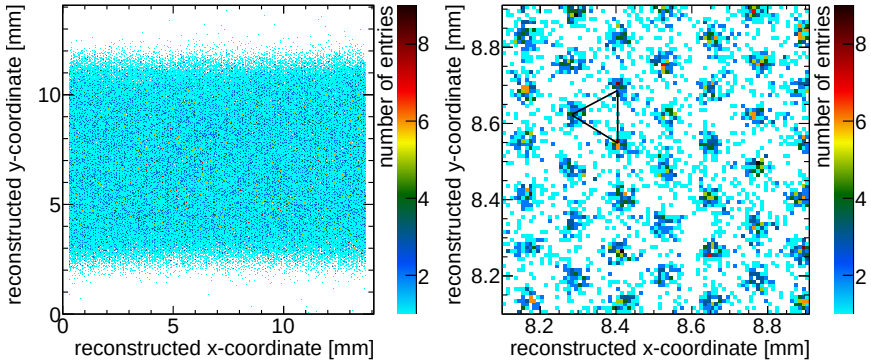

(a) (b)

Figure 4.13: a) 2-dimensional histogram showing the reconstructed x- and y-coordinates of the primary electrons taken into account for further analyses.
b) Zoomed display of (a). The side length of the equilateral triangle is exactly the GEM pitch of 140 µm.

The 2-dimensional histograms, depicted in figure 4.13, show the reconstructed x- and y-coordinates of all primary electrons accepted for further analysis. Close inspection of the data shows that the reconstructed coordinates are arranged in the hexagonal pattern of the top GEM.

From this observation, it is concluded that the spatial resolution of the readout chip exceeds the GEM resolution. In consequence, the readout pads might be enlarged without degrading the intrinsic detector resolution. This has been tested in [150, 156]. Alternatively, the granularity of the gas amplification stage can be increased in order to enhance the intrinsic spatial resolution as done in [157].

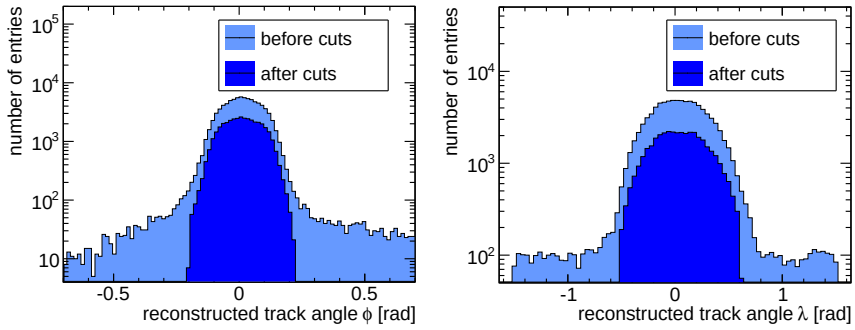

(a) (b)

Figure 4.14: Distribution of the reconstructed track angles ϕ and λ before (light blue) and after data selection (dark blue).

4.5.2 *Reconstructed Tracks*

As stated in section 3.1, it is aimed to record tracks of cosmic muons, triggered by coincident signals in the scintillators above and below the TPC. Therefore, the tracks are expected to be essentially vertically oriented, though with a small inclination due to the arrangement of the triggering scintillators. Tracks with angles other than $-0.2\,\text{rad} < \phi < 0.218\,\text{rad}$ and $-0.58\,\text{rad} < \lambda < 0.64\,\text{rad}$ either originate not from a cosmic muon passing both scintillators or are not correctly reconstructed. In both cases, such tracks can be discarded. Histograms showing the angles of all reconstructed tracks before and after application of the full data selection are depicted in figure 4.13.

In general, one track per recorded event is expected. If an event contains more than one event, it is most likely that at least one is reconstructed with the wrong z-coordinates, c.f. section 4.4.2. Furthermore, it might happen that the 2-dimensional Hough transformation on the small chip surface can not correctly assign all primary electrons to the tracks. This shortcoming could be improved by application of a 3-dimensional Hough transformation or by executing the Hough transformation not in the xy- but in the significantly larger yz-plane. However, as long as no improved track identification algorithm is available, events with more than one track are excluded from the later analyses.

4.6 SUMMARY

In this chapter, the algorithms used for data reconstruction have been introduced. Furthermore, a very basic analysis of the data recorded with the pixel TPC has been presented.

On basis the of a representative example, the observed ToT and ToA spectra have been discussed. The drift velocities reconstructed from the reviewed ToA spectra are stable over time and in good agreement

with the expectation from Magboltz Monte Carlo simulations. These results are taken as indication for stable operating conditions.

The characteristics of the observed ToA spectra have revealed a negligible malfunction of the trigger electronics as well as the existence of so-called delayed electrons, which are discussed in more detail in chapter 6.

Investigation of the x-, y- and z-distributions of the reconstructed positions of the primary electrons, together with the track parameter distributions, has allowed to define criteria which the reconstructed data must fulfill in order to be valuable for the detailed track analyses presented in chapter 5. A comprehensive list is given in table 4.1.

Besides, the periodical pattern of the top GEM has been observed in the spatial distributions, proving the outstanding resolving power of the pixel readout.

CRITERION	TRACKS
NONE	93 037
TRACK BETWEEN $y = 2.8\,\text{mm}$ AND $y = 11.2\,\text{mm}$	43 581
ALL PRIMARY ELECTRONS WITHIN $0\,\text{mm} < z < 265.8\,\text{mm}$	43 431
TRACK ANGLE WITHIN $-0.2 < \phi < 0.218$	42 747
TRACK ANGLE WITHIN $-0.58 < \lambda < 0.64$	41 386
ONE TRACK PER EVENT	41 134
NO DELAYED HIT ON TRACK	40 371

Table 4.1: Criteria fulfilled by the tracks analyzed in chapter 5 (accumulative cut flow). For track reconstruction, primary electrons outside $0.3\,\text{mm} < x < 13.7\,\text{mm}$ are discarded.

5 DETECTOR PERFORMANCE

As discussed in section 4.5, the analyzed data set is restricted to self-contained, properly reconstructed tracks. This allows for benchmarking the pixel TPC on the basis of the recorded data. Preliminary results on the detector performance have already been presented in [126–128]. After largely improving the algorithms for data selection and reconstruction, updated results have been published in [129, 130]. These most recent findings are discussed in the following.

In the first section of this chapter, the properties of the recorded clusters are investigated. The effective gain of the GEM stack and the number of pixels activated by single primary electrons are extracted from the data. Besides, the specific energy loss in the drift volume and the single-point resolution of the pixel TPC are examined.

5.1 CLUSTER CHARACTERISTICS

As long as overlapping charge depositions of neighboring primary electrons can not be separated, they appear as a large cluster, carrying more charge than clusters caused by single electrons. With increasing drift distance, the primary electrons diffuse apart and it becomes more likely that charge depositions of individual electrons are identified as separate clusters. This so-called declustering effect is illustrated in figure 5.1.

5.1.1 *Charge per Cluster*

Due to the expected dependency on the drift distance, the charge per cluster is analyzed for drift distance intervals of 1 cm width. Illustra-

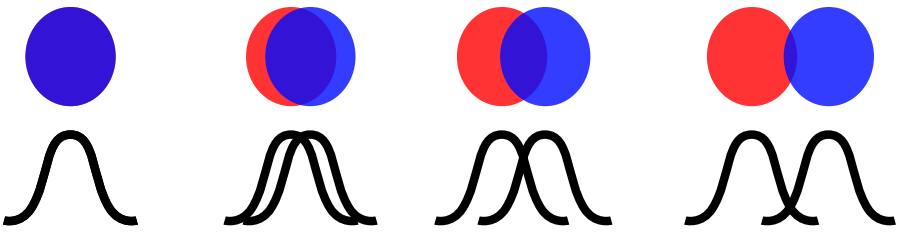

Figure 5.1: Profile of the charge cloud caused by two neighboring primary electrons. With increasing drift length, the mean distance between primary electrons rises due to diffusion.

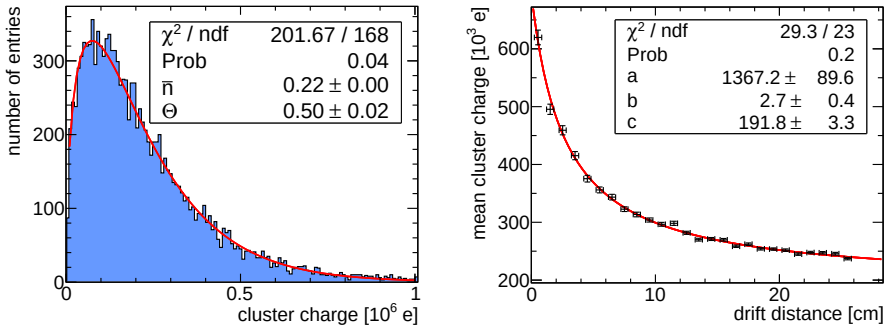

(a) (b)

Figure 5.2: a) The charge of clusters associated with a track and with z between 25 cm and 26 cm can be approximated by a Polyá distribution.
b) Mean charge per cluster associated with a track in dependence on the drift distance. The functional relation is approximated by equation 5.1.

tively, the cluster charge distribution obtained for z between 25 cm and 26 cm is shown in figure 5.2a.

Since the gain of the GEM stack is described by a Polyá distribution, it is convenient to describe the charge per cluster in each investigated interval by a Polyá function. However, for small drift distances, where a cluster may or may not originate from more than one primary electron, the validity of this approximation is limited. Therefore, instead of the mean of the fitted Polyá distributions, the mean values of the original distributions are shown in figure 5.2b.

The mean charge per cluster Q drops with increasing drift distance of the parent primary electron. Empirically, it has been found that this drop can be described by:

$$Q(z) = \frac{a}{b+z} + c, \tag{5.1}$$

with the free parameters a, b and c. A χ^2-optimization yields the asymptotically approached limit c, which is roughly 190 000 e. This value can be identified with the effective gain of the GEM stack since it corresponds to the mean amount of charge in electron avalanches which are caused by single primary electrons. Actually, the effective gas gain is slightly larger, since some electrons emerging from the GEM stack are distributed on pixels which do not pass the threshold level.

5.1.2 *Cluster Size*

If two primary electrons traverse the GEM stack at the same position, the charge in the resulting cluster is approximately twice the charge of a single primary electron. The cluster size, given by the number of

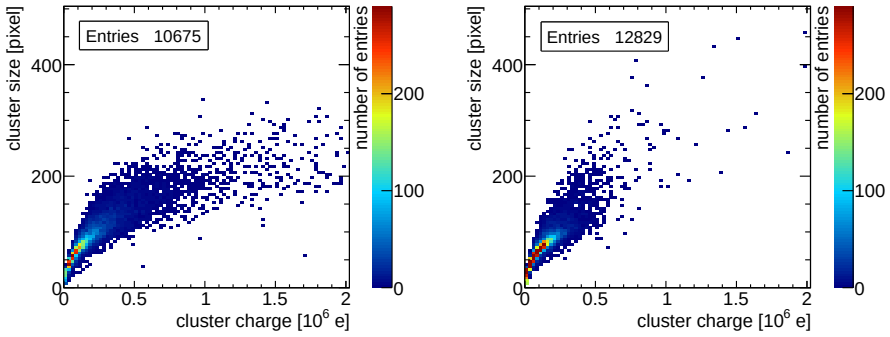

(a) $0\,\text{cm} < z < 1\,\text{cm}$ (b) $25\,\text{cm} < z < 26\,\text{cm}$

Figure 5.3: Correlation between the detected cluster charge and the number of pixels forming a cluster (cluster size) for different drift distance intervals.

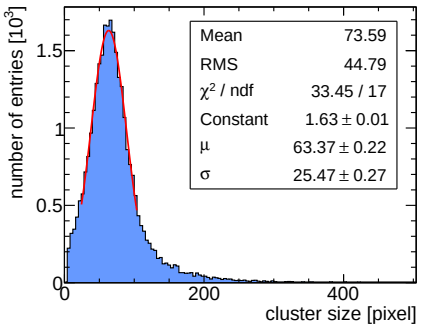

Figure 5.4: Size of clusters associated with a particle track. The z-position of the parent primary electron is between 10 cm and 11 cm. The peak follows approximately a Gaussian distribution. The tail is caused by unseparated multi-electron clusters.

pixels forming a cluster, is not increased to the same degree, since the spread of the charge cloud is primarily determined by the transversal diffusion in the transfer and induction gaps of the GEM stack. Cluster charge and size are only correlated due to secondary effects like coulomb repulsion and the probability that the threshold limit of pixels in the outer region of the charge cloud is exceeded.

The cluster size rises, therefore, not continuously with the cluster charge but saturates, see figure 5.3a. At large drift distances, virtually all clusters represent individual primary electrons due to the declustering effect. Therefore, only the non-linear relation between cluster size and charge, but neither extreme cluster charges nor the cluster size saturation are observed in figure 5.3b.

As the cluster charge, the cluster size is examined for drift distance intervals of 1 cm width. For illustration, the distribution of the cluster sizes caused by primary electrons with a drift length between 10 cm and 11 cm is depicted in figure 5.4. The cluster size distributions show a dominant Gaussian peak. The tail to large clusters originates from extraordinarily large charge clouds, e.g. from mis- or unseparated multi-electron clusters.

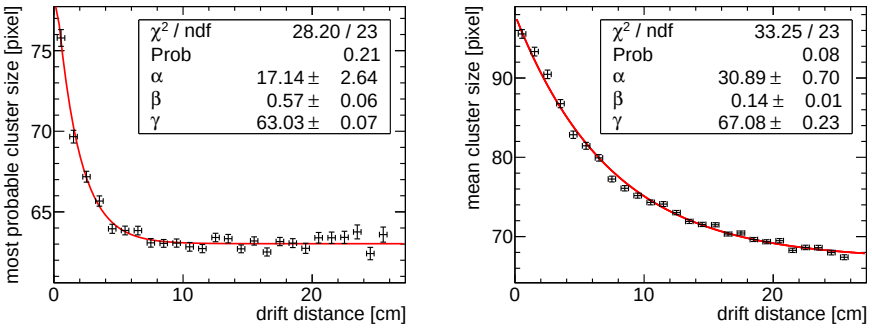

(a) (b)

Figure 5.5: Most probable (a) and mean cluster size (b) in dependence on the drift distance of the parent primary electrons. The data are approximated by function 5.2.

The relation between the most probable cluster size and the drift distance of the parent primary electrons is shown in figure 5.5a. The most probable cluster size stabilizes already at rather short drift distances. This indicates that the majority of the detected clusters originates from single primary electrons. Since it is strongly influenced by occasionally occurring extraordinary large clusters, the mean cluster size, in contrast, does not settle within the available 26 cm drift length, see figure 5.5b.

Given that the cluster size is not linearly dependent on the cluster charge, it can not be expected that the dependency on the drift length can be described by the same surrogate function. Instead, it has been found empirically that the most probable and the mean cluster size follow an exponential function:

$$f(z) = \alpha \exp(-\beta z) + \gamma, \tag{5.2}$$

with the free parameters α, β and γ. The limit approached by the most probable cluster size is identified with the size of clusters originating from single primary electrons. Naturally, the limit found for the mean cluster size is slightly larger, since it is systematically shifted to larger values by the presence of large clusters.

5.2 IONIZATION DENSITY

Due to the declustering effect, it is expected that the number of detected clusters increases with the drift distance of the parent primary electrons and approaches asymptotically the limit given by the total number of primarily created electron-ion pairs.

Inspection of the observed ionization density, depicted in figure 5.6, shows that it is not only subject to the declustering effect but also affected by attachment of the primary electrons to molecular oxygen. The latter causes the number of detected clusters to drop with rising

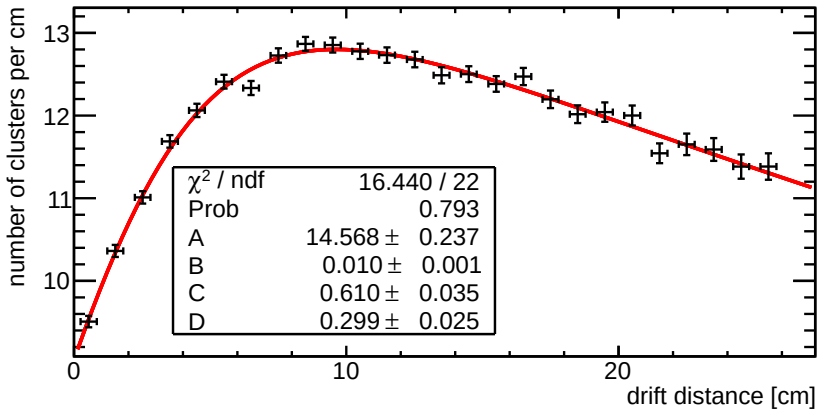

Figure 5.6: The number of detected clusters per unit track length is a measure for the ionization density. The dependency on the drift distance is reproduced by eq. 5.5.

drift distance. A surrogate function describing the data while taking both effects into account is motivated in the following.

If A is the total number of primary electrons and B the attachment rate, then

$$n_e(z) = A \exp(-Bz) \tag{5.3}$$

primary electrons arrive at the readout plane after they have covered the distance z, c.f. sections 1.4.1 and 3.4.2.2.

Following equation 5.2, the number of primary electrons per detected cluster can be expressed by:

$$n_{e/cluster}(z) = 1 + C \exp(-Dz), \tag{5.4}$$

where $(1 + C)$ is the mean number of primary electrons per detected cluster at $z = 0$. The transversal diffusion and the power of the cluster separation algorithm determine the separation rate D.

Dividing $n_e(z)$ by $n_{e/cluster}(z)$ yields:

$$n_{cluster}(z) = \frac{A \exp(-Bz)}{1 + C \exp(-Dz)}, \tag{5.5}$$

describing the observed ionization density in dependence on the drift distance of the parent primary electrons. A χ^2-optimization of the free parameters allows to extract the attachment rate $B = 0.01\,cm^{-1}$ from the data. According to the Magboltz simulations presented in section 3.4.2.2, this attachment rate equates to an oxygen contamination of about 10 ppm, which is a realistic value. No direct measurement of the oxygen contamination is available for comparison (c.f. Sec. 2.5.2).

Furthermore, the χ^2-optimization yields $A = 14.6\,cm^{-1}$, which is the number of primary electrons that would be detected without attachment. This value is significantly lower than expected from the

HEED simulations presented in section 3.4.1. According to the simulations presented in chapter 7, only about 3 % of the incident primary electrons do not initiate an electron avalanche in the top GEM. Hence, the deficit in detected primary electrons is only partially explained by the single electron efficiency of the gas amplification stage. More relevant is the fact that the HEED simulation produces the total number of created primary electrons, including those created by high energetic δ-electrons which might form a secondary track. The cuts that are applied to the analyzed data exclude events with more than one reconstructed particle track. As a result, the number of observed primary electrons is systematically lowered.

Concluding, it has to be admitted that the construction of the surrogate function is partially arbitrary, since there is no strong motivation to derive the number of primary electrons per detected cluster from eq. 5.2 and not from eq. 5.1. The validity of eq. 5.5 is discussed furthermore in section 7.3.3.

5.3 SINGLE-POINT RESOLUTION

The single-point resolution σ is defined as the mean distance of a reconstructed track point to the original particle track. Usually, a hodoscope is employed to provide the parameters of the reference track for determination of the spatial resolution of a detector under test. Since no hodoscope data is available for the investigated data set, the spatial resolution of the pixel TPC is estimated from the recorded data itself as described below.

The standard deviation of the distances between a fitted track and the associated track points defines σ_N. This value is systematically smaller than the actual single-point resolution, since the fitted track is biased by the investigated track points. An unbiased value is $\sigma_{N\text{-}1}$, which denotes the standard deviation of the distances between a track point and the corresponding track fitted to all track points except the one under investigation. However, exclusion of recorded data points degrades the accuracy with which the reference track is determined. Hence, $\sigma_{N\text{-}1}$ is larger than the actual single-point resolution of the detector. Following [132, 158], the geometric mean of σ_N and $\sigma_{N\text{-}1}$:

$$\sigma_{geo} = \sqrt{\sigma_N \sigma_{N-1}}, \tag{5.6}$$

is a valid estimation of the actual spatial resolution of the detector under test.

In case of the pixel TPC, the achieved single-point resolution is not only determined by the intrinsic detector resolution, but also affected by the electron diffusion during drift. As discussed in section 1.2.2, the latter is dependent on the drift distance, since the probability to

locate an electron that has drifted the distance z in the TPC is Gaussian distributed around the expected value with the width

$$\sigma_{xy,\text{Diff.}}(z) = \sqrt{D_T^2 z} \tag{5.7}$$

in transversal and

$$\sigma_{z,\text{Diff.}}(z) = \sqrt{D_L^2 z} \tag{5.8}$$

in longitudinal direction, where D_T is the transversal and D_L the longitudinal diffusion constant.

5.3.1 *Transversal Spatial Resolution in Dependence on the Drift Distance*

As shown in section 4.5.1, the hole pattern of the GEMs is visible in the distribution of the reconstructed cluster centers. From this, it can be deduced that the intrinsic transversal single-point resolution $\sigma_{xy,0}$ of the pixel TPC is limited by the spatial resolution of the GEMs:

$$\sigma_{\text{GEM}} = \frac{140\,\mu\text{m}}{\sqrt{12}} \approx 40\,\mu\text{m}. \tag{5.9}$$

For drift distances larger than a few centimeters, basically all detected clusters originate from single primary electrons. Thus, in this regime, the contribution of the diffusion to the transversal spatial resolution of the pixel TPC is given by equation 5.7. As already seen from the z-dependency of the cluster size, the cluster charge and the ionization density some of the clusters detected at small drift distances originate from more than one primary electron. For such clusters, the reconstructed xy-position is closer to the original particle track, since it is the mean of at least two values, which are individually Gaussian distributed around the same expectation value. Consequently, the effect of the transversal diffusion on the spatial resolution is suppressed at small drift distances. This is modeled by introducing the number of electrons per detected cluster (eq. 5.4) to equation 5.7:

$$\sigma_{xy,\text{Diff.}}(z) = \sqrt{\frac{D_T^2}{1 + a\exp(-bz)} \cdot z}. \tag{5.10}$$

As seen in figure 5.7, the transversal single-point resolution extracted from the data recorded with the pixel TPC is described by:

$$\sigma_{\text{geo},xy}(z) = \sqrt{\sigma_{xy,0}^2 + \frac{D_T^2}{1 + a\exp(-bz)} \cdot z}. \tag{5.11}$$

However, the data are not exactly resembled by equation 5.2 as seen from the reduced χ^2. In consequence, the obtained intrinsic resolution $\sigma_{xy,0}$ is larger than expected. Close inspection of σ_{geo} for small

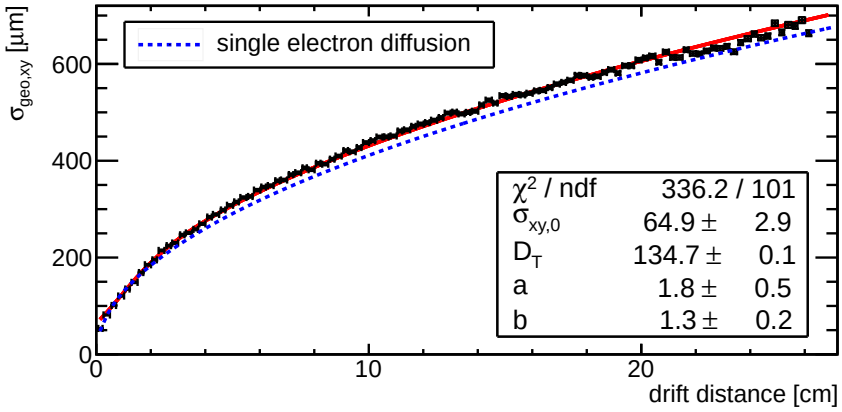

Figure 5.7: The transversal single-point resolution extracted from the data is close to the theoretical limit (blue, dotted) given by the single electron diffusion (eq. 5.7). The data are approximated by equation 5.2 (red, solid).

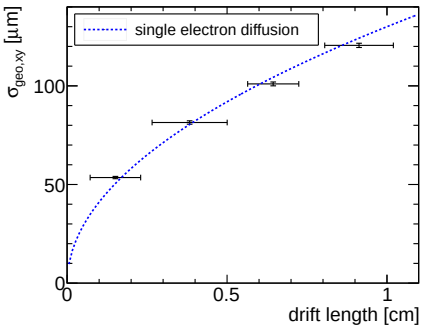

Figure 5.8: Zoomed display of the transversal single-point resolution (c.f. Fig. 5.7). Extrapolating the data down to zero drift distance yields an intrinsic detector resolution of about 40 µm.

drift distances reveals that the fit overestimates $\sigma_{xy,0}$. As shown in figure 5.8, the actually observed resolution for $z = 1.5\,\text{mm}$ is about 50 µm. Extrapolating the depicted data points down to $z = 0\,\text{mm}$ shows that the intrinsic detector resolution is, as expected, about 40 µm.

5.3.2 *Longitudinal Spatial Resolution in Dependence on the Drift Distance*

As the single-point resolution in transversal direction, the longitudinal single-point resolution of the pixel TPC is given by the intrinsic resolution and a contribution from the diffusion of the electrons during drift:

$$\sigma_{geo,z}(z) = \sqrt{\sigma_{z,0}^2 + \sigma_{z,\text{Diff.}}^2}. \tag{5.12}$$

Obviously, the intrinsic detector resolution in longitudinal direction is limited by the precision of the ToA measurement. Following eq. 3.2 and neglecting secondary effects, the latter is given by:

$$\Delta(\text{ToA}) = \sqrt{\Delta t_{\text{shutter}}^2 + \Delta\left(\frac{n}{f_{\text{clock}}}\right)^2} = \sqrt{\frac{2T_{\text{clock}}^2}{12}}, \tag{5.13}$$

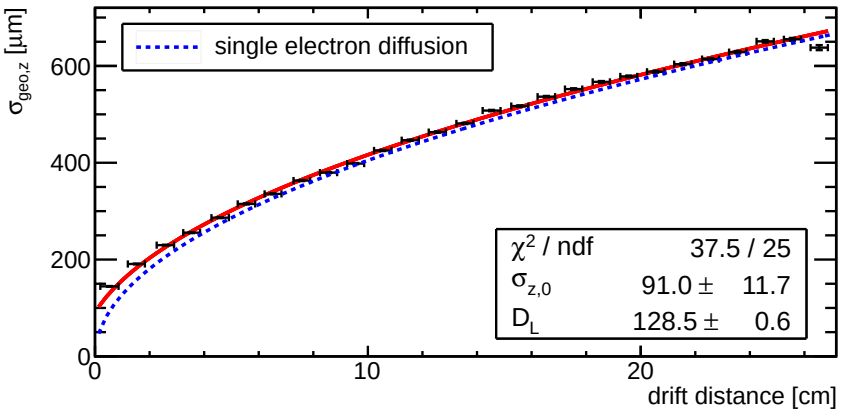

Figure 5.9: The longitudinal single-point resolution extracted from the data is close to the theoretical limit given by the single electron diffusion, dotted in blue. The data are approximated by eq. 5.12 (red, solid).

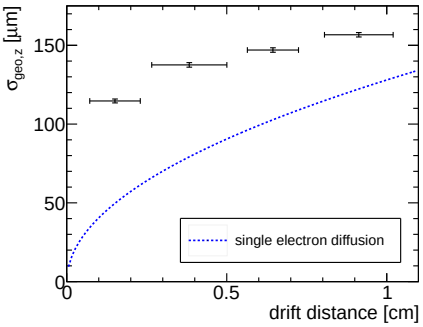

Figure 5.10: Display of the longitudinal single-point resolution at small drift distances (c.f. Fig. 5.9). The extrapolated intrinsic resolution is about 100 µm.

with the clock period $T_{clock} = 1/f_{clock} = 18$ ns. Taking into account the drift velocity ($v_{Drift} = 9.74$ µm/ns), the intrinsic detector resolution in drift direction reads therefore:

$$\sigma_{z,0} = \frac{T_{clock} v_{Drift}}{\sqrt{6}} \approx 72\,\mu m. \tag{5.14}$$

However, a somewhat larger intrinsic resolution has to be expected since the secondary effects, especially the time walk, are not entirely negligible.

As mentioned in section 3.2.1.3, the Timepix chip is not capable to distinguish between two subsequent hits arriving at different times on the same pixel. Other than in transversal direction, the detection of clusters originating from more than one primary electron does, hence, not counter the influence of the longitudinal electron diffusion. In consequence, the contribution of the diffusion to the observed longitudinal single-point resolution is directly given by eq. 5.8.

The longitudinal single-point resolution achieved with the pixel TPC is depicted in figure 5.9. While the intrinsic detector resolution dominates the diffusion at short drift distances, the data are close to the single electron diffusion limit for long drift distances. The parameters obtained from a χ^2-optimization of equation 5.12 are compatible

with above discussed expectations. Inspection of the data for small drift distances, depicted in figure 5.10, shows that the intrinsic resolution is only slightly underestimated.

5.4 SUMMARY

The diffusion during the first centimeters of drift gives rise to the so-called declustering effect after which primary electrons cause individually detectable charge depositions. Therefore, as soon as the distance between the primary electrons is larger than a few GEM hole pitches, a true single electron detection becomes available with the pixel TPC.

Due to the declustering effect, both charge and dimensions of the recorded pixel clusters are dependent on the drift distance of the the parent primary electrons. Asymptotically, the characteristic size and charge of clusters caused by individual primary electrons are approached. From this, the effective gas gain of the GEM stack is estimated to be about 190 000. Since virtually every individual charge deposition corresponds to a single primary electron, mere cluster counting suffices to reasonably obtain the specific energy loss of particles traversing the pixel TPC. Hence, a simple and generic particle identification is available.

The resolution with which the track points are determined is limited by the diffusion of the individually detected primary electrons. In comparison, the single-point resolution of TPCs with standard pad readout is better since not the position of individual primary electrons but the mean position of several primary electrons is measured. Due to the significantly larger number of track points in case of the pixel TPC, it is eventually expected that the track resolution of a pixel TPC is at least comparable with the resolution of a pad TPC. This, however, could not be proven up to now since no reference data from a hodoscope is available for the investigated data set. The pixel TPC provides the benefit that a plus in track points potentially allows a better multi track separation. However, the recent track identification algorithm does not fully exploit the potential of the detector, since it operates only in the xy-plane.

6 DELAYED PRIMARY ELECTRONS

As mentioned in section 4.4.2, occasionally one of the charge depositions associated with a particle track shows significantly lower ToA counts than the others. The primary electrons causing such clusters seem to be delayed with respect to the others. Exemplary events are depicted in figures 4.9 and 6.1a respectively.

Since drift time and reconstructed z-coordinate of a primary electron are proportional to each other, it is equivalent to speak either of a delay or of the z-residual, which denotes the distance between a primary electron and the associated track fitted to all track points except for the one under investigation.

All delayed clusters are located on a straight line with unobtrusive clusters originating from the same primary track, at least within the expected transversal diffusion. Thus, the claim that the delayed clusters are not related to the associated track is waived. Since exclusively pixels of single clusters show low ToA counts while all other pixels show normal functionality, an electronic cause is excluded as well.

In this chapter, it is investigated whether the delay is caused by a combination of attachment, interrupting the drift process, and detachment, allowing the attached electron to resume drift and to be eventually detected. Recalling section 1.4.1, two conceptually different attachment mechanisms can be thought of:

- Three body attachment to molecular oxygen may occur throughout the whole gas volume. Though, since it is the largest section, most three body attachment processes take place in the drift volume, where the only available detachment mechanism is autodetachment. Collisional detachment is unlikely because the gas temperature of about 300 K corresponds to molecule energies of only a few 10 meV.

- Dissociative attachment in helium with 30 % CO_2 admixture takes place only in regions with electric fields of several kilovolts per centimeter, c.f. figure 3.18b. In the pixel TPC, such fields occur only in the direct vicinity of the GEMs. In this region, anions may gain significant kinetic energies. Hence, besides autodetachment, collisional detachment is possible.

In the following, the criteria used to identify delayed electrons are discussed. Afterwards, the characteristics of the delayed electrons are analyzed before it is attempted to reproduce the observed data by means of a Monte Carlo simulation in section 6.3.

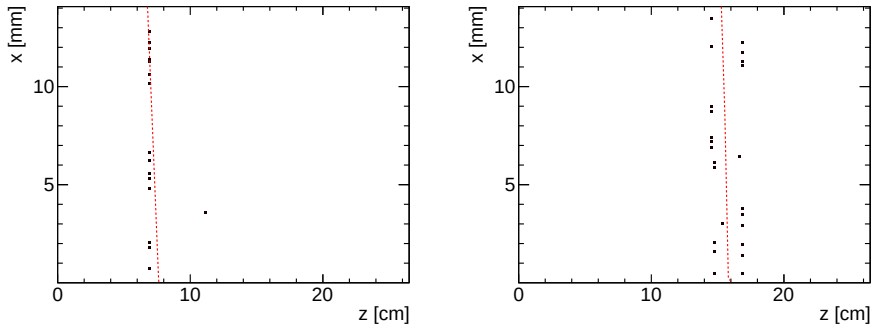

(a) (b)

Figure 6.1: a) Representative event showing a delayed primary electron together with the fitted track in the zx-plane of the detector.
b) Display of an unrecognized double track event together with the unsuitably reconstructed particle track. The worst outlier in such events is falsely tagged as delayed, since the distances to the reconstructed track are large.

6.1 DATA SELECTION

For previously presented analyses, events without delayed primary electrons have been selected by requiring that the residual r of all track points is less than six times the mean expected distance between the recorded track points and the reconstructed track (c.f. section 4.4.2 and eq. 5.12):

$$r \leqslant 6\sigma_{\text{geo},z}. \tag{6.1}$$

Although this identification criterion is robust in general, primary electrons are very likely misidentified as delayed electrons, if the assignment between primary electrons and tracks is incorrect in the first place. As shown in figure 6.1b, events in which two tracks differ in z but overlap in the xy-plane may be reconstructed as a single track in between of the original tracks. In consequence, several primary electrons of such events fulfill the 6σ-criterion and the worst outlier is falsely tagged as delayed electron. Since it results in the exclusion off falsely reconstructed tracks, such misidentifications support the selection of good events.

For characterization of the delayed electrons, however, a pure sample of events exclusively with tracks with delayed electrons needs to be selected. This is ensured by requiring that all but the potentially delayed electron are within $6\sigma_{\text{geo},z}$ of the track formed by the non-delayed electrons. Besides, correct track reconstruction is ensured by application of the criteria summarized in table 4.1, certainly except for the limited track angle λ and the restricted z-range.

Still, an electron may be falsely identified as delayed electron due to the track reconstruction or corrupted drift time measurements:

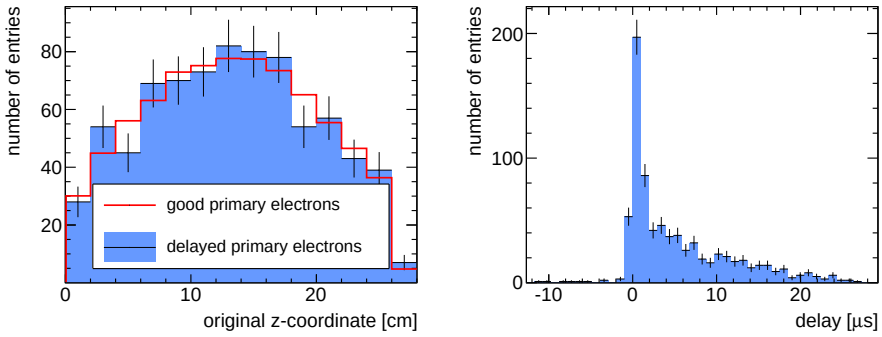

(a) (b)

Figure 6.2: a) The expected z-coordinates of delayed electrons (blue, solid) are distributed as the z-coordinates of unobtrusive primary electrons (red line, scaled).
b) Spectrum showing distances between delayed electrons and the corresponding track.

A. The parameters of tracks defined by only a few primary electrons are poorly determined and may change drastically if an electron is discarded during track reconstruction.

B. The straight line fitted by default is no valid description of the recorded data if the original track has a kink due to a significant scattering process.

C. Since the reconstructed z-coordinates are too small, the observed diffusion is larger than expected if charges have been created in the TPC before the shutter was opened.

D. If the cluster charges in an event are inhomogeneous, the time walk has different effects on the reconstructed z-coordinates. Especially at small drift distances, this can suffice to cause large residuals.

Misidentifications due to A or B may result in any residual. The net effects of C and D, in comparison, are small. Therefore, their relative effect is larger for tracks with small drift distances, for which only small residuals are expected.

6.2 OBSERVED DELAY DISTRIBUTION

Assuming that the track reconstructed without the delayed electron is correct, the originally expected z-coordinates of delayed electrons can be calculated. As seen in figure 6.2a, the distribution of the original z-coordinates is compatible with the z-coordinates of unobtrusive primary electrons.

If the delayed electrons are caused by a combination of attachment and detachment, the delays should be positive and exponentially distributed. With the anion lifetime τ_{anion}, the expected exponential distribution reads:

$$N_{delay}(t_{delay}) \propto \exp\left(-\frac{t_{delay}}{\tau_{anion}}\right). \tag{6.2}$$

Other than expected, negative values are observed in the delay distribution depicted in figure 6.2b. Besides, the number of extremely small delay times does not match the rest of the distribution. Obviously, the negative delays originate from primary electrons which are falsely tagged as delayed electrons. It is claimed that also most of the small delays originate from misidentifications. Consequently, delayed electrons with residuals less than 2 µs are not discussed. For larger delays, the distribution should not be affected by misidentifications.

The exponential distribution expected from eq. 6.2 can not be observed directly in the data since the maximally detectable delay is limited individually for each event by the shutter period $t_{shutter}$ and the original z-coordinate of a delayed electron. If for instance the drift time t_{org} is expected, then at most a delay of:

$$t_{delay,max} = t_{shutter} - t_{org} \tag{6.3}$$

can be observed, longer lifetimes are truncated. In consequence, short lifetimes are significantly overrepresented in the recorded data sample.

6.3 MONTE CARLO SIMULATION OF DELAYED ELECTRONS

The previously described characteristics for the detection of delayed electrons are resembled by a simple Monte Carlo simulation:

1. A random number is drawn from the z-distribution of regular primary electrons, yielding the originally expected position of a simulated primary electron.

2. With the probability p_{att}, a primary electron may or may not get attached to a gas constituent before it is finally detected. If the attachment occurs in direct proximity of the GEM stack, the probability is independent of the original z-coordinate:

   $$p_{att} = \text{const.} \tag{6.4}$$

   Alternatively, the attachment happens during drift. This would imply that the attachment probability is dependent on the drift distance z:

   $$p_{att} = p_{att}(z) = 1 - \exp(-zB), \tag{6.5}$$

   with the attachment rate B.

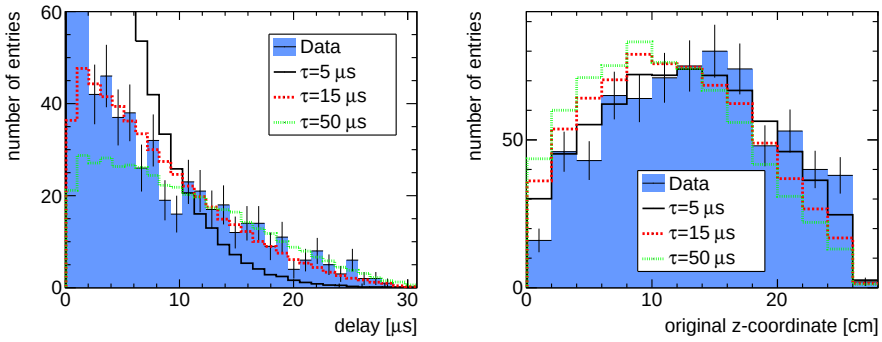

(a) (b)

Figure 6.3: a) Delay spectrum showing the distribution of residuals of delayed electrons. The data, plotted in blue, are shown together with results from a Monte Carlo simulation assuming attachment near the GEM stack and different anion lifetimes τ.
b) Originally expected z-coordinates of simulated and actually observed delayed electrons. With above assumptions, the simulated distributions are skewed, other than the data.

3. Only if the exponentially distributed random lifetime of an individual anion is within the window of sensitivity, defined in eq. 6.3, it contributes to the observed delay distribution and the distribution of expected z-coordinates. Otherwise, it gets truncated by the end of the shutter window.

Assuming that attachment and detachment happen in the vicinity of the gas amplification stage, only the anion lifetime τ is a tunable parameter in the sketched Monte Carlo simulation. Inspection of the simulation results, depicted in figure 6.3, shows that the measured delay spectrum can be resembled if τ is chosen to be about 15 µs. Compared with the data, the simulations, however, show an excess for small drift distances in the distribution of original z-positions

Since the probability for attachment during drift follows an exponential distribution, a second parameter, the attachment rate B, is introduced to the Monte Carlo simulation when attachment during the drift phase is assumed. With $B = 0.01\,/\text{cm}$, as derived from the data in section 5.2, and an anion lifetime of about 25 µs, the delay spectrum obtained from the Monte Carlo simulation reproduces the observed residual distribution, see figure 6.4a. In contrast, the distribution of original z-positions is skewed to large drift distances and not compatible with the data, see figures 6.5a and 6.5b.

As shown in figure 6.5b, the skewness of the distribution of original z-positions is controlled by the assumed attachment rate. The distribution becomes less skewed when high attachment rates are assumed. The delay spectrum on the other hand is rather insensitive to varia-

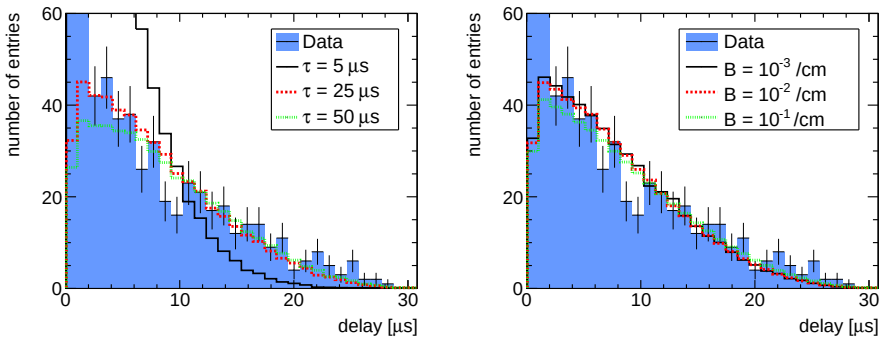

(a) $B = 10^{-3}$ /cm (b) $\tau = 25$ ns

Figure 6.4: Delay spectra showing the residual distribution of delayed electrons. The data (solid, blue) are shown together with results from a Monte Carlo simulation assuming attachment during drift with different anion lifetimes τ (a) and attachment rates B (b).

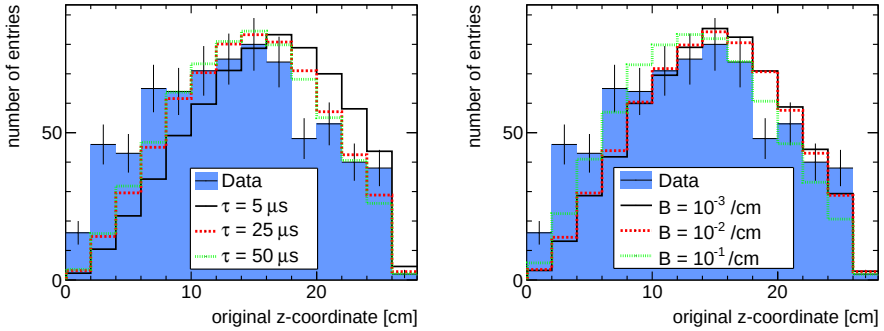

(a) $B = 10^{-3}$ /cm (b) $\tau = 25$ ns

Figure 6.5: Originally expected z-coordinates of simulated and actually observed delayed electrons (solid, blue). Attachment during drift, different anion lifetimes τ (a) and attachment rates B (b) have been assumed for simulation.

tions of this parameter, see figure 6.4b. The large attachment rates needed for symmetrization of the skewed z-distribution are unreasonable since they would imply that the TPC is basically insensitive to charge depositions at large z-positions.

6.4 SUMMARY

The pixel readout of the TPC allows for the first time to detect delayed electrons. Until now, delayed electrons have not been observed, since TPCs with classical pad readout are not sensitive to individual primary electrons.

Investigation of the delay mechanism by means of Monte Carlo calculations is not conclusive. Neither attachment in the gas amplification region nor in the drift volume alone suffices for minute reproduction of the characteristic distributions of delayed electrons. A

combination of both however might explain the observed distributions.

A possible delay mechanism not yet investigated is based on the penning effect and radiation trapping [159, 160]. The latter is caused by repeated resonance absorption of photons emitted by excited atoms or molecules. In a Penning gas mixture, such radiative transfer of excitation energy between two molecules of the same species results eventually in a reasonable extension of the time until a molecule of another species is ionized. Hence, radiation trapping might suffice to explain delay times in the microsecond regime. This could be subject to a future study, possibly involving dedicated measurements with different drift gas compositions and electric fields.

7 DETECTOR SIMULATION

Simulations of the primary ionization and the charge transport in a gaseous detector by means of HEED [151] and Magboltz [33, 153], respectively, have been presented in section 3.4. Such simulations are well established nowadays.

Simulating the gas amplification stage, in contrast, has been challenging until recently Garfield++ [161] became available. Garfield++ is developed as an object oriented framework for the detailed simulation of gaseous detectors, based on the work presented in [162]. The toolkit combines the functionality of Magboltz and HEED with finite element tools like CST [163], TCAD [164], Elmer [165] or ANSYS [166]. Thus, it is possible to simulate the movement of charge carriers in inhomogeneous electromagnetic fields on a microscopic level.

The findings of the single GEM simulation, described in section 7.1, allow to model a triple GEM stack purely on basis of statistical considerations, as outlined in section 7.2. Combining HEED with this heuristic GEM stack simulation yields a fast, yet accurate, simulation of the pixel TPC. Results of this simulation are compared with the recorded data in section 7.3.

7.1 MICROSCOPIC SIMULATION OF A SINGLE GEM

The exact field configuration has to be known in order to microscopically track the movement of a drifting electron. The electric field in a GEM detector cannot be calculated analytically, but it can be derived by means of the Finite Element Method (FEM). In the following, the steps taken for a FEM based simulation of electron avalanches in a single GEM are sketched.

7.1.1 *FEM Model*

In simple terms, the FEM approach is to divide a problem, which is originally described by partial differential equations, into small domains. These subproblems are approximated by a set of linear equations and possibly a system of ordinary differential equations, both solvable by means of numerical methods.

Segmenting the investigated volume into small elements for FEM is called meshing. By definition, none of the elements crosses a material boundary. Hence, properties like conductivity or permeability can be

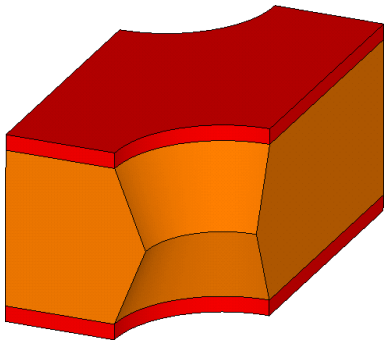

Figure 7.1: Unit cell of a standard CERN GEM. The hole pitch is 140 µm, outer and inner diameter measure 70 µm and 50 µm, respectively. The copper coating (red) is 5 µm thick on either side of the 50 µm thick Kapton foil (orange).

uniquely assigned to each element. Most FEM tools use cuboids for the meshing. ANSYS, in contrast, utilizes parabolically curved elements, defined by ten nodes which are shared between neighboring elements. The curvature of the element boundaries allows to precisely resemble round surfaces in a model. A beneficial feature when for example the GEM holes need to be modeled.

A fine mesh is used near small geometrical structures, while a rough mesh patterns areas with tiny gradients – a technique referred to as smart meshing. Without a significant loss in precision, this allows to reduce the demands on the computing power by decreasing the total number of elements to examine.

Since Garfield++ allows for exploitation of symmetry properties, only the GEM unit cell, depicted in figure 7.1, needs to be crafted for simulation of a complete GEM. Considering the material properties and the boundary conditions, the electric potential is calculated for each node after the model has been meshed, see figure 7.2a.

In a next step, the electric field could be derived from the distances of neighboring nodes and their potential differences. However, since every node is neighbor to several others, in such way obtained fields are ambiguous and discontinuous. Therefore, the configuration of the electric field, displayed in figure 7.2b, is computed from the potentials without taking numerical derivatives by GARFIELD++.

7.1.2 *Electron Avalanches*

Based on the potential map imported from a FEM tool, GARFIELD++ computes the electric field. Utilizing Magboltz routines, this allows for microscopic tracking of the movement of charge carriers through the GEM. Collisions of the charge carriers with the medium are classified as elastic or inelastic, newly created secondary charge carriers are tracked together with the primary ones. A typical simulated elec-

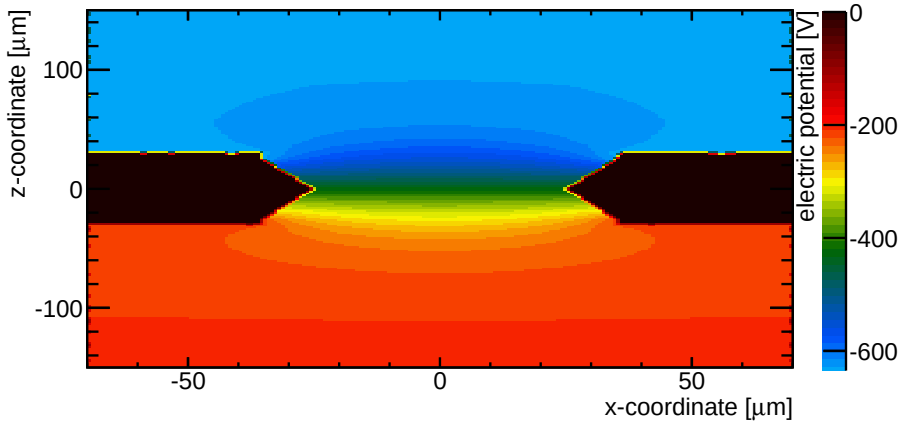

(a)

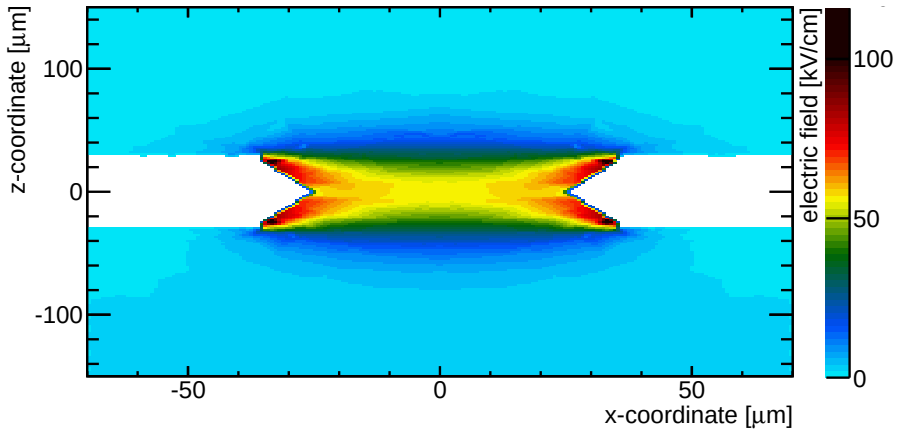

(b)

Figure 7.2: Potential (a) and field (b) in a hole of the upper most GEM in the pixel TPC GEM stack. The GEM voltage is $\Delta U_{GEM} = 415\,V$, drift and transfer fields are 495 V/cm and 2200 V/cm, respectively.

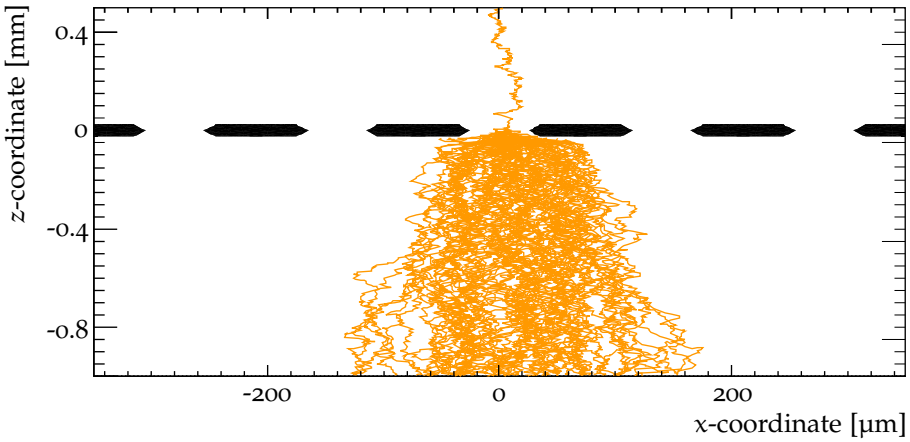

Figure 7.3: Display of a simulated electron avalanche in a standard CERN GEM operated at $\Delta U_{GEM} = 415\,V$ in Helium with 30 % CO_2 admixture. Only 71 of the 111 created electrons arrive on the plane 1 mm below the GEM. The others are attracted to the lower electrode of the GEM or are lost in attachment processes.

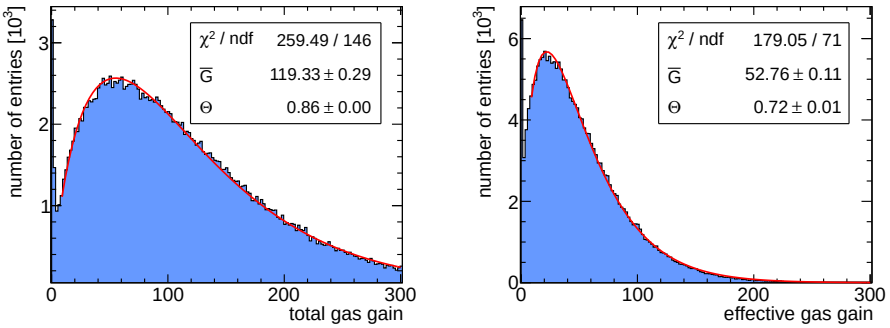

(a) (b)

Figure 7.4: Total (a) and effective (b) gas gain in the upper most GEM of the pixel TPC GEM stack. The GEM voltage is $\Delta U_{GEM} = 415\,V$, drift and transfer fields are 495 V/cm and 2200 V/cm, respectively.

tron avalanche is shown in figure 7.3. Comparison of the total and the effective gas gain, depicted in figures 7.4a and 7.4b, shows the rather low extraction efficiency achieved in the pixel TPC setup. The peak at zero or unity gas gain is caused by events in which attachment occurs before secondary ionization has taken place. For larger multiplicities, the data can be approximated by a Polyá distribution, as expected from section 1.3.

Because of the transversal diffusion below the GEM, the electron positions within the avalanches follow a Gaussian distribution, see figure 7.5a. No correlation between the entry point of an incident electron and the center of the charge cloud emerging from a GEM hole is observed. As shown in figure 7.5b, the centers of the electron avalanches are basically Gaussian distributed within an active region σ_{active} of approximately 21 µm below the GEM hole centers.

Certainly, such straightforward simulations of electron avalanches in a GEM can not be considered to be exact since, other than in [167], the electric field is calculated without taking into account the charge-up effect introduced in section 1.3.4. While the charge-up clearly has a significant effect on the gain, the collection and extraction efficiencies, it is assumed that neither the distribution of the electrons within the charge cloud nor the distribution of the charge cloud centers are influenced.

7.2 HEURISTIC GEM STACK SIMULATION

Although technically possible, the microscopic simulation of a complete GEM stack with a large gain is not advisable since the computing time scales with both, the number of electrons in an avalanche and the investigated volume. Though, simulation of a complete GEM

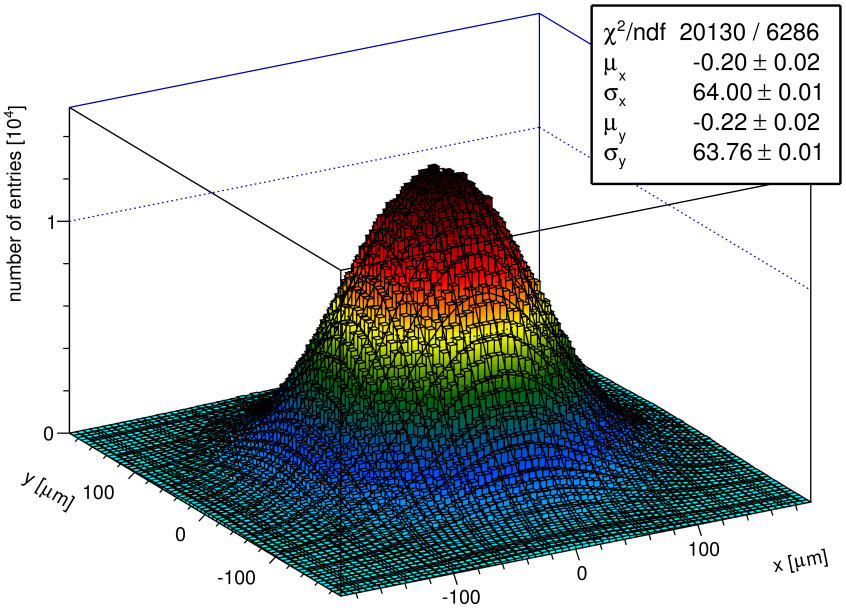

(a) Positions of avalanche electrons

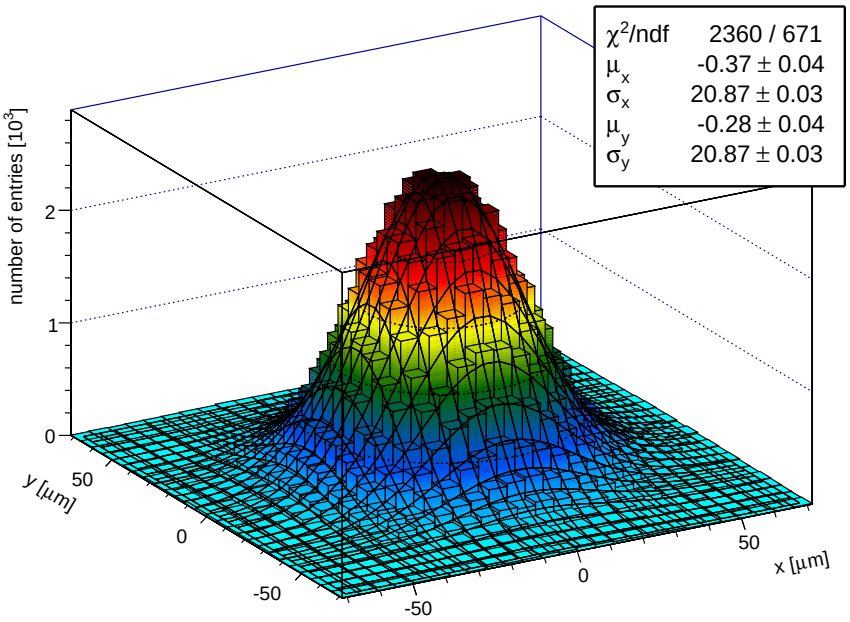

(b) Distribution of avalanche centers

Figure 7.5: Characteristics of simulated electron avalanches, emerging from a standard CERN GEM operated at $\Delta U_{GEM} = 415\,V$ in Helium with 30 % CO_2 admixture. 1 mm underneath the GEM, the positions of the avalanche electrons (a) and the avalanche centers (b) are almost Gaussian distributed.

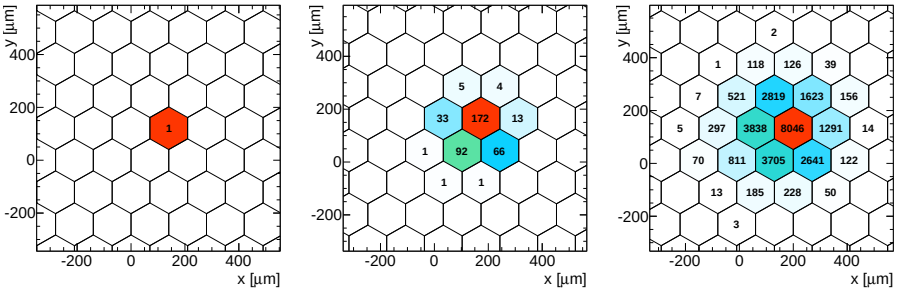

(a) (b) (c)

Figure 7.6: Heuristic GEM stack simulation. For one incident electron, the number of secondary electrons traversing each GEM hole is shown for the GEMs of a triple GEM stack. Electrons arriving on the upper most GEM (a) are multiplied and distributed on the GEM underneath (b). Here, they are again multiplied and redistributed to the third GEM (c). After a third amplification process, the electron cloud drifts towards the readout plane.

stack becomes reasonable, when the electrons are not tracked microscopically but propagated on basis of statistical considerations.

Due to the pattern of the holes, a standard CERN GEM can be seen as plane which collects incident electrons on hexagonal panels and releases a random number of avalanche electrons into the volume beneath. This allows to model the gas amplification in a GEM stack as follows:

1. The transversal coordinates of the incident electrons determine which hexagonal panel of the GEM plane is hit.

2. The number of avalanche electrons released into the volume below the GEM is randomized from the microscopically determined effective gain distribution of that particular GEM.

3. The position of the charge cloud center is randomized from a Gaussian distribution around the GEM hole center.

4. Below the traversed GEM, the individual avalanche electrons are Gaussian distributed within the charge cloud due to the transversal diffusion.

5. Finally, the x- and y-coordinates of the avalanche electrons are determined by the center of the traversed GEM hole, the random charge cloud center and the transversal diffusion.

Recursive repetition of these steps allows for heuristic simulation of a complete GEM stack, see figure 7.6.

7.3 FULL DETECTOR SIMULATION

Besides the physics processes discussed in chapter 1, the characteristics of the readout ASIC, recapitulated in section 3.2, have to be reproduced by a simulation of the pixel TPC. In turn, a fully fletched simulation of the pixel TPC allows for conclusive understanding of the detector. Furthermore, it becomes possible to investigate the effect of small variations in the setup, for instance the pixel or GEM hole pitch, without actually modifying the detector.

7.3.1 *Simulation Chain*

The primary ionization, caused by cosmic muons in the pixel TPC, is simulated with HEED++. For convenience, only events with single particle tracks, in parallel with the x-axis of the readout ASIC, are simulated. The penetration point at which the tracks enter the TPC volume is randomized. Knowledge of the diffusion constants, computed with Magboltz, allows to resemble the diffusion of each primary electron by variation of the original HEED++ coordinates. Based on the attachment probability, which is calculated for each primary electron from the globally assumed attachment rate and the individual z-coordinate, primary electrons are randomly removed from the simulated particle track.

The gas amplification in the triple GEM stack of the pixel TPC is simulated as outlined in section 7.2. It has been found that the electron avalanche of a single primary electron is never spread out over more than 15×15 GEM holes on the bottom GEM. Thus, simulation of a larger part is not necessary. Therefore, only a small segment of the GEM stack, which is then stepped over the full sensitive area, is crafted for simulation. An arbitrary offset, shifting the individual GEMs with respect to each other in xy-direction, is assumed to model a possible misalignment in the GEM stack.

The pixels of the Timepix chip, employed for charge collection, are resembled by 256×256 quadratic panels with 55 µm edge length. The final coordinates of the electrons emerging from the bottom GEM determine which panel, pixel respectively, is hit. Due to the small pixel effect [168], only this endpoint of the electron movement is relevant for signal development. Based on the findings presented in [150], it is assumed that the complete pixel surface is sensitive, even though only a small fraction is actually metalized.

After computation of the charge distribution on the readout chip, the number of electrons collected by each pixel is compared to the threshold. As in case of the real readout ASIC, it is assumed that the pixels measure either the total collected charge via the time over threshold method or the time at which the threshold is exceeded for the first time. The analogue behavior of the readout chip is not modeled.

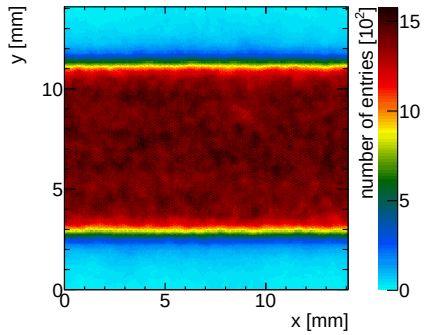

Figure 7.7: Occupancy of the simulated readout chip, only horizontal tracks within the sensitive area are computed.

parameter	value
electron drift velocity	0.978 $\frac{\text{cm}}{\mu\text{s}}$
transversal diffusion during drift	133 $\frac{\mu\text{m}}{\sqrt{\text{cm}}}$
longitudinal diffusion during drift	131 $\frac{\mu\text{m}}{\sqrt{\text{cm}}}$
transversal diffusion in the transfer gaps	50 $\frac{\mu\text{m}}{\sqrt{\text{cm}}}$
transversal diffusion in the induction gap	60 $\frac{\mu\text{m}}{\sqrt{\text{cm}}}$
width of the active hole region	20 µm
clock frequency ($\hat{=}$1/time bin size)	55 MHz
shutter length	30 µs

Table 7.1: Predefined simulation parameters.

Computation of a single event takes a few seconds, dependent on the number of primary electrons. The occupancy of the readout chip after 29 000 simulated events is depicted in figure 7.7. No simulation artifacts are observed.

7.3.2 *Adjustment of the Simulation Parameters*

Most simulation parameters are predefined by choice of the drift gas and the boundary conditions. These fixed parameters are stated in table 7.1. Besides, there are three free parameters which have to be determined from comparison between simulation results and real data:

- The oxygen contamination in the drift gas is unknown. In turn, the attachment rate is undetermined.
- The charge-up effect in the GEMs is not modeled. The simulated gas gain is, hence, too low. This is addressed by introduction of a multiplicative gain correction factor which is applied to the randomly determined gas gain in each amplification step.
- The actual pixel threshold is not precisely known. Only an estimate from the calibration presented in section 3.3.3 is available.

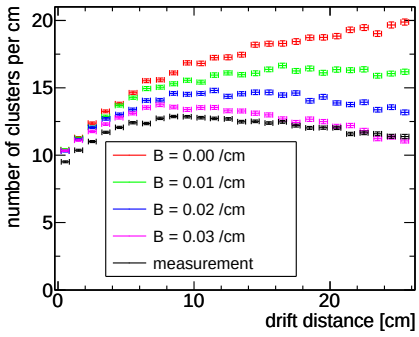

Figure 7.8: Ionization density observed in simulated data for various attachment rates B. No gain correction is applied. The assumed threshold is 175 e.

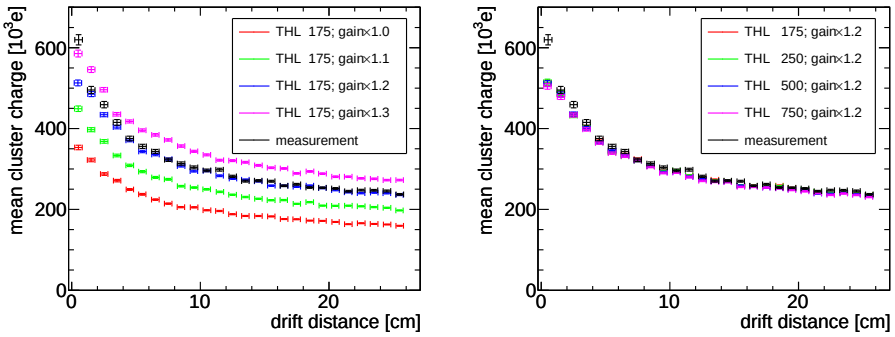

(a) (b)

Figure 7.9: Mean charge per cluster in dependence on the drift distance. The measured data, plotted in black, are compared with simulation results for different gain (a) and threshold settings (b). The assumed attachment rate is B = 0.02 /cm.

By affecting the probability to have superimposed clusters, the attachment rate influences the mean charge per cluster as well as the mean cluster area. Besides, it is the only mechanism that causes the number of detected clusters per unit track length to drop with increasing drift distance. Consequently, the correct attachment rate can be identified by comparing the drop in the measured ionization density with the drop in simulated data. From figure 7.8, it can be seen that simulated and measured ionization density show the same negative gradient if an attachment rate of 0.02 /cm is assumed.

The simulated mean charge per cluster, depicted in figure 7.9, varies with the applied gain correction factor while it is virtually independent on the set threshold. This is expected since the outer regions of the quasi Gaussian clusters contribute only little to the integrated charge. From figure 7.9a, it is deduced that the the simulated gas gain roughly 20 % smaller than the actual gas gain.

Investigation of the simulated cluster size, shown for various gain correction and threshold values in figure 7.10, strongly suggests a threshold of 175 e which is at least a factor of 2 smaller than expected. However, for drift distances larger than a few centimeters, the simulation and measurement results match each other with this setting.

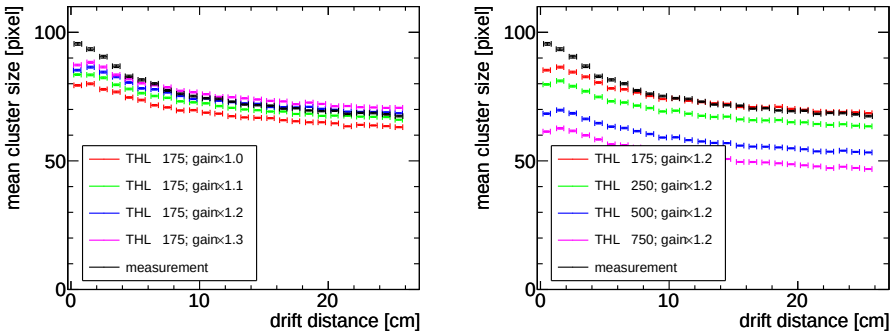

(a) (b)

Figure 7.10: Mean cluster size for recorded data (black) and simulations with various gain correction (a) and threshold values (b). The attachment rate is assumed to be 0.02 /cm.

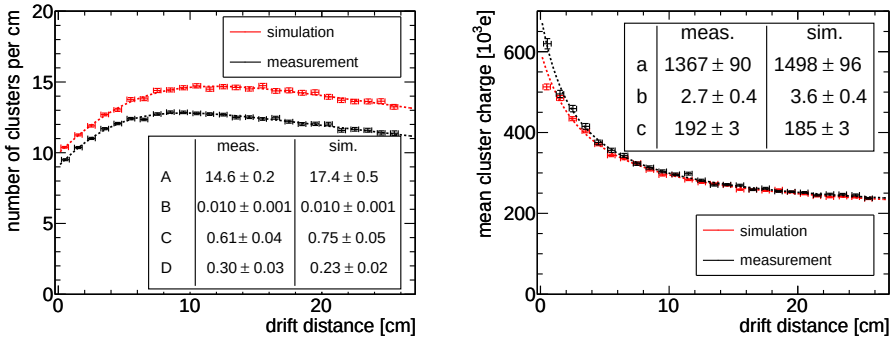

(a) (b)

Figure 7.11: a) Number of detected clusters per unit track length in dependence on the drift distance for simulated (red) and measured (black) data. Both data sets can be approximated by eq. 7.1.
b) The mean simulated cluster charge in dependence on the drift distance (red) resembles the measured data (black) nearly exactly. The data are described by eq. 7.2.

7.3.3 *Comparison with Measurement Data*

The results from the pixel TPC simulation are, with some exceptions, in good agreement with the measurement if the attachment rate is set to 0.02 /cm, the gain correction factor to 1.2 and the threshold to 175 e. In the following, real and simulated detector characteristics are compared in detail.

As shown in figure 7.11a and motivated in section 5.2, both the measured and the simulated number of individually detected clusters per unit track length can be approximated by:

$$n_{\text{Cluster}}(z) = \frac{A \exp(-Bz)}{1 + C \exp(-Dz)}. \tag{7.1}$$

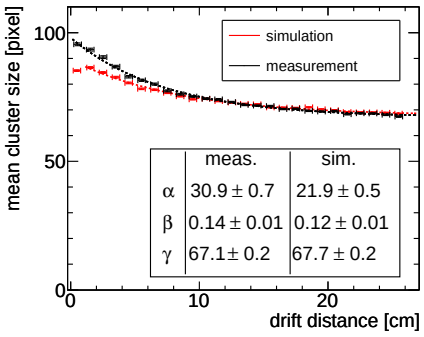

Figure 7.12: Dependency of the mean cluster size on the drift distance of the parent primary electrons. Simulated (red) and measured data (black) are reproduced by eq. 7.3.

The curves describing simulated and measured data feature similar values for the average number of primary electrons per cluster at zero drift distance $(1 + C)$, as well as compatible attachment and separation rates B and D, respectively. The number of ideally detected clusters (A), in contrast, differs. Under the assumption that the primary ionization is correctly simulated in the first place, this difference shows that the probability to individually detect single primary electrons is larger in the simulation than in reality.

The attachment rate, obtained by χ^2-optimization of equation 7.1, is a factor of 2 smaller than originally set for computation of the simulated data. This points out that equation 7.1 describes the data only qualitatively. The oxygen contamination in the drift gas is in consequence not 10 ppm as stated in section 5.2 but twice that value.

Following section 5.1.1, the dependency of the mean cluster charge on the drift distance is described by:

$$Q(z) = \frac{a}{b+z} + c \tag{7.2}$$

It is depicted in figure 7.11b for both, simulated and measured data. Since the declustering effect is not exactly reproduced, the simulated mean cluster charge is slightly too small in the first centimeters of drift. The agreement between measured and simulated data is nevertheless almost perfect.

The dependency of the cluster size on the drift distance is shown in figure 7.12. Following section 5.1.2, it is described by:

$$f(z) = \alpha \exp(-\beta z) + \gamma. \tag{7.3}$$

Again, the difference between measured and simulated data can be explained by inadequate modeling of the declustering effect. Taking into account also the rather low threshold that is assumed for simulation, it is reasoned that the simulated electron avalanches are too narrow. Wider avalanches would result in a decreased probability for the separation of overlapping clusters. In consequence, the declustering effect would be enhanced. Besides, if the avalanches were wider,

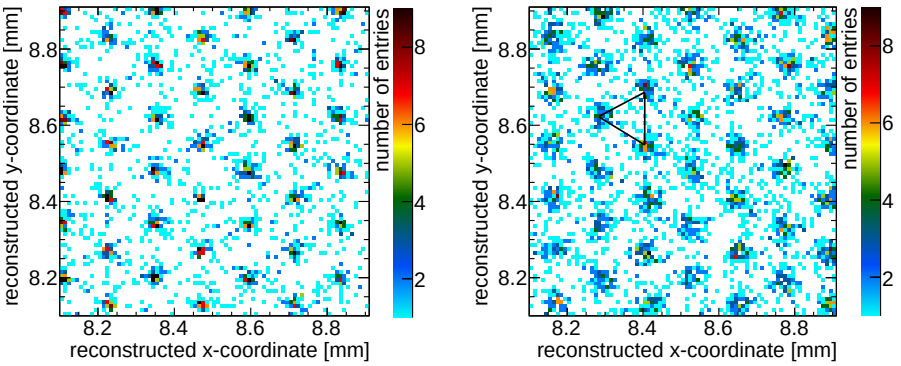

(a) (b)

Figure 7.13: Reconstructed x- and y-coordinates of the primary electrons of simulated (a) and measured (b) data.

a higher and therefore more realistic threshold could be set for simulation.

Another shortcoming of the simulation routines is the strong localization of the avalanche centers. The centers of simulated electron avalanches, depicted in figure 7.13a, are rather closer to the primarily traversed hole in the upper most GEM. The centers of the actually measured electron avalanches are, in comparison, less localized, see figure 7.13b.

The transversal single-point resolution is described by:

$$\sigma_{\text{geo},xy}(z) = \sqrt{\sigma_{xy,0}^2 + \frac{D_T^2 z}{1 + a \exp(-bz)}}, \tag{7.4}$$

as shown in figure 7.14a and discussed in section 5.3.1. The parameters obtained from a χ^2-optimization for simulated and measured data are in good agreement with each other.

Following section 5.3.2, the longitudinal single-point resolution is described by:

$$\sigma_{\text{geo},z}(z) = \sqrt{\sigma_{z,0}^2 + D_L^2 z}. \tag{7.5}$$

The simulated and the measured longitudinal single-point resolution, shown in figure 7.14b, differ in the first centimeters of drift. In consequence, the simulated longitudinal single-point resolution is undetermined. This behavior is not understood yet, since only modest effort has been put into modeling of the ToA detection characteristics of the readout chip up to now.

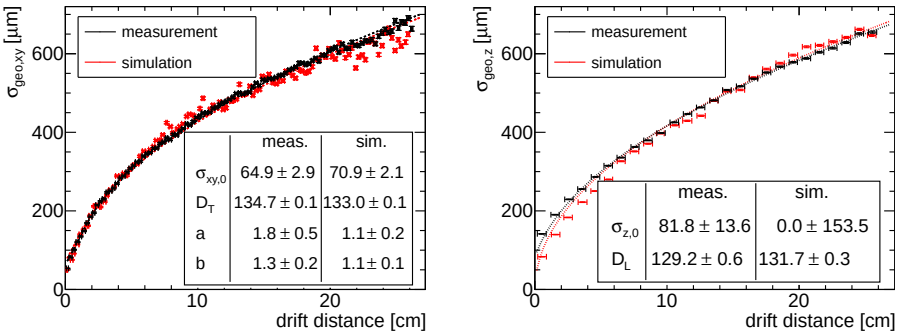

(a) (b)

Figure 7.14: Transversal (a) and longitudinal (b) single-point resolution extracted from the measured (black) and the simulated data (red). The data are approximated by eq. 7.4 and eq. 7.5 respectively.

7.4 SUMMARY

In this chapter, characteristics of the electron avalanches in a standard CERN GEM have been determined from microscopic GARFIELD++ simulations. The observed avalanche characteristics allowed for modeling of a triple GEM stack, purely on the basis of statistical considerations.

The high speed of this heuristic GEM stack simulation enables simulation of a large number of particle tracks in the pixel TPC. The fully fletched TPC simulation is made of three consecutive modules:

- Simulation of the primary ionization by means of HEED++,
- Charge transport through the drift volume according to the parameters obtained from Magboltz calculations.
- Gas amplification and signal detection with the newly developed heuristic GEM stack simulation.

Simulation and measurement results match each other, after the undetermined simulation parameters, namely the attachment rate, the actual gas amplification and the threshold of the readout chip, have been set to the appropriate values. Observed differences are explained by an underestimation of the charge spread within the individual electron avalanches. This underestimation might be caused by unaccounted effects as coulomb repulsion in the charge cloud or field inhomogeneities between the GEMs. The latter might be also the reason why the simulated avalanche centers are more localized than the measured ones.

8

GOSSIP AND NEXT GENERATION READOUT ELECTRONICS

GOSSIP is an acronym for Gas On Slimmed SIlicon Pixels. Similar to classical TPCs, GOSSIP detectors are made of a gas volume, a gas amplification stage and a segmented readout anode. The latter is formed by a pixelized readout chip which is slimmed down to approximately 30 µm. The thickness of the drift gas volume is about 1 mm [169, 170]. This design results in a small amount of material in the detector. Hence, track distortions by multiple scattering are suppressed.

In contrast to classical TPCs, the particle tracks are running rather perpendicularly than parallelly to the readout plane in a GOSSIP detector, see figure 8.1a. Despite the short length of the track in the detector, even minimally ionizing particles create enough primary ionization points for a 3-dimensional track reconstruction if a suitable drift gas is chosen [171].

First tests of a GOSSIP like detector have been conducted with a standard Micromegas mesh resting on polyimide pillars with 50 µm height on a Timepix ASIC. Since the Micromegas pattern has not been matched to the pixel pattern, a Moiré effect was observed in the data [172]. Alignment of the grid holes with the pixels eliminates this effect. An almost perfect alignment is achieved, when the amplification grid is integrated on top of the readout ASIC by means of photo-lithographic post-processing. The production process and the performance of such INtegrated GRIDs (InGrids) are presented in [43, 173]. A scanning microscope photograph is shown in figure 8.1b.

As in TPCs with long drift distances, the track reconstruction in a GOSSIP detector is based on the xy-projection and the measured drift times of the primary electrons. Since the track segments are very short, the achieved single-point resolution is of increased importance.

Due to the small drift distances in GOSSIP detectors, the readout times are rather short and diffusion effects are strongly suppressed. Consequently, the spatial resolution in the xy-direction is basically defined by the pixel pitch. The resolution in drift direction is limited by the precision of the Time of Arrival (ToA) measurement in the pixel chip.

In case of the readout chips nowadays available, the ToA precision is limited by the counting frequency ($\leqslant$ 100 MHz) and the time walk caused by the analog electronics in the pixels. The latter is caused

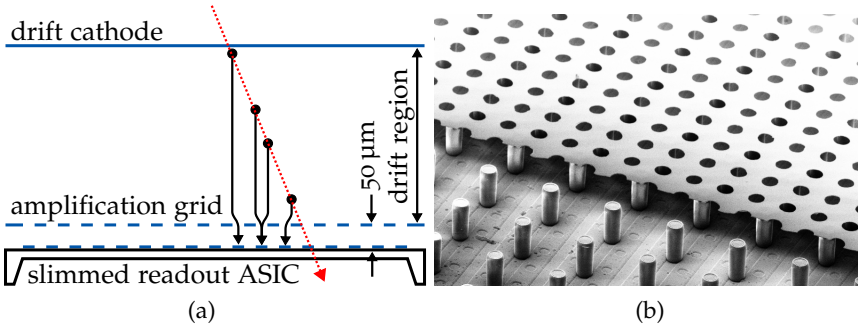

Figure 8.1: a) Operation principle of a GOSSIP detector. The angle between incident particles and the readout plane is rather large. Position and pitch of the holes in the amplification grid are matched to the pixel pattern of the readout ASIC.
b) Scanning electron microscope picture of an InGrid. The amplification grid is partially removed. Hence, the supporting pillars, usually hidden between the grid holes, are visible. A high-resistive layer, deposed between ASIC and InGrid, protects the electronics from discharges.

by the constant peaking time of the preamplifier, as discussed in section 3.3.4.

These limitations have to be overcome by GOSSIP readOut (GOSSIPO) chips. In fact, the next generation of gaseous detector readout chips should not only come with an enhanced ToA precision, but also with the capability to simultaneously measure the arrival time of a hit and the amount of charge deposited in a pixel. An application in a high rate environment would also require a sparse and zero suppressed readout.

Once a readout ASIC with above listed features, especially a ToA precision of at least 2 ns, is available, GOSSIP detectors might replace silicon detectors. This would allow to improve track reconstruction, while the material budget is reduced at the same time. Although the gas amplification stage might undergo some aging, the aging observed in case of silicon sensors would become irrelevant. Consequently, it was proposed to develop GOSSIP detectors for the upgrade of the inner ATLAS tracker at LHC [174].

First steps towards a full featured pixel chip for the readout of GOSSIP detectors have been presented in [175, 176]. The features of the subsequent ASIC, GOSSIPO-3, are discussed in section 8.1. The follow up projects GOSSIPO-4 and Timepix3 are briefly described in sections 8.2 and 8.3.

8.1 GOSSIPO-3

GOSSIPO-3 [177–179] is a demonstrator front-end chip developed in a joined effort between the University of Bonn and NIKHEF (Am-

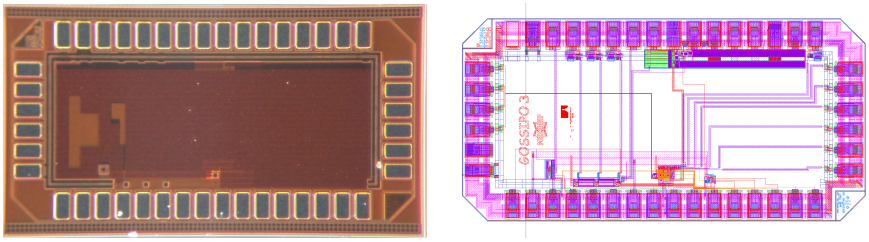

(a) (b)

Figure 8.2: Photograph (a) [179] and top-level layout view of GOSSIPO-3 (b). ©IOP Publishing Ltd. and Sissa Medialab srl. Reproduced by permission of IOP Publishing. All rights reserved.

sterdam). The chip, operated at a supply voltage (vdd) of 1.2 V, is produced in a 130 nm CMOS technology from IBM.

A high-range, high-accuracy Time to Digital Converter (TDC), aiming for applications in GOSSIP detectors as well as in TPCs with long drift distances, is tested on GOSSIPO-3. The ToA measurement technique is described in section 8.1.2. It introduces the need for a controllable voltage source which is realized as low drop out regulator (LDO), see section 8.1.3. Furthermore, a charge sensitive amplifier (CSA) with extremely high gain and a novel discharge-protection circuit is tested, c.f. 8.1.4. A photograph as well as the top-level layout view of the 2 mm² GOSSIPO-3 die is shown in figure 8.2.

The demonstrator IC features no complete pixel matrix. The circuits under investigation are only exemplarily implemented. Three CSAs, each connected to a discriminator, are implemented on the chip. Analog and digital part of this circuitry are located at opposite sides of the die. Besides, a pixel featuring only the digital circuitry as well as a full featured pixel are implemented. Furthermore, two different LDOs, placed in the upper right edge of the die, are tested.

8.1.1 *Test-Board*

The test-board for GOSSIPO-3 has been developed for usage in combination with the S3MultiIO board [180]. Both boards are shown in figure 8.3. The S3MultiIO board is built around a Spartan-3 FPGA. It is used to generate the logic stimuli needed to operate the test-chip. If no logic IO is needed, the test-board can be operated without the S3MultiIO Board.

GOSSIPO-3 has three different power domains: $\mathrm{vdd}_{\mathrm{analog}}$, vdd and $\mathrm{vdd}_{\mathrm{LDO}}$. All voltages can be provided either externally or are created on the test-board by commercial LDOs (LP38841-ADJ, LP3882ES-1.2). Only one single 5 V supply, provided either by USB or by an external connector, is needed in the latter case.

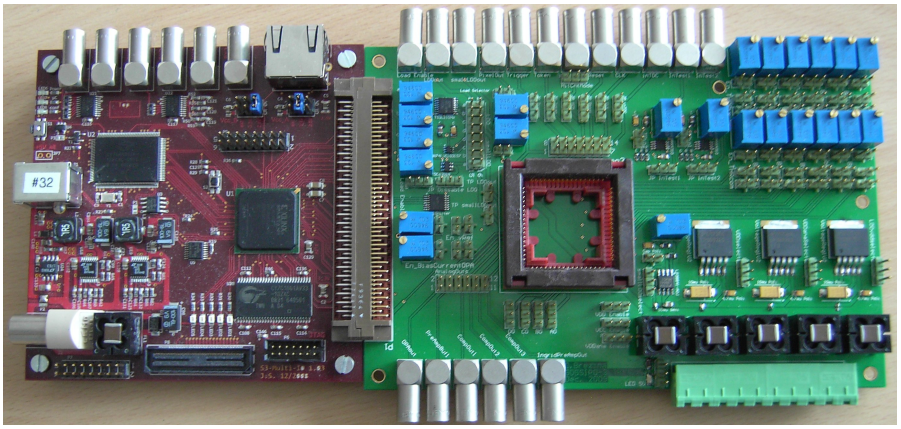

Figure 8.3: Photograph showing the S3MultiIO board (left PCB) together with the GOSSIPO-3 test-board (right PCB).

Although all bias voltages are generated on-chip, it is possible to override these by variable voltage dividers on the PCB.

Two high-speed multiplexers (MAX4310) are placed on the test-board allowing charge injection into the charge sensitive amplifiers. Alternatively, the injection may also be done directly by sending voltage steps via external connectors.

8.1.2 *High-Resolution TDC*

GOSSIP detectors require time resolutions in the order of nanoseconds. Such values can be achieved in principle with the ToA measurement technique known from the Timepix chip. However, the counting frequency has to be increased to several hundred megahertz.

A chip wide high-frequency clock network requires high-performance clock buffers sinking an enormous current. This may not only cause voltage drops or ground bounces on the supply rails but results also in excessive heating. At the same time, crosstalk signals disturbing the analog circuitry are emitted by the clock network. Clearly, these effects are highly undesirable.

The need for a chip wide high-frequency network is eliminated, if the clock signal is generated locally in each pixel. Though, neither synchronicity nor long term stability are guaranteed in this case.

These issues have been taken into account during the development of the ToA measurement technique realized in GOSSIPO-3. A block diagram of the pixel logic is depicted in figure 8.4, the timing diagram in figure 8.5.

The discrimination of a hit activates a 580 MHz oscillator in the pixel. The generated fast clock periods are counted by a 4 bit counter until the next rising edge of a chip wide 40 MHz clock stops the local oscillator and enables a 12 bit counter. The latter counts the number of

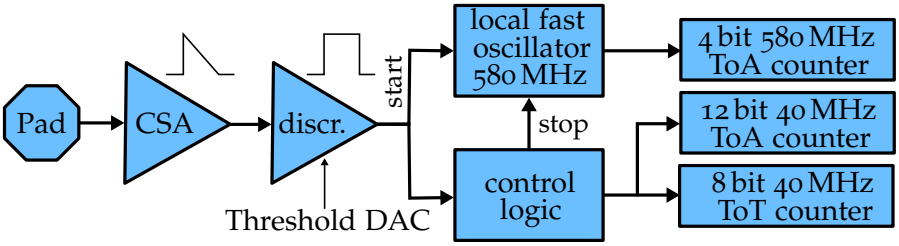

Figure 8.4: Block diagram of the GOSSIPO-3 pixel electronics.

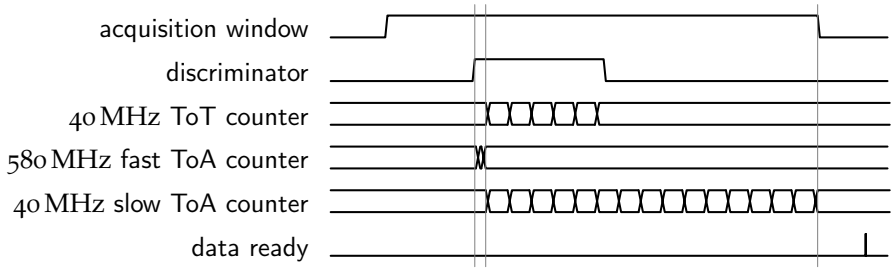

Figure 8.5: Timing diagram of GOSSIPO-3. The ToA measurement is executed by two counters running subsequently.

slow clock cycles until the chip wide common stop signal is received. Dividing the number of fast and slow clock counts n_{fast} and n_{slow} by the corresponding frequencies f_{fast} and f_{slow} allows to calculate the arrival time $t_{arrival}$ of the hit:

$$t_{arrival} = t_{shutter} - \left(\frac{n_{fast}}{f_{fast}} + \frac{n_{slow}}{f_{slow}} \right). \tag{8.1}$$

As in case of the Timepix ASIC, $t_{shutter}$ denotes the width of the acquisition window. In case of very late hits, the ToT counting might last longer than the acquisition window. Thus, the data is available only a short time after the window is closed.

Since the local fast oscillators are operated only for time intervals shorter than one slow clock cycle (25 ns), neither synchronization nor long term stability are of importance.

8.1.2.1 *Local Fast Oscillator*

As indicated in figure 8.6, the local fast oscillators are made of nine daisy chained inverters. The enable signal controls the circuit by activating the feedback loop.

The performance of any device implemented on a micro chip is strongly dependent on the exact conditions during the production process and the quality of the lithography masks. Even small deviations from the standard conditions can result in variations of the device characteristics.

Monte Carlo simulations where used to investigate the pixel to pixel variation of the oscillation frequency on one die. The results

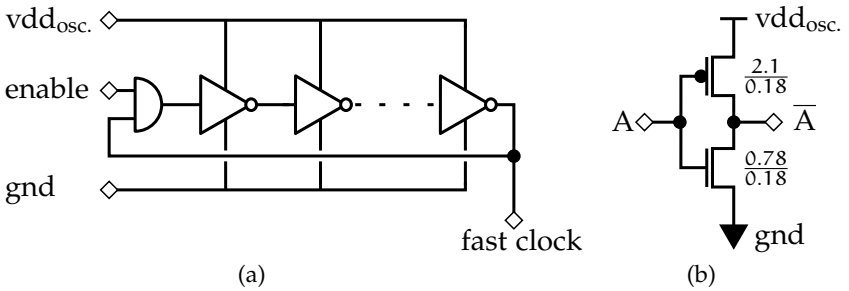

(a) (b)

Figure 8.6: a) Schematic of the local fast oscillator placed in each pixel. Nine inverters are daisy chained in total.
b) Each inverter is made of a p- and a n-MOSFET. Transistor dimensions W/L are given in µm.

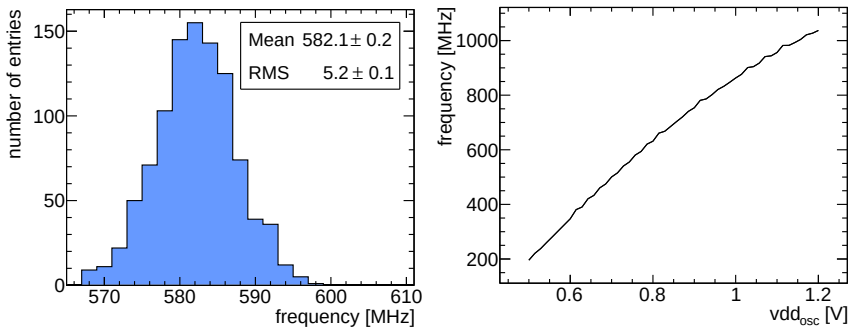

(a) (b)

Figure 8.7: a) Fequency spread of the local oscillators on one die (Monte Carlo simulation). The RMS is only 5 MHz.
b) Simulated oscillation frequency of the local fast oscillators in dependence of the supply voltage. Under nominal conditions the target frequency of 580 MHz is reached at vdd$_{osc.}$ = 760 mV.

are shown in figure 8.7a. Based on these simulations, it is expected that, on one chip, the oscillation period varies only by 10 ps within 3σ of the distribution.

While the frequency mismatch on one die is acceptable, the variations between different chips or even wafers are worse. The oscillation frequency in the fast process corner is doubled with respect to the slow process corner.[1] Necessarily, theses variations have to be compensated by tuning.

The oscillation frequency is not only defined by the number of daisy chained inverters, but also by their driving strength. The latter can be regulated by the supply voltage. As shown in figure 8.7b, the oscillation frequency is nearly linearly dependent on the supply voltage. It is found that the implemented oscillators reach the nomi-

1 In the fast (slow) process corner, all process parameters are shifted such that the switching speed becomes maximal (minimal).

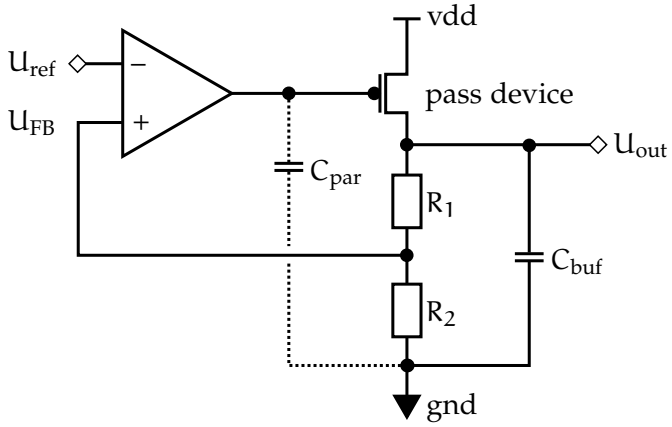

Figure 8.8: Generic LDO schematic.

nal oscillation frequency in all process corners if the supply voltage vdd_{osc} can be adjusted between 0.6 V and 1.1 V.

The current consumption of a single oscillator is always below 100 µA. An average occupancy of 0.37 % (240 pixels) per acquisition window is expected for a fully operational GOSSIP-ASIC with 256 × 256 pixels. A peak occupancy of 0.67 % (440 pixels) will never be exceeded. Therefore, the supply rail is exposed to a current step of 24 mA respectively 44 mA, if all hits are detected at the same time. Depending on the quality of the power supply, this causes voltage drops which in turn can degrade the frequency stability of the local fast oscillators. The time measurement based on the local oscillators remains acceptable, as long as the deviations from the nominal period, integrated over one slow clock cycle, are less than one fast clock cycle. Hence, frequency drops up to 20 MHz are acceptable. Taking into account the voltage control characteristics of the oscillators, this translates to an acceptable voltage drop of $\Delta vdd_{osc} \approx 20\,mV$ lasting for 25 ns. This limit may be exceeded, if the voltage drop lasts less than one slow clock cycle.

8.1.3 *Low Drop Out Regulator*

A Low Drop Out regulator (LDO) is a variable voltage source. It can be used as power supply in applications with changing load conditions. A LDO can be operated at very small differences between the input and the output voltage (drop-out voltage), e.g. $U_{out} = 1.1\,V$ is achievable at $vdd = 1.2\,V$. On the GOSSIPO-3 demonstrator, it is tested whether a LDO can fulfill the requirements introduced by above described ToA measurement technique on a future full-size pixel chip with 256 × 256 pixels.

The generic circuit of a LDO is drafted in figure 8.8. The error-amplifier is controlled by U_{ref} which is externally set. The output of

the error-amplifier is fed back to the input via the pass device and a voltage divider formed by resistors R_1 and R_2. The pass device is not necessarily a p-MOSFET, but could be any other voltage controlled current source, e.g. a bipolar transistor, a n-MOSFET or a Darlington pair. However, the lowest drop-out voltages are achieved with p-channel devices [181].

In good approximation, virtually no current is sunk or sourced by the input nodes of the error-amplifier. Therefore, the current through R_1 equals the current through R_2. Besides, due to the negative feedback, both input nodes are at the same potential. Thus,

$$I_R = \frac{U_{FB}}{R_2} = \frac{U_{ref}}{R_2} \tag{8.2}$$

and

$$I_R = \frac{U_{out}}{R_1 + R_2} \tag{8.3}$$

holds. Combination of both gives the DC-transfer function of a LDO:

$$U_{out} = U_{ref} \cdot \left(1 + \frac{R1}{R_2}\right). \tag{8.4}$$

In first order, the output voltage is defined only by the reference voltage. Ideally, it is not dependent on the load. Due to the finite gain of the error-amplifier, this is not completely true in reality, c.f. Sec. 8.1.3.2. The slightly more complex frequency dependent transfer function is given in appendix A.

The simulated and measured relation between output and reference voltage are shown in figure 8.9a for the two LDOs implemented on GOSSIPO-3 (c.f. Sec. 8.1.3.1).

The buffer capacitor C_{buf} at the LDO output ensures stability of the circuit. Furthermore, it reduces the magnitude of the voltage drop caused by transient load changes. Although in turn, it increases the settling time of the LDO [182].

8.1.3.1 *LDO Implementation*

Two different LDO designs have been implemented for testing purposes on GOSSIPO-3. These LDOs are identical except for the size of the pass device transistor. Therefore, they are referred to as large and small LDO.

The schematics of the single staged error-amplifiers which control the LDOs are depicted in figure 8.9b. Both LDOs are stabilized by off-chip 22 µF buffer capacitors with a Equivalent Series Resistance (ESR) of roughly 300 mΩ. The voltage dividers are formed by $R_1 = 1.14\,k\Omega$ and $R_2 = 2\,k\Omega$.

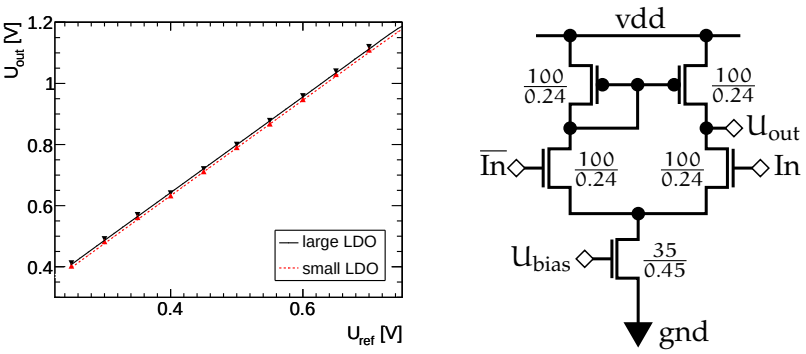

(a) (b)

Figure 8.9: a) The output voltage of both LDOs (c.f. Sec. 8.1.3.1) is linearly dependent on the reference voltage. The measurements (triangles) resemble the values predicted by simulations (lines).
b) Schematic of the error-amplifier controlling the LDO. Transistor dimensions W/L are given in µm.

Large LDO

Neglecting channel length modulation, the current through a saturated MOSFET device is given by:

$$I_{DS,sat} = \mu C_{Ox.} \frac{W}{2L} (U_{GS} - U_{Thr.})^2 . \tag{8.5}$$

Equation 8.5 introduces the mobility of the majority charge carriers μ, the specific capacitance of the gate oxide $C_{Ox.}$, the gate-source voltage U_{GS}, the threshold voltage $U_{Thr.}$ as well as transistor width and length W and L, respectively [183].

The large LDO is designed such that the output p-MOSFET stays in saturation even for $U_{out} = 1.1\,V$ (implying $U_{DS,sat.} \leqslant 100\,mV$) and a load of 44 mA. Fulfilling the design goal, the dimensions of the pass device are chosen to be $W = 48\,000\,\mu m$ and $L = 0.24\,\mu m$. The parasitic gate capacitance is roughly 45 pF.

Small LDO

The period in which a large current is required by the local fast oscillators is shorter than 25 ns. It is followed by several slow clock cycles of inactivity. If the output potential is maintained by the buffer capacitor during the short load periods, it is not necessary to have a huge pass device delivering the whole current. In this case, a small pass device which recharges the buffer capacitor during the quiescent phases is sufficient.

Following this idea, the postulation of a saturated pass device in all operating conditions is dropped for the small LDO and the size of the p-MOSFET is reduced to $W/L = 2000\,\mu m/0.24\,\mu m$.

The output voltage is not only buffered by the off-chip capacitor, but also by a 42 pF capacitor on the die. This capacitor introduces virtually no ESR. Furthermore, the capacitance seen by the error-amplifier is reduced by a factor of 24. Both, reduction of the parasitic gate capacitance and implementation of the very low ESR on chip buffer capacitor, enhances the transient response of the small LDO and enables the application in scenarios where the maximum load occurs with a low frequency only.

8.1.3.2 *LDO Performance*

The error-amplifier in each LDO is biased with about 100 µA. The quiescent current running through the voltage divider is roughly 350 µA if the output voltage is at the maximum value of 1.1 V. Therefore, the total power consumption of each LDO itself is less than 0.5 mW in all operating conditions.

Transient Response

Results shown in the following are obtained with the maximal output voltage of 1.1 V. This is the most demanding operating point for the LDOs, since the drop-out voltage is minimal. This minimizes the transconductance of the pass device, the LDO gain and the closed-loop bandwidth.

Switchable resistive loads, located on the test-board allow to test the LDO performance under almost realistic conditions. They are activated by a discrete n-MOSFET, which is controlled either by the FPGA on the S3Board or directly by an external signal.

When the LDOs had been designed, the most critical question was whether the reaction to fast load changes would be fast enough, c.f. Sec. 8.1.2.1. The magnitude of a voltage drop ΔV caused by a fast load change ΔI is given by:

$$\Delta V = \frac{\Delta I}{C_{buf}} \Delta t_1 + \Delta U_{ESR}, \tag{8.6}$$

where C_{buf} is the buffer capacitance and ΔU_{ESR} the voltage drop caused by the ESR of this capacitor. The time needed by the LDO to compensate for the load change is labeled Δt_1. Neglecting internal slew rates, Δt_1 is given by the inverse of the LDO closed-loop bandwidth [184].

The transient response to a load change of 40 mA is shown in figure 8.10 for both implemented LDOs. The results obtained from simulations based on the netlist extracted from the LDO layout are in qualitative agreement with the measurement results. However, quantitative differences between the predicted and the observed response function are obvious. The time needed to compensate for the load change measures several nanoseconds in reality, while less than 1 ns is expected from simulations.

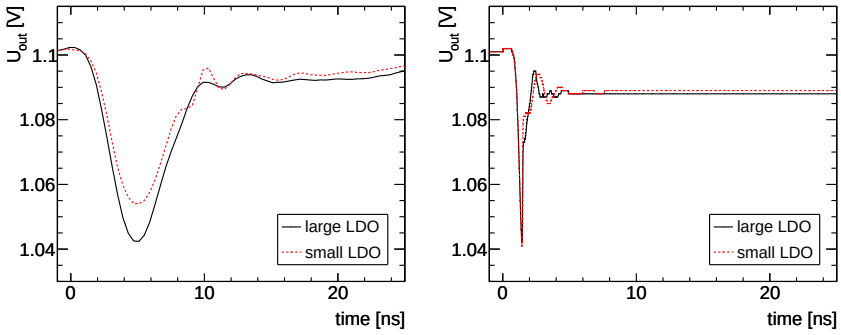

(a) (b)

Figure 8.10: a) Measured LDO response to a 40 mA load step at U_{out} =1.1 V. b) Simulated LDO response to a load step at similar conditions.

These differences can be caused by several effects:

- Parasitic devices might have a larger influence than expected. This would reduce the effective bandwidth of the LDOs and degrade the transient response.
- Constant inductance and series resistivity have been assumed for the buffer capacitors in the simulations. In reality, they come with a frequency dependence.
- Finally, a direct dependence of the response function on shape and rise time of the load step was found. The n-MOSFET used as load switch on the test-board can not be modeled exactly since the transistor characteristics are not known.

Although all of these effects have been investigated in post layout simulations, it was not possible to exactly reproduce the measurement results. The LDOs are especially rather robust against parasitic RC-elements in the error-amplifier or the feedback loop.

In the end, the measurement results are investigated for evaluation of the LDOs. Although these are worse than predicted by simulations, the performance of both LDOs is sufficient for application as power supply for the local fast oscillators. This is emphasized by the results shown in figure 8.11. Here, the time needed by the LDOs to settle within 2 % of the target potential of 1.1 V is shown together with the magnitude of the voltage drop for different load steps. Both LDOs violate the 20 mV ($\approx$2 % for U_{out} = 1.1 V) limit given by the control characteristics of the local fast oscillators only for nanoseconds.

When exposed to a maximum load step of 44 mA, the large and the small LDO exceed the defined limit for only 7 ns and 8 ns, respectively. The observed magnitude of the voltage drop is roughly 70 mV for the large and 55 mV for the small LDO. The control characteristics of the local fast oscillators allow a continuous voltage drop of these sizes for

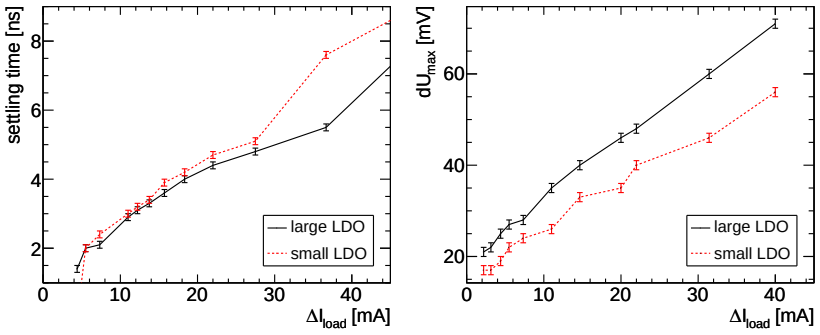

(a) (b)

Figure 8.11: a) Time needed by the LDOs to settle within 2 % of the nominal output voltage of 1.1 V.
b) Maximal magnitude of the voltage drop in response to a load step at U_{out}=1.1 V.
Both plots show measured data.

roughly 8 ns. Taking into account the shape of the transient response function, both LDOs stay within the specification.

The local fast oscillators are stopped synchronously with the first rising edge of the global slow clock. Therefore, the LDO response to negative load steps has no influence on the performance of the local fast oscillators. Consequently, it is neither shown nor discussed in detail. However, it should be mentioned that both LDOs require some time ($\mathcal{O}(10\,\text{ns})$) to fully recover the output potential after exposure to a load step of 44 mA. If the frequency of the load steps does not allow a full recovery of the quiescent output potential, the potential will eventually drop down to the potential achieved with a DC load.

Power Supply Rejection Ratio

Besides sudden load changes, distortions on the LDO power supply rail can result in variations of the output potential. Commonly, the suppression of such distortions is labeled power supply rejection ratio (PSRR). It is dependent on the frequency f of the power supply ripple and defined as:

$$\text{PSRR}(f) = 20\log\frac{\Delta\text{vdd}(f)}{\Delta U_{out}(f)}. \tag{8.7}$$

For $f \to 0$, the PSRR is usually called line regulation. As a LDO keeps the output potential stable, it is easy to understand that distortions on the power supply are compensated in general: LDOs with a good transient response come with a good PSRR and vice versa.

In [185], the PSRR of an LDO is expressed by:

$$\text{PSRR}(f) = 20\log\frac{A_{FB}(f)}{A_{IO}(f)}, \tag{8.8}$$

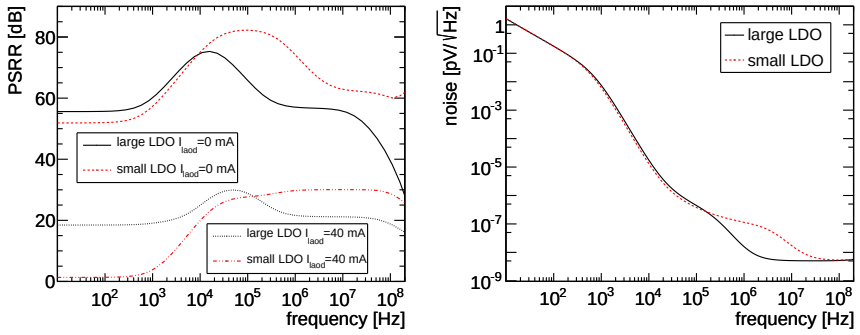

(a) (b)

Figure 8.12: a) Simulated Power Supply Rejection Ratio (PSRR) of the LDOs at $U_{out} = 1.1\,V$ under different load conditions.
b) Simulated noise frequency spectrum for both LDOs at an output potential of 1.1 V.

where A_{FB} denotes the gain of the feedback loop and A_{IO} the gain from the LDO supply (vdd) to the LDO output (U_{out}). The output impedance of the LDOs drops with rising load, since the current is proportional to the conductance of the pass device ($I \propto g_{DS}$). This causes a reduction of the gain in the feedback loop. At the same time, the dominant pole in the transfer function is shifted to higher frequencies. Hence, increasing the load results in a decreased PSRR at low frequencies and in an increased PSRR at higher frequencies. A comparable effect occurs if the pass device leaves the region of saturated operation. The resulting gain reduction causes also a PSRR degradation.

The PSRR of both LDOs is rather good when no load is applied, see figure 8.12a. However, the PSRR degrades when the load is increased. In case of the small LDO, low frequency power supply variations are seen nearly without any damping at the output for a load current of 40 mA since the pass device is no longer saturated. The large LDO in comparison maintains a PSRR of 18 dB even when it is loaded with 40 mA.

Electronic Noise

Usually, noise in a LDO is given as output-referred noise. It is calculated by referring the noise sources to the LDO input and multiplying them with the LDO gain afterwards [186].

The resistors in the feedback loop emit mainly thermal noise. The thermal noise-power density $S_{U,therm.}$ is given by:

$$S_{u,therm.} = \frac{d\langle u^2_{therm.}\rangle}{df} = 4k_B TR. \tag{8.9}$$

The frequency f, the noise amplitude $u_{therm.}$, the Boltzman constant k_B and the resistor value R have been introduced here. When small

signals are investigated, R_1 and R_2 are seen as parallel combination at the input of the error-amplifier. Their noise contribution is directly amplified by the LDO.

When referred to the input node, any noise originating from the error-amplifier is divided by the gain of the error-amplifier. The latter is large in comparison with the LDO gain. Hence, noise originating from the error-amplifier appears damped at the LDO output.

Noise originating from the pass device contributes directly to the noise at the LDO output. It undergoes neither damping nor amplification. Thus, the pass device is only a minor noise contributor.

Neither the load nor the buffer capacitor have a direct effect on the LDO noise. However, both influence the closed-loop gain of the LDO as seen in equation A.1. In turn, this influences the LDO output noise.

Summing up, it is seen that the devices connected directly to the LDO input cause the most output noise. The noise can be effectively reduced if small resistors are used in the feedback. However, this comes with the cost of an increased quiescent current. Noise originating from the reference voltage can be suppressed by a low-pass filter at the input.

The simulated noise frequency spectrum of both LDOs is given in figure 8.12b. The integrated noise is roughly 80 pV_{RMS} for either LDO. Obviously, the performance of the local fast oscillators is not affected by LDO noise.

Load Regulation

The DC performance of the LDOs is not of much interest in general since the LDOs are only exposed to short load steps. However, the load regulation illustrates the LDO performance in applications where the maximum load occurs with frequencies that disallow a recovery of the quiescent output potential between the load periods.

Due to the limited gain of the error-amplifier, the LDO output potential is not totally independent of the load current. Following equation 8.5, the maximally available error-amplifier output potential corresponds to the maximal current that can be drawn from the pass device. If more than this current is drawn from the pass device, secondary effects like drain-induced barrier lowering and channel length modulation become important [183, 187]. Both result in a mild increase of the drop out voltage. Eventually, the pass device is pushed out of the region of saturated operation, and the LDO output resistance rises drastically. In turn, this causes a severe drop in the output potential.

For both LDOs, the achieved output potential for different DC-loads is shown in figure 8.13. The quiescent output potential is 1.1 V in either case.

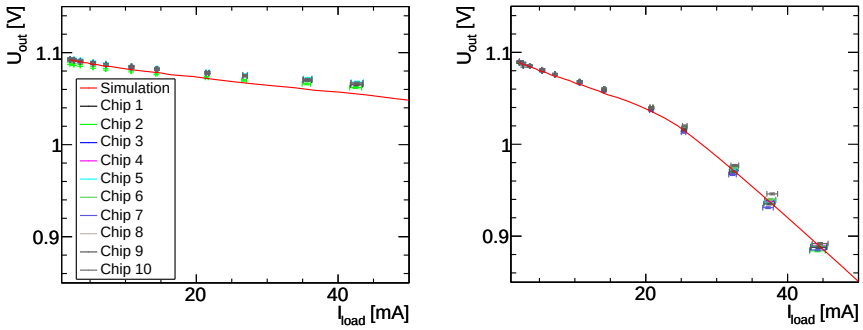

Figure 8.13: Load regulation of (a) the large and (b) the small LDO. The solid line represents simulation results. Measurements for several chips are shown as data points.

The measurement results for different chips are close to the values predicted by simulations. Since the pass device of the large LDO stays in saturation even for large loads, the output potential drops only slowly with increasing load. In contrast to the pass device of the large LDO, the pass device of the small LDO leaves the region of saturated operation at some point. In consequence, the output potential drops drastically.

8.1.3.3 *LDO Bottom Line*

It has been shown that both LDOs come with negligible output noise and a good PSRR. The PSRR of the small LDO is degraded if the load forces the pass device out of saturated operation. For the same reason, the performance of the small LDO is exceeded by the large LDO in DC applications.

The transient response of both LDOs is acceptable and allows an application as power supply for the fast oscillators located in each pixel of a final ASIC. However, it has to be noted that a load step exceeding $\Delta I = 44\,mA$ will degrade the precision of the ToA measurement.

Some undesirable properties have been revealed also. First of all, the need for a large buffer capacitor, which can be realized only off-chip, has to be mentioned. Furthermore, the pass device requires a huge area on the die: $0.058\,mm^2$ and $0.012\,mm^2$ for the large and the small LDO, respectively.

Obviously, it is necessary to introduce a dedicated powering network to control the local oscillators via the supply voltage. In order to reduce the voltage drop along the wiring, the conductive path has to be wide. This complicates the routing in a full featured chip with a large pixel matrix. Besides, it is necessary to tune the frequency of the local oscillators manually for each chip.

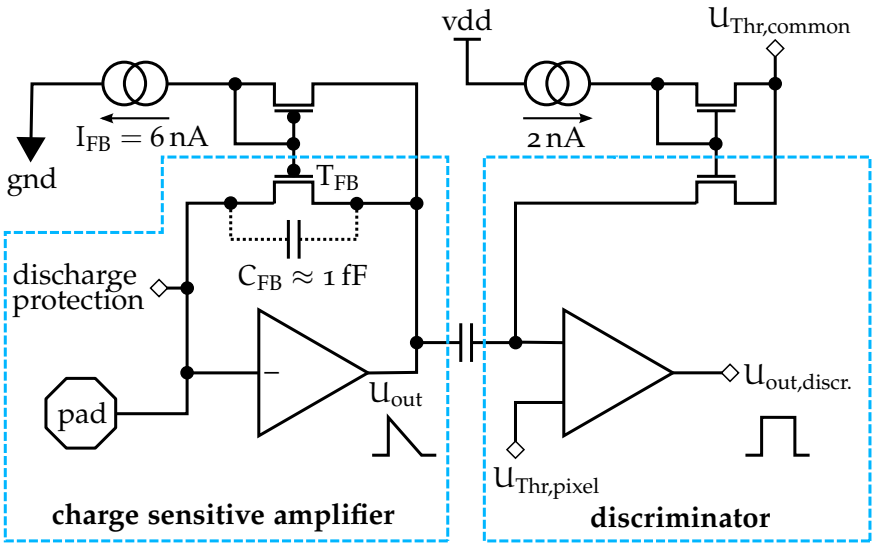

Figure 8.14: Schematic of the GOSSIPO-3 front-end, consiting of a charge sensitive amplifier and a discriminator. The parasitic capacitance of the transistor T_{FB} is used as feedback capacity.

It is concluded, that the presented solution for high-precision time measurements is feasible but not ideal. Consequently, a modified approach is followed up in the subsequent test-chip GOSSIPO-4, see section 8.2.

8.1.4 *Front-End*

The GOSSIPO-3 front-end, designed by A. Kruth [188] and V. Gromov [189], was first presented in [178]. It consists of a charge sensitive amplifier which is AC-coupled to a discriminator, see figure 8.14. The threshold is globally defined by $U_{Thr,common}$ and individually fine tuned for each pixel by $U_{Thr,pixel}$.

In first order, the CSA output potential U_{out} is given by the ratio of the injected charge Q_{in} and the feedback capacitance C_{FB}:

$$U_{out} = \frac{Q_{in}}{C_{FB}}. \tag{8.10}$$

The basic idea in the GOSSIPO-3 front-end is to maximize the charge gain by usage of a minimal feedback capacitance. In fact no dedicated feedback capacitance is implemented at all. The only device placed in the feedback path is a p-MOSFET (T_{FB}) operated as floating current source. The parasitic capacitance between drain and source of this device is used for charge integration. According to simulations, this capacitance measures 1 fF. Therefore, a charge gain of 0.16 mV/e is achieved.

The constant discharge-current through the transistor T_{FB} results in a linear drop of the output signal allowing precise ToT charge

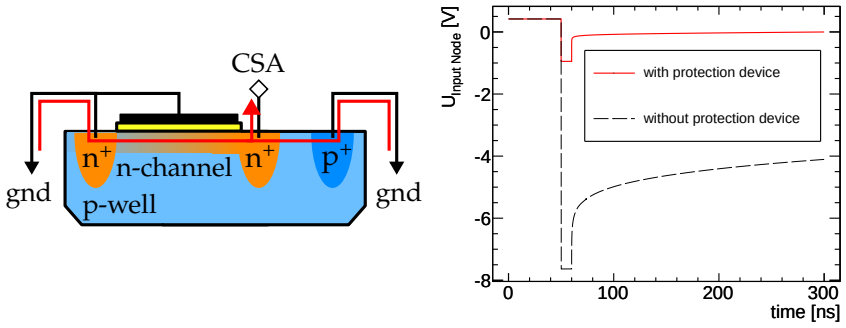

(a) (b)

Figure 8.15: a) Schematic of the protection device realized in GOSSIPO-3. The potential of the CSA input node is usually $\approx 0.4\,V$. In case of a HV-breakdown, it drops below ground potential. The red arrow indicates the current flowing in this case.
b) Time dependent simulation of the CSA input potential for a charge injection of 8 pC with and without the protection device.

measurements. When the potential difference between CSA in- and output is close to 0 mV, T_{FB} appears as 30 MΩ resistor.

For analysis purposes, the CSA signal is made available off-chip by means of a unity-gain buffer connected to a wire bond pad.

8.1.4.1 *Discharge-Protection*

In case of a discharge between the InGrid and the readout electronics, a huge amount of charge is injected into the pixels. This causes a severe voltage drop at the input node and can eventually destroy the chip. The amount of injected charge is reduced down to a few picocoulomb if a high-resistive layer is placed between the InGrid and the chip [43, 190, 191], c.f. Fig. 8.1b. Nevertheless, a HV-breakdown may still damage the input MOSFET of the CSA.

For improved protection of the GOSSIPO-3 front-end, a grounded-gate n-MOSFET is connected to the CSA input node. As described in [192], a grounded-gate n-MOSFET is made of a n-MOSFET with bulk, drain and gate connected to ground potential, see figure 8.15a. In case of a discharge, both the p-n junction and the inversion layer in the MOSFET drain excess charges.

The simulation of a HV-breakdown is shown in figure 8.15b. The capacitance between a pixel and the protection layer is estimated to be roughly 20 fF. Thus, the total charge injected by a discharge from −400 V will be −8 pC, distributed over a spark duration of about 10 ns [193]. The simulation shows that even a small protection device with $W/L = 1\,\mu m/0.24\,\mu m$ prevents voltages less than −1 V at the input node in case of such a HV-breakdown. During normal operation, the n-MOSFET introduces only a negligible leakage current of

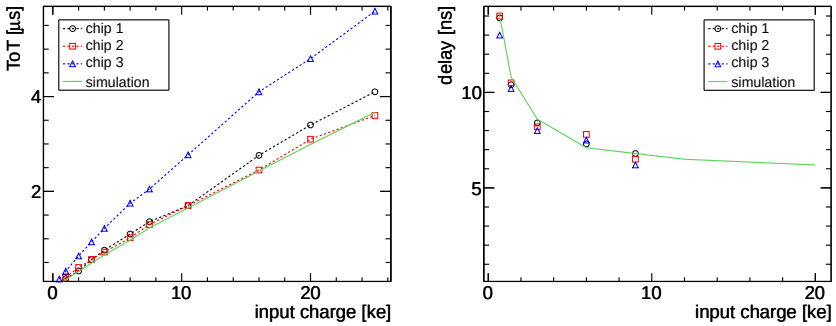

(a) (b)

Figure 8.16: a) ToT for different input charges (simulation and measurements).
b) Time needed from charge injection to discriminator response.

250 pA. The parasitic capacitance seen at the CSA input is less than 2 fF [178].

8.1.4.2 *Front-End Performance*

The measurements on the front-end performance have already been published in [179]. Depending on the input charge, the GOSSIPO-3 front-end features a response time less than 20 ns. Nevertheless, it consumes only a few µW per pixel.

The off-chip RMS noise measures 4 mV. Taking into account the charge gain of 16 mV/e, this translates to an Equivalent Noise Charge (ENC) of only 25 e.

Measurements show that the charge gain undergoes negligible variations from chip to chip. The feedback current on the other hand varies. Therefore, the measured Time over Threshold (ToT) varies up to a factor of two between different chips, see figure 8.16a. Investigating the effects of process variations by means of Monte Carlo simulations explains these results. It is found that process variations influence especially the transistor T_{FB} since the transistor length is close to the minimal feature size. This results in a bad quality of the feedback current mirror, thus causing bad reproducibility of the feedback current. Enlarging the feedback transistor would decrease the charge gain of the CSA since the parasitic capacitance is increased simultaneously. A trade off between mismatch, charge gain and noise performance has to be found.

The measured delay between charge injection and the discriminator response is depicted in figure 8.16b. For large input charges, this delay is about 6 ns. Due to the time walk effect, the delay rises for small input charges.

Post-layout simulations have shown that the pad drivers, implemented to make the discriminator signal available off-chip, contribute

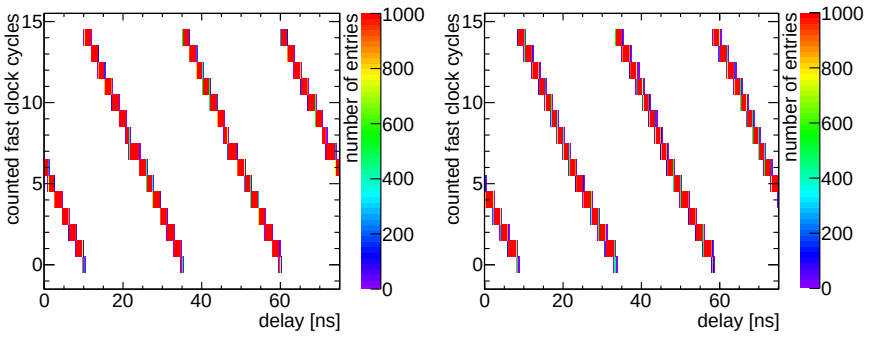

(a) (b)

Figure 8.17: Fast clock cycles counted for test-pulses sent at different times (a) directly to the discriminator and (b) through the complete front-end.

largely to the observed delay. In a final chip, such pad drivers are not needed since the signal is processed directly in the pixels. Without the pad drivers, simulations predict a reduced delay of roughly 2 ns for large input charges.

8.1.5 *Time to Digital Conversion*

Test and characterization of the TDC have been performed at NIKHEF. The results summarized below have already been published in [179] and [194].

For TDC characterization, test-pulses have been sent with delay times from 0 ns to 75 ns in 0.1 ns steps (1 000 pulses per step) to the analog and the digital pixel. The results of this delay scan are shown in figure 8.17.

The oscillation frequency of the fast oscillator is not exactly matched to the slow clock frequency. Thus, the rising edge of the slow clock arrives in the beginning of the last fast clock counting bin. In consequence, this last bin is significantly shorter than the others.

Even when the last bin is excluded from the analysis, it is found that the width of the counting bins is not uniform. The bin size varies by 18 % in case of the digital and by 12 % in case of the analog pixel. The larger spread in case of the digital pixel is caused by the central bins. These show a significant deviation from the nominal value. It appears that this deviation is caused by the falling edge of the slow clock. It is not fully understood yet why this effect occurs only in the digital pixel and not when the full signal chain is tested. The reason is found most likely in the layout, especially the different ground connections.

Finite signal rise times and noise cause a jitter in the transition region measuring a few hundred picoseconds between two different

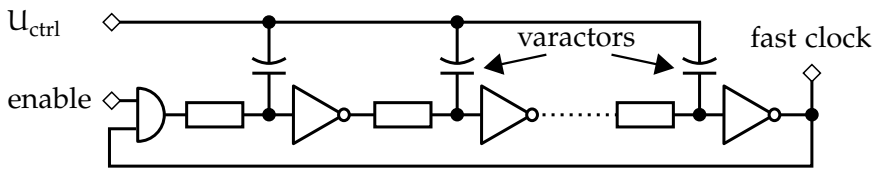

Figure 8.18: Schematic of the local fast oscillator implemented in the super pixels of GOSSIPO-4 and Timepix3.

counter values. Naturally, the transition region in the analog pixel is larger than in the digital pixel.

Despite the minor limitations mentioned above, the presented ToA measurement technique is applicable and allows time resolutions in the order of a few nanoseconds. Therefore, the concept is followed up in the subsequent ASICs for gaseous detector readout.

8.2 GOSSIPO-4

As shown in previous sections, the general usability of the ToA measurement technique described in section 8.1.2 could be verified with GOSSIPO-3. However, as stated in section 8.1.3.3, it is recognized that the need for a large LDO with an external buffer capacitor together with a dedicated powering network for the local oscillators in the pixels is not ideal. Consequently, a different design of the local fast oscillators is tested on GOSSIPO-4. The measurement scheme itself remains unchanged.

A schematic of the modified oscillator is shown in figure 8.18. Adjusting the effective capacitance in the RC-elements by U_{ctrl} allows to tune the oscillation frequency. Distribution of the control voltage U_{ctrl} across the pixel matrix is much easier than in case of GOSSIPO-3 since it is an unloaded and almost static potential. It is created by a Phase Locked Loop (PLL), which is derived from the FE-I4 PLL described in [195].

Other circuits implemented on GOSSIPO-4 for testing purposes are described in some detail in [194].

8.3 TIMEPIX3

Some of the circuitry of Timepix3 is derived from the recently finalized Medipix3 ASIC [196]. Therefore, the Timepix successor is named Timepix3, the label Timepix2 is skipped.

Timepix3 will be produced during 2013, a first outline of the ASIC is presented in [197]. Each of the 256×256 Timepix3 pixels measures 55×55 µm² and consists of a CSA, a single threshold discriminator and a counting logic.

The ToA is measured with the circuitry verified on GOSSIPO-4. The locally created 640 MHz fast clock is counted by a 4 bit counter. A

counter with 14 bit depth counts the cycles of a global 40 MHz clock. Thus, ideally a dynamic range of 409.6 µs and an precision of 1.56 ns can be achieved.

The charge measurement is executed with a dedicated 10 bit ToT counter driven by the global 40 MHz clock. The maximal detectable charge is 500 000 e with a resolution of roughly 500 e. Reduction of the feedback current allows an enhanced charge resolution, though with a reduced range only.

The pixels are organized in double columns. Eight pixels form a so-called super pixel. The pixels of one super pixel share one local oscillator and some control logic. Depending on the configuration, the pixels are sensitive to positive or negative input charges. The predicted ENC is roughly 75 e. The peaking time of the CSA is $\leqslant$ 25 ns, the discriminator response time less than 2 ns.

It is either possible to operate the chip in a shutter controlled mode with a zero suppressed readout at the end of the shutter or with a continuous sparse readout. In the latter case it is aimed to have a double hit resolution of 375 ns.

Eight LVDS (Low Voltage Differential Signal) data lines, each providing a data rate of 640 Mbit/s, are foreseen for the readout. The data stream is transferred 8b/10b encoded which leads to a total transfer rate of roughly 85 pixel/µs.

8.4 SUMMARY

Based on a two level counting scheme, a high-precision TDC without the need for a power consuming high-frequency clock network is tested on the demonstrator ASIC GOSSIPO-3. The fast clock, providing high TDC accuracy, is created directly in the pixel by an oscillator made of daisy-chained inverters. A LDO allows for control of the oscillation frequency by regulation of the power supply voltage.

Both LDOs tested on GOSSIPO-3 meet the requirements defined by the oscillator characteristics and the peak occupancy expected for a full featured pixel chip. Nevertheless, this approach is discarded since it imposes the need for a large off-chip buffering capacitor. Besides, it is difficult to accurately distribute the tuned supply voltage to the oscillators in the pixels of a large chip.

Consequently, the oscillators operated in the pixels of the subsequent test-chip (GOSSIPO-4) are not controlled by the power supply voltage, but by a static potential which is automatically tuned by a PLL. This improved and validated approach is followed up eventually by Timepix3, the full featured Timepix successor.

CONCLUSION AND OUTLOOK

Both the large number of recorded track points and the low material budget make a TPC the ideal central tracking detector for a particle-flow-optimized experiment at a future linear collider. The desired single-point resolution of better than 100 µm in the xy-plane can be achieved only with modern gas amplification devices, namely GEMs or Micromegas. The charge collecting anode plane necessarily exploits the high granularity of these structures. Pads of a few square millimeters size, which are usually employed for charge collection, can be replaced by the bare pixels of a CMOS readout chip. The potential of this approach was investigated in this thesis.

A versatile gas mixing system and a TPC prototype with pixel readout and 26 cm drift length have been set up. A Timepix ASIC, featuring 256×256 pixels with a pitch of 55 µm, has been placed as readout device in a central position underneath a stack of three standard CERN GEMs. The bare bump-bond pads of the individual pixels, originally foreseen for interconnection with a silicon sensor, act as charge collecting anode pads.

After improvement of the reconstruction and analysis algorithms, the MarlinTPC framework has been employed for analysis of a dataset recorded in a cosmic-ray test-stand with a mixture of 70 % He and 30 % CO_2 as drift gas. Techniques for time walk correction and charge calibration of the recorded data have been presented.

The single-point resolution of the pixel TPC is predetermined by the intrinsic detector resolution as well as the single electron diffusion which is dominant after a few centimeters of drift. The intrinsic longitudinal single-point resolution is limited by the accuracy of the hit arrival time measurement which is predetermined by the 55 MHz counting clock of the TDC. Besides, it suffers from a residual time walk effect. Eventually, the intrinsic longitudinal single-point resolution is about 100 µm. The intrinsic transversal single-point resolution of about 40 µm is limited by the pitch of the GEM holes. In fact not only the projection of the GEM pattern is resolved by the pixel chip, but it is even possible to investigate the properties of electron avalanches triggered by individual primary electrons.

Because of the transversal diffusion, mean charge and area of the detected charge depositions are dependent on the drift distance of the parent primary electrons. These dependencies are described by heuristically determined equations. In average, individual primary electrons result in charge clouds of about 2×10^5 electrons, distributed over 63 pixels respectively 0.19 mm^2.

The sensitivity to individual primary electrons allows not only for the measurement of the specific energy loss by mere counting of the detected charge depositions, but also for the observation of so-called delayed electrons. Interplay of attachment and detachment processes has been investigated as possible delay mechanism but could not be established conclusively.

After tuning the unknown parameters, the results of the newly developed GEM TPC simulation are generally in agreement with the data. In future, a more detailed model of the charge clouds will further improve the accuracy of the simulation.

The high granularity of the pixel readout is both a blessing and a curse. On the one hand, it allows for a good spatial resolution and other remarkable features, as the sensitivity to single primary electrons and the possibility to resolve characteristics of individual charge clouds. On the other hand, it necessitates a large gas gain, which in turn fosters ion backdrift and might prevent stable operation.

Small modifications on the presented setup, which reduce the number of pixels hit by an electron cloud, would enable an operation with a lower gas gain. Obviously, this can be achieved if larger pixels are used for charge collection. Alternatively, the diameter of the charge cloud emerging from the GEM stack can be reduced – either by reduction of the gaps in the GEM stack, or by application of a strong magnetic field which would result in a reduced transversal diffusion between the GEMs. These modifications might be easily investigated with the newly developed simulation of the pixel TPC before they are applied.

Once they are technically advanced enough, Micromegas-like InGrid devices might be used as replacement for the GEM stack. Hence, intrinsically reducing the ion backdrift. Besides, this would further enhance the intrinsic transversal single-point resolution. The currently used Timepix chip, however, does not match the needs of such a setup, especially due to the limited accuracy of the arrival time measurement. The latter is significantly degraded by the time walk effect which can not be compensated for if only individual pixels are activated. This is taken as motivation for development of the Timepix3 ASIC featuring high TDC accuracy and simultaneous charge and time measurements.

Although the proof that this technique is feasible also for TPCs with large readout areas is pending, it can be concludingly stated that direct charge collection with the bare pixels of a CMOS readout ASIC underneath a highly segmented gas amplification stage meets the requirements of a linear collider TPC.

Dann promovier ich halt einen Tag später.
(unknown PHD student)

ACKNOWLEDGMENTS

I warmly thank my supervisor Prof. Dr. K. Desch for allowing me to be part of his research group at the University of Bonn. He and all coworkers created always a positive atmosphere, encouraged and supported me in my studies.

I have to thank all former and current MarlinTPC developers for creating the basis I built on for analysis of the pixel TPC data.

The microscopic GEM simulations would not have been possible without the work of H. Schindler and R. Veenhof from CERN. They reacted within shortest times to reported bugs in Garfield++ and willingly shared their wisdom, not only on drift gas physics.

I would like to express my gratitude to my colleagues in the chip design department: M. Karagounis, X. Fang, Y. Fu, A. Kruth, H. Krüger (all University of Bonn), V. Gromov, R. Kluit, F. Zappon (all NIKHEF) and X. Llopart (CERN). They have been available for fruitful discussions and gave me private lessons when necessary.

A

LDO TRANSFER FUNCTION

The transfer function of an amplifier with negative feedback is in general given by:

$$H(f) = \frac{U_{out}}{U_+} = \frac{A(f)}{1 + \beta A(f)} \approx \beta^{-1} \quad (\text{if } A \gg 1). \tag{A.1}$$

U_{out} denotes the output voltage, U_+ the voltage applied at the non inverting input, $A(f)$ the frequency dependent open-loop gain of the amplifier and β the feedback factor.

The schematic of the LDOs realized on the GOSSIPO-3 test-chip are depicted in figure A.1. Here, the feedback factor is: $\beta = R_2/(R_1 + R_2)$. Thus, equation 8.4 is obtained for large open loop gains.

Following [187], the open loop gain for the GOSSIPO–3 LDOs can be calculated:

$$A(f) = \frac{(2g_m^{T1}/g_{DS}^{T3}) \cdot (g_m^{T5}/\tilde{g})}{(1 + f\tau_1)(1 + f\tau_2)}. \tag{A.2}$$

Transconductance and conductance of transistors Ti are denoted by g_m^{Ti} and g_{DS}^{Ti}, respectively. $\tilde{g}$ is given by:

$$\tilde{g} = g_{DS}^{T5} + \frac{1}{R_1 + R_2} + \frac{1}{R_{Load}} \approx g_{DS}^{T5}. \tag{A.3}$$

The poles in the open loop gain of the LDO are located at:

$$\tau_1 = \frac{C_{par.} \cdot g_{DS}^{T5}}{\tilde{g} \cdot g_{DS}^{T3}} \quad \text{and} \quad \tau_2 = \frac{C_{DS}^{T5} + C_{Buf.}}{\tilde{g}}. \tag{A.4}$$

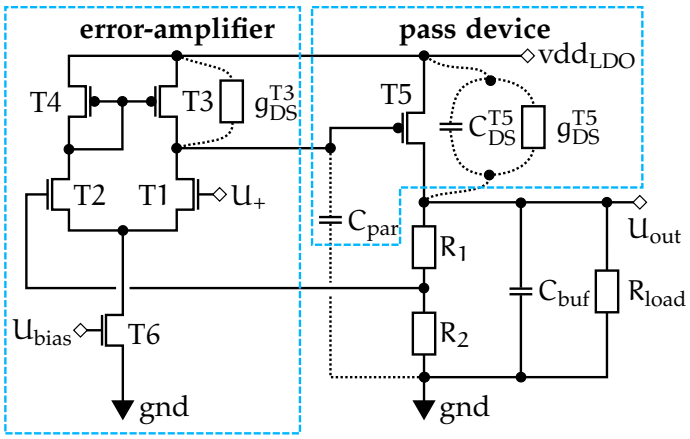

Figure A.1: Detailed schematic of the GOSSIPO–3 LDOs. The relevant parasitics are drawn with dotted wires.

BIBLIOGRAPHY

[1] The ATLAS Collaboration. "Observation of a new particle in the search for the Standard Model Higgs boson with the ATLAS detector at the LHC." In: *Phys. Let. B* 716.1 (2012), pp. 1–29. DOI: 10.1016/j.physletb.2012.08.020.

[2] The CMS Collaboration. "Observation of a new boson at a mass of 125 GeV with the CMS experiment at the LHC." In: *Phys. Let. B* 716.1 (2012), pp. 30–61. DOI: 10.1016/j.physletb.2012.08.021.

[3] I. Brock, T. Schörner-Sadenius, M. Schumacher, et al. "The Higgs Boson: Still Elusive After 40 Years." In: *Physics at the Terascale*. Wiley-VCH, 2011. ISBN: 978-3-527-41001-9.

[4] J. Brau, Y. Okada, N. Walker, et al. *International Linear Collider Reference Design Report*. Aug. 2007. URL: http://www.linearcollider.org/about/Publications/Reference-Design-Report.

[5] H. Braun, R. Corsini, J. P. Delahaye, et al. *CLIC 2008 Parameters*. CERN-OPEN-2008-021, CLIC-Note-764. Oct. 2008. URL: http://cds.cern.ch/record/1132079?ln=de.

[6] A. Roeck, J. Ellis, C. Grojean, et al. "From the LHC to future colliders." In: *Eur. Phys. J. C* 66 (3–4 2010), pp. 525–583. DOI: 10.1140/epjc/s10052-010-1244-3.

[7] H. Aihara, P. Burrows, and M. Oreglia. "SiD Letter of Intent." In: *ArXiv e-prints* (Oct. 2009). arXiv:0911.0006 [physics.ins-det].

[8] ILD Concept Group. *International Large Detector DBD*. 2013. URL: http://ilcild.org/documents.

[9] M.Horiuchi. *ILD illustrations*. URL: http://ilcild.org/documents/mdi/ild-illustrations/tentative-version-as-of-2011-aug.30.

[10] M.A. Thomson. "Particle flow calorimetry and the PandoraPFA algorithm." In: *Nucl. Instr. and Meth. A* 611.1 (2009), pp. 25–40. DOI: 10.1016/j.nima.2009.09.009.

[11] A. Vogel. "Beam-Induced Backgrounds in Detectors at the ILC." DESY-THESIS-2008-036. Aug. 2008. DOI: 10.3204/DESY-THESIS-2008-036.

[12] Y. Giomataris, Ph. Rebourgeard, J.P. Robert, et al. "MICROMEGAS: a high-granularity position-sensitive gaseous detector for high particle-flux environments." In: *Nucl. Instr. and Meth. A* 376.1 (1996), pp. 29–35. DOI: 10.1016/0168-9002(96)00175-1.

[13] F. Sauli. "GEM: A new concept for electron amplification in gas detectors." In: *Nucl. Instr. and Meth. A* 386.2–3 (1997), pp. 531–534. DOI: 10.1016/S0168-9002(96)01172-2.

[14] D. Attié, P. Colas, M. Dixit, et al. "Results with Micromegas modules at LP-TPC." In: *EUDET Memo* 23 (2010). URL: http://www.eudet.org/e26/e28/e86887/e105077/EUDET-Memo-2010-23.pdf.

[15] Matsuda. T. "Results of the first beam test of a GEM TPC large prototype." In: *JInst* 5.1 (2010), P01010. DOI: 10.1088/1748-0221/5/01/P01010.

[16] P. Christiansen, P. Gros, L. Jönsson, et al. "Particle tracking and energy loss measurements with the LCTPC: A comparison to simulation models." In: *EUDET Memo* 36 (2010). URL: http://www.eudet.org/e26/e28/e86887/e107367/EUDET-Memo-2010-36.pdf.

[17] R. Diener, T. Behnke, S. Caiazza, et al. "Beam Test with a GridGEM TPC Prototype Module." In: *ArXiv e-prints* (Feb. 2012). arXiv:1202.6510.

[18] X. Llopart, R. Ballabriga, M. Campbell, et al. "Timepix, a 65k programmable pixel readout chip for arrival time, energy and/or photon counting measurements." In: *Proceedings of the 11th International Vienna Conference on Instrumentation*. Vol. 581. 1–2. 2007, pp. 485–494. DOI: 10.1016/j.nima.2007.08.079.

[19] D. Nygren. "The Time-Projection Chamber - A new 4π detector for charged particles." In: *PEP Summer Study*. PEP-144. Aug. 1974, pp. 58–78. URL: http://lss.fnal.gov/conf/C740805/p58.pdf.

[20] W. Lohmann, R. Kopp, and R. Voss. *Energy Loss of Muons in the Energy Range 1-10 000 GeV*. CERN-85-03. URL: http://cdsweb.cern.ch/search?sysno=000070026CER.

[21] J. Beringer et al. "Review of Particle Physics." In: *Phys. Rev.* D86.010001 (2012). URL: http://pdg.lbl.gov/.

[22] C. Grupen. *Particle Detectors*. Cambridge University Press, 1996. ISBN: 0521552168.

[23] F. Bloch. "Bremsvermögen von Atomen mit mehreren Elektronen." In: *Zeitschrift für Physik - A Hadrons and Nuclei* 81 (5 1933), pp. 363–376. DOI: 10.1007/BF01344553.

[24] K. Nakamura, H. Bichsel, D. E. Groom, et al. "Passage of Particles Through Matter." In: *Review of Particle Physics*. Particle Data Group, 2010. URL: http://pdg.lbl.gov/.

[25] E. Fermi. "The Ionization Loss of Energy in Gases and in Condensed Materials." In: *Phys. Rev.* 57 (6 1940), pp. 485–493. DOI: 10.1103/PhysRev.57.485.

[26] L. D. Landau. "On the energy loss of fast particles by ionization." In: *J. Phys. (USSR)* 8 (1944), p. 201.

[27] H. Bichsel. "A method to improve tracking and particle identification in TPCs and silicon detectors." In: *Nucl. Instr. and Meth. A* 562.1 (2006), pp. 154–197. DOI: 10.1016/j.nima.2006.03.009.

[28] B. Rossi. *High Energy Particles*. Prentice-Hall, 1952. ISBN: 0133873242.

[29] A. Sharma. "Properties of some gas mixtures used in tracking detectors." In: *SLAC-Journal-ICFA* 16.3 (1998). URL: http://www.slac.stanford.edu/pubs/icfa/summer98/paper3/paper3a.html.

[30] Paul Langevin. "Sur la Théorie du Mouvement Brownien." In: *C. R. Acad. Sci. Paris* 146 (1908), pp. 530–533.

[31] D. S. Lemons and A. Gythiel. "Paul Langevin's 1908 paper "On the Theory of Brownian Motion" ["Sur la théorie du mouvement brownien,"]" in: *Am. J. Phys.* 65.11 (1997), pp. 1079–1081. DOI: 10.1119/1.18725.

[32] L. Rolandi, W. Riegler, and W. Blum. *Particle Detection with Drift Chambers*. Particle Acceleration and Detection. Springer Berlin Heidelberg, 2008. ISBN: 978-3540564256. DOI: 10.1007/978-3-540-76684-1.

[33] S. Biagi and R. Veenhof. *Magboltz - transport of electrons in gas mixtures*. URL: http://consult.cern.ch/writeup/magboltz/.

[34] H. J. Hilke. "Time projection chambers." In: *Reports on Progress in Physics* 73.11 (2010), p. 116201. DOI: 10.1088/0034-4885/73/11/116201.

[35] N. Abgrall, B. Andrieu, P. Baron, et al. "Time projection chambers for the T2K near detectors." In: *Nucl. Instr. and Meth. A* 637.1 (2011), pp. 25–46. DOI: 10.1016/j.nima.2011.02.036.

[36] A. Gareis. "Studies of Electron Avalanches in the Vicinity of an Anode Wire with Pad and Pixel-Readout." June 2012. URL: http://lhc-ilc.physik.uni-bonn.de/thesis.php.

[37] F. Sauli. *Principles of operation of multiwire proportional and drift chambers*. CERN, Geneva, 1975–1976.

[38] R. Veenhof and S. Biagi. *Cross sections used by Magboltz 7.1*. 2012. URL: http://rjd.web.cern.ch/rjd/cgi-bin/cross.

[39] V. Lepeltier. "Review on TPC's." In: *Journal of Physics: Conference Series* 65.1 (2007). DOI: 10.1088/1742-6596/65/1/012001.

[40] G. Charpak, R. Bouclier, T. Bressani, et al. "The use of multiwire proportional counters to select and localize charged particles." In: *Nucl. Instr. and Meth.* 62.3 (1968), pp. 262–268. DOI: 10.1016/0029-554X(68)90371-6.

[41] G. Dellacasa, L. Ramello, E. Scalas, et al. *ALICE time projection chamber: Technical Design Report*. CERN-OPEN-2000-183. 2000.

[42] M. Killenberg. "Resolution Studies of a GEM-Based TPC." Dec. 2006. URL: http://web.physik.rwth-aachen.de/~tpcmgr/downloads/theses/dissertation-killenberg.pdf.

[43] M. Chefdeville. "Development of micromegas-like gaseous detectors using a pixel readout chip as collecting anode." Jan. 2009. URL: http://purl.utwente.nl/publications/62815.

[44] Y. Giomataris. "Development and prospects of the new gaseous detector 'Micromegas'." In: *Nucl. Instr. and Meth. A* 419.2–3 (1998), pp. 239–250. DOI: 10.1016/S0168-9002(98)00865-1.

[45] A. Delbart, R. De Oliveira, J. Derré, et al. "New developments of Micromegas detector." In: *Nucl. Instr. and Meth. A* 461.1–3 (2001), pp. 84–87. DOI: 10.1016/S0168-9002(00)01175-X.

[46] S. G. Kappler. "Higgs Search Studies in the Channel $t\bar{t}H$ with the CMS Detector at the LHC and Development of a GEM-based TPC Readout for Future Collider Experiments." IEKP-KA/2004-17. July 2004. URL: http://cds.cern.ch/record/1387975.

[47] B. Sobloher. "Simulationsstudien zu GEM-Folien für die Auslese einer TPC." Mar. 2002. URL: http://web.physik.rwth-aachen.de/~tpcmgr/en/papers.html.

[48] O. Schäfer. "Ein Monitorsystem für Gasbasierte Detektoren am International Linear Collider (ILC)." Jan. 2006. URL: http://adweb.desy.de/~oschfer/Diplomarbeit.pdf.

[49] S. Bachmann, A. Bressan, L. Ropelewski, et al. "Charge amplification and transfer processes in the gas electron multiplier." In: *Nucl. Instr. and Meth. A* 438.2–3 (1999), pp. 376–408. ISSN: 0168-9002. DOI: 10.1016/S0168-9002(99)00820-7.

[50] R. Bouclier, W. Dominik, M. Hoch, et al. "New observations with the gas electron multiplier (GEM)." In: *Nucl. Instr. and Meth. A* 396.1–2 (1997), pp. 50–66. DOI: 10.1016/S0168-9002(97)00648-7.

[51] B. Azmoun, W. Anderson, D. Crary, et al. "A Study of Gain Stability and Charging Effects in GEM Foils." In: *IEEE NSS CR*. Vol. 6. Nov. 2006, pp. 3847–3851. DOI: 10.1109/NSSMIC.2006.353830.

[52] S. Lotze. "Ion Backdrift Minimisation in a GEM-Based TPC Readout." Apr. 2006. URL: http://web.physik.rwth-aachen.de/~tpcmgr/downloads/theses/dissertation-lotze.pdf.

[53] C. Krieger. "Messung von Transferkoeffizienten einer GEM-Auslesestruktur." July 2009. URL: http://lhc-ilc.physik.uni-bonn.de/thesis.php.

[54] R. Menzen. "Charakterisierung von GEMs." Aug. 2010. URL: http://lhc-ilc.physik.uni-bonn.de/thesis.php.

[55] F. Sauli. "Development and applications of gas electron multiplier detectors." In: *Nucl. Instr. and Meth. A* 505.1–2 (2003), pp. 195–198. DOI: 10.1016/S0168-9002(03)01050-7.

[56] S. Duarte Pinto. "Gas Electron Multipliers: Development of large area GEMs and spherical GEMs." BONN-IR-2011-09. July 2011. URL: http://hss.ulb.uni-bonn.de/2011/2742/2742.pdf.

[57] S. Duarte Pinto, M. Villa, M. Alfonsi, et al. "Making spherical GEMs." In: *JInst* 4.12 (2009), p. 12006. DOI: 10.1088/1748-0221/4/12/P12006.

[58] J. Kaminski. "Developing Studies for a Time Projection Chamber at the International Linear Collider." IEKP-KA / 2005-15. July 2005. URL: http://inspirehep.net/record/706650/files/iekp-ka2005-15.pdf.

[59] J. Kaminski, S. Kappler, B. Ledermann, et al. "Study of various anode pad readout geometries in a GEM-TPC." In: *IEEE TNS* 52.6 (Dec. 2005), pp. 2900–2906. DOI: 10.1109/TNS.2005.862797.

[60] P. Colas, I. Giomataris, and V. Lepeltier. "Ion backflow in the Micromegas TPC for the future linear collider." In: *Nucl. Instr. and Meth. A* 535.1–2 (2004), pp. 226–230. DOI: 10.1016/j.nima.2004.07.274.

[61] S. Blatt, M. Giffels, G. Kaußen, et al. "Charge Transfer of GEM Structures in High Magnetic Fields." In: *Nuclear Physics B - Proceedings Supplements* 150.0 (2006), pp. 155–158. DOI: 10.1016/j.nuclphysbps.2004.07.005.

[62] Y. Itikawa. "Cross Sections for Electron Collisions With Carbon Dioxide." In: *Journal of Physical and Chemical Reference Data* 31.3 (2002), pp. 749–767. DOI: 10.1063/1.1481879.

[63] L. G. Christophorou. *Atomic and Molecular Radiation Physics*. Wiley-Interscience, 1971. ISBN: 978-0471156291.

[64] N. E. Bradbury. "Electron Attachment and Negative Ion Formation in Oxygen and Oxygen Mixtures." In: *Phys. Rev.* 44 (11 1933), pp. 883–890. DOI: 10.1103/PhysRev.44.883.

[65] F. Bloch and N. E. Bradbury. "On the Mechanism of Unimolecular Electron Capture." In: *Phys. Rev.* 48 (8 1935), pp. 689–695. DOI: 10.1103/PhysRev.48.689.

[66] A. Herzenberg. "Attachment of Slow Electrons to Oxygen Molecules." In: *The Journal of Chemical Physics* 51.11 (1969), pp. 4942–4950. DOI: 10.1063/1.1671887.

[67] M. Huk, P. Igo-Kemenes, and A. Wagner. "Electron attachment to oxygen, water, and methanol, in various drift chamber gas mixtures." In: *Nucl. Instr. and Meth. A* 267.1 (1988), pp. 107–119. DOI: 10.1016/0168-9002(88)90635-3.

[68] H. Shimamori and H. Hotta. "Mechanism of thermal electron attachment to O_2: Isotope effect studies with $^{18}O_2$ in rare gases and some hydrocarbons." In: *The Journal of Chemical Physics* 81.3 (1984), pp. 1271–1276. DOI: 10.1063/1.447813.

[69] K. Nakamura and D. Karlen. "Particle Detectors at Accelerators." In: *Review of Particle Physics*. Particle Data Group, 2010. URL: http://pdg.lbl.gov/.

[70] D. M. Neumark, K. R. Lykke, T. Andersen, et al. "Laser photodetachment measurement of the electron affinity of atomic oxygen." In: *Phys. Rev. A* 32.3 (Sept. 1985), pp. 1890–1892. DOI: 10.1103/PhysRevA.32.1890.

[71] Kent M. Ervin, Iwona Anusiewicz, Piotr Skurski, et al. "The Only Stable State of O_2^- Is the X $^2\Pi_g$ Ground State and It (Still!) Has an Adiabatic Electron Detachment Energy of 0.45 eV." In: *The Journal of Physical Chemistry A* 107.41 (2003), pp. 8521–8529. DOI: 10.1021/jp0357323.

[72] J. Franck and E. G. Dymond. "Elementary processes of photochemical reactions." In: *Trans. Faraday Soc.* 21.02 (1926), pp. 536–542. DOI: 10.1039/TF9262100536.

[73] Edward U. Condon. "Nuclear Motions Associated with Electron Transitions in Diatomic Molecules." In: *Phys. Rev.* 32.6 (Dec. 1928), pp. 858–872. DOI: 10.1103/PhysRev.32.858.

[74] N. L. Aleksandrov and E. M. Anokhin. "Electron detachment from O_2^- ions in oxygen: the effect of vibrational excitation and the effect of electric field." In: *Journal of Physics B* 44.11 (2011), p. 115202. DOI: 10.1088/0953-4075/44/11/115202.

[75] F. W. Stöver. "Drift Velocity Studies at a Time Projection Chamber for various Water Contents in the Gas Mixture." DESY-THESIS-2007-011. Mar. 2007. URL: http://www-library.desy.de/cgi-bin/showprep.pl?desy-thesis-07-011.

[76] M. Titov, M. Hohlmann, C. Padilla, et al. "Summary and Outlook of the International Workshop on Aging Phenomena in Gaseous Detectors (DESY, Hamburg, October 2001)." In: *Nuclear Science, IEEE Transactions on* 49.4 (Aug. 2002), pp. 1609–1621. DOI: 10.1109/TNS.2002.801666.

[77] J. Adam, C. Baird, D. Cockerill, et al. "A study of ageing effects in wire chambers." In: *Nucl. Instr. and Meth. A* 217.1–2 (1983), pp. 291–297. ISSN: 0167-5087. DOI: 10.1016/0167-5087(83)90151-5.

[78] T. Akesson, E. Barberio, V. Bondarenko, et al. "Aging studies for the ATLAS Transition Radiation Tracker (TRT)." In: *Nucl. Instr. and Meth. A* 515.1–2 (2003), pp. 166–179. DOI: 10.1016/j.nima.2003.08.145.

[79] L. Malter. "Thin Film Field Emission." In: *Phys. Rev.* 50 (1 July 1936), pp. 48–58. DOI: 10.1103/PhysRev.50.48.

[80] M. Alfonsi, S. Baccaro, G. Bencivenni, et al. "Studies of Etching Effects on Triple-GEM Detectors Operated With CF_4-Based Gas Mixtures." In: *Nuclear Science, IEEE Transactions on* 52.6 (Dec. 2005), pp. 2872–2878. DOI: 10.1109/TNS.2005.855640.

[81] J. Miyamoto and I.P.J. Shipsey. "An aging study of semiconductive microstrip gas chambers and a gas electron multiplier." In: *Nuclear Physics B - Proceedings Supplements* 78.1–3 (1999), pp. 695–702. DOI: 10.1016/S0920-5632(99)00626-X.

[82] M.C. Altunbas, K. Dehmelt, S. Kappler, et al. "Aging measurements with the Gas Electron Multiplier (GEM)." In: *Nucl. Instr. and Meth. A* 515.1–2 (2003), pp. 249–254. DOI: 10.1016/j.nima.2003.09.006.

[83] M. Alfonsi, G. Bencivenni, P. de Simone, et al. "Aging measurements on triple-GEM detectors operated with CF4-based gas mixtures." In: *Nuclear Physics B - Proceedings Supplements* 150.0 (2006), pp. 159–163. DOI: 10.1016/j.nuclphysbps.2005.03.054.

[84] M. Capéans-Garrido, S. Konovalov, and A. Romaniouk. *About aging of gas detectors: a compilation of some validation studies carried out for LHC*. Tech. rep. PH-EP-Tech-Note-2009-002. CERN, Feb. 2009. URL: http://cdsweb.cern.ch/record/1164402.

[85] R. Kotthaus. "A laboratory study of radiation damage to drift chambers." In: *Nucl. Instr. and Meth. A* 252.2–3 (1986), pp. 531–544. DOI: 10.1016/0168-9002(86)91237-4.

[86] M. Capeans. "Aging and materials: lessons for detectors and gas systems." In: *Nucl. Instr. and Meth. A* 515.1–2 (2003), pp. 73–88. DOI: 10.1016/j.nima.2003.08.134.

[87] M. Capeans. "Recent aging studies for the ATLAS transition radiation tracker." In: *IEEE NSS CR*. Vol. 5. Oct. 2003, pp. 3709–3713. DOI: 10.1109/NSSMIC.2003.1352712.

[88] H. Yasuda. "New insights into aging phenomena from plasma chemistry." In: *Nucl. Instr. and Meth. A* 515.1–2 (2003), pp. 15–30. DOI: 10.1016/j.nima.2003.08.125.

[89] J. Va'Vra. "Review of wire chamber aging." In: *Nucl. Instr. and Meth. A* 252.2–3 (1986), pp. 547–563. DOI: 10.1016/0168-9002(86)91239-8.

[90] J. A. Kadyk. "Wire chamber aging." In: *Nucl. Instr. and Meth. A* 300.3 (1991), pp. 436–479. DOI: 10.1016/0168-9002(91)90381-Y.

[91] R. Veenhof. "Choosing a gas mixture for the ALICE TPC." In: *ALICE Internal Note/TPC* 29 (2003). URL: http://www-linux.gsi.de/~jcastill/docs/REF04-Choosing_Veenhof.pdf.

[92] Star Collaboration. *Star Conceptual Design Report*. 1992. URL: http://drupal.star.bnl.gov/STAR/starnotes/public/sn0499.

[93] W.B. Atwood, T. Barczewski, L.A.T. Bauerdick, et al. "Performance of the ALEPH Time Projection Chamber." In: *Nucl. Instr. and Meth. A* 306.3 (1991), pp. 446–458. DOI: 10.1016/0168-9002(91)90038-R.

[94] J. Alme, Y. Andres, H. Appelshäuser, et al. "The ALICE TPC, a large 3-dimensional tracking device with fast readout for ultra-high multiplicity events." In: *Nucl. Instr. and Meth. A* 622.1 (2010), pp. 316–367. DOI: 10.1016/j.nima.2010.04.042.

[95] N. Abgrall, B. Andrieu, P. Baron, et al. "Time projection chambers for the T2K near detectors." In: *Nucl. Instr. and Meth. A* 637.1 (2011), pp. 25–46. DOI: 10.1016/j.nima.2011.02.036.

[96] C. Garabatos. "The ALICE TPC." In: *Nucl. Instr. and Meth. A* 535.1–2 (2004). Proceedings of the 10th International Vienna Conference on Instrumentation. DOI: 10.1016/j.nima.2004.07.127.

[97] A. Bamberger, C. Brezina, K. Desch, et al. "Status of the Bonn R&D Activities for a Pixel Based TPC." In: *EUDET Memo* 34 (2007). URL: http://www.eudet.org/e26/e28/e182/e595/eudet-memo-2007-34.pdf.

[98] H. Blank, C. Brezina, K. Desch, et al. "Update to the Status of the Bonn R&D Activities for a Pixel Based TPC." In: *EUDET Memo* 30 (2008). URL: http://www.eudet.org/e26/e28/e615/e806/eudet-memo-2008-30.pdf.

[99] *TESLA Technical Design Report*. DESY. Mar. 2001. URL: http://tesla.desy.de/new_pages/TDR_CD/start.html.

[100] F. Müller. "Inbetriebnahme und erste Messungen eines Gaschromatographen zur Gasanalyse von Ionisationsdetektoren." Aug. 2008. URL: http://lhc-ilc.physik.uni-bonn.de/thesis.php.

[101] *EL-FLOW brochure*. Bronkhorst High-Tech B.V. 2008.

[102] K. Komiya, F. Higuchi, and K. Ohtani. "Characteristics of a thermal gas flowmeter." In: *Rev. Sci. Instrum.* 59.3 (1988), pp. 477–479. DOI: 10.1063/1.1139864.

[103] H. J. Boer. "Precision mass flow metering for CVD applications." In: *J. Phys. IV France* 09.PR8 (1999), pp. 869–876. DOI: 10.1051/jp4:19998109.

[104] D. Güleryüz, W. Smetana, H. Homolka, et al. "Aspects Concerning the Optimization of a Calorimetric Flow Sensor Built Up in Thick-Film Technology." In: *28th Int. Spring Seminar on Electronics Technology*. Vol. 19–20. 2005, pp. 384–390. DOI: 10.1109/ISSE.2005.1491059.

[105] *Kenics Helical Mixer*. Public Domain. Wikimedia, 2009.

[106] *Principle of a Static Mixer*. Samhwamix Co., LTD. 2009.

[107] *TF Series Panametrics Aluminum Oxide Moisture Probe*. GE Industrial, Sensing. 2005.

[108] A. L. Buck. "New Equations for Computing Vapor Pressure and Enhancement Factor." In: *Journal of Applied Meteorology* 20.12 (1981), pp. 1527–1532. DOI: 10.1175/1520-0450(1981)020<1527:NEFCVP>2.0.CO;2.

[109] D. Sonntag. "Important new values of the physical constants of 1986 , vapour pressure formulations based on the ITS-90, and psychrometer formulae." In: *Zeitschrift für Meteorologie* 40.5 (1990), pp. 340–344. ISSN: 0084-5361.

[110] *Humidity Conversion Formulas*. Vaisala Oyj. 2012. URL: http://www.vaisala.com/Vaisala%20Documents/Application%20notes/Humidity_Conversion_Formulas_B210973EN-D.pdf.

[111] *Manual for 3190 Series Trace Oxygen Analyzer*. Teledyne Analytical Instruments. 1999.

[112] W. Umrath. *Fundamentals of Vacuum Technology*. Oerlikon Leybold Vacuum GmbH, June 2007. URL: http://www.oerlikon.com/leyboldvacuum/ecomaXL/oe_VACUUM_EN_Download_Fundamentals_Vacuum_Technology.

[113] D. Linzmaier. "Development of a Monitor System for Gas Based Detectors and Measurement of Electron Attachment in the Chamber Gas." DESY-THESIS-09-003. Oct. 2008. URL: http://www-library.desy.de/cgi-bin/showprep.pl?desy-thesis-09-003.

[114] A. Gil, M. Ball, S. Carcel, et al. "Slow Control System for a NEXT-TPC prototype." In: *Real Time Conference, 16th IEEE-NPSS*. May 2009, pp. 110–112. DOI: 10.1109/RTC.2009.5322144.

[115] C. Krieger. "Construction and First Measurements of a GridPix based X-ray Detector." BONN-IB-2012-05. Oct. 2011. URL: http://lhc-ilc.physik.uni-bonn.de/thesis.php.

[116] M.S. Dixit, J. Dubeau, J.-P. Martin, et al. "Position sensing from charge dispersion in micro-pattern gas detectors with a resistive anode." In: *Nucl. Instr. and Meth. A* 518.3 (2004), pp. 721–727. DOI: 10.1016/j.nima.2003.09.051.

[117] D.C. Arogancia, A.M. Bacala, K. Boudjemline, et al. "Study in a beam test of the resolution of a Micromegas TPC with standard readout pads." In: *Nucl. Instr. and Meth. A* 602.2 (2009), pp. 403–414. DOI: 10.1016/j.nima.2009.01.014.

[118] R. Bellazzini, F. Angelini, L. Baldini, et al. "Reading a GEM with a VLSI pixel ASIC used as a direct charge collecting anode." In: *Proceedings of the 10th International Vienna Conference on Instrumentation*. Vol. 535. 1–2. 2004, pp. 477–484. DOI: 10.1016/j.nima.2004.07.269.

[119] P. Colas, A.P. Colijn, A. Fornaini, et al. "The readout of a GEM or Micromegas-equipped TPC by means of the Medipix2 CMOS sensor as direct anode." In: *Proceedings of the 10th International Vienna Conference on Instrumentation*. Vol. 535. 1–2. 2004, pp. 506–510. DOI: 10.1016/j.nima.2004.07.180.

[120] X. Llopart, M. Campbell, R. Dinapoli, et al. "Medipix2: A 64-k Pixel Readout Chip With 55-μm Square Elements Working in Single Photon Counting Mode." In: *IEEE TNS* 49.5 (Oct. 2002), pp. 2279–2283. DOI: 10.1109/TNS.2002.803788.

[121] I. Perić, L. Blanquart, G. Comes, et al. "The FEI3 readout chip for the ATLAS pixel detector." In: *Proceedings of the International Workshop on Semiconductor Pixel Detectors for Particles and Imaging*. Vol. 565. 1. 2006, pp. 178–187. DOI: 10.1016/j.nima.2006.05.032.

[122] A. Bamberger, K. Desch, U. Renz, et al. "Triple-GEM operated in different Gases with highly pixelated Readout using MediPix2 Chip." In: *Proceedings of the 10th Pisa Meeting on Advanced Detectors*. Vol. 572. 1. 2007, pp. 157–159. DOI: 10.1016/j.nima.2006.10.354.

[123] A. Bamberger, K. Desch, U. Renz, et al. "Readout of GEM detectors using the Medipix2 CMOS Pixel Chip." In: *Nucl. Instr. and Meth. A* 573.3 (2007), pp. 361–370. DOI: 10.1016/j.nima.2006.12.049.

[124] A. Bamberger, K. Desch, U. Renz, et al. "Resolution Studies on 5GeV Electron Tracks observed with triple-GEM and MediPix2/TimePix-readout." In: *Proceedings of the 11th International Vienna Conference on Instrumentation*. Vol. 581. 1–2. 2007, pp. 274–278. DOI: 10.1016/j.nima.2007.07.118.

[125] T. Kim, M. Freytsis, J. Button-Shafer, et al. "Readout of TPC tracking chambers with GEMs and pixel chip." In: *Nucl. Instr. and Meth. A* 589.2 (2008), pp. 173–184. DOI: 10.1016/j.nima.2008.02.049.

[126] J. Kaminski, M. Killenberg, A. Bamberger, et al. "Time projection chamber with triple GEM and pixel readout." In: *IEEE NSS CR*. Oct. 2008, pp. 2926–2929. DOI: 10.1109/NSSMIC.2008.4774978.

[127] C. Brezina, K. Desch, J. Kaminski, et al. "A Time Projection Chamber with triple GEM and pixel readout." In: *1st International Conference on Micro-Pattern Gaseous Detectors*. Vol. 4. 11. 2009, P11015. DOI: 10.1088/1748-0221/4/11/P11015.

[128] J. Kaminski, C. Brezina, K. Desch, et al. "Time projection chamber with triple GEM and highly granulated pixel readout." In: *Conf.Proc.* C0908171 (2009), pp. 533–535. DOI: 10.3204/DESY-PROC-2010-04/P47.

[129] C. Brezina, K. Desch, J. Kaminski, et al. "Operation of a GEM-TPC with pixel readout." In: *IEEE NSS CR*. Oct. 2011, pp. 1006–1013. DOI: 10.1109/NSSMIC.2011.6154310.

[130] C. Brezina, K. Desch, J. Kaminski, et al. "Operation of a GEM-TPC With Pixel Readout." In: *IEEE TNS* 59.6 (Dec. 2012), pp. 3221–3228. DOI: 10.1109/TNS.2012.2220981.

[131] M. Ummenhofer. "Inbetriebnahme einer Zeitprojektionskammer mit Pixel-Auslese." University Bonn, 2008. URL: http://lhc-ilc.physik.uni-bonn.de/thesis/Ummenhofer.pdf.

[132] S. Zimmermann. "Data Reconstruction and Analysis of GEM-Based Time Projection Chambers with Pixel Readout." University Bonn, 2008. URL: http://lhc-ilc.physik.uni-bonn.de/thesis/DiplomarbeitSimoneZimmermann.pdf.

[133] R. Ulman. "Calibration of the Timepix pixel chip for the readout of gaseous particle detectors." University Bonn, 2011. URL: http://lhc-ilc.physik.uni-bonn.de/thesis/UlmanThesis.pdf.

[134] S. Blatt. "Konstruktion und Inbetriebnahme eines Feldkäfigs für eine TPC." RWTH Aachen, 2004. URL: http://web.physik.rwth-aachen.de/~tpcmgr/downloads/theses/diplomarbeit-blatt.pdf.

[135] X. Llopart Cudie. "Design and Characterization of 64k Pixels Chips Working in Single Photon Processing Mode." Mid Sweden University, Sundsvall, 2007. ISBN: 978-91-85317-56-1. URL: http://cdsweb.cern.ch/record/1056683.

[136] F. Krummenacher. "Pixel detectors with local intelligence: an IC designer point of view." In: *Nucl. Instr. and Meth. A* 305.3 (1991), pp. 527–532. DOI: 10.1016/0168-9002(91)90152-G.

[137] H. Träff. "Novel approach to high speed CMOS current comparators." In: *Electronics Letters* 28.3 (Jan. 1992), pp. 310–312. DOI: 10.1049/el:19920192.

[138] D. San Segundo Bello, M. van Beuzekom, P. Jansweijer, et al. "An interface board for the control and data acquisition of the Medipix2 chip." In: *Nucl. Instr. and Meth. A* 509.1–3 (2003), pp. 164–170. DOI: 10.1016/S0168-9002(03)01566-3.

[139] Z. Vykydal, J. Jakubek, and S. Pospisil. "USB interface for Medipix2 pixel device enabling energy and position-sensitive detection of heavy charged particles." In: *7th International Workshop on Radiation Imaging Detectors, Grenoble*. Vol. 563. 1. 2006, pp. 112 –115. DOI: 10.1016/j.nima.2006.01.114.

[140] Z. Vykydal and J. Jakubek. "USB Lite – Miniaturized readout interface for Medipix2 detector." In: *11th International Workshop on Radiation Imaging Detectors, Prague*. Vol. 633, Supplement 1. 2011, S48–S49. DOI: 10.1016/j.nima.2010.06.118.

[141] J. Visser, B. van der Heijden, S.J.A. Weijers, et al. "A Gigabit per second read-out system for Medipix Quads." In: *11th International Workshop on Radiation Imaging Detectors, Prague*. Vol. 633, Supplement 1. 2011, S22–S25. DOI: 10.1016/j.nima.2010.06.110.

[142] M. Platkevic, J. Jakubek, and Z. Vykdal. "RUIN – rapid universal interface for medipix detector." In: *IEEE NSS CR*. Oct. 2008, pp. 2185–2187. DOI: 10.1109/NSSMIC.2008.4774785.

[143] V. Kraus, M. Holik, J. Jakubek, et al. "FITPix – fast interface for Timepix pixel detectors." In: *12th International Workshop on Radiation Imaging Detectors, Cambridge*. Vol. 6. 1. 2011. DOI: 10.1088/1748-0221/6/01/C01079.

[144] J. Vallerga, R. Raffanti, A. Tremsin, et al. "MCP detector read out with a bare quad Timepix at kilohertz frame rates." In: *JInst* 6.1 (2011). DOI: 10.1088/1748-0221/6/01/C01049.

[145] T. Holy, J. Jakubek, S. Pospisil, et al. "Data acquisition and processing software package for Medipix2." In: *Nucl. Instr. and Meth. A* 563.1 (2006), pp. 254–258. DOI: 10.1016/j.nima.2006.01.122.

[146] D. Turecek, T. Holy, J. Jakubek, et al. "Pixelman: a multi-platform data acquisition and processing software package for Medipix2, Timepix and Medipix3 detectors." In: *12th International Workshop on Radiation Imaging Detectors, Cambridge*. Vol. 6. 1. 2011. DOI: 10.1088/1748-0221/6/01/C01046.

[147] X. Llopart. *Timepix Manual*. 2006.

[148] J. Jakubek, A. Cejnarova, T. Holy, et al. "Pixel detectors for imaging with heavy charged particles." In: *9th International Workshop on Radiation Imaging Detectors, Erlangen*. Vol. 591. 1. 2008, pp. 155–158. DOI: 10.1016/j.nima.2008.03.091.

[149] J. Jakubek. "Precise energy calibration of pixel detector working in time-over-threshold mode." In: *11th International Workshop on Radiation Imaging Detectors, Prague*. Vol. 633, Supplement 1. 2011, S262–S266. DOI: 10.1016/j.nima.2010.06.183.

[150] V. Kroner. "Signal development and pad-size studies in a GEM TPC with pixel readout." Nov. 2012. URL: http://lhc-ilc.physik.uni-bonn.de/thesis.php.

[151] I.B. Smirnov. "Modeling of ionization produced by fast charged particles in gases." In: *Nucl. Instr. and Meth. A* 554.1–3 (2005), pp. 474–493. DOI: 10.1016/j.nima.2005.08.064.

[152] J.J. Beatty, J. Matthews, T.K. Gaisser, et al. "Cosmic rays." In: *Review of Particle Physics*. Particle Data Group, 2012. URL: http://pdg.lbl.gov/.

[153] S.F. Biagi. "Monte Carlo simulation of electron drift and diffusion in counting gases under the influence of electric and magnetic fields." In: *Nucl. Instr. and Meth. A* 421.1–2 (1999), pp. 234–240. DOI: 10.1016/S0168-9002(98)01233-9.

[154] J. Abernathy, K. Dehmelt, R. Diener, et al. "MarlinTPC: A common Software Framework for TPC Development." In: *IEEE NSS CR*. Oct. 2008, pp. 1704–1708. DOI: 10.1109/NSSMIC.2008.4774731.

[155] A. Deisting. "Rekonstruktion von Ladungsdepositionen in einer GEM-Pixel-TPC mit einem Algorithmus aus der Astronomie." Feb. 2012. URL: http://lhc-ilc.physik.uni-bonn.de/thesis.php.

[156] M. Schultens. "Teststrahlmessungen mit hochgranularer Auslese einer Zeitprojektionskammer bei verschiedenen Pixelgrößen." Sept. 2010. URL: http://lhc-ilc.physik.uni-bonn.de/thesis.php.

[157] F. Müller. "Commissioning and Characterization of a TPC with InGrid based Readout." Nov. 2011. URL: http://lhc-ilc.physik.uni-bonn.de/thesis.php.

[158] R.K. Carnegie, M.S. Dixit, J. Dubeau, et al. "Resolution studies of cosmic-ray tracks in a TPC with GEM readout." In: *Nucl. Instr. and Meth. A* 538.1–3 (2005), pp. 372–383. DOI: 10.1016/j.nima.2004.08.132.

[159] T. Holstein. "Imprisonment of Resonance Radiation in Gases." In: *Phys. Rev.* 72 (12 Dec. 1947), pp. 1212–1233. DOI: 10.1103/PhysRev.72.1212.

[160] T. Holstein. "Imprisonment of Resonance Radiation in Gases. II." In: *Phys. Rev.* 83 (6 Sept. 1951), pp. 1159–1168. DOI: 10.1103/PhysRev.83.1159.

[161] H. Schindler and R. Veenhof. *Garfield++*. URL: http://garfieldpp.web.cern.ch/garfieldpp/.

[162] R. Veenhof. "Garfield, recent developments." In: *Nucl. Instr. and Meth. A* 419.2–3 (1998), pp. 726–730. DOI: 10.1016/S0168-9002(98)00851-1.

[163] *CST Studio Suite*. URL: http://www.cst.com/Content/Products/CST_S2/Overview.aspx.

[164] *Synopsis TCAD*. URL: http://www.synopsys.com/Tools/TCAD/Pages/default.aspx.

[165] *Elmer*. URL: http://www.csc.fi/english/pages/elmer.

[166] *ANSYS*. URL: http://www.ansys.com/Products.

[167] M. Alfonsi, G. Croci, S. Duarte Pinto, et al. "Simulation of the dielectric charging-up effect in a GEM detector." In: *Nucl. Instr. and Meth. A* 671.0 (2012), pp. 6–9. DOI: 10.1016/j.nima.2011.12.059.

[168] L. Rossi, P. Fischer, T. Rohe, et al. *Pixel Detectors*. Springer, 2006. ISBN: 978-3-540-28333-1.

[169] M. Campbell, E.H.M. Heijne, X. Llopart, et al. "GOSSIP: A vertex detector combining a thin gas layer as signal generator with a CMOS readout pixel array." In: *Nucl. Instr. and Meth. A* 560.1 (2006), pp. 131–134. DOI: 10.1016/j.nima.2005.11.199.

[170] H. van der Graaf. "GridPix: An integrated readout system for gaseous detectors with a pixel chip as anode." In: *Nucl. Instr. and Meth. A* 580.2 (2007), pp. 1023–1026. DOI: 10.1016/j.nima.2007.06.096.

[171] Y. Bilevych, V.M. Blanco Carballo, M. van Dijk, et al. "Angular resolution of the gaseous micro-pixel detector Gossip." In: *Proceedings of the 12th Topical Seminar on Innovative Particle and Radiation Detectors*. Vol. 215. 1. 2011, pp. 51–55. DOI: 10.1016/j.nuclphysbps.2011.03.132.

[172] M. Campbell, M. Chefdeville, P. Colas, et al. "Detection of single electrons by means of a Micromegas-covered MediPix2 pixel CMOS readout circuit." In: *Nucl. Instr. and Meth. A* 540.2–3 (2005), pp. 295–304. DOI: 10.1016/j.nima.2004.11.036.

[173] M. Chefdeville, P. Colas, Y. Giomataris, et al. "An electron-multiplying 'Micromegas' grid made in silicon wafer post-processing technology." In: *Nucl. Instr. and Meth. A* 556.2 (2006), pp. 490–494. DOI: 10.1016/j.nima.2005.11.065.

[174] H. van der Graaf, F. Hartjes, and A. Romaniouk. "Performance and prospects of GridPix and Gossip detectors." In: *ATLAS note* ATL-P-MN-0016 (June 2009). URL: https://edms.cern.ch/file/808572/1/GossipBackupNoteV2-2.pdf.

[175] V. Gromov, R. Kluit, and H. van der Graaf. "Prototype of the front-end circuit for the GOSSIP (Gas On Slimmed Silicon Pixel) chip in the 0.13 µm CMOS technology." In: *12th Workshop on Electronics For LHC and Future Experiments* (2006). URL: http://cdsweb.cern.ch/record/1027474.

[176] R. Kluit, H. van der Graaf, and V. Gromov. "Development of a small-scale protope of the GOSSIPO-2 chip in 0.13 µm CMOS technology." In: *Topical Workshop on Electronics for Particle Physics* (2007). URL: http://cdsweb.cern.ch/record/1091456.

[177] C. Brezina, K. Desch, H. van der Graaf, et al. "GOSSIPO 3 - A front-end pixel chip prototype for readout of MPGDs." In: *EUDET Memo* 02 (2009). URL: http://www.eudet.org/e26/e28/e42441/e69295/EUDET-MEMO-2009-02.pdf.

[178] C. Brezina, K. Desch, H. van der Graaf, et al. "Gossipo-3: A prototype of a Front-End Pixel Chip for Read-Out of Micro-Pattern Gas Detectors." In: *TWEPP-09: Topical Workshop on Electronics for Particle Physics*. Sept. 2009, pp. 113–116. URL: http://cdsweb.cern.ch/record/1234879.

[179] A. Kruth, C. Brezina, S. Celik, et al. "GOSSIPO-3: measurements on the prototype of a read-out pixel chip for Micro-Pattern Gaseous Detectors." In: *Journal of Instrumentation* 5.12 (2010). DOI: 10.1088/1748-0221/5/12/C12005.

[180] H. Krüger and J. Schneider. *S3MultiIOSystem*. 2009. URL: http://icwiki.physik.uni-bonn.de/twiki/bin/view/Systems/S3MultiIOSystem.

[181] P.M. Alicea-Morales, C.J. Ortiz-Villanueva, R. Perez, et al. "Design of an Adjustable, Low Voltage, Low Dropout Regulator." In: *Devices, Circuits and Systems, 2004. Proceedings of the Fifth IEEE International Caracas Conference on*. Vol. 1. Nov. 2004, pp. 289–292. DOI: 10.1109/ICCDCS.2004.1393399.

[182] B.M. King. "Understanding the load-transient response of LDOs." In: *Analog Applications Journal* 11 (2000). URL: http://www.ti.com/lit/an/slyt151/slyt151.pdf.

[183] P.R. Gray, P.J. Hurst, S.H. Lewis, et al. *Analysis and Design of Analog Integrated Circuits*. John Wiley & Sons, 2001. ISBN: 978-0471321682.

[184] G.A. Rincón-Mora. "Current Efficient Low Voltage Low Dropout Regulators." Nov. 1996. URL: http://users.ece.gatech.edu/rincon-mora//publicat/books/thesis/.

[185] J.C. Teel. "Understanding power supply ripple rejection in linear regulators." In: *TI Analog Applications Journal* 4 (2005). URL: http://www.ti.com/lit/an/slyt202/slyt202.pdf.

[186] J.C. Teel. "Understanding noise in linear regulators." In: *TI Analog Applications Journal* 4 (2005). URL: http://ti.com/lit/an/slyt201/slyt201.pdf.

[187] P.E. Allen and D.R. Holberg. *CMOS Analog Circuit Design*. Oxford University Press, 2002. ISBN: 978-0195116441.

[188] A. Kruth. CMOS Analogue Design Engineer. URL: http://www.xing.com/profile/Andre_Kruth.

[189] V. Gromov. ASIC Design Engineer at NIKHEF (Amsterdam). URL: http://www.nikhef.nl/~vgromov/.

[190] A.A. Aarts, V.M. Blanco Carballo, M. Chefdeville, et al. "Discharge Protection and Ageing of Micromegas Pixel Detectors." In: *IEEE NSS CR*. Vol. 6. Nov. 2006, pp. 3865–3869. DOI: 10.1109/NSSMIC.2006.353833.

[191] V.M. Blanco Carballo. "Radiation Imaging Detectors Made by Wafer Post-processing of CMOS Chips." June 2009. ISBN: 978-90-365-2855-9. URL: http://doc.utwente.nl/61528/.

[192] A.Z. Wang, H.G. Feng, K. Gong, et al. "On-chip ESD protection design for integrated circuits: an overview for IC designers." In: *Microelectronics Journal* 32.9 (2001), pp. 733–747. DOI: 10.1016/S0026-2692(01)00060-X.

[193] H. van der Graaf. private comunication.

[194] F. Zappon, M. van Beuzekom, V. Gromov, et al. "GOSSIPO-4: an array of high resolution TDCs with a PLL control." In: *JInst* 7.01 (2012). DOI: 10.1088/1748-0221/7/01/C01081.

[195] A. Kruth, G. Ahluwalia, D. Arutinov, et al. "Charge Pump Clock Generation PLL for the Data Output Block of the Upgraded ATLAS Pixel Front-End in 130 nm CMOS." In: *TWEPP-09: Topical Workshop on Electronics for Particle Physics*. Sept. 2009, pp. 548–552. URL: http://cdsweb.cern.ch/record/1235880.

[196] R. Ballabriga, M. Campbell, E. Heijne, et al. "Medipix3: A 64 k pixel detector readout chip working in single photon counting mode with improved spectrometric performance." In: *Nucl. Instr. and Meth. A* 633, Supplement 1.0 (2011), S15–S18. DOI: 10.1016/j.nima.2010.06.108.

[197] V. Gromov, M. van Beuzekom, R. Kluit, et al. "Development and Applications of the Timepix3 Readout Chip." In: *Proceedings of Science: Vertex 2011*. June 2011. URL: http://pos.sissa.it/archive/conferences/137/046/Vertex%202011_046.pdf.